

HEAT AND MASS TRANSFER IN TUBULAR INORGANIC MEMBRANES

ARSHAD HUSSAIN



**Fakultät für Verfahrens-und Systemtechnik
Otto-von-Guericke Universität Magdeburg**

Heat and Mass Transfer in Tubular Inorganic Membranes

Dissertation

zur Erlangung des akademischen Grades

**Doktoringenieur
(Dr.-Ing.)**

**genehmigt durch die Fakultät für Verfahrens- und Systemtechnik
der Otto-von-Guericke-Universität Magdeburg**

von **M.Sc. Arshad Hussain**
geb. am 03. August 1970 in Kot-Adu, Pakistan

Gutachter:
Prof. Dr.-Ing. habil. E. Tsotsas
Prof. Dr.-Ing. habil. Andreas Seidel-Morgenstern

Promotionskolloquium am 27.06.2006

Progress lies not in enhancing what is, but in advancing toward what will be.

Khalil Gibran

ACKNOWLEDGEMENTS

First and foremost, I wish to express my sincere gratitude to Prof. Dr.-Ing. E. Tsotsas for giving me the opportunity to conduct research in this area. His enlightened mentoring was vital and inspiring for the accomplishment of this work. What I appreciate the most is his tireless support to formally complete my dissertation.

I also wish to express my appreciation and gratitude to my co-supervisor Prof. Dr.-Ing- A. Seidel-Morgenstern for providing me constructive suggestions and guidance during all times. His help and support was primal for the completion of this work.

Mr. D. Kürschner deserves special thanks for providing me technical support in carrying out the essential experimental work.

I wish, furthermore to acknowledge the help received from Dr.-Ing. M. Peglow, Mr. C. Kettner, Mrs. N. Degen, Ms M. Hesse, Mr. I. Farooq, Dr.-Ing. S. Thomas, Dr.-Ing. M. Mangold and Mr. V. Surasani. My thanks go to all my colleagues at the institute of process engineering and in the membrane research group for their support and comprehensive discussions. I am also thankful to all my friends for their help and moral support during my stay abroad.

Last but not least, I am happy to express my thanks to my family for their love, support and understanding, which deserve to be mentioned specially.

Index

1	Introduction	1
1.1	Membrane reactors	2
1.2	Membranes	6
1.2.1	Inorganic membrane formation	8
1.2.2	Membrane formation from sol-gel systems	9
1.2.2.1	Catalytic membranes	10
1.2.2.2	Inert asymmetric membranes	10
1.3	Starting point and objectives	12
2	Experimental methods and modelling	16
2.1	Experimental set-up	16
2.2	Materials	19
2.3	Experimental matrix	22
2.4	Modelling	24
2.4.1	Heat transfer model	24
2.4.2	Modelling mass transfer in porous media	26
2.4.3	Modes of gas transport in porous media	28
2.4.3.1	Knudsen flow	29
2.4.3.2	Molecular diffusion	31
2.4.3.3	Viscous flow in porous media	33
2.4.4	Combination of transport mechanisms for binary mixtures	35
2.4.5	Mass transfer model	38
3	Heat transfer	41
3.1	Identification experiments: Steady state heat transfer	41
3.2	Validation experiment: Transient heat transfer	49
4	Mass transfer	52
4.1	Identification experiment: Single gas permeation	52
4.1.1	Influence of membrane asymmetry	65
4.1.2	Influence of top layer	69
4.2	Validation experiment: Isobaric diffusion	75

4.3	Validation experiment: Transient diffusion	80
5	Combined heat and mass transfer	83
5.1	Influence of gas inlet temperature	85
5.2	Comparison between isothermal and non-isothermal case	93
5.3	Influence of shell temperature	95
5.4	Simulation results for the case of ethane-oxygen	96
5.5	Influence of heat transfer coefficient	98
6	General analysis of diffusion process	101
6.1	Non-dimensional form of the model equations	101
6.2	Non-dimensional analysis	104
6.2.1	Influence of axial dispersion coefficient	104
6.2.2	Influence of volumetric flow rate	108
6.2.3	Influence of temperature	111
7	Conclusion	114
8	Nomenclature	116
9	References	119
	Appendix A: Structured process modelling in ProMoT	130
A.1	Structured process modelling in ProMoT	130
A.2	Network theory	130
A.2.1	Process structuring levels	132
A.3	Process modelling tool (ProMoT) and simulating tool (DIVA)	133
	Appendix B: Analytical solution of 1D heat transfer equation	135
	Appendix C: Heat and mass transfer coefficients	139
	Appendix D: Experimental data	146
	Appendix F: List of equipment	165

Abstract

In this work heat and mass transfer in tubular asymmetric ceramic membranes suitable for applications in membrane reactors have been investigated. An experimental matrix has been employed to quantify the heat and mass transfer in the membrane, which leads to the identification and validation of respective parameters in a comprehensive and consistent manner. Two types of membranes have been investigated for the characterisation of their transport parameters. However, the main part of experiments have been carried out with the larger membranes (inner diameter of 21 mm), which were closer to realistic dimensions for application on industrial scale. Thermal conductivity of the membrane has been identified and validated by the steady state and dynamic heat transfer experiments. The structural parameters of the composite membrane (mass transfer parameters) are identified by single gas permeation experiments and validated by isobaric steady state and transient diffusion experiments. The mentioned single gas permeation experiments have been conducted for every composite, precursor and intermediate, starting from the support. The application of dusty gas model enables to understand and predict the influences of temperature, pressure and molar mass of the gas. It has been further shown that the characterisation of every single layer of the composite membrane is important.

A simulation analysis has been carried out to see the influence of flow direction and top layer on the mass transfer through the membrane, which reveals that the choice of flow direction may be significant, especially when employing the membrane for the selective dosing of educts in a catalytic reactor. Also the choice of the material of permselective layer is substantial in terms of fluxes and pressure drop in every individual layer.

A non-dimensional analysis of isobaric diffusion, based on simulations, shows the influences of axial dispersion, volumetric flow rate and temperature on the isobaric diffusion process in terms of mole fraction and gas flow rates. The consideration of axial dispersion may be substantial for reactions, where controlled dosing of educts is desired.

While identification and validation of membrane transport parameters are one important aspect, the work also shows that membrane reactor configurations can be reliably modelled in the limiting case without chemical reaction. Even in this case, thermal effects and the interrelation between heat and mass transfer should be accounted for.

1 Introduction

Chemical industry is persistently pushed towards more efficient processing in chemical reactors due to increased economical and environmental pressure on it. It is desired to convert the expensive feedstock more completely by reducing the unwanted by-products and effective management of energy requirement. These goals can be accomplished by employing a multifunctional reactive system within a chemical reactor. Multifunctional reactive concept offers the combination of several functions or processes to occur simultaneously, aimed at achieving an optimal integration of heat and mass transfer processes within a single reactor vessel. The integration of different possible unit operations is advantageous not only in terms of process simplification and lower capital costs but also improvement in the utilization of heat and mass transfer processes for an optimised reaction scheme. As the majority of chemical compounds is produced predominantly by catalytic reactions in the chemical process and refining industry, so the active research is focused on the process intensification of catalytic reactions by employing multifunctional reactive concept. A multifunctional approach is more successful when integrating clearly defined macroscopic phenomena into the reactor operation, as the underlying process can be reliably modelled, permitting one to identify suitable operating conditions and possible advantages over traditional operations [1].

Multifunctional reactors can be classified in terms of

- 1) the type and direction of the predominant heat and mass transfer process (by considering diffusive or convective transport mechanisms for heat or mass parallel or perpendicular to the flow direction),
- 2) coupling of endothermic and exothermic reactions (auto-thermal multifunctional reactor [2]),
- 3) the taxonomy that just combines the reaction with various unit operations of chemical engineering, i.e. absorption, crystallization, distillation, extraction, pervaporation etc.
- 4) the interaction between the various participating phases and mixing modalities within the reactor.

A common feature of the multifunctional reactors covered in this classification scheme is their potential to attain more favourable temperature and concentration profiles in the reactor. Though a broad variety of multifunctional reactors, like catalytic wall reactors or membrane reactors, are employed in many catalytic reactions, the development of truly multifunctional reactors with more than one additional functionality is still in its infancy [1].

1.1 Membrane reactors

Membrane reactors can be attributed to the group of multifunctional reactors combining chemical reactions and separation in a single unit, consequently offering a great potential to replace the traditional, pollution-prone and energy consuming separation processes. The combination of reaction and separation upon a membrane was suggested by Michaels [2,3]; the goal was to attain higher conversions by overcoming the equilibrium limitations through the selective permeation of the reaction product(s).

Membrane reactors usually consist of two chambers separated by a membrane. The membrane acts as a physical barrier (or a catalyst too) between the reactants which are fed to the two sides of the membrane respectively. The reactants diffuse into the membrane and a reaction takes place when the reactants meet. If the reaction rate is fast compared to the mass transfer rate, a small reaction zone will exist at a place determined by the stoichiometry of the reaction, the diffusion coefficients and the concentration of the reactants. Variation of concentration of one of the reactants results in a shift of the reaction zone without affecting the stoichiometry of the reaction. This property makes the reactor attractive for performing reactions that require a strict stoichiometric feed of reactants.

Another application of this type of membrane reactor is for kinetically fast, strongly exothermic heterogeneous reaction. These reactions are often accompanied with severe problems like formation of explosive mixtures and the occurrence of thermal runaways (with more or less destructive effects). By introducing the reactants on both sides of the membrane, premixing of the reactants is avoided and therefore the above mentioned thermal problems can be hindered [4-6].

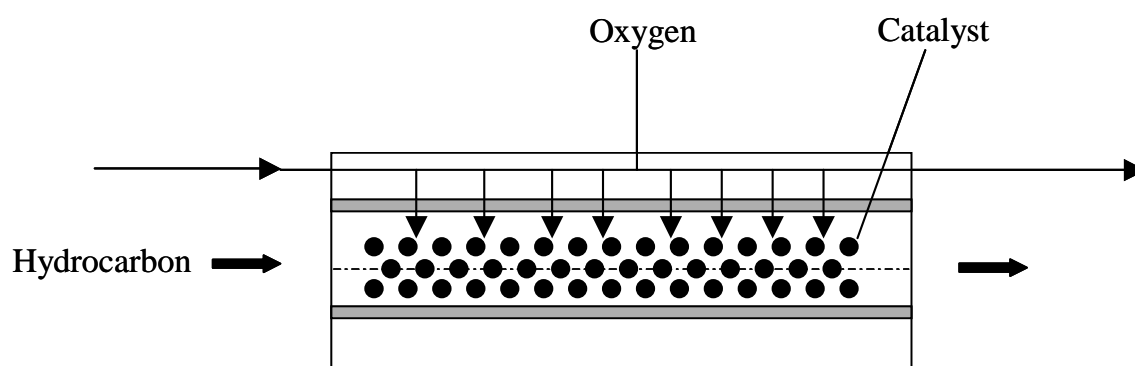


Fig. 1.1: Membrane reactor concept for partial oxidation reactions.

Some potential advantages of membrane reactors can be classified in to three types;

Yield enhancement:

In case of yield enhancement, purpose of the membrane reactor is mainly to increase the conversion of chemical reactions which suffer by equilibrium limitations such as (alkane-) dehydrogenation reactions [7-10], selectively extracting the hydrogen produced [11], decomposition (H_2S and HI) and production of synthesis gas. In this case, membrane acts as an extractor. The H_2 permselectivity of the membrane and its permeability are two important factors controlling the efficiency of the process. Though most extractor applications focus on H_2 removal, some decomposition reactions feature the removal of O_2 [12].

Selectivity enhancement:

Selectivity enhancement is the main objective with series-parallel reactions such as partial oxidation [13-15] or oxy-dehydrogenation of hydrocarbons or oxidative coupling of methane. For these applications the membrane, which acts as a distributor (Fig. 1.1), is generally used to control the supply of O_2 in a fixed bed of catalyst in order to by-pass the flammability area, to optimise the O_2 profile concentration along the reactor and to maximize the selectivity in the desired oxygenate product, mitigating the temperature rise in exothermic reactions [15]. Controlled dosing of the reactant(s) [16-18] in the membrane reactor results in two immediate benefits, it decreases the potential side reactions due to high concentration of reactant(s) and it reduces the subsequent need of separating the unconverted reactants. In these reactors, the O_2 permselectivity of the membrane is an important factor, because air can be used instead of pure O_2 . The higher, stable and controllable permeability of porous membranes is attractive for a number of oxidative reactions [19-30].

Catalyst recovery and engineered catalytic reaction zone:

Another advantage for which the membrane need not be permselective is the catalyst recovery in the reaction system. This is mainly done by the appreciable size difference between the catalyst and the reaction components in relation to the pore diameter of the membrane. The catalyst loss is minimized in this way.

Membrane reactors are also beneficial in providing a well engineered catalytic reaction zone in the porous structure of the membrane, especially in biocatalysis where the biocatalyst, enzymes or cells, is immobilized [31]. The use of these catalyst-impregnated membranes provides some interesting reactor configuration, like opposing reactants mode. Both, equilibrium and irreversible reactions can be carried out in this mode [19, 32], if the reaction is sufficiently fast compared to transport resistance (diffusion rate of reactants in the membrane). In such case a small reaction zone forms in the membrane (if membrane is sufficiently thick and symmetric) in which reactants are in stoichiometric ratio. This concept

has been worked out experimentally for reactions requiring strict stoichiometric feeds such as Claus reaction or strongly exothermic heterogeneous reactions like partial oxidations [33-34].

Additionally, the membrane reactors can be operated in a safer environment compared to conventional reactors. The literature provides ample evidence of these membrane reactor benefits [11]. In particular, the studies by [11, 20, 35] have revealed that membrane reactor conversions can exceed equilibrium values for reversible reactions.

The different configurations of membrane reactors can be classified according to the relative placement of two most important elements of this technology: the membrane and the catalyst [36-37]. Three main configurations of membrane reactors are illustrated in Fig. 1.2,

- 1) *the catalyst is physically separated from the membrane (inert membrane reactor)*
- 2) *the catalyst is impregnated in the membrane (catalytic membrane reactor)*
- 3) *the membrane is inherently catalytic (catalytic membrane reactor)*

1) **Catalyst physically separated from the membrane:**

In this case inert membrane just acts as a compartmentalizer without being directly involved in the catalytic reaction. The catalyst pellets are usually packed or fluidised on the membrane (Fig. 1.2a) which acts as an extractor and/or distributor (fractionation of products or controlled addition of products). This is the promising configuration to control the separative function of the membrane or recovering catalyst.

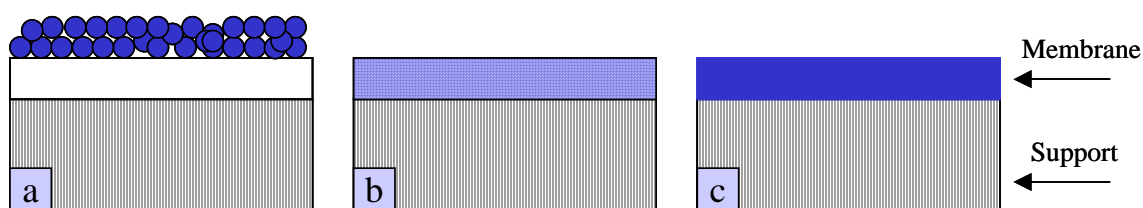


Fig. 1.2: Membrane/catalyst combinations: (a) bed of catalyst on the inert membrane (b) catalyst dispersed in an inert membrane and (c) inherently catalytic membrane.

Packed bed membrane reactors (PMBR) are the most frequently used examples of this type of configuration. Reactors using a dense Pd alloy membrane as a separator and a packed bed of catalyst pellets have been utilized for many dehydrogenation reactions [38]. Successful applications of porous alumina or glass membrane reactors, containing a packed bed of catalyst pellets for enhanced reaction conversions, have been demonstrated [39].

The PMBR has often been compared to the classical plug-flow or fixed-bed reactor (FBR) as a measure of its performance. The proper way to do this, short of a complete

economic analysis, is not obvious. Some researchers [40-42] have considered the question at length, for membrane reactors used for removal of intermediate products from partial oxidations and for yield increases in reversible dehydrogenation reactions and shown that the membrane reactor could compete with the PFR on the basis of yield alone [43].

2) Catalyst impregnated within the membrane:

The catalyst is attached on the membrane surface or, in case of porous membrane, on the pore surface (Fig. 1.2b). In a conventional (packed or fluidised bed) reactor, the reaction conversion is often limited by the diffusion of reactants in the pores of catalyst or catalyst carrying pellets. If the catalyst is inside the pores of the membrane, the combination of open pore path and the transmembrane pressure difference provides the reactants an easier access to the catalyst [35]. It is estimated that a membrane catalyst could be 10 times more active than in the form of pellets [44], if the membrane thickness and texture along with the quantity and location of the catalyst in the membrane are adopted to the kinetics of the reaction [19].

3) Membrane inherently catalytic:

In this type of membrane reactor, an inherently catalytic membrane serves as both separator and catalyst by controlling the two most important functions of the reactor. As in the previous case, membrane improves the access of reactants to the catalyst. A number of meso- and microporous membrane materials have been investigated for their intrinsic catalytic properties like alumina, titania, zeolites etc. The membrane must not to be permselective but highly active for the desired reaction, contain sufficient active sites, have low permeability and operate in the diffusion controlled regime [19]. The catalytic membrane composition, activity and texture need to be optimised for a specific reaction. This is a challenging work in the area of membrane technology and explains the limited number of applications given in the literature for development of catalytic membranes. A potential example is γ -alumina for the Claus reaction where hydrogen sulfide reacts with sulfur dioxide to form elemental sulfur and water.

It can be concluded that in its ultimate configuration, a membrane reactor uses the membrane as a catalyst or a catalyst support and, at the same time, as a physical barrier for separating reactants and products. In addition to the integration of separation and reaction in a single unit, transport of reactants and products by convection rather than by diffusion alone has been estimated to result in reduction of operating costs by as much as 25% [45]. Many catalytic processes of industrial interest are carried out at high temperature [46-50] and chemically harsh environment, a factor that strongly favors the use of inorganic membranes.

So by the development of inorganic membranes, especially the ceramic ones, there has been a dramatic surge of interest in the field of membrane reactor or membrane catalysis [10,11,18].

1.2 Membranes

A membrane can be defined as a semipermeable active or passive barrier which, under a certain driving force, permits preferential passage of one or more selected species [11]. Both organic and inorganic membranes are used in the application of membrane reactor. The choice of membrane materials is stipulated by the application environment, the separation mechanism by which they operate and economic considerations. The advantages of inorganic membranes have been recognized mainly due to their thermal and chemical resistance characteristics [51-52]. The operable temperature limits of inorganic membranes are obviously much higher than that of organic (polymeric) membranes. The majority of the organic membranes starts structurally deteriorating around 100 °C. Thermal stability of the membrane is not only a technical issue but also an economic issue. Another important operating characteristic of inorganic membrane has to do with the problem of fouling and concentration polarization. Inorganic membranes are more fouling resistant due to their low protein adsorption and less susceptible to biological and microbial degradation. Finally with some inorganic membranes like porous ceramic or metallic membranes backflushing can be done to clean the membrane, consequently prolonging the maintenance cycle of membrane system. In this work inorganic (ceramic) membranes have been investigated due to their unique characteristics mentioned above.

Inorganic membranes can be divided into two types: *dense* (palladium-alloy, solid electrolyte) and *porous* (metal, ceramic, glass) membranes, regarding their structural characteristics which can have significant impact on their performance in the membrane reactor or membrane catalysis. Dense membranes are free of discrete, well defined pores or voids. The difference between the two types can be identified by the presence or absence of pore structure under the electron microscope. The effectiveness of dense membrane strongly depends on its material, the components to be separated and their interaction with the membrane. The micro-structure of porous membrane can vary depending on the pore shape which is stipulated by the method of preparation (casting, pressing/sintering, chemical vapour deposition, sol-gel etc). The membranes having straight pores across their thickness are referred to as straight pore membranes. However, the majority of porous membranes rather have interconnected pores with tortuous paths and hence are called tortuous pore membranes.

A membrane is called *symmetric* if it has an integral and homogeneous structure and composition in the direction of membrane thickness. Since the flow rate through the membrane decreases as the membrane thickness increases, it is desirable to make the homogeneous membrane layer as thin as possible. However, a very thin stand-alone membrane layer can not exhibit the desired mechanical integrity to withstand the usual handling procedures and processing pressures found in the separation processes.

A practical solution to this dilemma is the use of asymmetric membrane, where the thin separating layer and the bulk support structure, which gives the mechanical stability, are remarkably different. In this arrangement, the separation of the species and the pressure drop takes place mainly in the thin membrane layer. The underlying bulk support structure must be mechanically strong and should not contribute to the flow resistance of the membrane. A membrane is called *asymmetric* if it has graded pore structure made in one processing step, frequently from the same material. But if the membrane has two or more remarkably different layers made at different steps, then the resulting structure is termed as *composite membrane* [8]. In case of a composite membrane, a predominantly thick layer, called bulk support or a support layer, provides the required mechanical strength to other layers and a flow path to the permeate. Composite membranes have the advantage that support layer(s) and the separating layer can be made of different materials. A composite membrane may have more than two layers in which the separating layer is superimposed on more than one support layers. In this case, the intermediate layers, typically thin, serve to regulate the pressure drop across the membrane-support composite.

The feasibility of a separation process can be mainly determined by three parameters. The first parameter, *stability*, is related to the membrane thermal and chemical resistiveness which is a crucial factor regarding the replacement and maintenance costs of the system. The second parameter, *permeability*, is the ability of a membrane to transmit a fluid through it. It determines the required membrane area and is related to the productivity. The third parameter, *permselectivity*, defined as the selectivity of the membrane toward the gases to be separated, is a process economic issue. Permselectivity is a critical factor to the application of a membrane. Higher permselectivity means cleaner separation and hence no need for further separation. Usually dense membranes are preferred when a permeate of higher purity is desired. There may also be situations where higher permeability with moderate permselectivity is acceptable. High permeability and permselectivity can not be achieved at the same time in any kind of membranes (either polymer or inorganic). Typically, the dense membranes are highly permselective and have relatively low permeability. In contrary to the

dense membranes, porous membranes offer an alternative with high permeability and moderate permselectivity.

A composite inorganic membrane is a potential solution regarding the aforementioned parameters of the membrane material. It offers a trade-off between permeability and permselectivity due to its multi-layer structure as well as provides the required thermal and chemical stability to the membrane separation process [11, 53].

1.2.1 Inorganic membrane formation

The membrane is a fundamental part of the membrane process and the transport properties (permeation and separation efficiency) of the inorganic membrane systems depend, to a large extent, on the microstructural features (pore shape, size, tortuosity) as well as the architecture of the membrane. Pores can be an inherent feature of crystalline structures (zeolites, clay minerals) or be obtained by packing and consolidation of small particles. The following classification of pore size has been recommended by IUPAC (International Union of Pure and Applied Chemistry): macropores $d_p > 50$ nm, mesopores: $2 \text{ nm} < d_p < 50$ nm, and micropores $d_p < 2$ nm. The inorganic membranes can be described as asymmetric porous materials formed by a macroporous support with successive thin layers deposited on it. The support provides mechanical resistance to the medium. The aim of ceramic membrane production is to obtain defect-free supported films with a good control of the structure (pore size, pore volume and surface area). The thermal stability of such materials is also a crucial parameter for applications.

The development of new inorganic membrane materials has gained the advantage of an interdisciplinary task. A number of methods (sol-gel, impregnation, ion-exchange, chemical vapour disposition (CVD)) [54-56] have been developed for inorganic membrane preparation. However, the sol-gel process is considered as an appropriate method to produce purely inorganic or even hybrid organic–inorganic membranes with various reactivity or permselective properties in inert or catalytic membrane [57-59]. Sol-gel process is attractive for multilayer depositions which lead to a controlled structure, composition and activity for the membrane [60-62].

1.2.2 Membrane formation from sol–gel systems

The sol-gel process is a general process which converts a colloidal or polymeric solution (sol) to a gelatinous substance (gel). It involves the hydrolysis and condensation reactions of alcoxide or salts dissolved in water or organic solvents. In most of the sol-gel processes, a stable sol is first prepared as an organometallic oxide precursor and, if necessary, some viscosity modifiers and binders are added. The thickened sol is then deposited as a layer on the porous support as a result of capillary forces by dip coating. This is followed by the gelation of the layer, upon drying to form a gel which is a precursor to ceramic membrane prior to thermal treatment. Sol-gel processes are generally grouped into two major routes according to microstructural nature of the sol. A major difference lies in the amount of water involved in the hydrolysis step and resulting hydrolysis rate to the polycondensation rate. In the first route (colloidal), a metal salt or hydrated oxide is added to excess amount of water, a particulate solution is precipitated which consists of gelatinous hydroxide particles. The second route (polymeric) involves hydrolysis in an organic medium with a small amount of water, which leads to the formation of soluble intermediate species which then in turn undergoes condensation to form inorganic polymers or polymeric sol. Hydrolysis rate is faster in the first route than in the second route. Figure 1.3 shows the general steps involved in the sol-gel process [11].

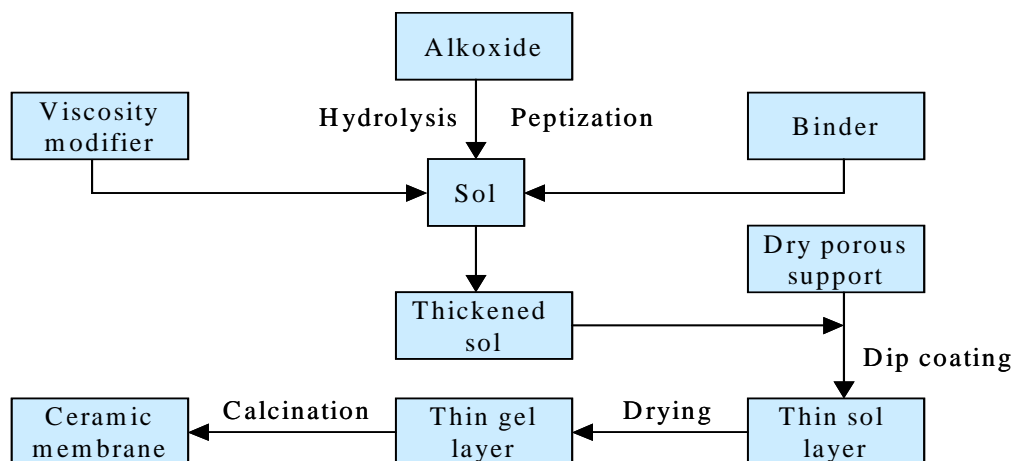


Fig. 1.3: Simplified process flow for the formation of inorganic membranes by sol-gel method.

The inorganic membranes are formed following a three-step thermal treatment of freshly cast sol layers. At first, the thin sol layer is dried at low temperature (373 K). Then the dried layer is fired up to an intermediate temperature (ca. 623 K) in order for residual organic groups and carbon to be burned out. Finally, the consolidation of the membrane is performed through

viscous or conventional sintering depending on the amorphous or crystalline structure of the membrane material. During sol-gel processing of inorganic membranes, sols and gels evolve in a different way depending on the category of the precursors used. This evolution has a great influence on the porous structure of final membrane materials. A number of examples of supported nanophased ceramic layers are presented hereafter dealing with separation and catalytic membrane applications.

1.2.2.1 Catalytic membranes

The sol-gel process allows the preparation of catalytically active materials which can be directly casted on supports at the sol stage. This is a great advantage for catalytic membrane development [35]. The classical synthesis methods for conventional catalysts often start from salts or oxide precursors and involve precipitation, impregnation or even solid-solid reactions. These methods are usually not adapted to the homogeneous casting of catalysts on supports and may lead to limited specific surface areas and to heterogeneous distributions of active species. The sol-gel process, starting from the homogeneous distribution of precursors at the molecular level, often improves these specific criteria for obtaining powders or film-shaped materials either as pure phases or homogeneously doped or dispersed in a matrix. Furthermore, the specificity of the process can lead to original catalytic materials, which can be helpful for a better understanding of the active sites in a specific reaction. Many examples show the potentialities of the sol-gel process for catalyst synthesis and applications to catalytic membrane preparation [23, 25, 63-64]. Lanthanum oxychloride catalytic membrane, VMgO catalytic and CeO₂-based supported catalytic layers are the major examples of catalytic inorganic membranes [35, 65].

1.2.2.2 Inert asymmetric Membranes

Ceramic membranes with adequate permeability and selectivity can only be obtained in an asymmetric configuration, which consists of a multilayer system with a macroporous support (with the largest pore diameter), providing the mechanical strength to the system, intermediate layer(s), which reduces any inherent defects of the support and prevents the infiltration of the top layer material into the pores of the support, and the top layer, which is the decisive membrane of the system. The exigence during the formation of this layer is a comprehensive control of the pore size [66-67].

Alumina, silica, titania or zirconia are considered as the main ceramic materials for the formation of the asymmetric structures [68-69]. The main synthesis route for the preparation of top layer is the modification of intermediate layers using a sol-gel method [68,70]. The advantages of sol-gel derived films include a lower densification temperature, a narrow pore size distribution with nanometer pore-scale, a high degree of chemical homogeneity and the possible production of multicomponent films [71,72].

Generally, the forming process of the supports has been extrusion. Two different ceramic materials are chosen for the preparation of the supports of these systems. One is alumina because of its chemical stability and the possibility to get a narrow pore size distribution [73]. The other one is a reactive mix, which sinters to form cordierite ($2\text{MgO}\cdot 2\text{Al}_2\text{O}_3\cdot 5\text{SiO}_2$). The reactive mixture is chosen because of its excellent plastic behaviour in extrusion step, since it is formed by talc, kaolinite and magnesite [73]. The intermediate layer and the top layer are alumina. The particle size and the sintering temperature for each layer are optimized to get a suitable pore size for the deposition of the next layer.

Support layer:

Alumina and cordierite pipes are obtained from their corresponding pastes. Alumina pastes are prepared using $\alpha\text{-Al}_2\text{O}_3$, 2 wt.% of colloidal SiO_2 , 0.5 wt.% of polyethylene glycol with a medium molecular weight (1000 g mol^{-1}), which acts as plastificant, 1.5 wt.% of carboxymethylcellulose of high viscosity, which acts as binder, 1 wt.% polyethylene glycol with a low molecular weight (200 g mol^{-1}), which acts as lubricant and 40 wt.% of distilled water. The extrudate is dried for 24 h at ambient temperature and sintered vertically in a furnace for 2 h using heating and cooling rates of 633 K/h. The paste for cordierite support is formed by the reactive mix plus 30 wt.% of distilled water. The extrudate is dried for 24 h at ambient temperature, and sintered vertically for 2 h using a heating and cooling rates of 573 K/h [74].

Intermediate layer(s):

Deposition of $\alpha\text{-Al}_2\text{O}_3$ intermediate layer is performed with a colloidal process. This involves the preparation of a stable suspension, prepared by using $\alpha\text{-Al}_2\text{O}_3$, 0.75 wt.% of deflocculant and 1 wt.% of carboxymethylcellulose of low viscosity. The obtained suspension

has a 8 wt.% solids content. Unsupported layers are obtained by slipcasting of the suspension on plaster molds. Intermediate layers are obtained by pouring the suspension on the internal side of the support and allowing to stand for 1 min. The system is dried vertically for 24 h at ambient temperature and sintered vertically (kept for 2 h) with heating and cooling rates of 573 K/h [74].

Top layer:

The top layer ($\gamma\text{-Al}_2\text{O}_3$) is obtained from a boehmite sol ($\gamma\text{-AlOOH}$) by a sol-gel process [75-78]. This starts from aluminium secbutoxide, which is hydrolysed totally with water above 363 K in a proportion of 2 l H_2O per mol alcoxide. The resulting precipitate is peptised with 0.07 mol HNO_3 per mol alcoxide. The suspension is maintained at reflux conditions for 16 h and at 363 K. The addition of 33 wt.% of polyvinylalcohol (PVA) is recommended to obtain a defect-free supported membrane [74]. In tubular configurations, boehmite sol concentrations of 0.5 and 0.72 M are used, and the sol viscosity is adjusted by addition of three different amounts (33, 40, and 45 wt.%) of PVA, suggested by Agrafiotis and Tsetsekou [79]. Non-supported membranes are prepared by gelling the sol in a climate chamber at 313 K and 60% relative humidity. The deposition of this membrane on the intermediate layer consists of three pouring steps. Between each step the membrane is dried and calcined. The resulting gels are calcined at temperature about 673 K at a heating and cooling rates of 333 K/h in an electric furnace. It is necessary to reach this temperature to obtain $\gamma\text{-Al}_2\text{O}_3$ membrane as the transition of $\gamma\text{-AlOOH}$ (boehmite) to $\gamma\text{-Al}_2\text{O}_3$ takes place at about 673 K [80].

1.3 Starting point and objectives

Composite, inorganic membranes are porous materials with complicated and varied structure from layer to layer. Application of such membranes as a fundamental part of a membrane reactor is being strongly advocated to carry out complex chemical reactions (partial oxidation and dehydrogenation of hydrocarbons) where coupled heat and mass transfer phenomena are extensively involved. Therefore theoretical modelling of such phenomena is a demanding task. Heat and mass transfer in porous inorganic membrane is a topic of growing interest. Numerous studies have contributed to this topic in the recent years. Heat and mass transfer processes have been developed from empirical to theoretical and from

one dimensional to two or three dimensional models with improvement of experimental designs and computer techniques.

The rate of transport processes which take place in the pore structure is affected or determined by the transport resistance of the pore structure. Because of the unique nature of different materials, the structure characteristics relevant to transport in pores have to be determined experimentally. Inclusion of transport processes into the description of the whole process is essential when reliable simulations or predictions have to be made. A reliable prediction of transport parameters using theoretical models gives insight into the nature of heat and mass transport in the porous materials which will help the process industry towards attractive applications of membrane reactors.

The complicated structure of porous membranes demands a careful consideration of the characterization of its transport properties. The first step of this is to choose the mathematical model that describes the process kinetics. The transport properties are estimated as parameters of the selected mathematical models by fitting them to experimental data. The main transport properties incorporated in most transport models are the thermal conductivity, effective diffusion coefficient and structural parameters of the membrane. Pressure and temperature influence the diffusion coefficient and thermal conductivity, while mass and heat transfer coefficients are functions of gas characteristics and system geometry.

“The ultimate goal of any field of research is to know the subject so thoroughly that predictions can be made in the full confidence that they will be correct” [88]. However, in practice, any single research is restricted to a small aspect of the entire field. For instance, most membrane reactor studies focus on a particular system, aiming to quantify its performance in terms of attainable yield and selectivity (see, among others [81-87]). Comprehensive reviews develop and treat general mathematical models for membrane reactors, providing solutions for special cases [89-90]. While isothermal conditions are often assumed [84-86], thermal effects are recognized as an important issue and receive attention in some membrane reactor models [81-82]. The thermal conductivity of membranes is usually taken constant, assuming negligible temperature gradients in the membrane [85-87].

Every membrane reactor model must describe transport kinetics through the membrane accounting for its complicated structure and based on a careful characterization of its transport properties. The transport properties are estimated as parameters of the selected mathematical model by fitting it to the experimental data. Several researchers have contributed to the characterization of porous inorganic membranes by identifying the mass transfer parameters of the membrane during the recent years [91-93]. In [94-96] single layer glass and metallic

membranes are investigated by experiments of steady state gas permeation, isobaric diffusion and transient diffusion in order to obtain the parameters of the dusty gas model (DGM). Surface diffusion is additionally taken into consideration in [95]. The approach is extended to two layer ceramic membranes in [97]. Finally, multilayer porous ceramic membranes are characterized on the basis of steady state permeation experiments in [98-99]. Measurements of thermal properties are not available.

The present work focuses on the independent and separate determination of all data about heat and mass transfer through multilayer tubular ceramic membranes (porous aluminium oxide) that is necessary for modelling and optimisation of membrane reactors. Though we do not yet consider chemical reaction, the partial oxidation of ethane to ethylene or butane to maleic acid anhydride is the background of the investigation. Consequently, the controlled dosage of oxygen is the purpose of the membrane. We take over the methods described in [94-99] and expand them to a comprehensive experimental matrix consisting of six different experiments. Some of these experiments are steady-state, some others dynamic; some are used to identify the transport parameters of the membrane, some others to validate them by predicting the measured results without any fitting. Special attention has been paid to the separate characterisation of the various layers that constitute the asymmetric membrane in respect to mass transfer, and to the combination of heat and mass transfer.

For the first time in literature, heat transfer as well as combined heat and mass transfer are integrated to this analysis, giving insight on how mass transfer is influenced by temperature distribution and heat transfer through porous membranes. Some aspects of multilayer gas permeation that have not been discussed before are pointed out. Furthermore, the membranes used in this work are comparatively larger than the membranes used in earlier investigations [94-99], realistically corresponding to membrane dimensions for application on industrial scale.

The work is organized by first giving a brief introduction of different types of membranes and their preparation. Then some details are given on the experimental set-up, materials and a short overview of the six conducted experiments followed by the models used for heat and mass transfer, described in general form. Subsequently, the conducted experiments and their evaluation are discussed one-by-one, starting with heat transfer, continuing with mass transfer and ending with coupled heat and mass transfer.

Additionally, a general analysis of diffusion process in porous inorganic membranes has been conducted considering the dispersion in the gas streams at both membrane sides, which has been neglected in the evaluation of isobaric diffusion experiments. Previous analysis was

focused on specific experimental conditions. This analysis has been generalized in the sense of a thorough parametric study. Results are presented in form of dimensionless quantities solved by subsequent transformations.

2 Experimental methods and modelling

A literature review on heat and mass transfer through inorganic membranes, including relevant previous work mentioned in section 1.3, has revealed that the main body of investigations in literature is based on just one or two types of steady state mass transfer experiments. Isothermal conditions and a homogeneous structure of the membrane are usually assumed. Furthermore, many investigations refer either to planar, or to very small tubular membranes. In a remarkable number of publications on reactor analysis the transport properties of the membrane are not even measured, but only roughly estimated or deduced from reactor operation data.

Such assumptions can be very restrictive. Many technically important reactions are both strongly exothermal and temperature dependent in terms of conversion and selectivity. Modern membranes are not homogeneous, but asymmetric composites consisting of a complex sequence of layers with different composition and / or structure. Tubular membranes are, from the point of view of application, more interesting than planar ones. Small tubular membranes may be appropriate for laboratory research, but are not adequate for large-scale production, especially not in the most usual type of reactor configuration with a bed of catalyst pellets filled in the tube. Identification of transport parameters without separate validation may be misleading. And, any mistake in the derivation of permeate streams will severely impact reactor design, since it is this very aspect of dosing educts or removing products through the reactor wall that makes the difference between membrane reactors and, e.g., conventional packed bed configurations.

Therefore, and as summarised in the objectives, the introduction and application of a comprehensive matrix of experiments for the separate investigation of transport phenomena in the membrane, the evaluation of experimental results within a consistent modelling frame, the clear distinction between parameter identification and validation, the consideration of heat transfer by its own or in combination with mass transfer, the separate or combined investigation of different mechanisms of mass transfer, the consideration of membrane asymmetry, and the application of tubular membranes with a large membrane diameter have been considered to be important elements and potential contributions of the present work.

2.1 Experimental set-up

The experimental set-up is illustrated in Fig. 2.1. The tubular membranes to be investigated are placed in the measuring cell. Various valves and mass flow controllers enable to

accurately dose gases at the tube and / or annulus side of the measuring cell. The gas flow rates are measured at both outlets by various instruments, depending on their absolute value. Additionally, a thermal conductivity GC sensor measures after appropriate calibration the gas composition. Not only absolute pressures are measured in the tube and the annulus, but the respective pressure difference is also determined separately, in order to increase the accuracy in the evaluation of non-isobaric experiments. Isobaric conditions are attained by fine-adjustment of the needle valves at both gas outlets, and are monitored with the mentioned differential pressure gauge. As the different mass transport mechanisms are temperature dependent, it is necessary to conduct the experiments at various temperature levels, which is achieved by placing the measuring cell in a controllable oven. Additional gas pre-heaters, post-coolers and insulations facilitate specific modes of operation. Furthermore, an electrical heater can be placed in the tube. The capacity of this heater is measured accurately. Apart from gas inlet and outlet temperatures, temperatures at the inner and outer membrane wall are also determined in some experiments. From various techniques that have been checked to this purpose the most efficient was to fix miniature thermocouples (type K, outer diameter: 0.5 mm) with a ceramic glue (Fortafix, Fa. Detakta, Norderstedt), which is especially suitable for metal-ceramic fixations and stable up to 1000°C. In order to avoid damage of the thermocouple and / or the membrane, and establish a good contact, the fixing must be done very carefully. Trendows software enables the automatic acquisition of experimental data. In the total, the experimental set-up can be seen as a generalised Wicke-Kallenbach-cell for annular specimens – generalised in the sense of enabling much more modes of operation than the classical configuration.

Appropriate sealing has been a crucial topic of experimental work. After trying out conventional O-rings and slightly conical graphite rings, ceramic glue has been found to be optimal. A sketch of the measuring cell with this type of sealing is depicted in Fig. 2.2 Tightness to the environment as well as between the compartments of the cell has been checked by a helium leakage detector and by pressure measurements.

Concerning the identification of mass transport parameters of the membrane, it is worth to mention here that there is no automatic commercial instrument to carry out such processes experimentally. Thus, the necessary apparatus has been made as a part of the present work. To obtain the desired transport parameters a large number of experiments has been performed.

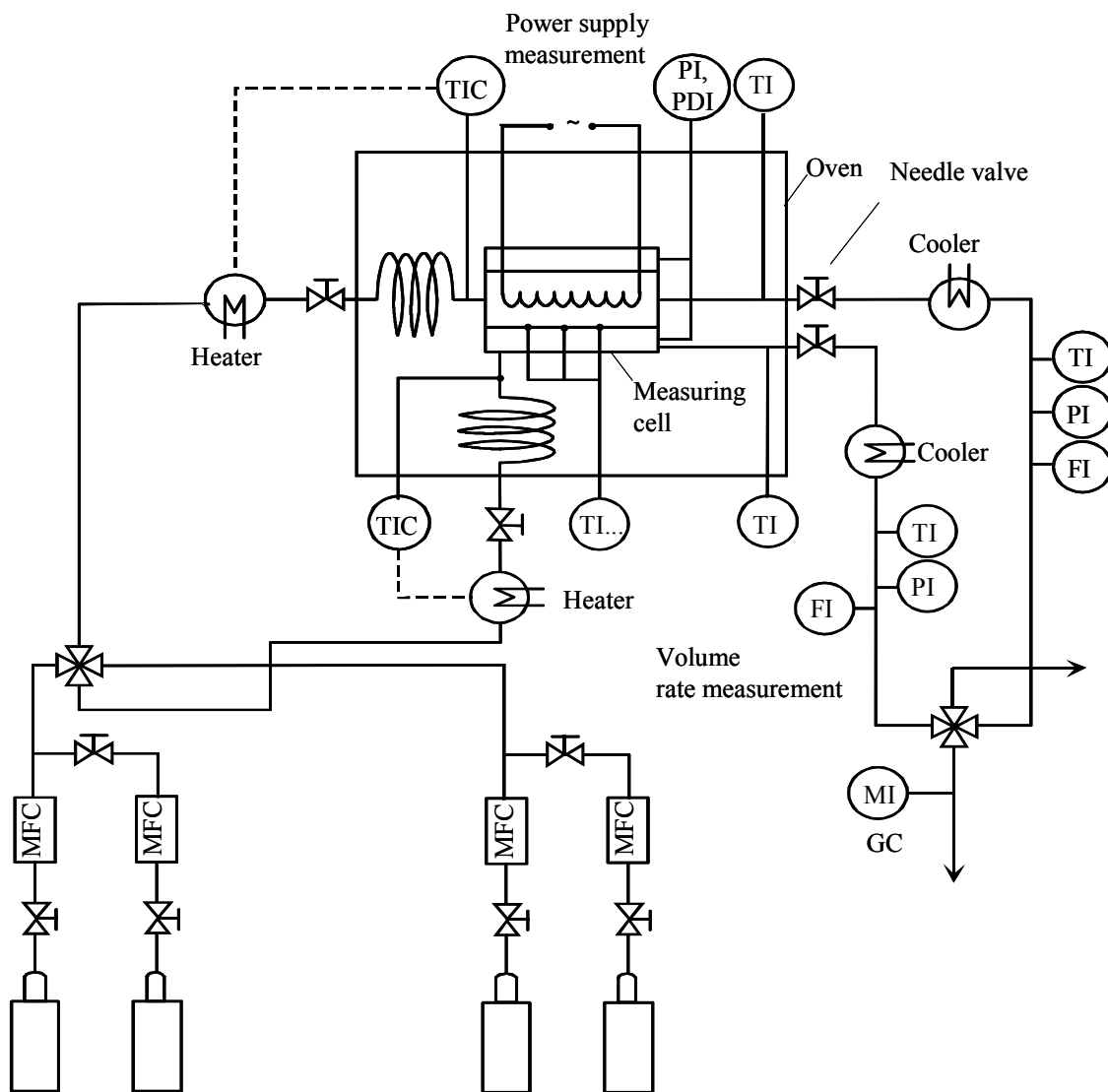


Fig. 2.1: Flow diagram of the experimental set-up; (MFC: mass flow controller).

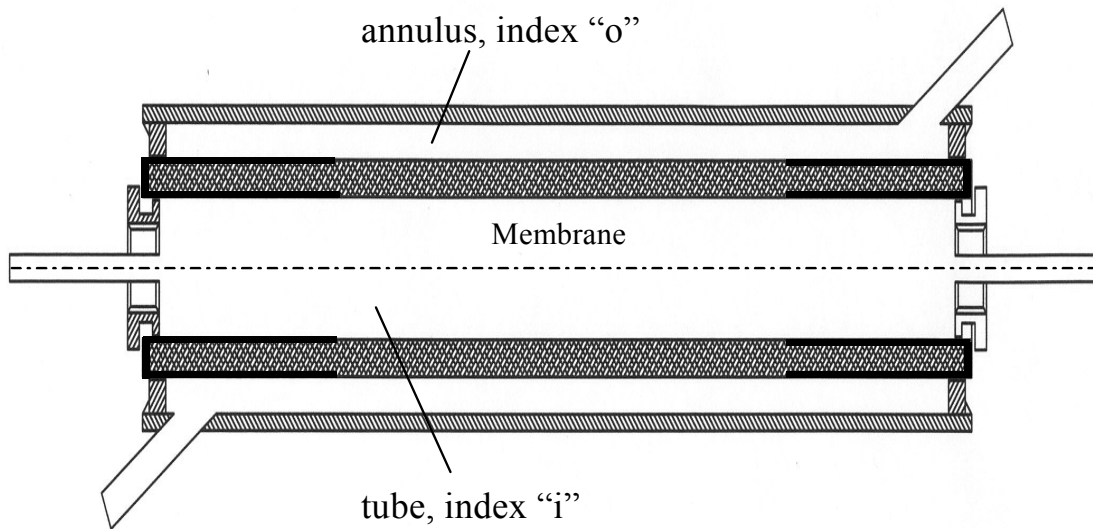


Fig. 2.2: Sketch of the measuring cell sealed by ceramic glue.

2.2 Materials

The main part of experiments reported here have been carried out with tubular ceramic membranes produced by the Inoceramic GmbH, Hermsdorf, with a length of $L = 250$ mm and inner radius of $r_{m,i} = 10.5$ mm. These membranes have been produced by the sol-gel method as alluded in section 1.2.2. Both membrane ends were sealed by glass coating to a distance of 65 mm, so that the length effective for the mass transfer was $L = 120$ mm. The density and volume of this membrane are $\rho_m = 2820$ kg/m³, $V_m = 1.14 \times 10^{-4}$ m³ respectively. Specific heat capacity of the membrane has been determined separately by DSC (differential scanning calorimetry) and it increases slightly with increasing temperature, especially in the low temperature range (Fig. 2.3).

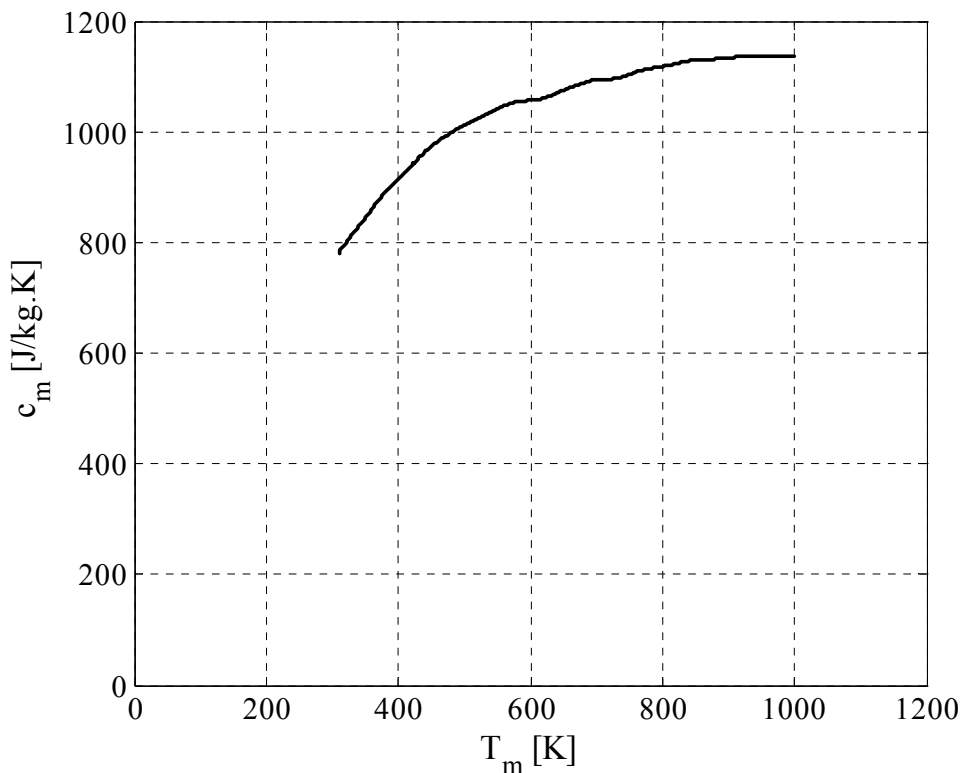


Fig. 2.3: Specific heat capacity of the membrane vs. membrane temperature.

The specific heat capacity of the membrane, c_m , is empirically correlated as

$$c_m = -0.0009T_m^2 + 1.6804T_m + 388.8, \quad (2.1)$$

with c_m in J/kg K and T_m in K.

The composite consisted of a support, two further α -Al₂O₃ layers and the separation layer of γ -Al₂O₃ at the inner side. Respective layer thicknesses according to the producer are summarised in Table 2.1, along with nominal, coarsely approximate pore diameters.

Layer	Composition	Nominal pore diameter [m]	Thickness [m]
Support	α -Al ₂ O ₃	3.0×10^{-6}	5.5×10^{-3}
1 st layer	α -Al ₂ O ₃	1.0×10^{-6}	25×10^{-6}
2 nd layer	α -Al ₂ O ₃	60×10^{-9}	25×10^{-6}
3 rd layer	γ -Al ₂ O ₃	10×10^{-9}	2×10^{-6}

Table 2.1: Producer information about the thickness and pore diameter of each membrane's layer (M1).

Every precursor of the asymmetric composite (only support, support plus one additional layer, support plus two additional layers) was available. Since the experiments with glued thermocouples are possible only with these larger membranes, the main experimental set-up has been designed for larger membranes with $d_{m,i} = 21$ mm. However, some additional mass transfer experiments have been carried out with another tubular ceramic membrane, with an effective length of $L = 200$ mm and inner radius of $r_{m,i} = 7$ mm. The volume of this smaller membrane is $V_m = 8.01 \times 10^{-6}$ m³, with the same density as M1. Respective layer thicknesses and nominal, coarsely approximate pore diameters according to the producer are summarised in Table 2.2.

Layer	Composition	Nominal pore diameter [m]	Thickness [m]
Support	α -Al ₂ O ₃	3.0×10^{-6}	1.5×10^{-3}
1 st layer	α -Al ₂ O ₃	1.0×10^{-6}	25×10^{-6}
2 nd layer	α -Al ₂ O ₃	0.2×10^{-6}	25×10^{-6}
3 rd layer	α -Al ₂ O ₃	60×10^{-9}	25×10^{-6}
4 th layer	γ -Al ₂ O ₃	6.0×10^{-9}	2×10^{-6}

Table 2.2: Producer information about the thickness and pore diameter of each membrane's layer (M2).

Mole fraction of helium at the outlet of the measuring cell was determined by a thermal conductivity detector (TCD) which operates by comparing thermal conductivity of the sample gas to the thermal conductivity of reference gas housed in a sealed cell. This comparison is performed in a two cell sensor housing. A temperature sensitive heated filament is mounted in each cell. Heat conduction through these filaments varies by changing the gas composition. These filaments detect any change in gas composition in terms of electrical signal output (mV). The gas composition is then evaluated by constructing a calibration plot (Fig. 2.4) of known mole percent of helium in nitrogen.

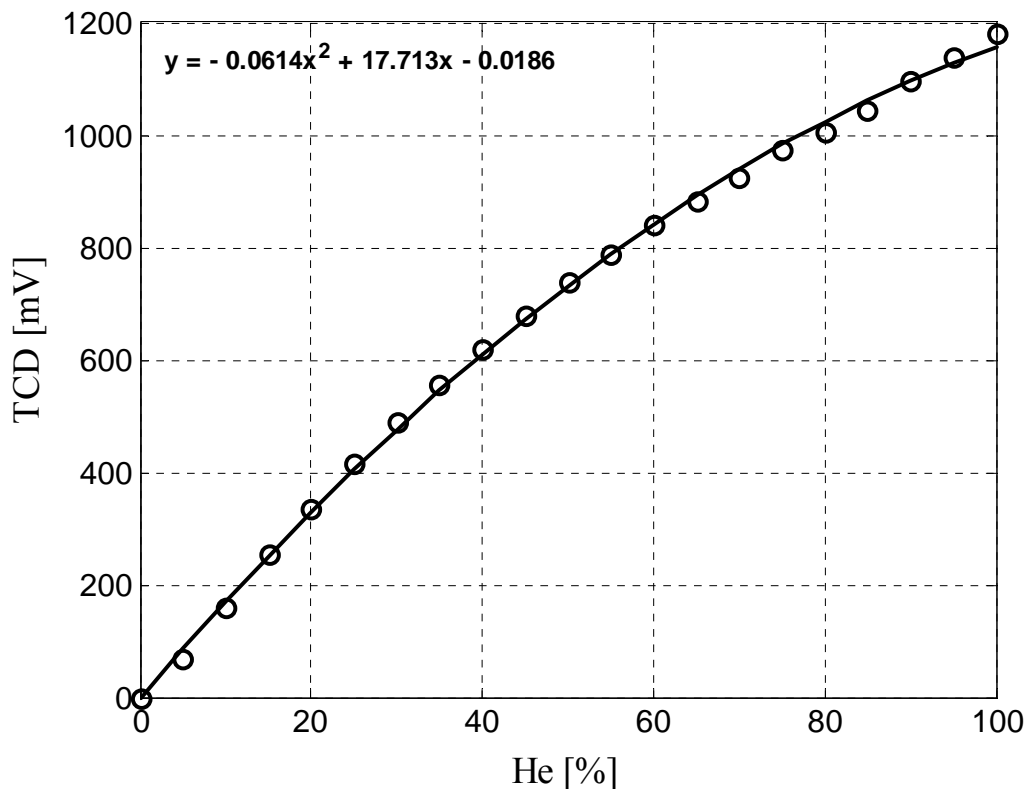


Fig. 2.4: Calibration curve for the measurement of helium mole fraction.

2.3 Experimental Matrix

The six types of experiments conducted in the present work are:

- steady state heat transfer (identification),
- transient heat transfer (validation),
- single gas permeation (identification),
- steady state isobaric diffusion (validation),
- transient diffusion (validation),
- steady state heat and mass transfer (validation).

Figure 2.5 recapitulates the principle of every experiment, indicating state variables and operating parameters that are set, measured in order to derive the heat and mass transport parameters of the membrane, or measured to the purpose of validation by comparison with model predictions. It will be pointed out later that the single gas permeation experiment has also validation components. Notice that the sketches realistically show the reactor geometry, consisting of a shell-side (annulus, index “o”) and a tube-side (index “i”) space. The latter will be filled with particulate catalyst in reactor operation, oxygen will be supplied from the annulus.

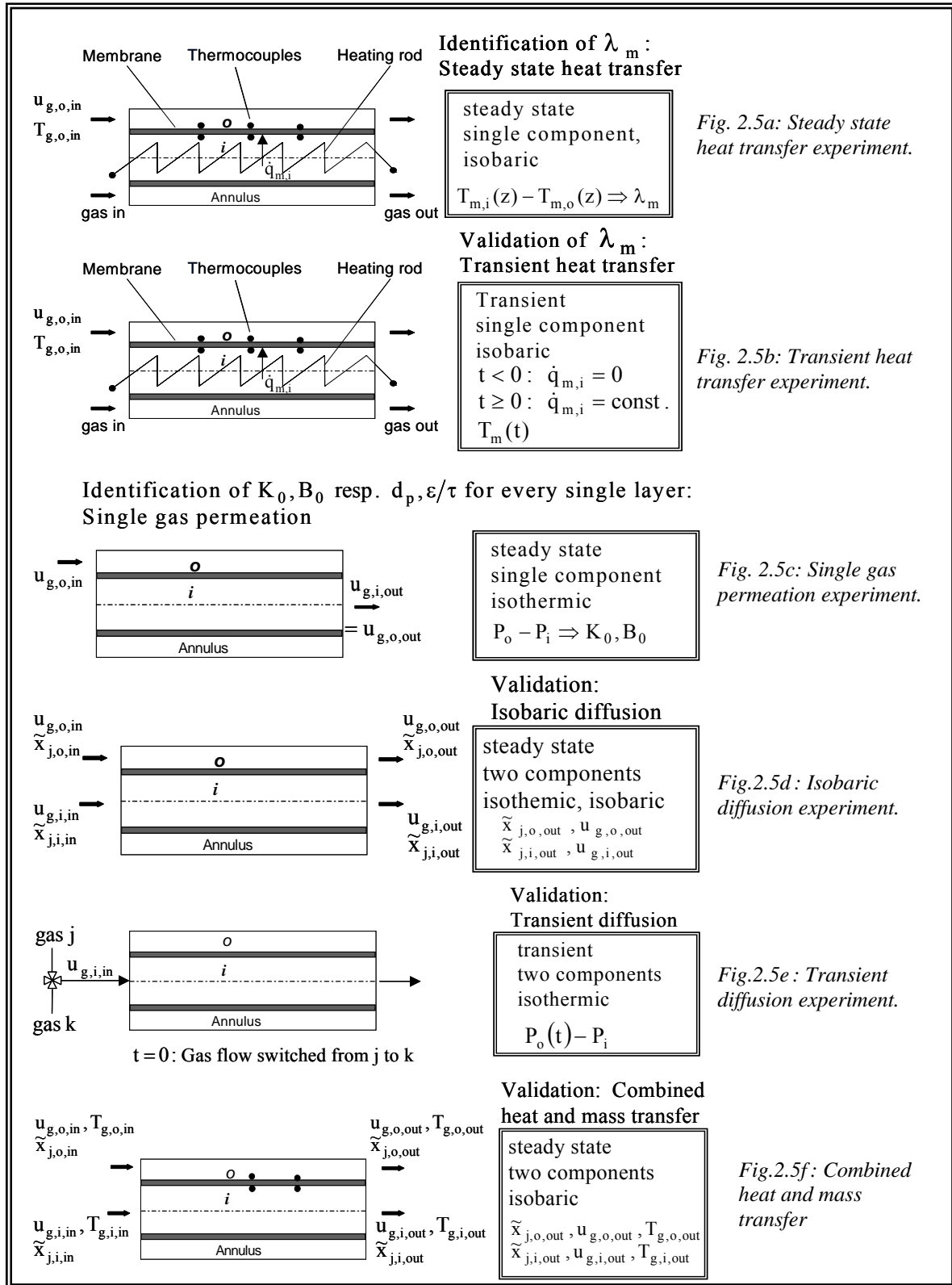


Fig. 2.5: Experimental matrix for the identification and validation of transport parameters.

2.4 Modelling

Mathematical models based on the good understanding of transport processes in the membrane and the reactor configuration provide an important tool for the optimal design and control of the membrane reactor. There are numerous process and equipment configurations for a membrane reactor, mainly due to different membrane geometries, possibilities of feed inflow and flow directions.

In this work, the focus has been a relatively common geometry of shell-and-tube reactor, divided into tubular and annular regions by placing a tubular membrane in it. The gas(es) is/are introduced at the entrance to the reactor configuration. As mentioned before, no chemical reaction has been considered in this work.

2.4.1 Heat transfer model

The model equations for thermal experiments with and without mass transfer consider in the general case all important heat transfer modes in and along the membrane without radiation. Boundary and initial conditions are also expressed here in a general way. During the evaluation of experiments, some of them will be discarded, modified or specified.

The energy balance for the membrane, i.e. for the space

$$r_{m,i} < r < r_{m,o}, \quad 0 < z < L,$$

is formulated in two dimensions and cylindrical coordinates to

$$\rho_m \frac{\partial(c_m T_m)}{\partial t} = \frac{1}{r} \frac{\partial}{\partial r} \left(r \lambda_m \frac{\partial T_m}{\partial r} \right) + \frac{\partial}{\partial r} \left(\sum_j \dot{n}_j \tilde{c}_{p,g,j} T_m \right) + \frac{\partial}{\partial z} \left(\lambda_m \frac{\partial T_m}{\partial z} \right). \quad (2.2)$$

Local thermal equilibrium has been assumed between gas and solid in the membrane. The respective boundary and initial conditions are:

$$r = r_{m,i} : -\lambda_m \frac{\partial T_m}{\partial r} = \dot{q}_{m,i}, \quad (2.3)$$

$$r = r_{m,o} : -\lambda_m \frac{\partial T_m}{\partial r} = \dot{q}_{m,o}, \quad (2.4)$$

where

$$\dot{q}_{m,i} = \alpha_{g,i} (T_{g,i} - T_{m,i}), \quad (2.5)$$

$$\dot{q}_{m,o} = \alpha_{g,o} (T_{m,o} - T_{g,o}), \quad (2.6)$$

$$z = 0: \quad \frac{\partial T_m}{\partial z} = 0, \quad z = L: \quad \frac{\partial T_m}{\partial z} = 0, \quad (2.7a,b)$$

$$t = 0: \quad T_m = T_{m,0}. \quad (2.8)$$

As eq. (2.2) shows, the dependence of the thermal conductivity (λ_m) and heat capacity of the membrane (c_m) upon temperature is accounted for. Equations (2.3), (2.5) and (2.4), (2.6) define boundary conditions of the third kind at the inner and outer side of the membrane, respectively. Equations (2.7) assume both membrane ends to be insulated, while eq. (2.8) sets the initial condition in the transient heat transfer case.

The energy balance for the gas flowing in the annulus has been formulated in an one dimensional way to

$$\Lambda_{ax,o} \frac{d^2 T_{g,o}}{dz^2} - \frac{d(u_{g,o} n_{g,o} \tilde{c}_{p,g,o}^{av} T_{g,o})}{dz} + \left\{ \dot{q}_{m,o} + \sum_j (\dot{n}_{j,m,o} \tilde{c}_{p,g,j} T_{m,o}) \right\} \frac{2\pi r_{m,o}}{F_o} = 0. \quad (2.9)$$

By analogy, the energy balance of gas flowing in the tube can be written as

$$\Lambda_{ax,i} \frac{d^2 T_{g,i}}{dz^2} - \frac{d(u_{g,i} n_{g,i} \tilde{c}_{p,g,i}^{av} T_{g,i})}{dz} - \left\{ \dot{q}_{m,i} + \sum_j (\dot{n}_{j,m,i} \tilde{c}_{p,g,j} T_{m,i}) \right\} \frac{2\pi r_{m,i}}{F_i} = 0. \quad (2.10)$$

The required boundary conditions at the inlet and outlet of the annulus and tube are taken after Danckwerts,

$z = 0$:

$$u_{g,o} n_{g,o} \tilde{c}_{p,g,o}^{av} (T_{g,o,in} - T_{g,o}) + \Lambda_{ax,o} \frac{dT_{g,o}}{dz} = 0, \quad (2.11)$$

$$u_{g,i} n_{g,i} \tilde{c}_{p,g,i}^{av} (T_{g,i,in} - T_{g,i}) + \Lambda_{ax,i} \frac{dT_{g,i}}{dz} = 0, \quad (2.12)$$

$z = L$:

$$\frac{dT_{g,o}}{dz} = 0, \quad \frac{dT_{g,i}}{dz} = 0. \quad (2.13a,b)$$

It, furthermore, holds:

$$z = 0: \quad u_{g,o} = u_{g,o,in}, \quad u_{g,i} = u_{g,i,in}. \quad (2.14a,b)$$

Molar gas density and average specific heat capacity are calculated according to

$$n_g = \frac{P}{\bar{R}T_g}, \quad (2.15)$$

$$\tilde{c}_{p,g}^{av} = \sum_j \tilde{c}_{p,g,j} \tilde{X}_j,$$

$$(2.16)$$

and may change with changing temperature and composition along the reactor, which must also be considered in the inlet boundary conditions.

The described model equations and boundary conditions are modified to solve every specific case of heat transfer from the mentioned experimental matrix.

2.4.2 Modelling mass transfer in porous media

Mass transport parameters, i.e. model parameters that are material constants of the porous media (independent of temperature, pressure, nature and concentration of gases) are evaluated through application of a suitable model of mass transfer in porous media to results of measurements of transport processes in the porous structure. Two models are widely used for the description of combined (permeation and diffusion) mass transport through porous media: the **Mean Transport Pore Model** (MTPM) and the **Dusty Gas Model** (DGM) [100-104].

Both Models are based on the modified Stefan-Maxwell description of multi-component diffusion in pores and on Darcy (DGM) or Weber (MTPM) equation for permeation. For mass transport due to composition difference (i.e. pure diffusion) both models are represented by an identical set of differential equations with two parameters (transport parameters) which characterize the pore structure. Because both models drastically simplify the real pore structure, the transport parameters have to be determined experimentally.

MTPM assumes that the decisive part of the gas transport takes place in transport pores that are visualized as cylindrical capillaries with radii distributed around the mean value (\bar{r}_p)

(first model parameter). The second transport parameter, the width of the transport pore radius distribution, is characterized by the mean value of the squared transport pore radii [105] and is required for description of viscous flow in pores. The third parameter (F_0 , see later) can be looked upon as the ratio of tortuosity to porosity of transport pores.

DGM visualizes the porous media as giant spherical molecules (dust particles). The movement of gas molecules in the space between dust particles is described by the kinetic theory of gases. Formally, the MTPM transport parameters (\bar{r}_p and F_0) can be used also in DGM. The third DGM transport parameter characterizes the viscous (Poiseuille) gas flow in pores. Both models include the contributions of bulk diffusion, Knudsen diffusion, and permeation flow that accounts both for viscous flow and Knudsen flow. MTPM includes also the slip at the pore wall. In MTPM the transport parameters (\bar{r}_p and F_0) are derived directly from the experimental results, in DGM they are interrelated to the Knudsen and permeability coefficients (K_0 , B_0).

The common way to obtain the transport parameters of porous membranes is to employ experimentally simple transport processes in the pores under simple process conditions of temperature and pressure and to evaluate the model parameters by fitting the obtained experimental results to the theory [105]. The experimentally employed transport processes used for the evaluation (identification and validation) of transport parameters are: steady state permeation of a single gas, steady state isobaric binary gas diffusion and the dynamic binary gas diffusion.

So dealing with modelling of gas transport in porous media, it is important to consider the motion of gas molecules through the pores and the interaction of the molecules of gas and solid. In porous media with larger pores the fraction of media available for the gas transfer and the winding nature of the path that gas takes through the pores are to be considered. When the pore size of the porous media is very fine, the sizes of gas molecules and solid particles become comparable, and the interaction between the gas and solid molecules is significant.

Thus, modelling of gas transport through porous media is generally based on two considerations: motion of gas molecules through the pores and interaction of gas molecules with the solid. The Dusty Gas Model based on Stefan-Maxwell equations (for multi-component gas diffusion) is derived by applying the kinetic theory to the interaction of gas-gas molecules and gas-solid molecules, where the porous media is treated as dust in the gas. It is vital to recognize here that the term 'Dusty Gas' refers to the mathematical formulation of transport equations and not the nature of porous media.

The Fickian diffusion model is much simpler than the Stefan-Maxwell equations but can not be used for multi-component mixtures (unless a binary mixture approximation is used), that's why it can not be applied to the Dusty Gas concept (2 gases and dust). In the present work Dusty Gas Model is used for the quantification of mass transport through the membrane.

2.4.3 Modes of gas transport in porous media

It is necessary to distinguish the different mechanisms by which mass transport through porous media can occur before developing a general mass transport equation. These are (Fig. 2.6): Knudsen diffusion, (molecular/continuum) diffusion, viscous flow, and surface diffusion (not considered here, considerable for adsorbable gases). With the help of kinetic theory, they can all be written as separate functions of gas properties and textural properties of the material and combined for the total transport of gas through the porous membrane.

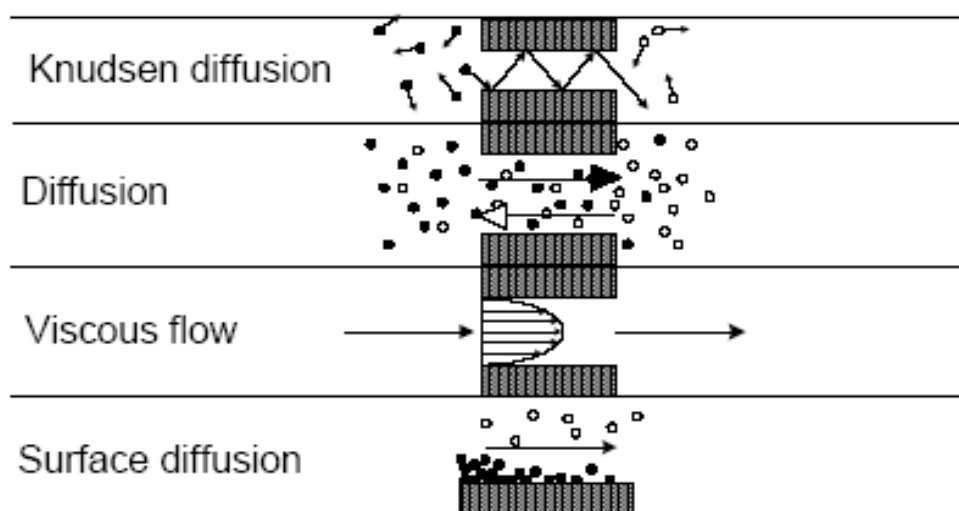


Fig. 2.6: Different transport mechanisms in porous media.

2.4.3.1 Knudsen flow

Knudsen flow describes the case when gas molecules collide more frequently with flow boundaries than with other gas molecules. It occurs when the mean free path of the gas molecules is larger than the pore diameter. This regime is important at very small pore diameters and/or very low gas density (large mean free path).

The original studies of Knudsen flow were limited to small holes in very thin plates. This assured that the molecules do not interact with each other during the passage through the hole and that they move independently of each other. Under these circumstances the number of molecules passing through the hole is determined by the number of molecules entering the hole, and the probability of a molecule that enters the hole to pass through is high (molecule not bouncing back). In this regime there is no distinction between flow and diffusion (which is a continuum phenomenon), and gas composition is of no importance as there is no interaction between like and unlike gas molecules. This phenomenon was studied extensively by Knudsen around 1907-1908, hence the free molecule flow is termed as Knudsen flow.

Consider a gas with a molecular density of n_{mol} (molecules/m³) at one side of a hole and a vacuum at the other side. The free molecule flux $\dot{n}_{\text{K,mol}}$ (molecules/m² s) through the hole can be written as

$$\dot{n}_{j,\text{K,mol}} = \omega n_{j,\text{mol}} \bar{u} \quad (2.17)$$

where ω is a dimensionless probability factor, and \bar{u} is the mean molecular speed (m/s). If there is gas on both sides of the hole, the net flux is proportional to the difference in the gas number densities at both sides (1, 2)

$$\dot{n}_{j,\text{K,mol}} = \omega \bar{u} (n_{j,2,\text{mol}} - n_{j,1,\text{mol}}). \quad (2.18)$$

In order to use this equation, expressions are required for the mean molecular speed and the dimensionless probability factor. The mean molecular speed can be calculated to

$$\bar{u} = \sqrt{\frac{8\tilde{R}T}{\pi\tilde{M}}} \quad (2.19)$$

using kinetic theory.

Calculation of the probability factor is considerably more complicated, requiring knowledge about the whole geometry and the appropriate scattering law. The value of the probability factor ω for a long straight circular tube of radius r and length L ($L \gg r$) is given by $(2/3)(r/L)$. The method of derivation of this expression is presented in [106]. By putting the values of ω and \bar{u} , the flux equation (eq. (2.18)) is transformed to

$$\dot{n}_{j,K,mol} = \frac{2}{3} \frac{r}{L} \sqrt{\frac{8\tilde{R}T}{\pi\tilde{M}_j}} (n_{j,2,mol} - n_{j,1,mol}) \quad (2.20)$$

$$\dot{n}_{j,K,mol} = \frac{2}{3} r \sqrt{\frac{8\tilde{R}T}{\pi\tilde{M}_j}} \frac{dn_{j,mol}}{dz} \quad (2.21)$$

Considering the flux in mol/m²s instead of molecules/m²s, eq (2.21) is re-written to

$$\dot{n}_{j,K} = \frac{2}{3} r \sqrt{\frac{8\tilde{R}T}{\pi\tilde{M}_j}} \frac{dn_j}{dz} \quad (2.22)$$

Hence, by analogy to continuum gas diffusion a Knudsen diffusion coefficient D_K can be defined for flow in a long straight pore with diffuse scattering as

$$D_{K,j} = \frac{2}{3} r_p \sqrt{\frac{8\tilde{R}T}{\pi\tilde{M}_j}} \quad (2.23)$$

Equation (2.23) shows that D_K is proportional to the pore radius and to the mean molecular velocity. The formula is specific to cylindrical pores. However, analysing different geometries gives equations of similar form but with different geometrical parameters. For this reason, a general equation is defined by using a Knudsen coefficient K_0 , namely

$$D_{K,j} = \frac{4}{3} K_0 \sqrt{\frac{8\tilde{R}T}{\pi\tilde{M}_j}}. \quad (2.24)$$

By comparison of eq. (2.24) with eq. (2.23) it can be deduced that $K_0 = d_p/4$. By additionally considering the fact that the porous medium consists of only a certain percentage of open space (porosity) where Knudsen flow can take place, and has paths through the solid, which are by some percentage longer than a direct path (tortuosity), the Knudsen coefficient is written as

$$K_0 = \frac{\varepsilon}{\tau} \frac{d_p}{4}. \quad (2.25)$$

2.4.3.2 Molecular diffusion

Molecular diffusion is the most familiar diffusion mechanism. It describes the case when gas molecules collide more frequently with each other than to the pore walls. It occurs when the mean free path of the gas molecules is smaller than the pore diameter. Mathematical formulations for it were developed in mid to late 19th century from two different considerations, Maxwell and Stefan from kinetic theory and Graham and Fick from binary mixture experiments. For binary mixtures and equimolar diffusion the two approaches yield the identical result that species diffusive flux is directly proportional to its concentration gradient:

$$\dot{n}_{jD} = -D_{jk} \nabla n_j, \quad (2.26)$$

$$\dot{n}_{kD} = -D_{kj} \nabla n_k. \quad (2.27)$$

In the absence of pressure or temperature gradient it is

$$\nabla n_j + \nabla n_k = \nabla (n_j + n_k) = \nabla n = 0. \quad (2.28)$$

Thus, it follows: $D_{jk} = D_{kj}$.

Kinetic theory is the basis for extension to multi-component mixtures as it casts light to the importance of all species fluxes for the diffusive transport of any component. This is explained by considering the restriction on diffusion rate due to momentum transfer between

molecules. Clearly, the momentum transfer to every component will depend on the relative motion of all other components. The result of the full analysis is the Stefan-Maxwell equation [100]

$$-n\nabla\tilde{x}_j = \sum_{k=1, k \neq j}^N \frac{\tilde{x}_k \dot{n}_{jD} - \tilde{x}_j \dot{n}_{kD}}{D_{jk}}, \quad (2.29)$$

$$-\frac{1}{\tilde{R}T} \frac{dp_j}{dz} = \sum_{k=1, k \neq j}^N \frac{\tilde{x}_k \dot{n}_{jD} - \tilde{x}_j \dot{n}_{kD}}{D_{jk}}. \quad (2.30)$$

In this equation diffusion coefficients are the binary diffusion coefficients. However, the equation gives the concentration gradient of each component in terms of the fluxes of other components, while usually the component fluxes are required in terms of concentration gradients. Hence, the equation must be inverted.

It is possible to generalise the Fickian binary law to yield the flux of a single component in terms of the concentration gradients of other components, but in the resulting equation

$$\dot{n}_j = -\sum_{k=1}^N D_{jk} \nabla n_k, \quad (2.31)$$

the diffusion coefficients are not the same as the binary diffusion coefficients [100]. This relationship is in fact a form of inverse Stefan-Maxwell equation, where the Fickian multi-component diffusion coefficients are the conjugates of mole fraction of the gas mixture and binary diffusion coefficients.

While applying the binary diffusion coefficient to porous media, it is important to consider the porosity and the winding nature of the pores (tortuosity) in the solid. Hence, a binary diffusion coefficient for porous media, termed as effective binary diffusion coefficient, is defined as

$$D_{jk}^e = \frac{\varepsilon}{\tau} D_{jk}, \quad (2.32)$$

and can replace D_{jk} in eqs (2.29), (2.30).

2.4.3.3 Viscous flow in porous media

The term viscous flow refers to that portion of the flow in the laminar (continuum) regime that is caused by total pressure gradient. In calculating viscous flow, inertial terms are omitted from the equation of motion of the fluid (creeping flow). The behavior of the gas is thus determined by the dynamic viscosity, which for gases is independent of pressure. Furthermore, as bulk flow has no tendency to separate the components of gas mixtures, mixtures of different gases can be treated in the same manner as a pure gas. The viscous flow equation is commonly known as Darcy's law,

$$\bar{u} = -C \frac{dP}{dz}, \tag{2.33}$$

where \bar{u} is the steady mean velocity in the z direction and C is a permeability constant which is dependent on fluid, temperature and porous media.

A transport equation for the viscous flow of gases can be calculated by applying Newton's second law to any element, Fig. 2.7, of a compressible fluid (in the same manner as Poiseuille's law is derived for liquids), thus balancing viscous and pressure forces. Considering a cylindrical tube of radius r and steady flow (no acceleration) gives the force balance

$$-\frac{dp}{dz} dz \cdot \pi r^2 - \eta \frac{du}{dr} 2\pi r \cdot dz = 0, \tag{2.34}$$

$$\frac{du}{dr} = -\frac{r}{2\eta} \frac{dP}{dz}. \tag{2.35}$$

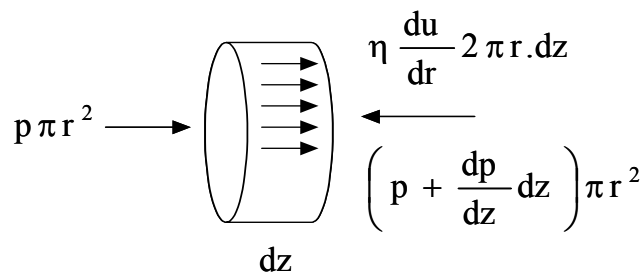


Fig. 2.7: Forces acting on fluid element.

Integrating the above equation radially gives the velocity as a function of radius

$$u = -\frac{r^2}{4\eta} \frac{dP}{dz} + c. \quad (2.36)$$

The viscous flux \dot{n}_{vis} (mol/s.m²) is given by the product of flow velocity u (m/s) and molar density n (mol/m³) to

$$\dot{n}_{\text{vis}} = -n \cdot \frac{r^2}{4\eta} \frac{dP}{dz} + nc. \quad (2.37)$$

Applying the no slip condition at the boundary ($u = 0$, $r = R$) allows the constant to be determined (any slip flow at the walls will be incorporated into the Knudsen flow). The total flow rate is obtained by integrating again over the cross-sectional area of the cylinder to give

$$\dot{N}_{\text{vis}} = -\frac{n\pi R^4}{8\eta} \frac{dP}{dz}, \quad (2.38)$$

and the mean flux is obtained by dividing the total flow rate by the cross-sectional area of the cylinder

$$\dot{n}_{\text{vis}} = -\frac{nR^2}{8\eta} \frac{dP}{dz}. \quad (2.39)$$

The compressibility of the fluid in the equation is accounted for by the calculation of n using the ideal gas equation,

$$n = P/\tilde{R}T, \quad (2.40)$$

where \tilde{R} is universal gas constant (J/mol.K). Equation (2.39) is specific to the flow in cylindrical passages. However, analyzing different geometries gives the same equation but with different geometrical parameters, and for this purpose a general equation is defined

$$\dot{n}_{\text{vis}} = -\frac{nB_0}{\eta} \frac{dP}{dz}, \quad (2.41)$$

where B_0 is called the viscous flow parameter or permeability constant. For straight, circular capillaries of radius r_p , $B_0 = r_p^2/8$ is obtained, which after consideration of the ratio of porosity to tortuosity in the porous media can be written as

$$B_0 = \frac{\varepsilon d_p}{\tau 32}. \quad (2.42)$$

2.4.4 Combination of transport mechanisms for binary mixtures

First considering the Knudsen and molecular diffusive fluxes, the transport equation for these two modes in the porous media for component j of a binary mixture can be written as

$$\dot{n}_{j,K} = -D_{K,j} \nabla n_j, \quad (2.43)$$

$$\dot{n}_{j,D} = -D_{jk} \nabla n_j + \tilde{x}_j \dot{n}_D. \quad (2.44)$$

Now the net diffusive flux, $\dot{n}_D = \dot{n}_{jD} + \dot{n}_{kD}$, which is present in all cases of non-equimolar diffusion, has been considered in eq. (2.44), compare with eqs (2.26), (2.27). By using ideal gas law eqs (2.43), (2.44) can be written as

$$\dot{n}_{jK} = -\frac{D_{K,j}}{\tilde{R}T} \nabla p_j, \quad (2.45)$$

$$\dot{n}_{jD} = -\frac{D_{jk}}{\tilde{R}T} \nabla p_j + \tilde{x}_j \dot{n}_D. \quad (2.46)$$

Equations (2.45) and (2.46) can be transformed to

$$-\nabla p_j = \frac{\tilde{R}T}{D_{K,j}} \dot{n}_{jK}, \quad (2.47)$$

$$-\nabla p_j = \frac{\tilde{R}T}{D_{jk}} (\dot{n}_{jD} - \tilde{x}_j \dot{n}_D) \quad (2.48)$$

As the total partial pressure gradient in the gas mixture is due to the sum of both contributions, the total mass transport is treated additively. Hence, the molecular and Knudsen diffusion are combined like resistances in series, therefore the equation for partial pressure gradient can be written as

$$-\nabla p_j = \frac{\tilde{R}T}{D_{K,j}} \dot{n}_j + \frac{\tilde{R}T}{D_{jk}} (\dot{n}_j - \tilde{x}_j \dot{n}). \quad (2.49)$$

By considering

$$\dot{n} = \dot{n}_j + \dot{n}_k, \quad (2.50)$$

$$\tilde{x}_j + \tilde{x}_k = 1, \quad (2.51)$$

the relationship

$$-\frac{\nabla p_j}{\tilde{R}T} = \frac{\dot{n}_j}{D_{K,j}} + \frac{\tilde{x}_k \dot{n}_j - \tilde{x}_j \dot{n}_k}{D_{jk}} \quad (2.52)$$

is obtained.

This equation holds for the diffusion of one component of a binary mixture and is valid for the entire pressure range between the Knudsen and molecular diffusion limit.

Incorporation of viscous flow is also additive. If a total pressure gradient exists, the resulting viscous flow is simply added to the diffusive flux. The reason for additivity is that in kinetic theory there are no viscous terms in the diffusion equation and no diffusion terms in the viscous-flow equations, the two are entirely independent terms [100]. The independence holds for any isotropic system, not just gases, and is sometimes referred to as Curie's theorem [107]. The total flux of a component j can be written as

$$\dot{n}_j^{\text{tot}} = \dot{n}_j + \tilde{x}_j \dot{n}_{\text{vis}}. \quad (2.53)$$

By adding and subtracting $\tilde{x}_j \dot{n}_{vis}$, eq. (2.52) can be transformed to

$$-\frac{\nabla p_j}{\tilde{R}T} = \frac{\dot{n}_j + (\tilde{x}_j \dot{n}_{vis} - \tilde{x}_j \dot{n}_{vis})}{D_{K,j}} + \frac{\tilde{x}_k (\dot{n}_j + \tilde{x}_j \dot{n}_{vis} - \tilde{x}_j \dot{n}_{vis}) - \tilde{x}_j (\dot{n}_k + \tilde{x}_k \dot{n}_{vis} - \tilde{x}_k \dot{n}_{vis})}{D_{jk}}, \quad (2.54)$$

$$-\frac{\nabla p_j}{\tilde{R}T} = \frac{\dot{n}_j^{tot} - \tilde{x}_j \dot{n}_{vis}}{D_{K,j}} + \frac{\tilde{x}_k \dot{n}_j^{tot} - \tilde{x}_k \tilde{x}_j \dot{n}_{vis} - \tilde{x}_j \dot{n}_k^{tot} + \tilde{x}_j \tilde{x}_k \dot{n}_{vis}}{D_{jk}}, \quad (2.55)$$

$$-\frac{\nabla p_j}{\tilde{R}T} = \frac{\dot{n}_j^{tot}}{D_{K,j}} - \frac{\tilde{x}_j \dot{n}_{vis}}{D_{K,j}} + \frac{\tilde{x}_k \dot{n}_j^{tot} - \tilde{x}_j \dot{n}_k^{tot}}{D_{jk}}. \quad (2.56)$$

Finally, and by removing the unnecessary superscript “tot”,

$$-\frac{\nabla p_j}{\tilde{R}T} + \frac{\tilde{x}_j \dot{n}_{vis}}{D_{K,j}} = \frac{\dot{n}_j}{D_{K,j}} + \frac{\tilde{x}_k \dot{n}_j - \tilde{x}_j \dot{n}_k}{D_{jk}} \quad (2.57)$$

is obtained.

For a multicomponent mixture eq. (2.57) can be written as

$$-\frac{\nabla p_j}{\tilde{R}T} + \frac{\tilde{x}_j \dot{n}_{vis}}{D_{K,j}} = \frac{\dot{n}_j}{D_{K,j}} + \sum_{k=1, k \neq j}^N \frac{\tilde{x}_k \dot{n}_j - \tilde{x}_j \dot{n}_k}{D_{jk}}. \quad (2.58)$$

From eqs (2.40) and (2.41) we know that

$$\dot{n}_{vis} = -\frac{P}{\tilde{R}T} \frac{B_0}{\eta} \nabla P.$$

It is, furthermore, $P_j = \tilde{x}_j P$.

Putting these values in eq. (2.58)

$$-\frac{P \nabla \tilde{x}_j}{\tilde{R}T} - \frac{\tilde{x}_j \nabla P}{\tilde{R}T} - \frac{\tilde{x}_j}{D_{K,j}} \frac{P}{\tilde{R}T} \frac{B_0}{\eta} \nabla P = \frac{\dot{n}_j}{D_{K,j}} + \sum_{k=1, k \neq j}^N \frac{\tilde{x}_k \dot{n}_j - \tilde{x}_j \dot{n}_k}{D_{jk}}, \quad (2.59)$$

$$-\frac{P}{\tilde{R}T} \nabla \tilde{x}_j - \frac{\tilde{x}_j}{\tilde{R}T} \left(1 + \frac{B_0}{D_{K,j} \eta} P \right) \nabla P = \frac{\dot{n}_j}{D_{K,j}} + \sum_{k=1, k \neq j}^N \frac{\tilde{x}_k \dot{n}_j - \tilde{x}_j \dot{n}_k}{D_{jk}}, \quad (2.60)$$

and finally the DGM equation for mass transport in a porous medium

$$\sum_{k=1, k \neq j}^N \frac{\tilde{x}_k \dot{n}_j - \tilde{x}_j \dot{n}_k}{D_{jk}^e} + \frac{\dot{n}_j}{D_{K,j}} = -\frac{P}{\tilde{R}T} \nabla \tilde{x}_j - \frac{\tilde{x}_j}{\tilde{R}T} \left(1 + \frac{B_0}{\eta D_{K,j}} P \right) \nabla P. \quad (2.61)$$

is obtained. With η the viscosity of the mixture is denoted, see Appendix C.

2.4.5 Mass transfer model

In its general form, the Dusty Gas Model [91-98, 108] for species j in a mixture of N components, for cylindrical coordinates, is expressed by the relationship

$$\sum_{k=1, k \neq j}^N \frac{\tilde{x}_k \dot{n}_j - \tilde{x}_j \dot{n}_k}{D_{jk}^e} + \frac{\dot{n}_j}{D_{K,j}} = -\frac{P}{\tilde{R}T} \frac{d\tilde{x}_j}{dr} - \frac{\tilde{x}_j}{\tilde{R}T} \left(1 + \frac{B_0}{\eta D_{K,j}} P \right) \frac{dP}{dr} \quad (2.62)$$

where $j = 1$ to N .

The driving forces are included in the right-hand part of eq. (2.62) in terms of total pressure and molar fraction (partial pressure) gradients, while the resulting fluxes, \dot{n}_j , appear at the left-hand side of the equation.

The mass balance for gas flowing in the annulus has been formulated (similar to energy balance for the gas, sec. 2.4.1) in an one-dimensional way to

$$D_{ax,o} \frac{d^2 \tilde{x}_{j,o}}{dz^2} - \frac{d}{dz} \left(u_{g,o} \frac{n_{g,o}}{n_{g,o,in}} \tilde{x}_{j,o} \right) + \frac{2\pi r_{m,o}}{F_o n_{g,o,in}} \dot{n}_{j,m,o} = 0. \quad (2.63)$$

In the tube it holds

$$D_{ax,i} \frac{d^2 \tilde{x}_{j,i}}{dz^2} - \frac{d}{dz} \left(u_{g,i} \frac{n_{g,i}}{n_{g,i,in}} \tilde{x}_{j,i} \right) - \frac{2\pi r_{m,i}}{F_i n_{g,i,in}} \dot{n}_{j,m,i} = 0. \quad (2.64)$$

The boundary conditions at the inlet and outlet of annulus and tube are taken again (sec. 2.4.1) after Danckwerts [109-110],

$z = 0$:

$$u_{g,o}(\tilde{x}_{j,o,in} - \tilde{x}_{j,o}) + D_{ax,o} \frac{d\tilde{x}_{j,o}}{dz} = 0, \quad (2.65)$$

$$u_{g,i}(\tilde{x}_{j,i,in} - \tilde{x}_{j,i}) + D_{ax,i} \frac{d\tilde{x}_{j,i}}{dz} = 0, \quad (2.66)$$

$z = L$:

$$\frac{d\tilde{x}_{j,o}}{dz} = 0, \quad \frac{d\tilde{x}_{j,i}}{dz} = 0, \quad (2.67a,b)$$

whereby eqs (2.13) still apply at the inlet. At the membrane-gas interfaces it is:

$$\dot{n}_{j,m,o} = \beta_{g,o} n_{g,m,o} (\tilde{x}_{j,m,o} - \tilde{x}_{j,o}), \quad (2.68)$$

$$\dot{n}_{j,m,i} = \beta_{g,i} n_{g,m,i} (\tilde{x}_{j,i} - \tilde{x}_{j,m,i}). \quad (2.69)$$

The relationship between flow rates and fluxes can be written as

$$\dot{n}_{j,m,o} = \dot{N}_j / (2\pi r_{m,o} L), \quad (2.70)$$

$$\dot{n}_{j,m,i} = \dot{N}_j / (2\pi r_{m,i} L). \quad (2.71)$$

The coefficients for Knudsen and for molecular diffusion can be expressed in the form of eq. (2.23) and

$$D_{jk}^e = F_0 D_{jk}, \quad (2.72)$$

respectively. Consequently, the model has three parameters B_0 , K_0 and F_0 , for capturing the influence of the structure of any specific porous body on viscous flow, bulk diffusion and molecular diffusion.

With the additional assumption of tortuous, mono-dispersed capillaries, which are to some degree interconnected and may not exhibit a direct path through the porous medium, the mentioned three parameters of the dusty gas model can be expressed as

$$B_0 = F_0 \frac{d_p^2}{32}, \quad (2.73)$$

$$K_0 = F_0 \frac{d_p}{4}, \quad (2.74)$$

$$F_0 = \frac{\varepsilon}{\tau}, \quad (2.75)$$

and are, thus, reduced to a set of only two morphological parameters, namely

$$d_p = \frac{8B_0}{K_0}, \quad (2.76)$$

the diameter of the assumed capillaries, and

$$\frac{\varepsilon}{\tau} = \frac{(K_0)^2}{2B_0}, \quad (2.77)$$

with ε the porosity and τ the tortuosity of the body.

It should be mentioned that K_0 may slightly depend on the absolute pressure of the gas, due to varying angular scatter patterns for different gas molecules during wall collisions. This dependence is known to be very small in porous media [92], and has been neglected in eq. (2.74). It should be also stressed that d_p and ε/τ are, inspite of their morphological reference, still more or less strongly lumped model parameters, which do not necessarily and exactly correspond to, e.g., the average pore diameter that might be determined by image analysis. A priori prediction of B_0 , K_0 and F_0 would presuppose the rigorous transition from microscopical structure to macroscopical properties. Though considerable efforts are invested in this direction, the problem of reliable micro-macro transition is still not solved.

Binary diffusion coefficients [111], D_{jk} , have been calculated in the present work by means of the Chapman-Enskog equation (Appendix C).

3 Heat transfer experiments

In heat transfer experiments, an electrical heater is placed in the tube to supply a constant heat flux at the inner side of the membrane (Fig. 2.5a). There is no gas flow in the tube, gas, in our case air, flows only through the annulus. The membrane investigated in heat transfer experiments is the support of the composite after Table 2.1, which dominates the thermal behaviour. Thermocouples (Fig. 2.5a) are placed at axial positions of approximately $z = 70, 125, 180$ mm to measure the membrane inner and outer temperatures. The exact axial position of every thermocouple is determined after fixing. Transient thermal experiments have been conducted in similar manner by monitoring the change in membrane temperature after switching on the electrical heater at $t = 0$, see Fig. 2.5b. In total 25 heat transfer experiments have been conducted (Appendix D) by different heater capacities and gas flow velocities. Some of these experiments are evaluated for the steady state case (identification of thermal conductivity of the membrane) and others are evaluated for the transient case.

3.1 Identification experiment: Steady state heat transfer

Steady state heat transfer experiments after Fig. 2.5a have been used for the determination of the thermal conductivity of the membrane, λ_m . In these experiments the inlet flow velocity of the gas in the annulus has been varied from $u_{g,o,in} = 0.15$ to 0.58 m/s and the imposed heat flux from $\dot{q}_{m,i} = 750$ W/m² to 5000 W/m², corresponding to heater capacities from $\dot{Q}_i = 15$ to 100 W. Axial temperature gradients of up to 9.4 K/cm and radial temperature gradients of up to 26.9 K/cm were found in the membrane.

Identification has not been conducted by the complete set of equations from section 2.4.1. Instead, the well known reduction of eq. (2.1) to one (the radial) dimension for the steady state with boundary conditions of the first kind at both $r_{m,i}$ and $r_{m,o}$ has been used (Appendix B). This involves the assumption of negligible axial conduction, and is only possible because we measure locally temperature differences between the inner and the outer side of the membrane. As there is no gas flow in the tube, the enthalpy flux term of eq. (2.1) has also been dropped. Apart from simplicity, this approach has the advantage of not requiring knowledge of the heat transfer coefficient to the annulus gas, $\alpha_{g,o}$. From every measured local temperature difference one value of the thermal conductivity of the membrane is derived in this way and attributed to the arithmetic average of the respective two temperatures. The results of this identification have been correlated empirically with the relationship

$$\lambda_m = -5.7372 \ln(T_m) + 38.853, \quad (3.1)$$

which is depicted as the bold solid line in Fig. 3.2. Broken lines indicate maximal deviations, defining the area where every derived thermal conductivity lies.

The findings reveal that the thermal conductivity of the membrane is temperature dependent and decreases significantly with increasing temperature. This behaviour can be explained by structural, stray and chain defect scattering during phonon transport. Phonons are considered as particles (quasi-particles) which have certain energy and momentum. The momentum of phonons is rather different to normal momentum. Due to phonon-phonon interactions a phonon alters the local atomic spacing, so that another phonon sees a difference in the crystal structure and is scattered by it. In case of heat transport, phonons are treated as a classical gas of particles, transporting energy at velocity v , the group velocity of the waves. Hot regions have higher density of phonons than cool regions. According to Debye [112], the thermal conductivity of solids can be derived by analogy to kinetic gas theory as

$$\lambda = \frac{1}{3} v c_v \Lambda, \quad (3.2)$$

where c_v is the specific heat per volume, v is the average velocity of the phonon and Λ is the phonon mean free path. The latter can be expressed in the form

$$\Lambda = a / (\alpha \gamma T), \quad (3.3)$$

where a is the inter-atomic distance, α is the thermal expansion coefficient and γ is the Gruneisen parameter [113]. Lawson transformed the equation to

$$\lambda = (a K^{3/2}) / (3\gamma^2 \rho^{1/2} T), \quad (3.4)$$

by assuming that average phonon velocity is the same as the dilatational wave velocity. Here K is bulk modulus and ρ is density of the crystal structure [114].

The mean free path, Λ , is limited by the size of specimen. Generally the specimen is polycrystalline so Λ is limited by the crystal size. Any irregularity in the crystal will scatter a wave equal to the size; an impurity or even a different isotope creates an irregularity. The defect size is that of about one atom. By scattering, two phonons can combine into one, or one phonon breaks into two. These are inelastic scattering processes (as in a non-linear interaction).

At the first glance, phonon scattering is expected to preserve the thermal current, as energy and momentum are both conserved (Fig. 3.1a), but in reality the preservation of thermal current is abrogated by the periodic dispersion of phonons. So the two initial wave vectors give after subtraction of G (a reciprocal lattice vector for the reduction of thermal current) a new vector in the opposite direction (Fig. 3.1b). Such a process is called Umklapp process [115]. Processes in which $G = 0$ are called N-processes.

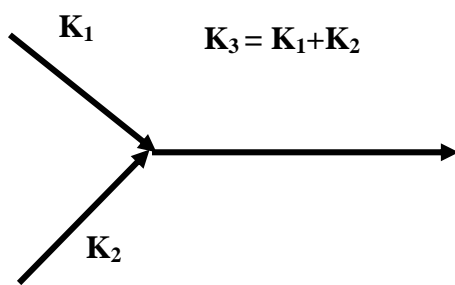


Fig. 3.1a: Phonon scattering in the crystals, non-linear wave interaction.

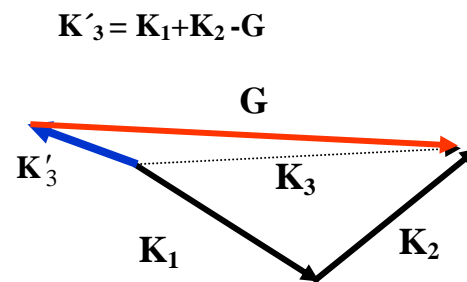


Fig. 3.1b: Phonon scattering in the crystals, Umklapp process (U-Process).

At high temperature, most of the phonons will undergo the U-process. Assuming that all the scattering processes are independent, each process acts independently to reduce the conductivity. Hence, at very low temperature the U-processes are frozen due to small scattering, and at high temperature enough phonons will be available for the U-process.

Consequently, enhancement of U-processes at higher temperature leads to intensified consumption of thermal current by phonons and this lowers the heat transfer through the specimen. So, it can be concluded that phonon scattering limits the thermal conductivity [115]. The proposed inversely proportional dependence of thermal conductivity on thermodynamic temperature is verified by the experimental data (Fig. 3.2), though the value of intercept would be different than zero (Fig. 3.3). Respective correlations are possible, with similar accuracy as eq. (3.1).

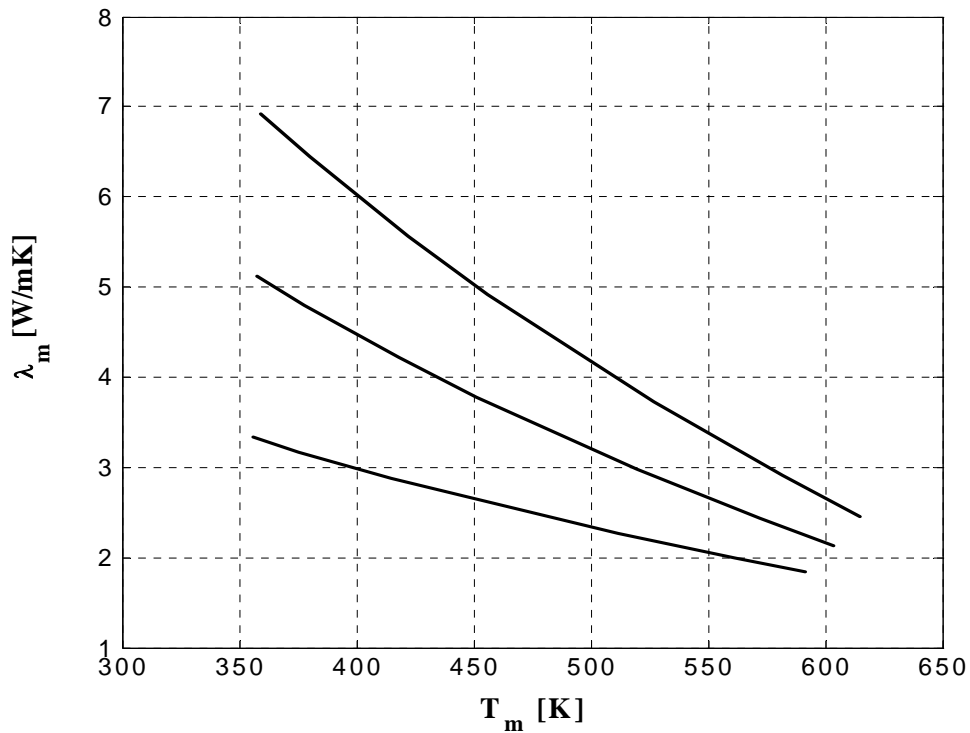


Fig. 3.2: Thermal conductivity of tubular inorganic membranes, made of $\alpha\text{-Al}_2\text{O}_3$, as derived from experimental data.

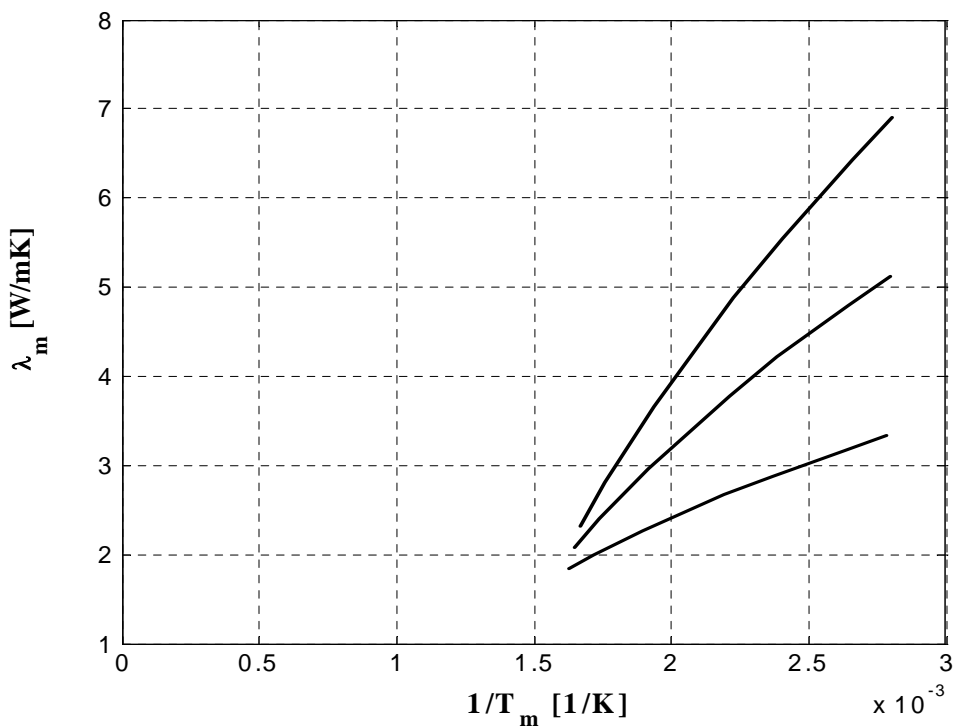


Fig. 3.3: Membrane thermal conductivity vs. the inverse thermodynamic temperature.

An orientation about the value of occurring temperature gradients is given in Figs 3.4 and 3.5 for different heat flow rates and gas flow velocities. Radial temperature gradients

reach maximal values of up to 26.9 K/cm (Fig. 3.4), maximal axial temperature gradients lie up to 9.4 K/cm (Fig. 3.5).

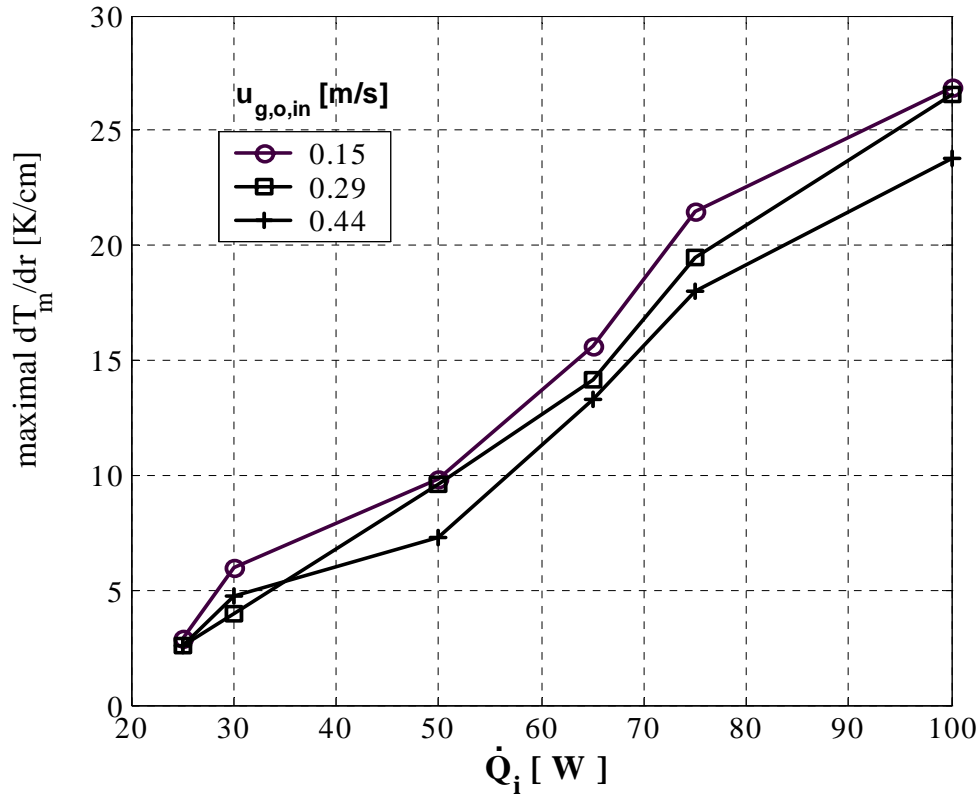


Fig. 3.4: Maximal radial temperature gradients in the membrane vs. heat flow rate for different gas flow velocities acc. to the experiments.

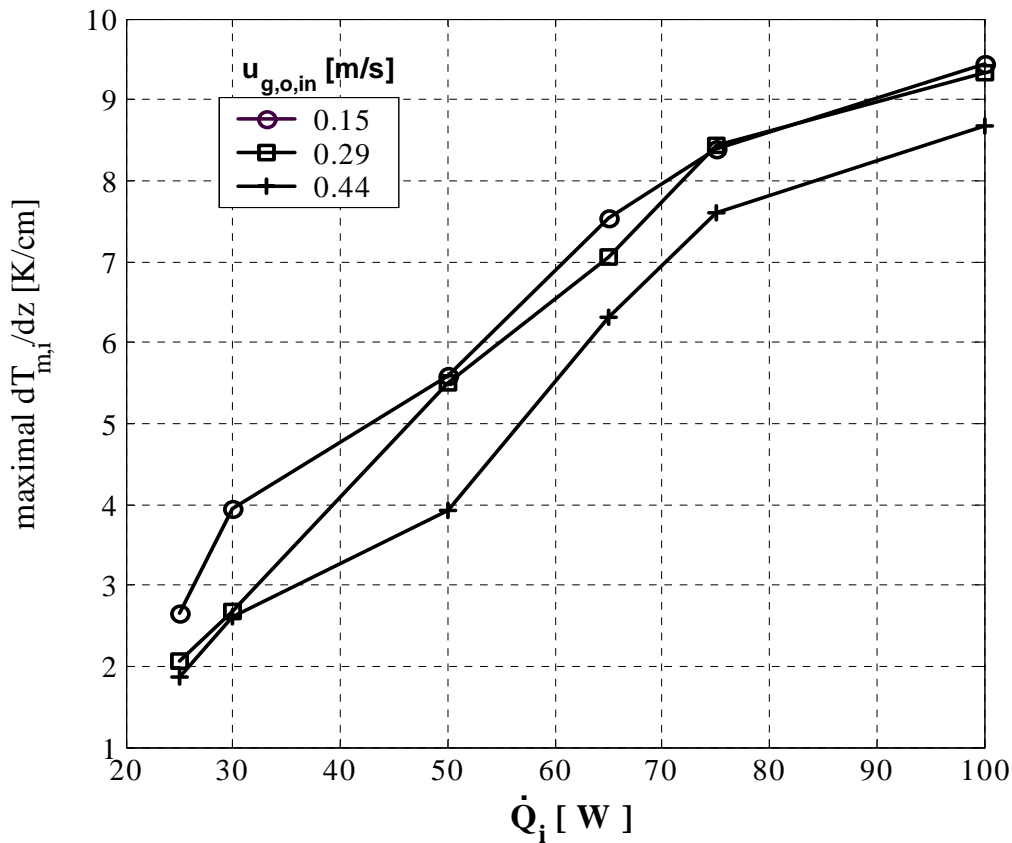


Fig. 3.5: Maximal axial temperature gradients in the membrane vs. heat flow rate for different gas flow velocities acc. to the experiments.

To obtain a more comprehensive picture of the temperature field in the membrane (Fig. 3.6) the complete equations after section 2.4.1 are solved numerically for the steady state, though without transmembrane enthalpy flux, tube-side convection, and axial dispersion of annulus flow. These simulations are two-dimensional in respect to the membrane and require, in contrary to the conducted identification of λ_m , knowledge of the gas-side heat transfer coefficient in the annulus, $\alpha_{g,o}$, see eq. (2.5). The latter has been determined after [116] for the case of thermally and hydrodynamically fully developed laminar flow for constant heat flux (Appendix C). The temperature profiles are flat at $z = 0$ and $z = L$, due to the consideration of axial conduction and the adiabatic boundary conditions of eqs (2.6), but approximately linear in the middle section of the membrane, where the temperature measurements take place (Fig. 3.6). Both the experimental and simulation results for the steady state reveal that – due to the moderate thermal conductivity and the large thickness of the membrane – significant temperature gradients are present in axial and radial direction, and may not be ignored in the design of membrane reactors.

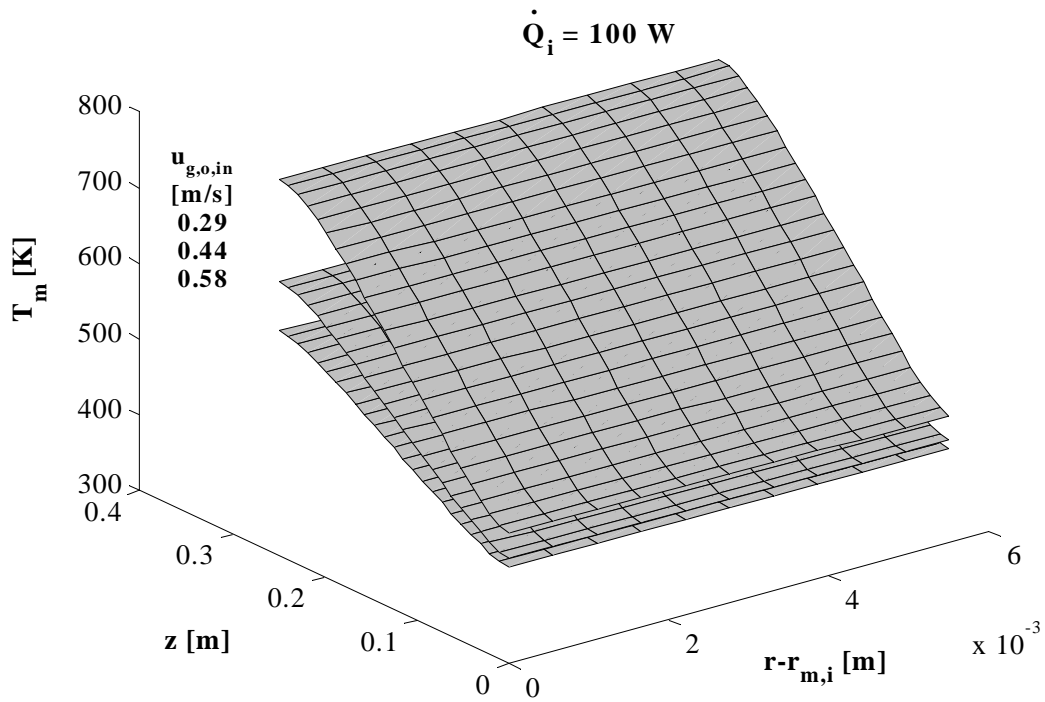


Fig. 3.6: Simulated steady state, two dimensional temperature field in the membrane for different gas flow velocities.

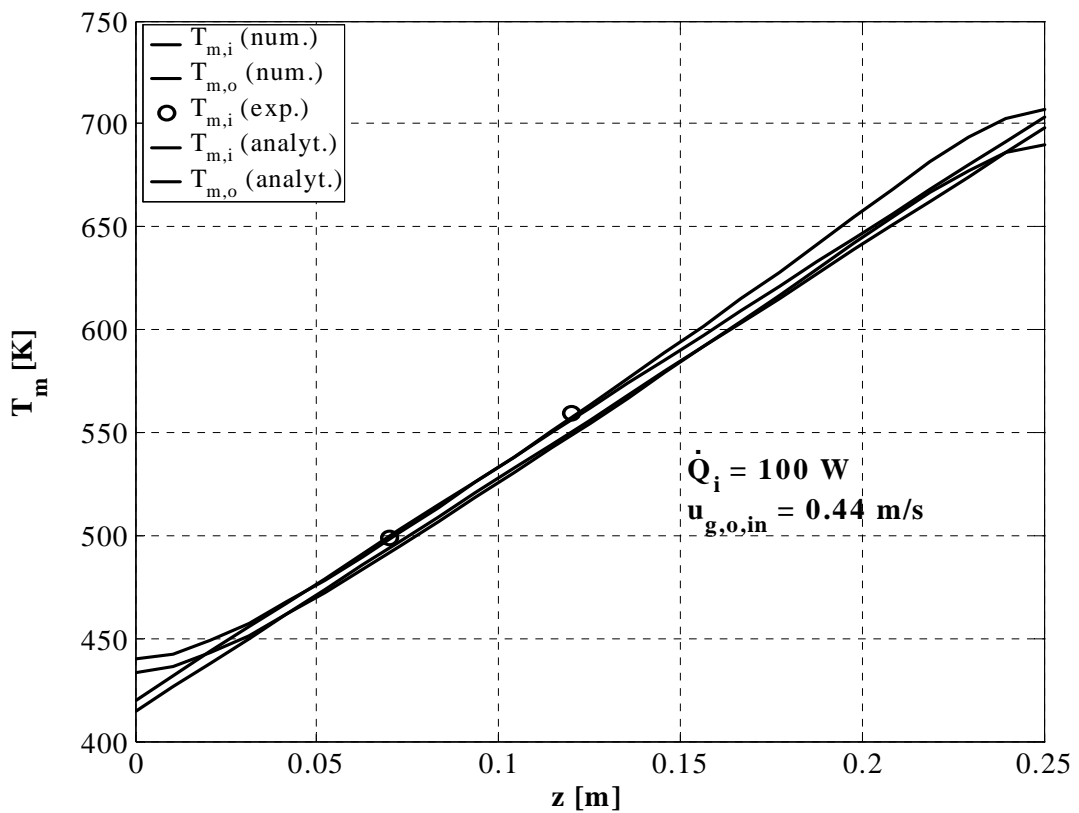


Fig. 3.7: Numerically and analytically calculated axial profiles of membrane temperature compared with measured values.

The problem solved numerically in Fig. 3.6 can be somewhat simplified by neglecting axial conduction in the membrane and the temperature dependence of membrane thermal conductivity. Then, analytical solution is possible (Appendix B). Axial membrane temperature profiles calculated after this analytical solution, calculated after the numerical solution, and measured are compared in Figs. 3.7 and 3.8, with good agreement. As already stressed, the coefficient of gas-side heat transfer, $\alpha_{g,o}$, is not important for the identification of λ_m , but is important for the level of temperature at different axial positions. It should also be mentioned that results like those of Figs 3.7 and 3.8 are the steady state asymptotes of transients that will be discussed in the subsequent section 3.2.

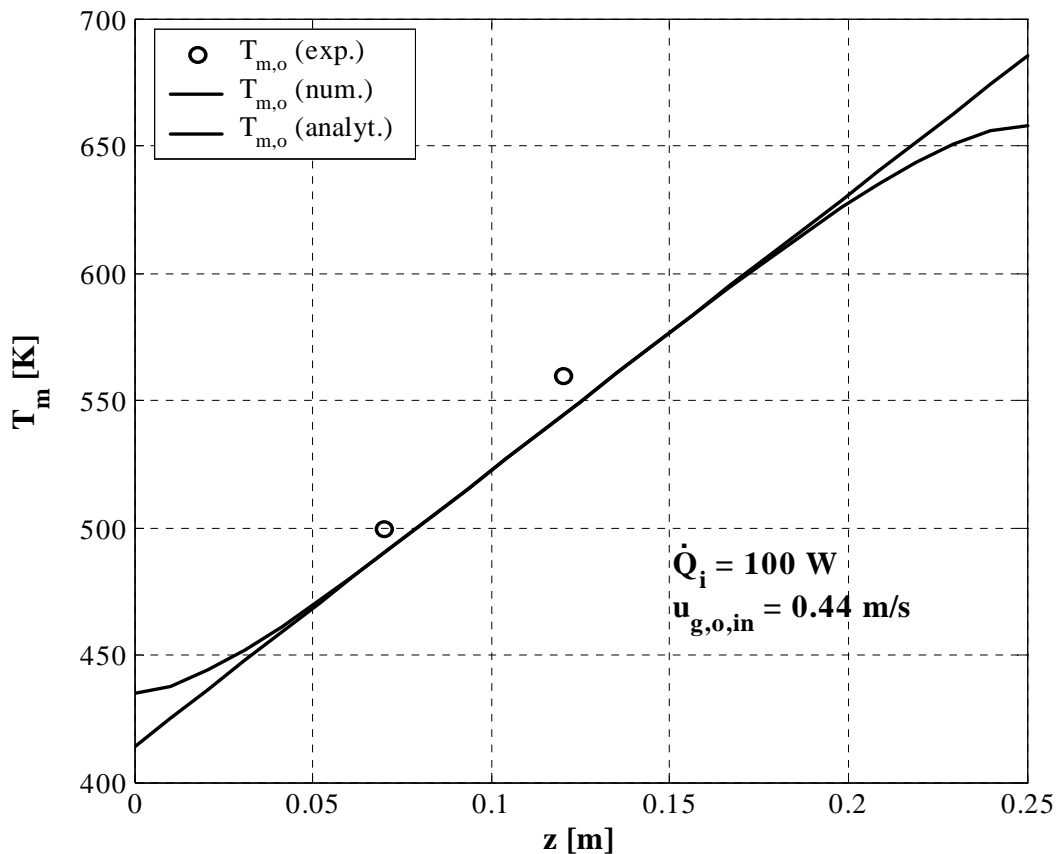


Fig. 3.8: Numerically and analytically calculated axial profiles of outer membrane temperature compared with measured values.

3.2 Validation experiment: Transient heat transfer

In transient thermal experiments the change of membrane surface temperature is monitored after switching on the electrical heater at the time $t = 0$ (Fig. 2.3b). These experiments are modelled by numerically solving the same set of equations as for the steady state heat transfer case, though expanded by the accumulation term at the left-hand side of eq. (2.1). To this purpose the thermal diffusivity of the membrane, is calculated from thermal conductivities after eq. (3.1).

Since nothing is fitted, the transient thermal experiments are pure validation experiments, confirming the values of membrane thermal conductivity that have been derived in the previous section. This validation is successful, as the good agreement between measurement and prediction in Figs 3.9 to 3.13 exemplarily shows. The respective experiments have, again, been conducted at various gas and heat flow rates.

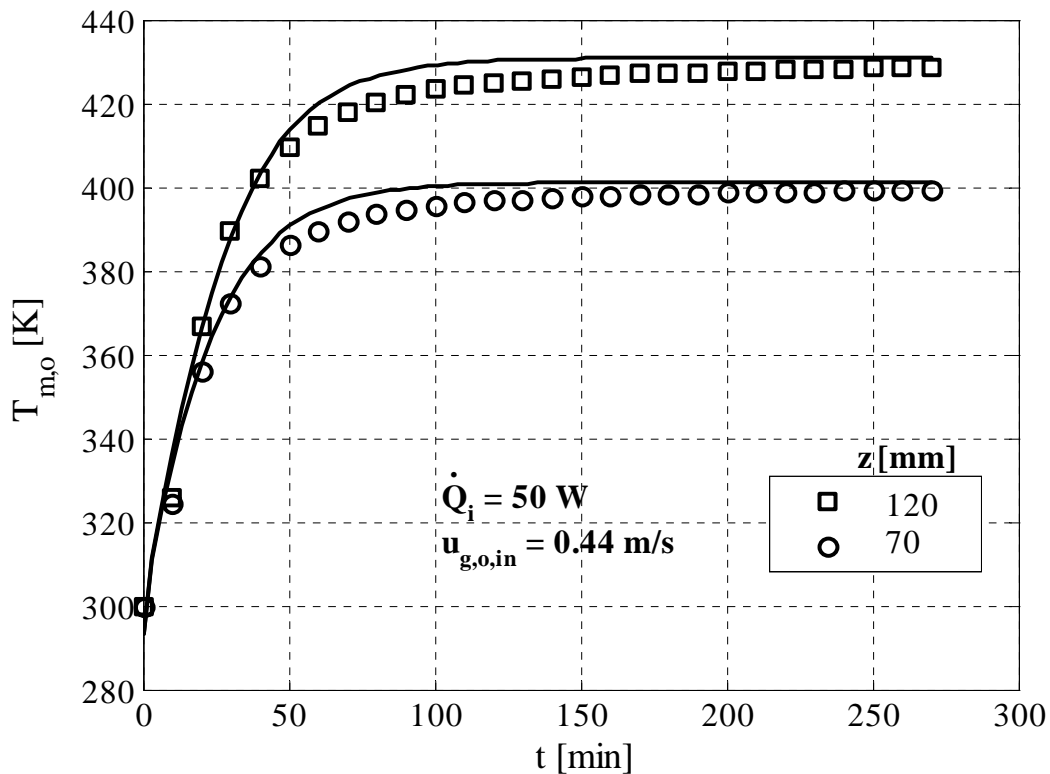


Fig. 3.9: Comparison between measured and predicted transients of membrane outer side temperature at $\dot{Q}_i = 50 \text{ W}$ and $u_{g,o,in} = 0.44 \text{ m/s}$ for two different axial locations.

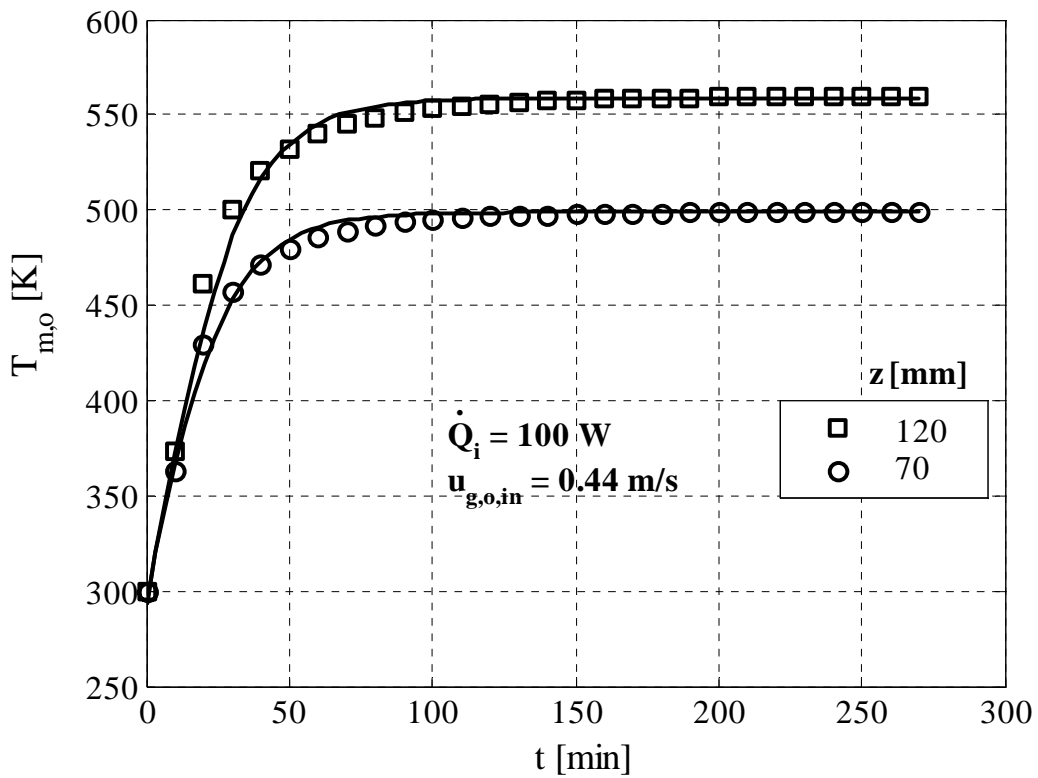


Fig. 3.10: As in Fig. 3.9, however for $\dot{Q}_i = 100$ W.

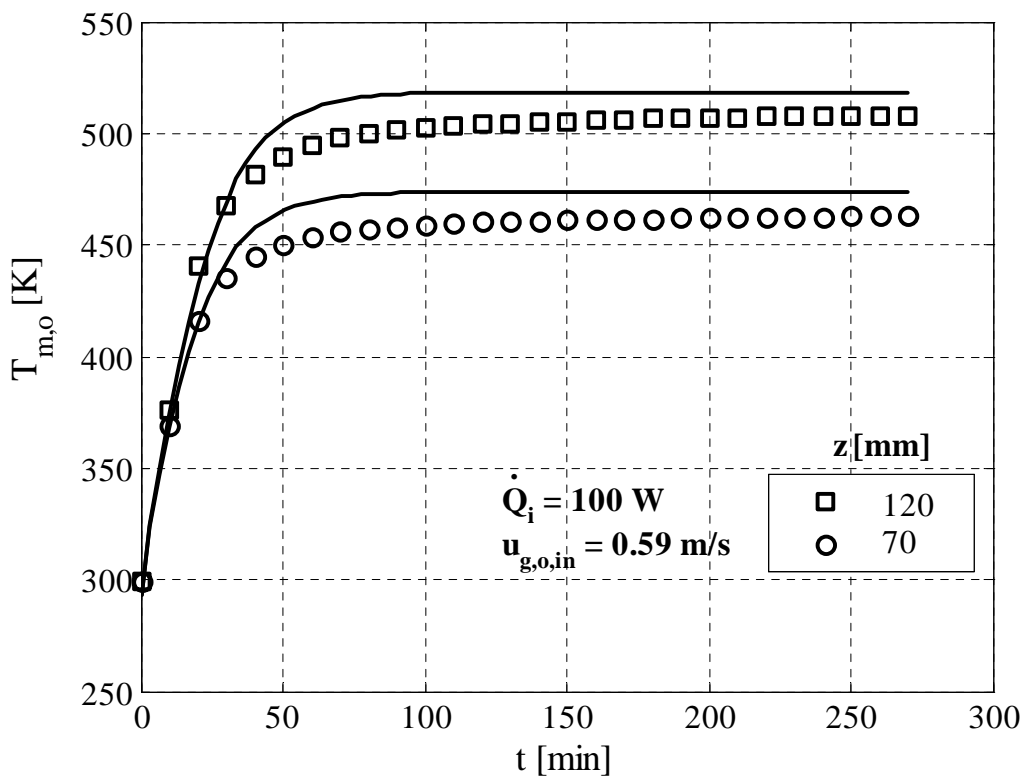


Fig. 3.11: Comparison between measured and predicted transients of membrane outer side temperature at $\dot{Q}_i = 100$ W and $u_{g,o,in} = 0.59$ m/s for two different axial locations.

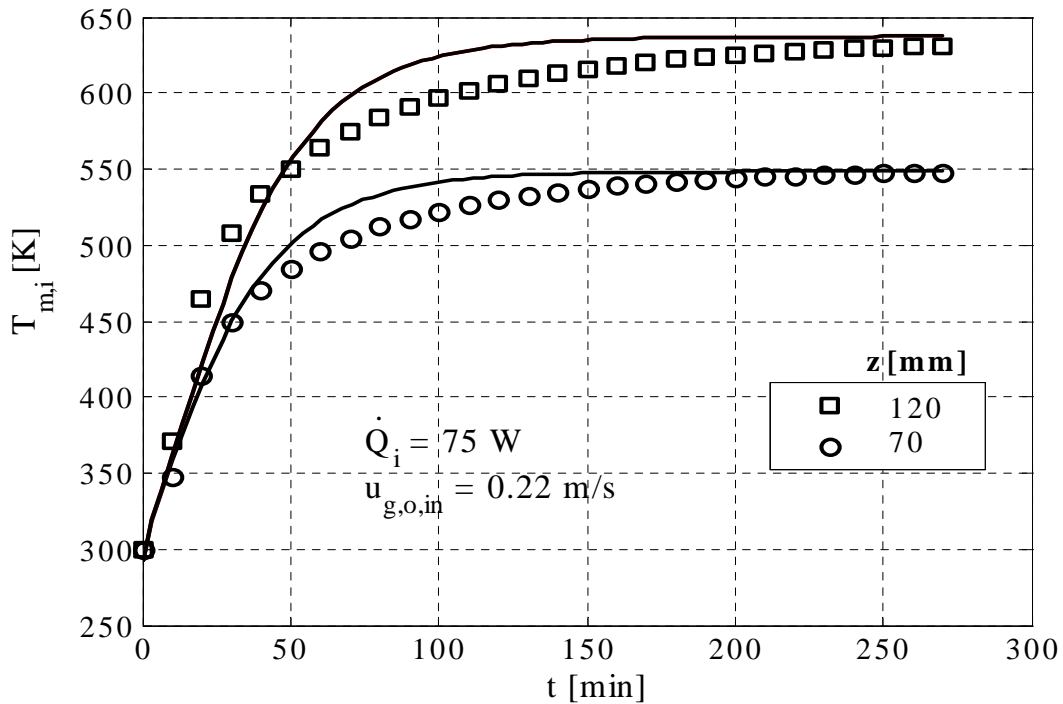


Fig. 3.12: Comparison between measured and predicted transients of membrane inner side temperature at $\dot{Q}_i = 75$ W and $u_{g,o,in} = 0.22$ m/s for two different axial locations.

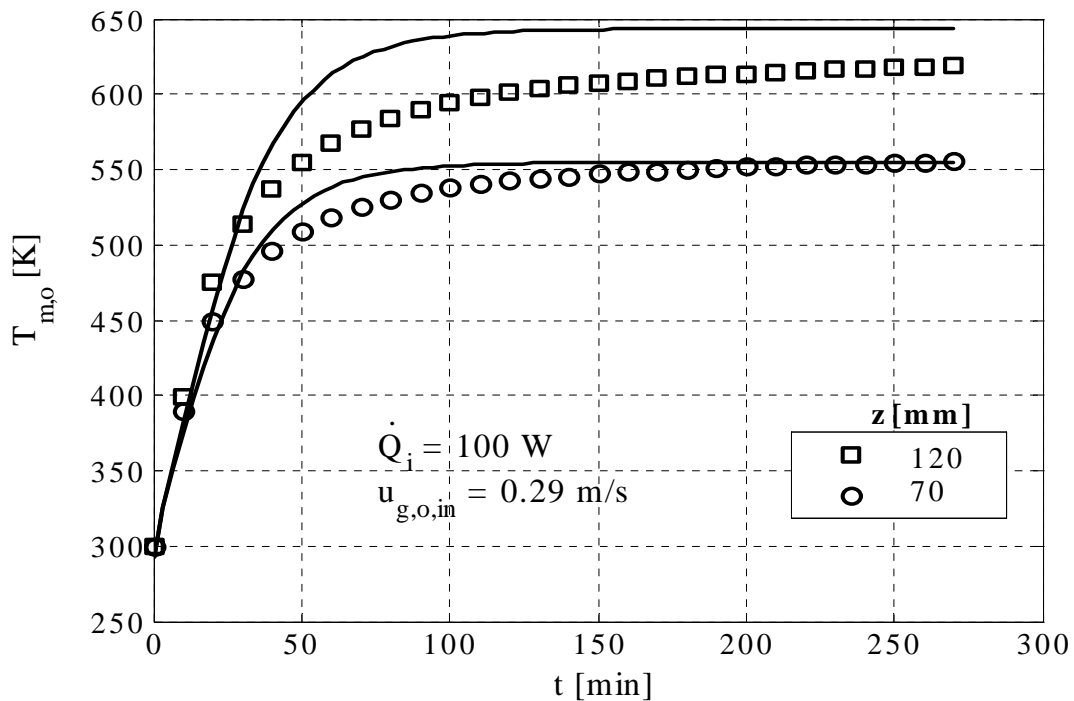


Fig. 3.13: As in Fig. 3.11, however for $u_{g,o,in} = 0.29$ m/s.

The influence of parameters like the thermal capacity of the electrical heater and the outer reactor cage, imperfect insulation of the reactor ends, and heat losses to the environment has been studied with the help of adequate, extended model versions, and found to be low in case of the transient heat transfer experiments.

4 Mass transfer experiments

Much effort has been devoted to the problem of predicting the parameters of the DGM which characterize a porous medium. From the practical point of view, it is still better to determine these parameters directly by mass transfer experiments. To test a theory whose mathematical formulation is based on adjustable parameters, a comprehensive set of experiments is required to determine the model parameters. It is also difficult to keep apart the two fundamental aspects of theory, the gas transport part of the theory as opposed to the geometrical structure part that refers to the porous membrane. In many cases reported in the literature, it is not clear if the transport equations themselves, the approximation of homogeneity of the porous medium (single values of K_0 , B_0 and ε/τ), or some combination of both is being tested [98].

Mass transfer experiments enable the identification and validation of all mass transport parameters of the membrane. Single gas permeation experiments (Fig. 2.5c) have been performed mainly for the identification of structural parameters of every membrane layer by using air, N_2 and He for different temperatures (20-500 °C) and pressures (1-3 bar). Isobaric diffusion experiments (Fig. 2.5d) and the transient diffusion experiments (Fig. 2.5e) have been conducted for validation of the layer transport parameters identified by single gas permeation. Hence, only the composite membrane has been used for these experiments, which have been performed for N_2 and He at room temperature.

4.1 Identification experiment: Single gas permeation

The principle of steady state, single gas permeation measurements is depicted in Fig. 2.5c, see also [95-99]. As the sketch shows, gas is introduced in the annulus, flows through the membrane due to the pressure difference ΔP , and leaves the cell at the end of the tube. In this case, and for a homogeneous membrane, the general DGM equation (2.62) reduces to:

$$\dot{n}_j = -\frac{1}{RT} \left(\frac{4}{3} K_0 \sqrt{\frac{8RT}{\pi M_j}} + \frac{B_0}{\eta_j} \bar{P} \right) \nabla P. \quad (4.1)$$

For cylindrical coordinates and a relatively moderate membrane thickness the expression

$$\frac{\dot{N}_j}{\Delta P} = -\frac{2\pi L}{\tilde{R}T \ln\left(\frac{r_{m,o}}{r_{m,i}}\right)} \left(\frac{4}{3} K_0 \sqrt{\frac{8\tilde{R}T}{\pi\tilde{M}_j}} + \frac{B_0}{\eta_j} \bar{P} \right) \quad (4.2)$$

is obtained by integration of eq. (4.1).

In eq. (4.2), \bar{P} is the mean pressure in the membrane, $\bar{P} = (P_o + P_i)/2$, ΔP is the pressure drop, $\Delta P = P_o - P_i$. In experiments with a homogeneous membrane the pressure level, i.e. \bar{P} , is varied, while the pressure difference, ΔP , and P_i , P_o , or both are measured. Additionally, the gas flow rate, which permeates through the membrane, is determined, and converted to the gas molar flow rate, \dot{N}_j . With known geometry of the membrane (L , $r_{m,o}$, $r_{m,i}$) and gas properties, the parameters of the dusty gas model, K_0 and B_0 , can then be derived, compare also with [117]. Specifically, and due to the linearity of eq. (4.2), the Knudsen coefficient, K_0 , is derived from the intercept, and the permeability constant, B_0 , from the slope of a plot of the ratio $\dot{N}_j/\Delta P$ (termed as permeability coefficient) versus \bar{P} , as shown in Fig. 4.1.

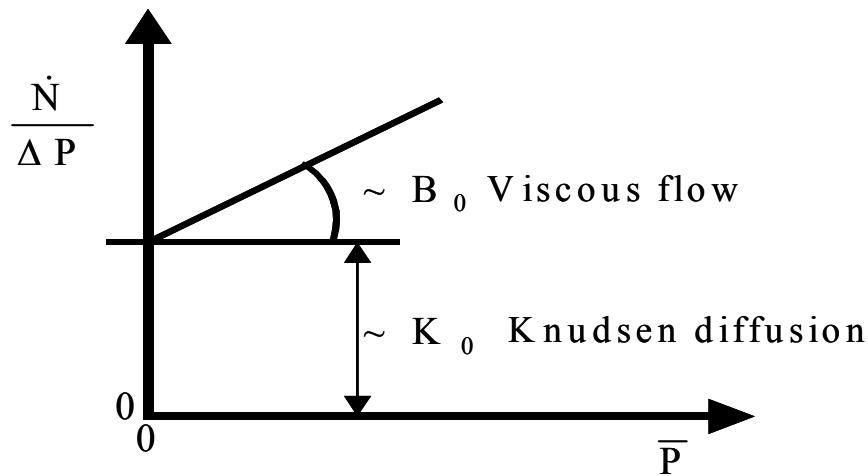


Fig. 4.1: Determination of membrane structural parameters.

The classical theory of viscous flow predicts that a plot of permeability coefficient versus the mean pressure should be a straight line through the origin, whose slope is inversely proportional to the gas viscosity. Later it was found that such a plot didn't go through the origin due to the fact that gas appeared to 'slip' over the solid surface. Equation (4.2) gives this result directly by representing the slip in terms of the value of intercept. This is the basis for the determination of gas viscosity by capillary flow, or the determination of structural parameters of the porous membrane by permeability measurements by a known gas [117].

If, now, a second homogeneous layer is added to the original membrane and the described series of permeation experiments repeated, then eq. (4.2) can be applied to calculate the pressure at the interface between the first and the second layer of the composite. In this manner, pressures and flux are known for the second layer, so that the derivation of K_0 and B_0 can be conducted also for this layer, in exactly the previously discussed way. Recursively, the parameters of every layer of any composite membrane can be derived individually, provided that all intermediate membranes, starting from the support and ending with the final composite, are available. The results of this derivation for the investigated membrane are summarized in Table 4.1.

Though the identification of K_0 and B_0 can be done with only one gas at only one temperature, a large amount of experiments have been conducted in the present work for different gases at various temperatures. For every temperature, gas and layer a value pair of K_0 and B_0 has been derived so that it could be controlled that K_0 and B_0 depend on the layer (Appendix D), but do not depend – apart from a moderate scatter – from temperature or the gas used. The opposite validation is to show that by means of the average values of K_0 and B_0 , as listed in Table 4.1 for every individual layer, all measured data can be predicted reliably, irrespectively of average pressure (in all experiments between 1 and 3 bar), temperature, or the kind of gas. This type of validation will be exemplified in the following on the basis of selected results, which also enable to discuss a number of interesting influences.

M1		L = 120 mm		$d_{m,o} = 32$ mm		$d_{m,i} = 21$ mm (approx.)	
Layer	Composition	Nominal pore diameter [m]	Thickness [m]	K_0 [m]	B_0 [m ²]	d_p [m]	$\frac{\varepsilon}{\tau}$
Support	α -Al ₂ O ₃	3.0×10^{-6}	5.5×10^{-3}	8.16×10^{-8}	2.96×10^{-14}	2.90×10^{-6}	0.112
1 st layer	α -Al ₂ O ₃	1.0×10^{-6}	25×10^{-6}	7.99×10^{-8}	2.73×10^{-14}	2.73×10^{-6}	0.124
2 nd layer	α -Al ₂ O ₃	60×10^{-9}	25×10^{-6}	2.98×10^{-9}	2.85×10^{-17}	76.5×10^{-9}	0.156
3 rd layer	γ -Al ₂ O ₃	10×10^{-9}	2×10^{-6}	2.03×10^{-9}	7.47×10^{-18}	29.4×10^{-9}	0.277

Table 4.1: Producer information and identified mass transfer parameters of membranes (M1).

This discussion is started, for the sake of simplicity, with data for the support layer, as depicted in Figs 4.2 to 4.4. Figure 4.2 shows the influence of gas molar mass, \tilde{M}_j , on the $\dot{N}_j/\Delta P$ over \bar{P} lines. According to eq. (4.2), the intercept (i.e. the Knudsen contribution) should depend on $\tilde{M}_j^{-1/2}$ and, thus, decrease with increasing \tilde{M}_j (Graham's law). While the molar mass does not explicitly appear in the slope, it does have an influence on viscous flow, via the dynamic viscosity of the gas, η_j , which is a function of, approximately, $\tilde{M}_j^{-1/6}$ (see, e.g., [118], p. 76). Consequently, the slope should depend on $\tilde{M}_j^{1/6}$, and moderately increase with increasing mass of the gas molecules. Both trends are convincingly verified by the experimental data.

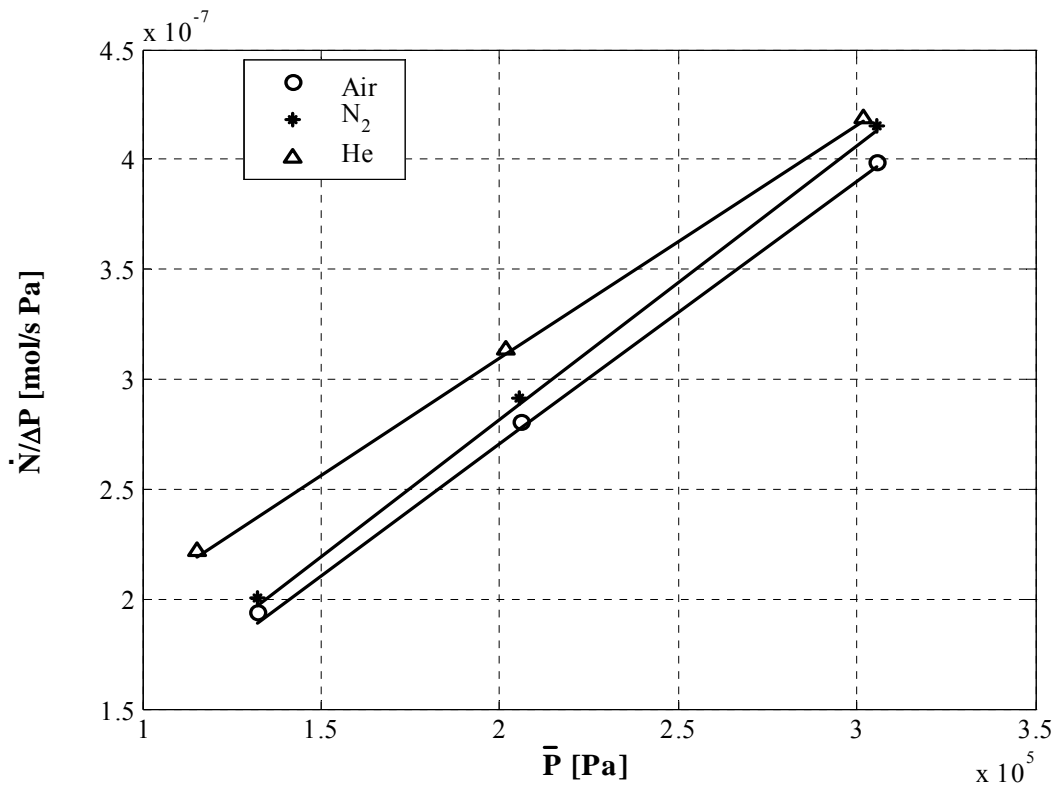


Fig. 4.2: Ratio of molar flow rate to pressure drop versus the average pressure for the support of the investigated membrane (M1) at 25°C for three different gases; (solid lines in this and the subsequent figures: calculations after the dusty gas model).

As to the influence of temperature, it should be proportional to $T^{-1/2}$ in the Knudsen, and very strong – proportional to approximately $T^{-1.75}$ – in the viscous regime. Notice that the explicit, inverse proportionality on temperature of eq. (2.62) and the temperature dependence of viscosity ($\eta_j \sim T^{0.75}$, see, again, [118]) go into the total influence of temperature on viscous flow. The described behaviour is verified by the intercepts and slopes

of the data of Fig. 4.3. In total, the temperature influence depends on the proportion between Knudsen diffusion and viscous flow, which is a matter of membrane structure and pressure level. For moderate pressures in the rather permeable support (Fig. 4.4), the flow rate comes out to depend approximately on $1/T$ according to the calculation and the measurements. The linearity between flow and average pressure is pointed out in both Figs 4.2 and 4.3.

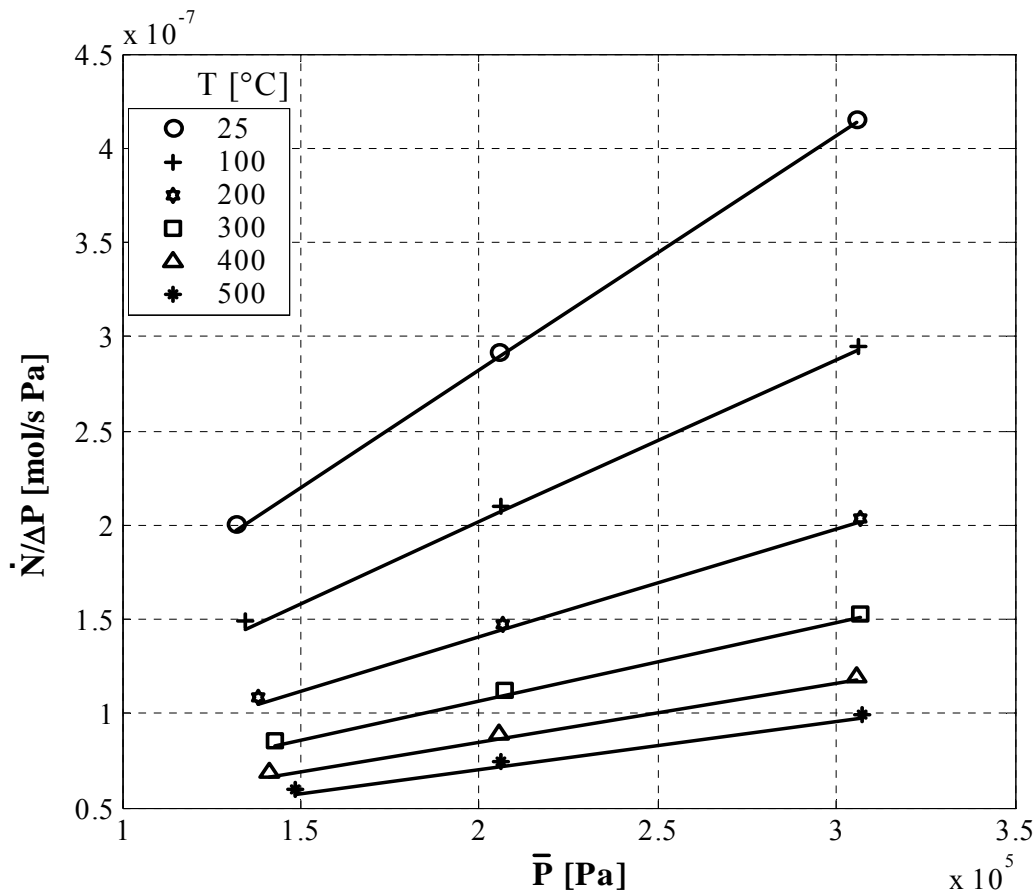


Fig. 4.3: Ratio of molar flow rate to pressure drop versus the average pressure for the support of the investigated membrane (M1) for N_2 at various temperatures.

The permeability coefficient ($\dot{N}_j/\Delta P$) of the top layer is calculated from the permeation experiments of the intermediate layer(s) on which it is deposited. As mentioned before, a previous characterization of the support and the intermediate layers is necessary to characterize the top layer. Figure 4.5 shows the molar flow rates of N_2 at ambient temperature through every individual layer of the membrane, divided by the respective pressure drop and plotted against the mean pressure. The support permeability coefficient is linearly dependent on pressure, the respective, large slope indicates the presence of viscous flow due to large pore sizes. The measured permeability coefficients of the intermediate layers deposited on the support show also a dependence with the pressure, but now with a lower slope, which indicates less transport by viscous flow than that of the support. It is obvious from the

diagram that the flow rate is strongly influenced by the mean pressure in case of the support and the 1st layer, as there is a large contribution of viscous flow in these membranes, due to their relatively large pore diameters. In contrary, Knudsen diffusion dominates in the 2nd and 3rd layer. Since Knudsen diffusion is independent of pressure, the respective lines are very flat in Fig. 4.5. Notice that the expression $\ln(r_{m,o}/r_{m,i})$ in eq. (4.2) reduces to the ratio of layer thickness to $r_{m,i}$ for large radii of the membrane.

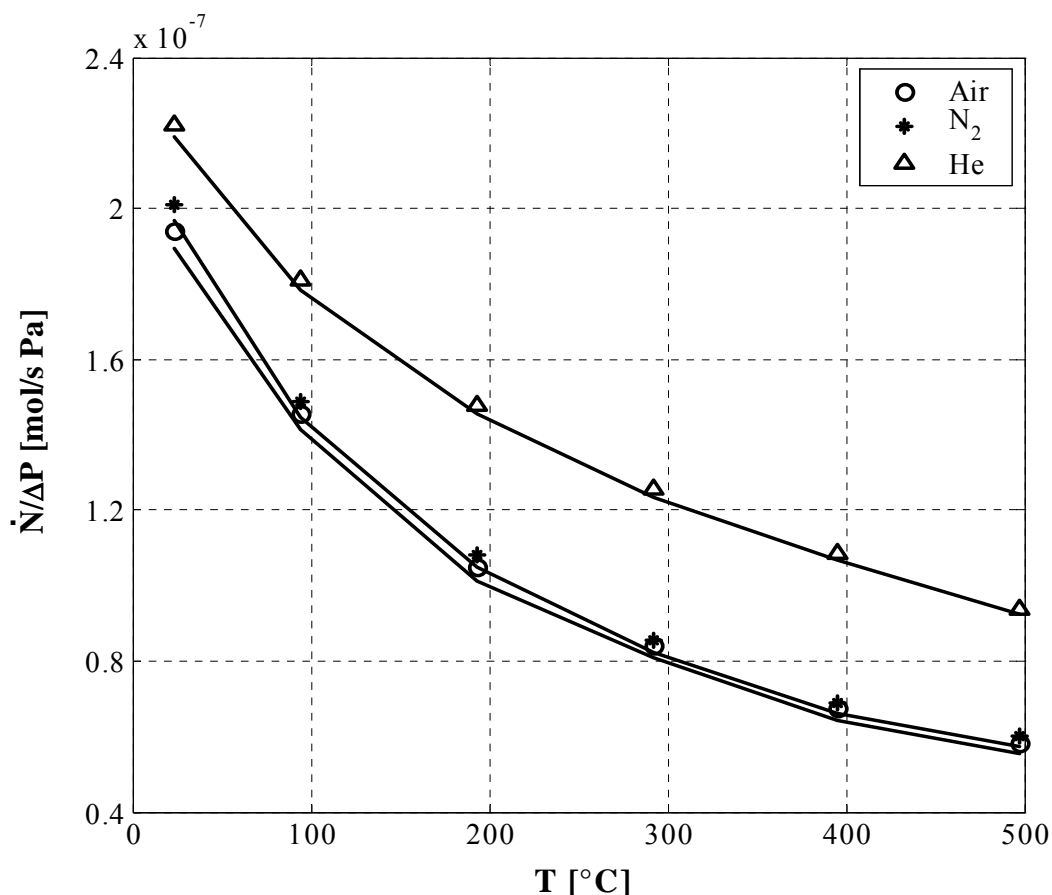


Fig. 4.4: Ratio of molar flow rate to pressure drop versus temperature for the support of the investigated membrane (M1) for three different gases at the lowest realised pressure level of approximately 1 bar.

It is believed that the intermediate layer(s) eliminates the defects of the support and provides a plane surface for deposition of the last layer [89]. However, the top layer thickness may vary by different infiltration of this layer into the intermediate one. The deposition may fill the pores of the intermediate layer, so that part of the subsequent particles are not used to form the top layer. The capillary force produced by the pores of the intermediate layer will affect more the particles which are inside the pores than those which form the top layer, so layer packing will be different. Hence, unsupported layers and the composite membrane show

a different structural behaviour, produced by the capillary forces of the intermediate layer. This influence is depicted (compare Figs 4.4 and 4.7).

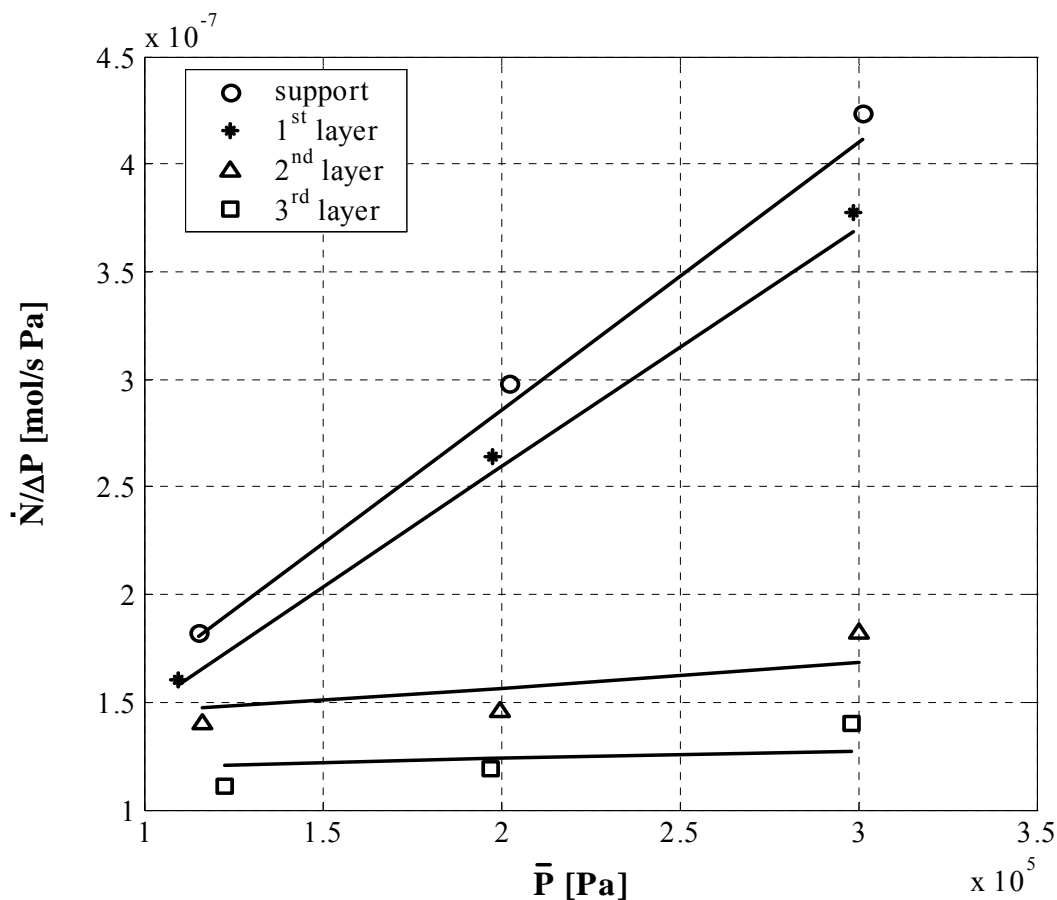


Fig. 4.5: Ratio of molar flow rate to pressure drop versus the average pressure for N_2 at $25^\circ C$ for every individual layer of the investigated membrane (M1).

Results for the complete composite membrane are presented in Figs 4.6 and 4.7. At a first glance, Fig. 4.6 appears to be a simple counterpart of Fig. 4.2. However, this impression is misleading. While Fig. 4.2 refers to one homogeneous layer (the support), and allows for a clear distinction between Knudsen and viscous contribution, various such contributions for different layers are combined in Fig. 4.6, with an overall enhancement of the role of Knudsen diffusion. The result are flatter curves than in Fig. 4.2. And, another striking result is that the slope of these curves increases with decreasing molar mass of the gas in Fig. 4.6, while it decreases with decreasing \tilde{M}_j in Fig. 4.2.

In other words, the composite shows in respect to a change of molar mass exactly the opposite behaviour than the support. This finding can be generalised: Indeed, the composite can behave in a different way than a homogeneous membrane, even in a different way than every of its own constituent layers. Otherwise, the behaviour of the composite and of the individual layer can also be similar, as the linearity of the curves in Fig. 4.6 shows.

Consequently, proper consideration of asymmetry and multilayer structure is a presupposition for the physically consistent description of mass transport in composite membranes. As to Fig. 4.7, it shows that the total influence of temperature is considerably weaker in the composite membrane than in the support (Fig. 4.4), due to the increased role of Knudsen diffusion. The flow rates are lower for the composite, as expected.

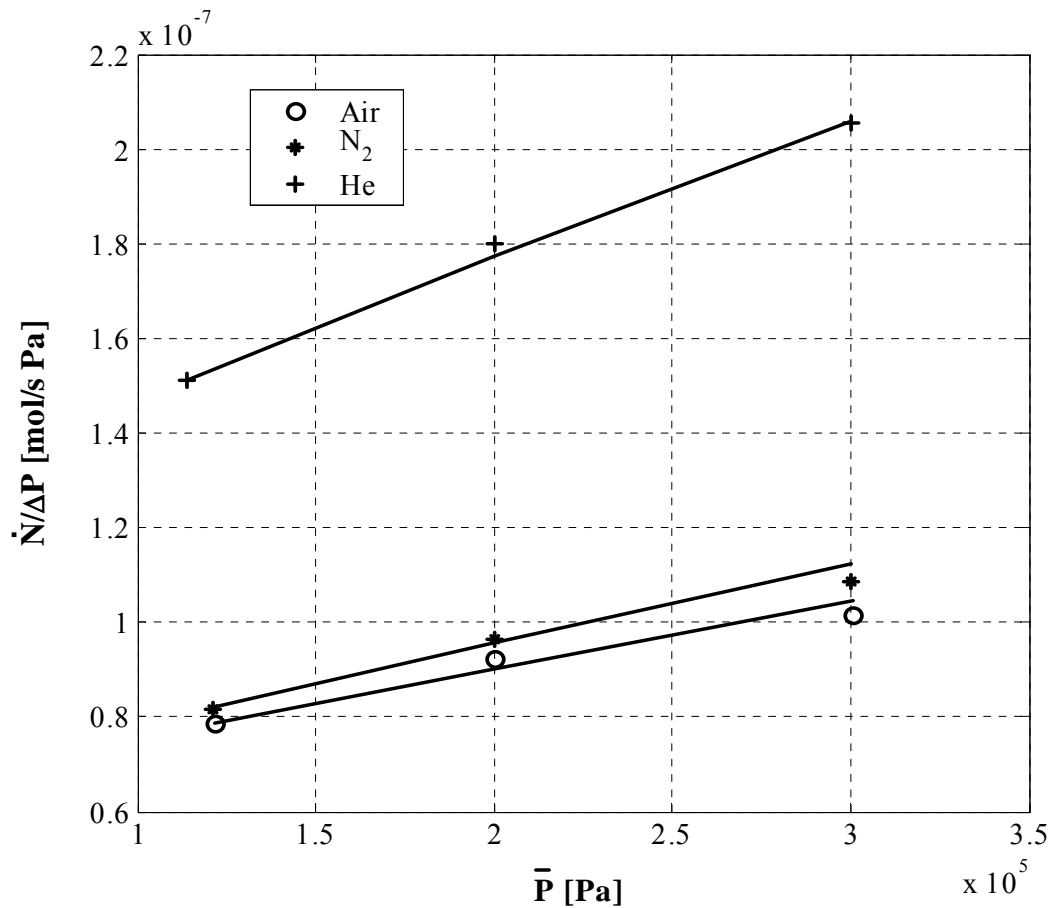


Fig. 4.6: Ratio of molar flow rate to pressure drop versus the average pressure for the composite membrane (M1) at 25°C for three different gases.

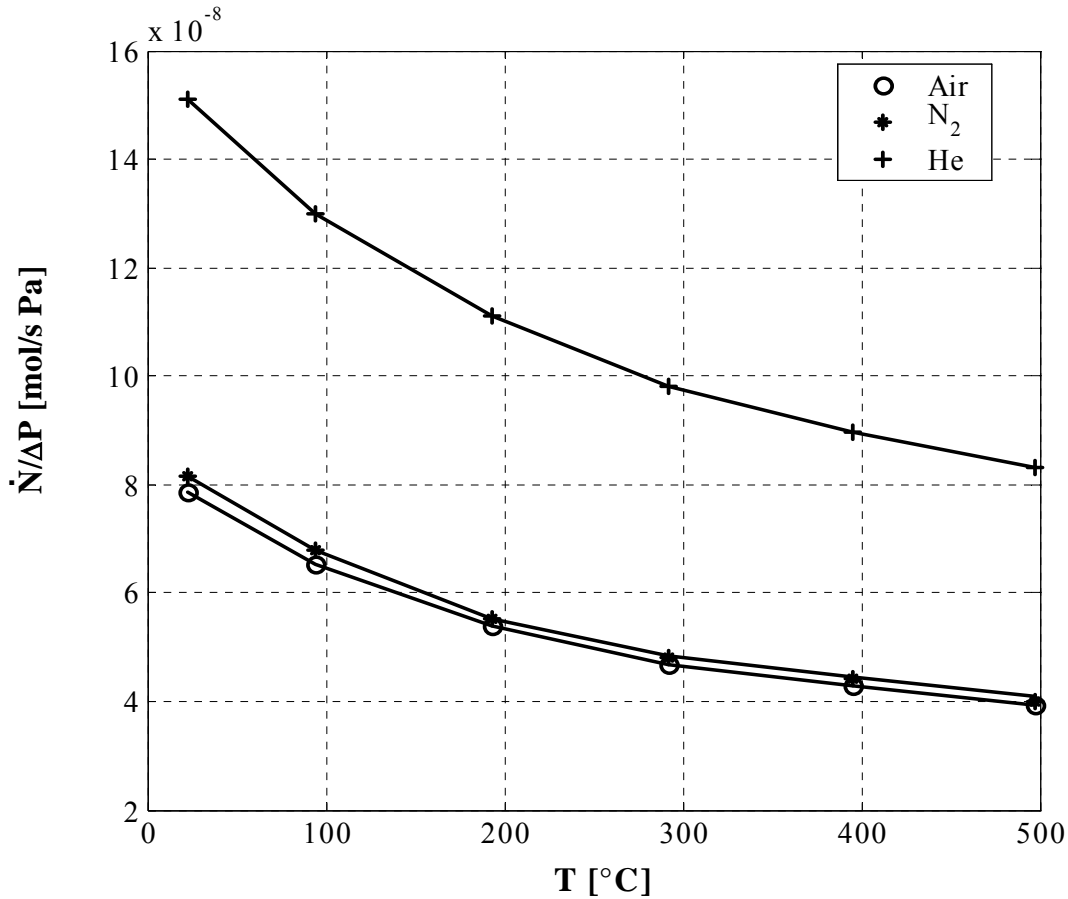


Fig. 4.7: Ratio of molar flow rate to pressure drop versus temperature for the composite membrane for three different gases at the lowest realised pressure level of approximately 1 bar.

The structural parameters d_p and ε/τ as derived from K_0 and B_0 by means of eqs (2.76) and (2.77), are given in Table 4.1 for every membrane layer. In respect to the pore diameter, d_p , we see a coarse agreement with the nominal values according to the producer – with exception of the 1st and 3rd layers, which appear to have wider pores than intended. As to the ratio ε/τ – essentially F_0 (eq. (2.73)) – it should be noticed that correlations exist in literature that describe this parameter as a function of porosity alone [119]. The values of ε/τ in Table 4.1 correspond, according to such correlations, to porosities in the range of 0.2 to 0.4, which is not unreasonable for layers consisting of small primary particles. However, such comparisons can only be indicative, for many reasons: Uncertainties of identification caused by the joint influence of d_p and ε/τ on K_0 and B_0 ; The fact that all present derivations have been carried out with the layer thicknesses indicated by the producer, while in reality the transition from one to the other layer is not sharp; Irregularities, inhomogeneities and defects of the real membranes. And, finally, the radical, unrealistic assumptions associated with eqs. (2.74) and (2.75). Realistic transition from the microstructure of porous media to their macroscopical properties is a major, but still unsolved problem.

The second investigated membrane series M2 had a smaller inner diameter of $d_{m,i} = 7$ mm and consisted of a total of 5 layers. The respective results are summarized in Table 4.2.

M2 $L = 200$ mm $d_{m,o} = 10$ mm $d_{m,i} = 7$ mm (approx.)

Layer	Composition	Nominal pore diameter [m]	Thickness [m]	K_0 [m]	B_0 [m ²]	d_p [m]	$\frac{\varepsilon}{\tau}$
Support	$\alpha\text{-Al}_2\text{O}_3$	3.0×10^{-6}	1.5×10^{-3}	8.80×10^{-8}	3.32×10^{-14}	3.01×10^{-6}	0.117
1 st layer	$\alpha\text{-Al}_2\text{O}_3$	1.0×10^{-6}	25×10^{-6}	7.95×10^{-8}	2.56×10^{-14}	2.57×10^{-6}	0.124
2 nd layer	$\alpha\text{-Al}_2\text{O}_3$	0.2×10^{-6}	25×10^{-6}	7.71×10^{-9}	2.74×10^{-16}	0.284×10^{-6}	0.109
3 rd layer	$\alpha\text{-Al}_2\text{O}_3$	60×10^{-9}	25×10^{-6}	5.72×10^{-9}	7.88×10^{-17}	110×10^{-9}	0.208
4 th layer	$\gamma\text{-Al}_2\text{O}_3$	6.0×10^{-9}	2×10^{-6}	8.83×10^{-11}	5.45×10^{-20}	4.94×10^{-9}	0.072

Table 4.2: Producer information and identified mass transfer parameters of membranes (M2).

The permeation experiments with smaller membranes (M2) have been conducted in a similar way as for M1 (layer to layer characterization of membrane structural parameters, 1 to 3 bar, 20 to 500 °C). However, instead of He, oxygen has been taken as the third permeation gas. For the sake of comparison between M1 and M2 membranes, some results with the support of M2 are presented in Figs 4.8 to 4.10. These figures are the counterpart of Figs 4.2 to 4.4 with the support of M1.

As mentioned before, the value of intercept (Knudsen contribution) depends on $\tilde{M}_j^{-1/2}$, hence by increasing molar mass of the gas, intercept decreases. However, the trends in Fig. 4.8 are not significant because the molar masses of the gases do not differ significantly. The effect of molar mass, in terms of gas dynamic viscosity, on the slope is very moderate. The influence of temperature (moderate in the Knudsen and stronger in the viscous regime) like in Fig. 4.3 is verified by the intercept and slope of the data of Fig. 4.9. Figure 4.10 being a counterpart of Fig. 4.4 verifies the inverse dependence of flow rate on the temperature both in calculation and experiments. The comparison of both types of membranes (M1 and M2)

reveals that the flow rates through the support layer of M2 are comparatively higher (for the same temperature, pressure and gas) than the flow rates through the support layer of M1. This difference can be attributed to the different thickness of the membrane. Since flow rate decreases as the membrane thickness increases, the thicker support layer of the M1 membrane permits lower flow rates than the relatively thinner support layer of the M2 membrane.

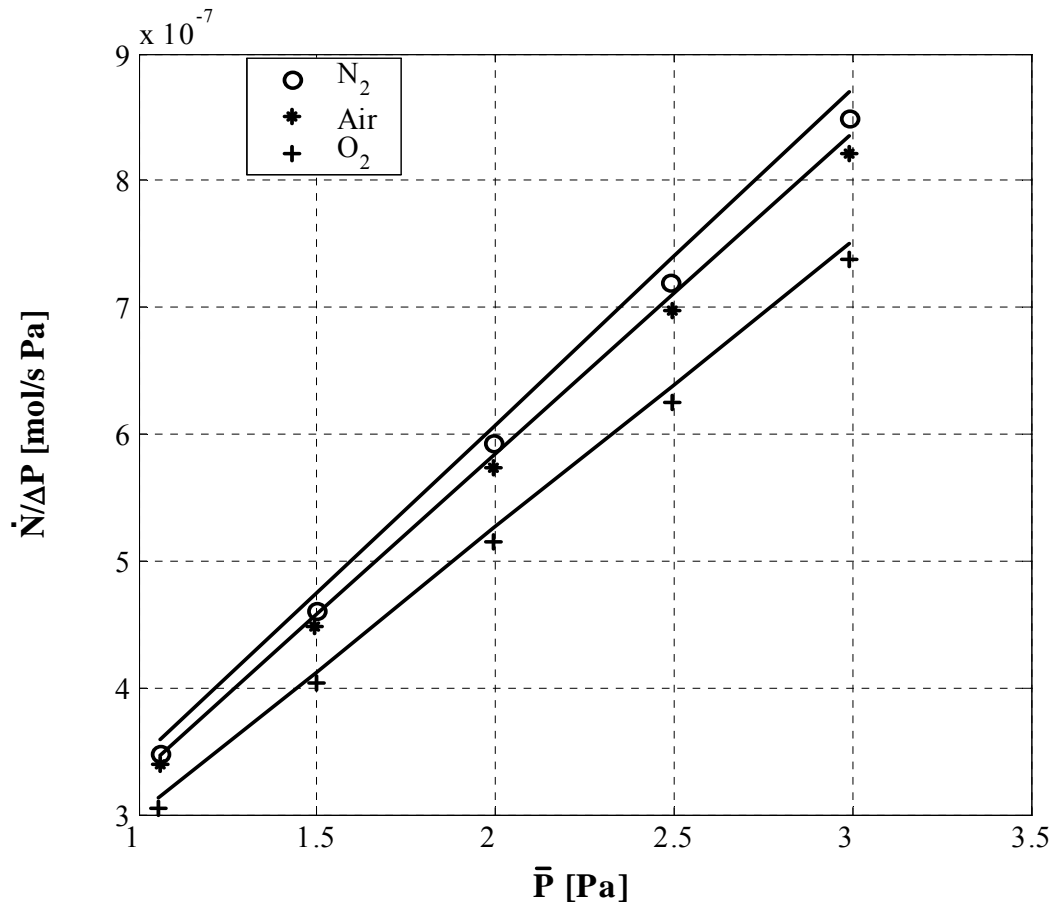


Fig. 4.8: Ratio of molar flow rate to pressure drop versus the average pressure for the support of the investigated membrane (M2) at 25°C for three different gases; (solid lines in this and the subsequent figures: calculations after the dusty gas model).

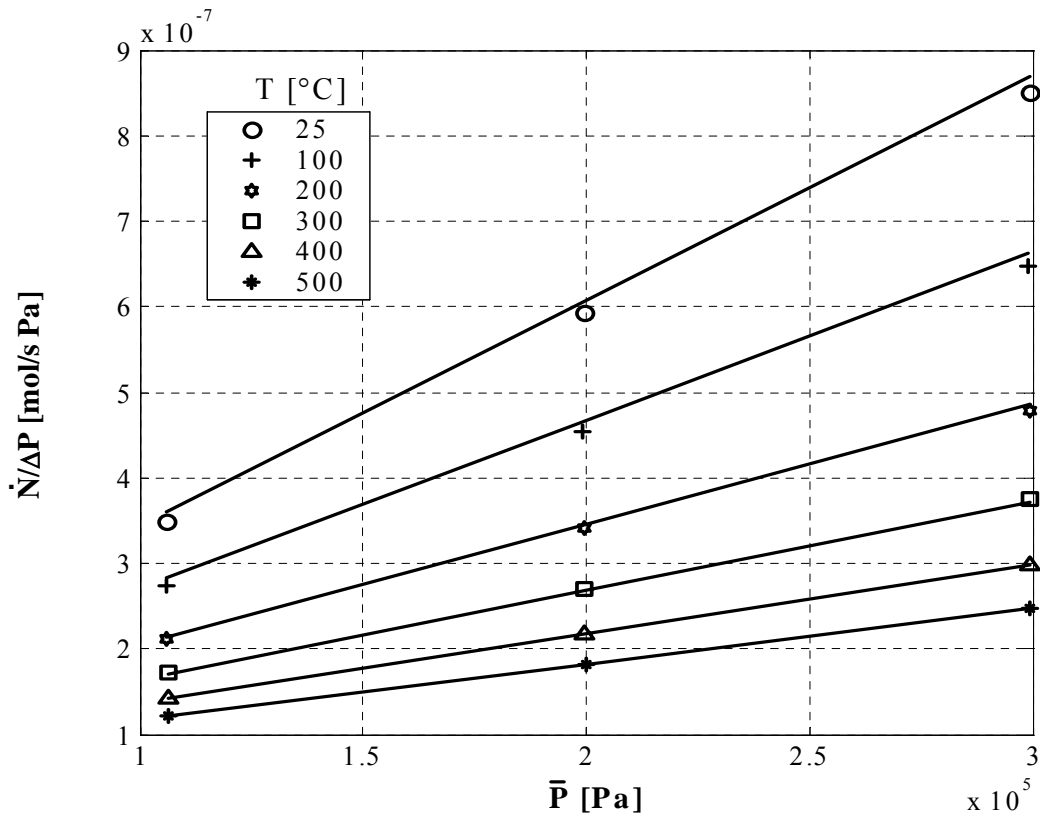


Fig. 4.9: Ratio of molar flow rate to pressure drop versus the average pressure for the support of the investigated membrane (M2) for N_2 at various temperatures.

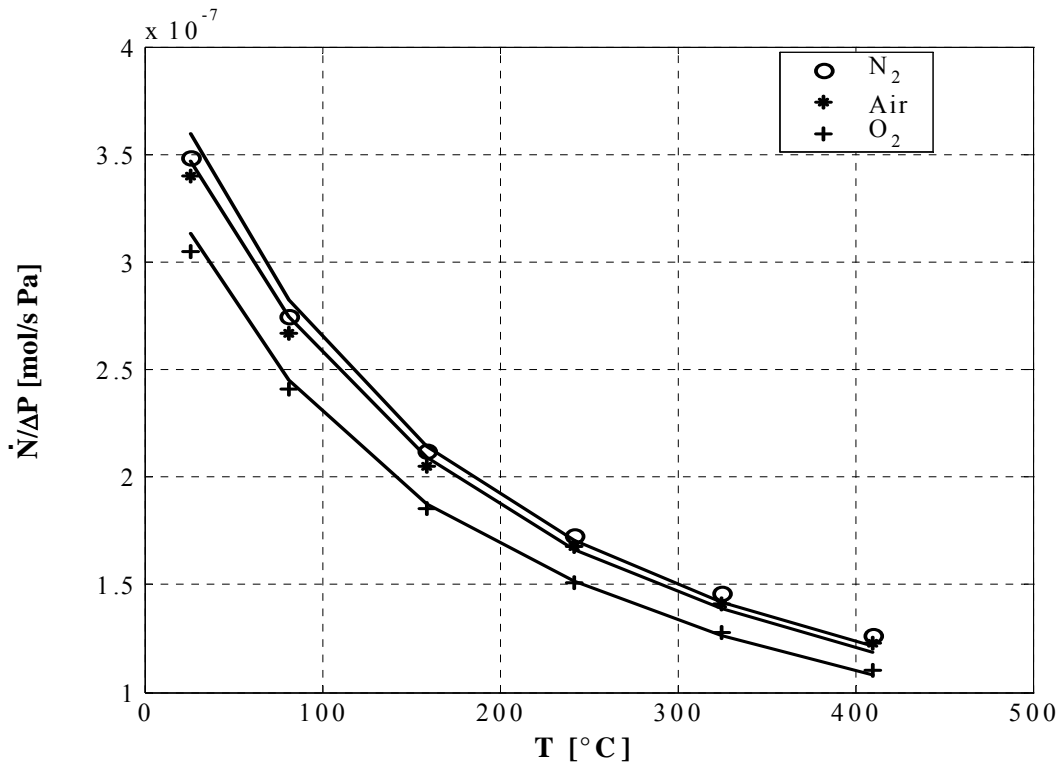


Fig. 4.10: Ratio of molar flow rate to pressure drop versus temperature for the support of the investigated membrane (M2) for three different gases at the lowest realised pressure level of approximately 1 bar.

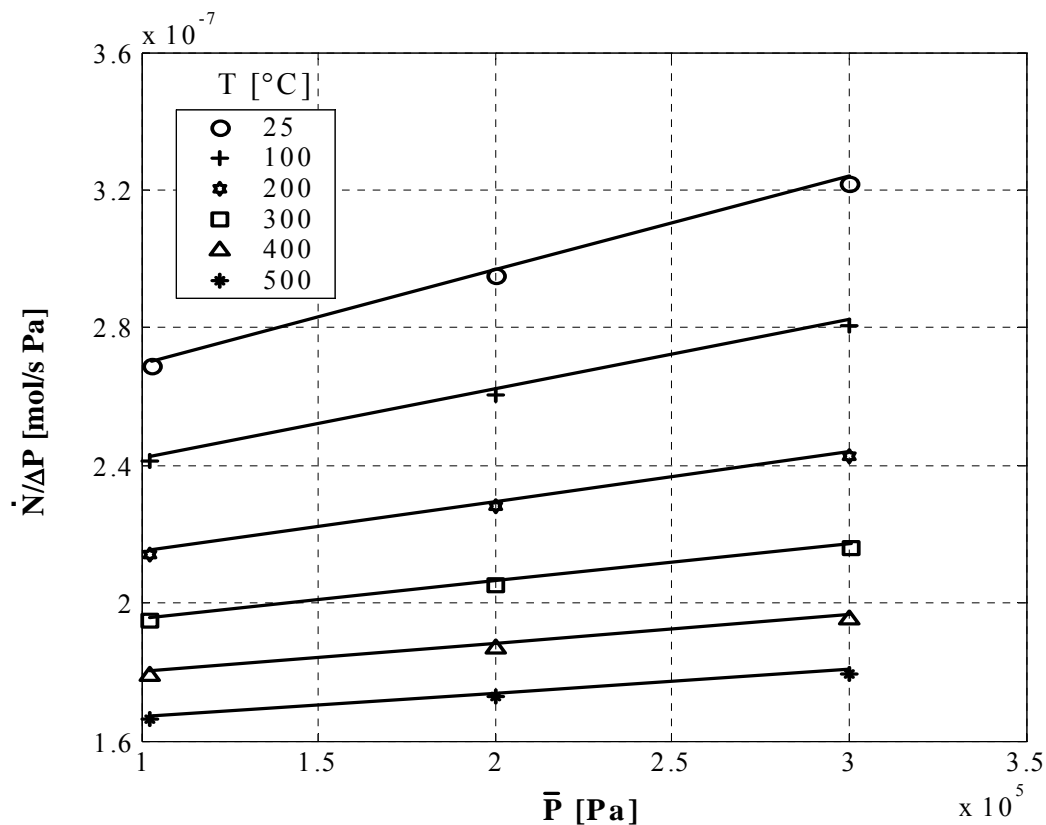


Fig. 4.11: Ratio of molar flow rate to pressure drop versus the average pressure for the 3rd layer of membrane M2 for O₂ at various temperatures.

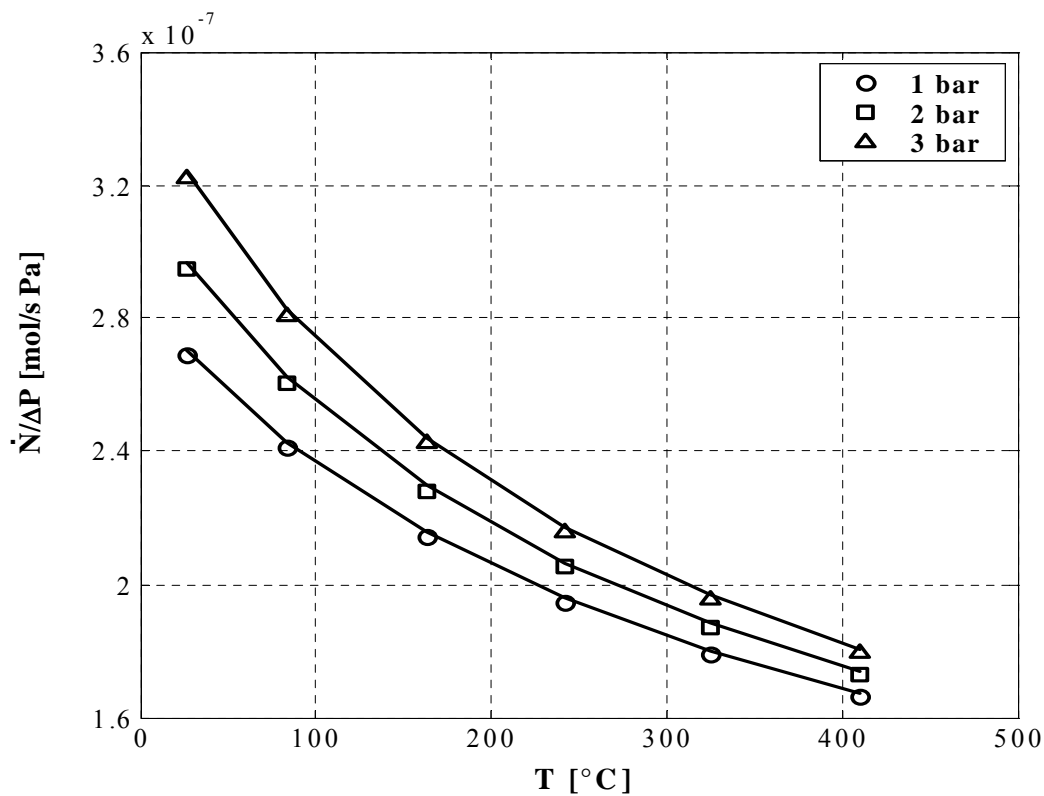


Fig. 4.12: Ratio of molar flow rate to pressure drop versus temperature for the 3rd layer of membrane M2 for O₂ at three different pressure levels.

Again, the agreement between calculations after the dusty gas model and measurements was very good, irrespectively of the gas used, temperature, and pressure. Some additional examples with oxygen as the permeating gas are given in Figs 4.11 and 4.12 for the 3rd layer of the membrane.

4.1.1 Influence of membrane asymmetry

The influence of composite nature of the membrane on the gas transport has been investigated, though mostly focused on polymeric composite membranes [120-122], to explain the membrane performance and selectivity. The asymmetry of the membrane can be used to facilitate the diffusion of one of the reactants while hindering the other one. Successive layers of different thicknesses and materials can also contribute to carrying out different consecutive reactions in different regions of the membrane [20]. The permeability of the membrane may also not be uniform along the entire length. The formation of top layer of different thickness on the support layer is a complicated process, which demands a perfect interaction between the materials of top and intermediate/support layers to produce a good composite membrane. But in practice it has been found that the structure of top layer is far from being homogenous throughout its thickness. Some regions adjoining the top layer to the support/intermediate layer can be abrupted. This shortcoming can be attributed to the phenomena of deformation-orientational order that occur during the formation of selective, thin layer on a porous support [123]. Hence, the interaction between the materials of top layer and the support profoundly affects the structure and properties of the composite membrane [124]. A schematic representation of a thin supported layer on an asymmetric support is given in Fig. 4.13.

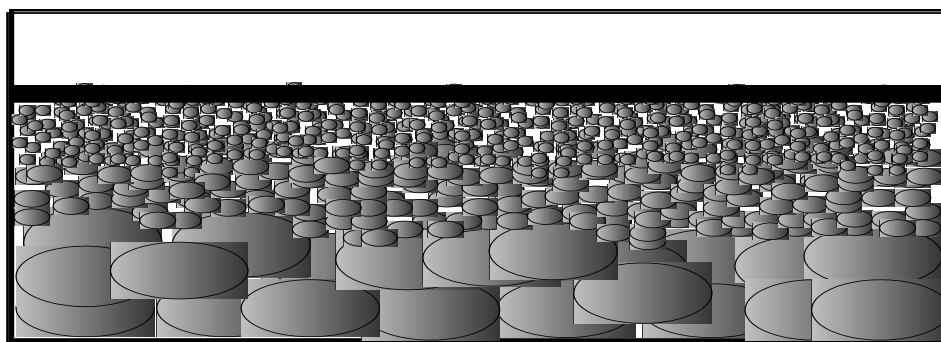


Fig. 4.13: Schematic representation of a thin selective layer on an asymmetric support.

Ignoring the multi-layer nature and asymmetry effects of the composite membrane while characterizing it, would be misleading for the quantification of mass transport. This effect is illustrated by the calculated results in Figs 4.14 to 4.17 based on structural parameters identified by assuming the composite membrane as a single layer (5.5 mm thick). The experimental data has been evaluated to identify the structural parameters of the assumed single layer of the membrane by plotting the ratio of molar flow rate to pressure drop versus the average pressure for the composite membrane at 500°C, once for He (Figs 4.14, 4.15) and once for N₂ permeation (Figs 4.16, 4.17). With the help of these parameters, simulations have been done for all three gases (Air, N₂, He) at various temperatures from 25°C to 500°C.

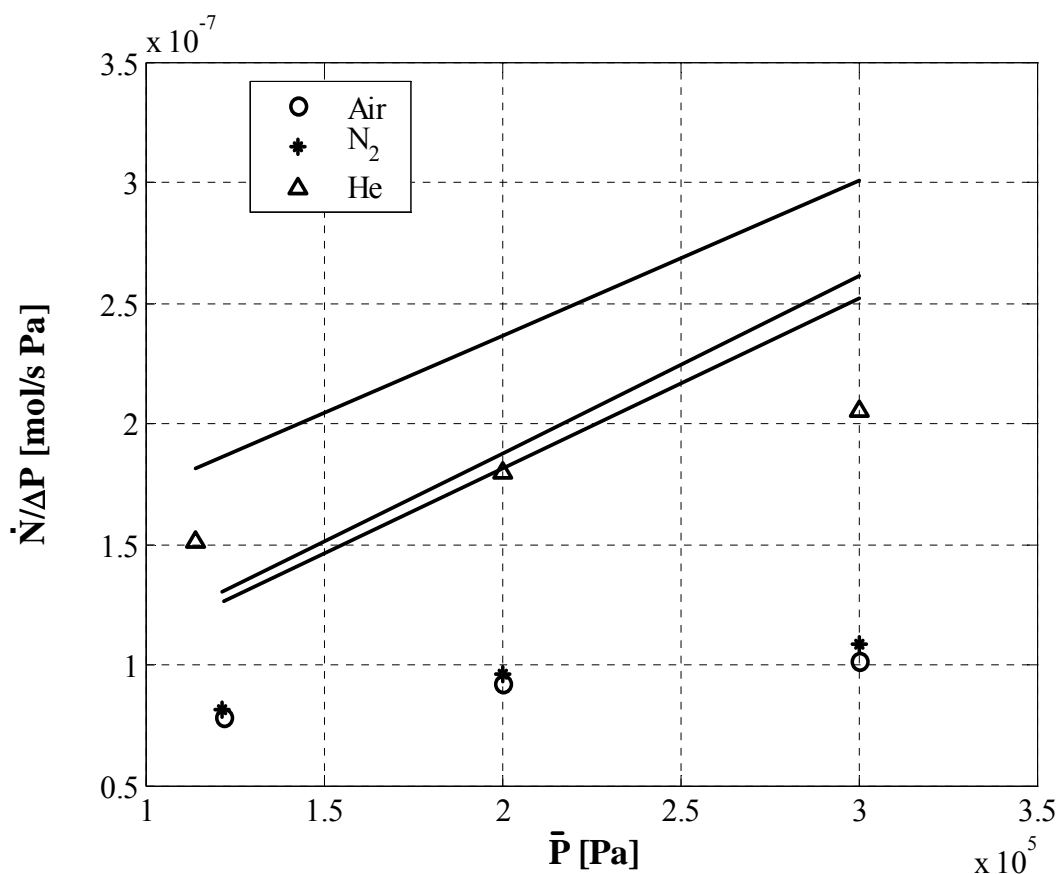


Fig. 4.14: Permeation of three different gases at 25 °C for composite membrane M1. Calculations based on single-layer parameters identified for He at 500 °C fail to meet the data.

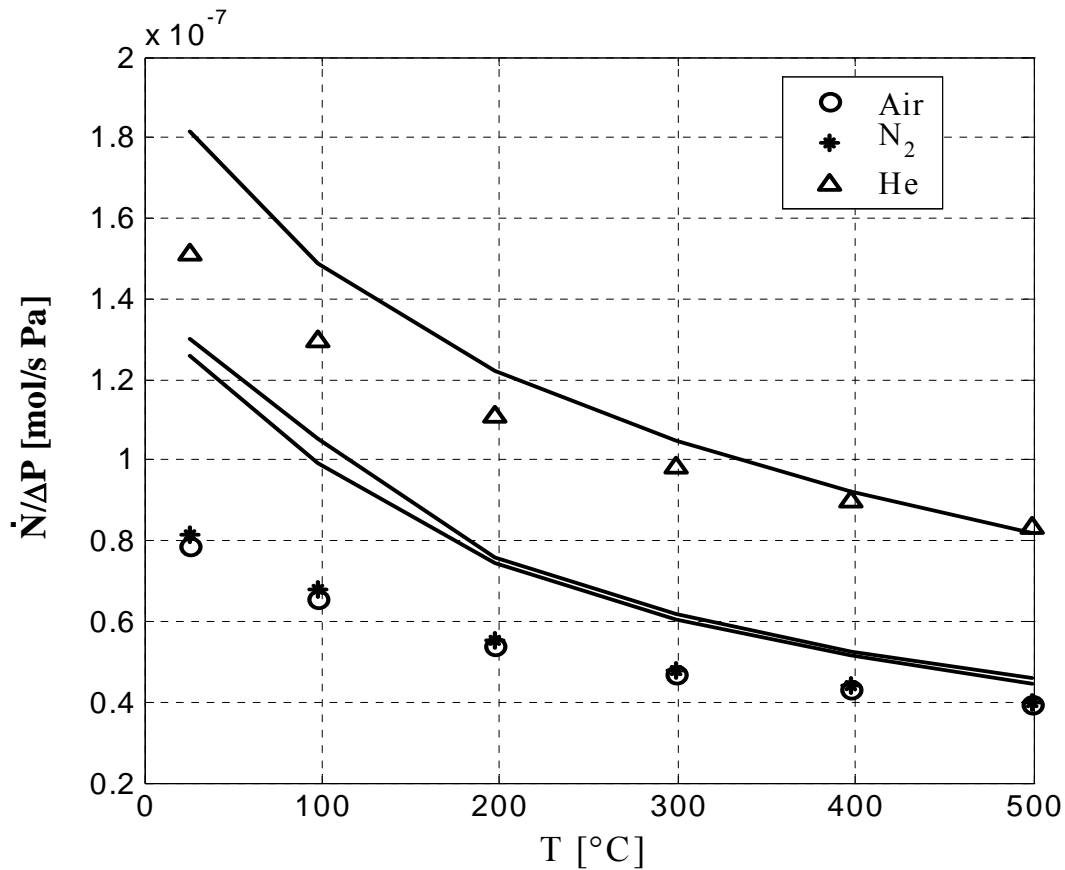


Fig. 4.15: Ratio of molar flow rate to pressure drop versus temperature for the composite membrane M1 for three different gases at the lowest realised pressure level of approximately 1 bar. Membrane parameters as in Fig. 4.14.

Both Figs 4.14 and 4.15 show significant differences between experimental results and calculations based on the values of membrane structural parameters derived from the experimental data after assuming that the membrane consists of a single layer. It is obvious from these diagrams that each layer of the composite membrane needs to be characterized separately. Furthermore, the comparison shows that membrane characterization based on a single layer assumption is dangerous. The structural parameters derived by this assumption will only describe this very data (best fit for He at 500 °C, Fig. 4.15), but can not be used for other gases or for the entire range of temperatures. It should also be noticed that a composite membrane may exhibit asymmetry dependent fluxes due to non-isometric pressure profiles [97]. Hence, it can be concluded that membrane asymmetry and its multilayer character play an important role while calculating the mass transfer by the dusty gas model. Each layer of the composite membrane must be characterized independently to get reliable mass transport parameters of the membrane. Figures 4.16 and 4.17 show the results of the same analysis done for single-layer parameter identification with nitrogen at 500 °C.

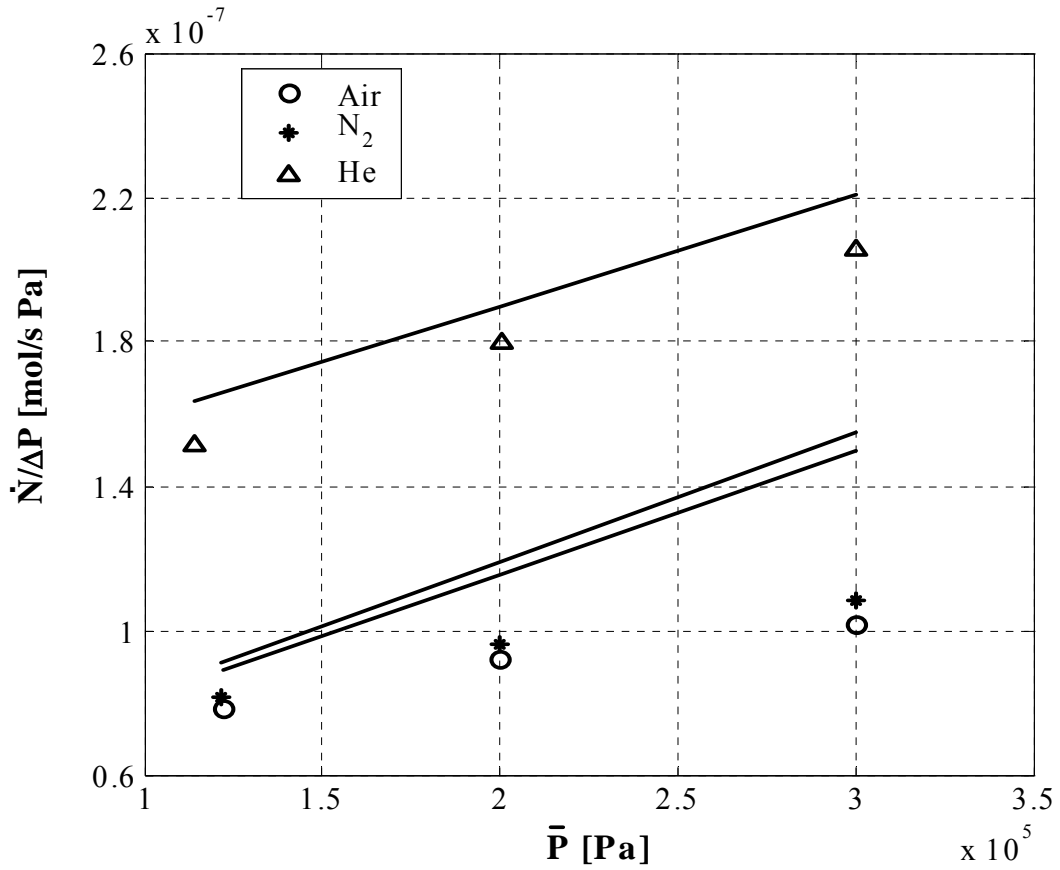


Fig. 4.16: The same data as in Fig. 4.14. Calculations based on single-layer parameters identified for N_2 at 500 °C also fail to meet the data.

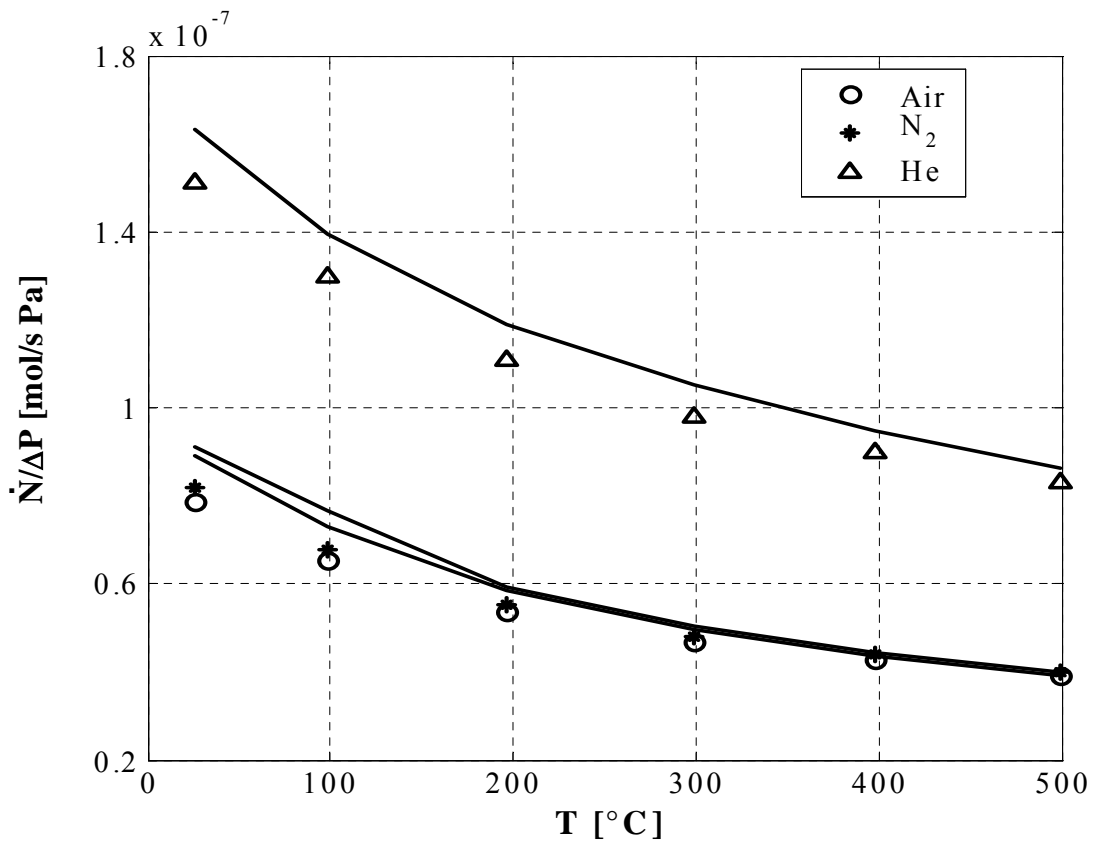


Fig. 4.17: Same data as in Fig.4.15, membrane parameters as in Fig 4.16; (N_2 , 500 °C).

4.1.2 Influence of top layer

The role of top layer (permselective layer) in an asymmetric membrane is to enhance the separation properties of the composite membrane. As the top layer thickness is very small ($\sim 2 \mu\text{m}$) so it can not sustain alone the pressure differences required to achieve reasonable fluxes. Hence it is deposited on support/intermediate membrane layers to provide the required mechanical strength. A simulation analysis for three different gases was done to study the influence of temperature, flow direction and the top layer's material on the gas flow rates and pressure profiles in the composite membrane. Simulation study has been done for two cases which correspond to two different top layer materials. Two constant pressures (1 and 2 bar) on the two sides of the membrane and three different temperatures have been taken for the calculations. The membrane structural parameters used were identified by [99]. However, a shorter membrane length was considered in these simulations. Membrane structural parameters and the geometrical information for both cases are given in Tables 1 and 2. All parameters of the membrane layers are same in both cases excluding the parameters of the top layer (permselective layer). In case A, the top layer is made of $\gamma\text{-Al}_2\text{O}_3$ while in case B, the top layer is made of TiO_2 .

Case A:

M2	L = 150 mm	$d_{m,o} = 10 \text{ mm}$			$d_{m,i} = 7 \text{ mm (approx.)}$		
Layer	Composition	Nominal pore diameter [m]	Thickness [m]	K_0 [m]	B_0 [m^2]	d_p [m]	$\frac{\varepsilon}{\tau}$
Support	$\alpha\text{-Al}_2\text{O}_3$	3.0×10^{-6}	1.5×10^{-3}	9.34×10^{-8}	3.58×10^{-14}	3.07×10^{-6}	0.122
1 st layer	$\alpha\text{-Al}_2\text{O}_3$	1.0×10^{-6}	25×10^{-6}	4.11×10^{-8}	9.47×10^{-15}	1.84×10^{-6}	0.089
2 nd layer	$\alpha\text{-Al}_2\text{O}_3$	0.2×10^{-6}	25×10^{-6}	9.40×10^{-9}	2.24×10^{-16}	0.19×10^{-6}	0.197
3 rd layer	$\alpha\text{-Al}_2\text{O}_3$	60×10^{-9}	25×10^{-6}	5.97×10^{-9}	5.69×10^{-17}	76×10^{-9}	0.313
4 th layer	$\gamma\text{-Al}_2\text{O}_3$	6.0×10^{-9}	2×10^{-6}	1.11×10^{-9}	2.18×10^{-18}	16×10^{-9}	0.283

Table 4.3: Parameters of all membrane's layers for case A.

Case B:

M2		L = 150 mm		$d_{m,o} = 10$ mm		$d_{m,i} = 7$ mm (approx.)	
Layer	Composition	Nominal pore diameter [m]	Thickness [m]	K_0 [m]	B_0 [m ²]	d_p [m]	$\frac{\varepsilon}{\tau}$
Support	α -Al ₂ O ₃	3.0×10^{-6}	1.5×10^{-3}	9.34×10^{-8}	3.58×10^{-14}	3.07×10^{-6}	0.122
1 st layer	α -Al ₂ O ₃	1.0×10^{-6}	25×10^{-6}	4.11×10^{-8}	9.47×10^{-15}	1.84×10^{-6}	0.089
2 nd layer	α -Al ₂ O ₃	0.2×10^{-6}	25×10^{-6}	9.40×10^{-9}	2.24×10^{-16}	0.19×10^{-6}	0.197
3 rd layer	α -Al ₂ O ₃	60×10^{-9}	25×10^{-6}	5.97×10^{-9}	5.69×10^{-17}	76×10^{-9}	0.313
4 th layer	TiO ₂	5.0×10^{-9}	2×10^{-6}	9.17×10^{-10}	1.51×10^{-18}	13.2×10^{-9}	0.278

Table 4.4: Parameters of all membranes layers for case B.

The simulations have been done by dusty gas model equation eq. (4.2) for the permeation of three different gases (H₂, N₂, SF₆) at three different temperatures (20 °C, 100 °C, 200 °C) for both types of composite membrane (Case A & Case B). The influence of flow direction was quantified by alternatively setting two different pressures on the membrane sides (differentiating that the gas first enters the membrane support or the permselective layer). Simulation results are presented in Figs 4.18 and 4.19.

Figure 4.18 shows the calculated values of the ratio of molar flow rate to pressure drop (permeability coefficient) plotted against the temperature for the case A for all gases. It can be seen, as expected and shown in the previous analysis in sec. 4.1, that the ratio of molar flow rate to pressure drop decreases as the molar mass of the gas increases. The ratio of molar flow rate to pressure drop decreases also by increasing the temperature, as the gas viscosity increases by the temperature. The major effect to show in these figures is the influence of flow direction on the ratio of molar flow rate to pressure drop (permeability coefficient). In both figures, full lines correspond to the gas entering first the support membrane and the broken lines correspond to the gas entering first the permselective layer. It can be seen that in both cases (A & B), the ratio of molar flow rate to pressure drop is higher when the gas first enters the support membrane. This behaviour of the composite membrane can be attributed to

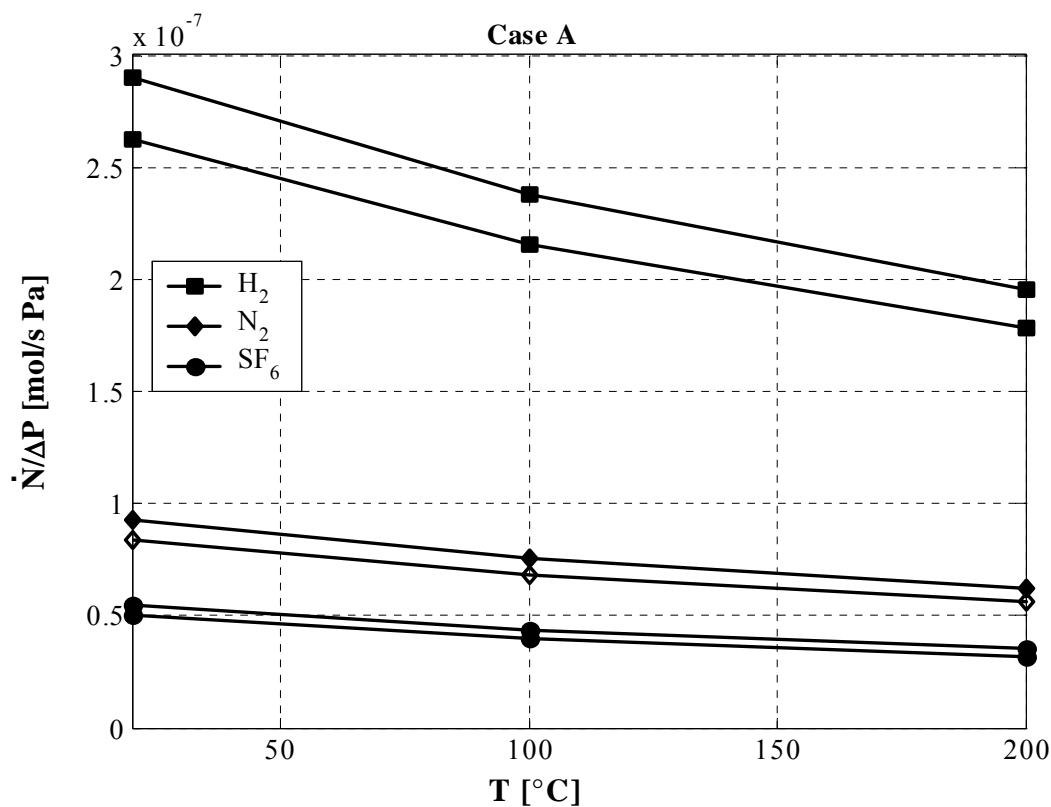


Fig. 4.18: Ratio of molar flow rate to pressure drop versus temperature for three different gases (solid lines: gas entering first the support layer, broken lines: gas entering first the permselective layer).

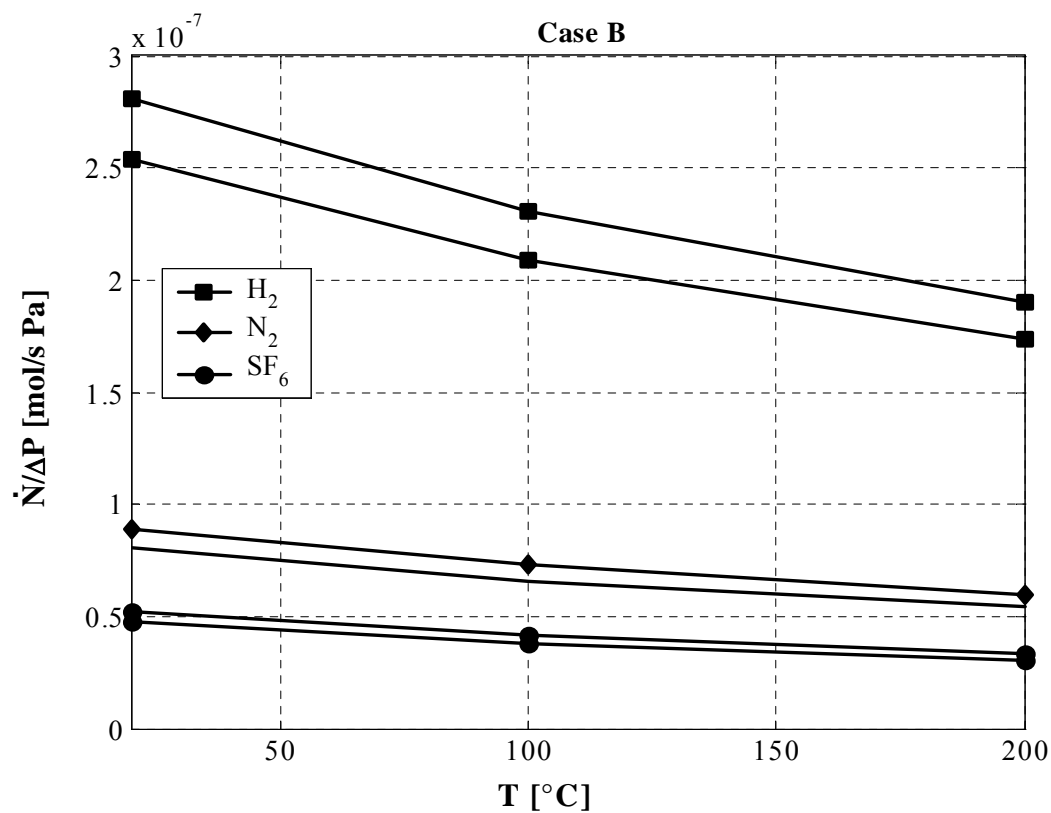


Fig. 4.19: As in Fig. 4.18, however for case B membrane.

the local distribution of resistances in the membrane [97, 98]. The differences in ratios of molar flow rate to pressure drop (permeability coefficients) are upto 9% for the case A and about 8% for the case B (Fig. 4.19). This deviation can be critical when employing the porous membrane for selective dosing of educts [93-94]. If both diagrams are compared, it can be further seen that the ratio of molar flow rate to pressure drop is higher in case A than in the case B. This is due to the fact that the permselective layer made of TiO_2 (case B) has smaller pores than the permselective layer made of $\gamma\text{-Al}_2\text{O}_3$ (case A). It is also to notice here that the rise in molar mass of the gas reduces the above mentioned deviation in both cases.

Figures 4.20 to 4.23 show the calculated pressure profiles in all membrane layers for different temperatures and gases. Again, the analysis has been done for two alternative situations, gas entering the support membrane first and gas entering the permselective layer first. In all figures, zero corresponds to support side of the membrane while 5 corresponds to the permselective side of the composite membrane and 1 to 4 are the interfaces of intermediate layers in the composite membrane. Consequently, the full lines correspond to the pressure profiles when gas enters the support layer first and broken lines correspond to the pressure profiles when gas enters the permselective layer first.

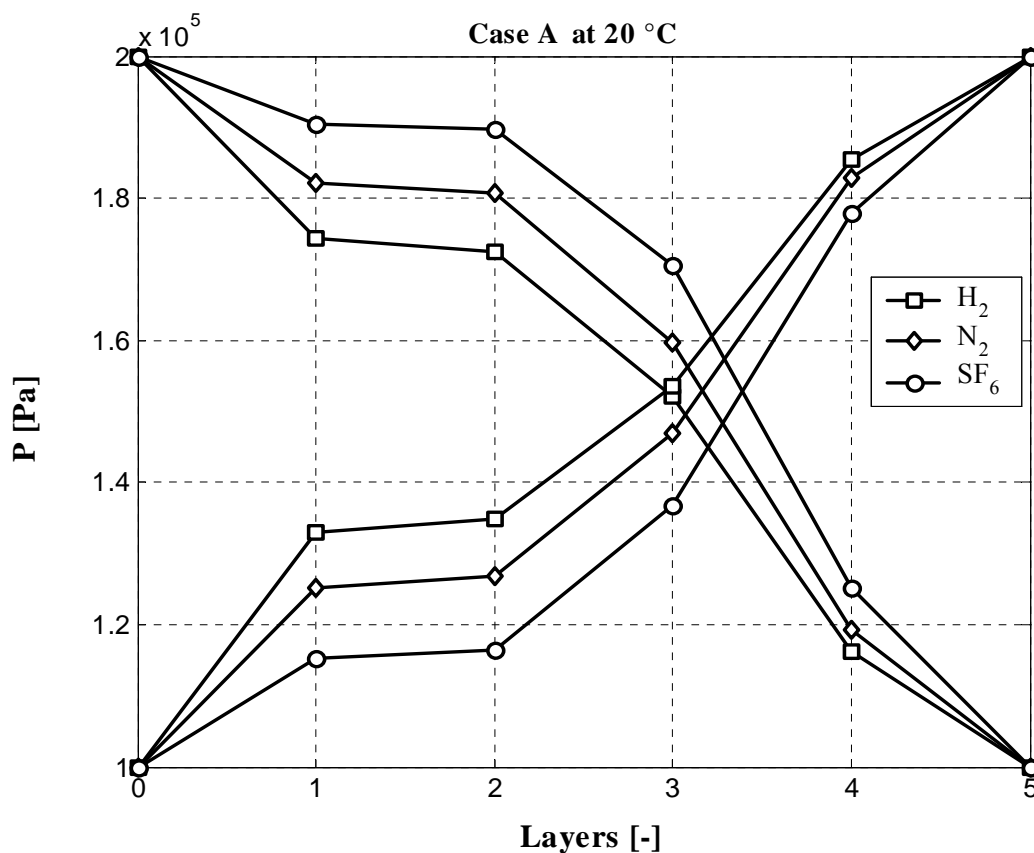


Fig. 4.20: Pressure profiles in the composite membrane at 20°C for three different gases at the pressure level of 1 & 2 bar.

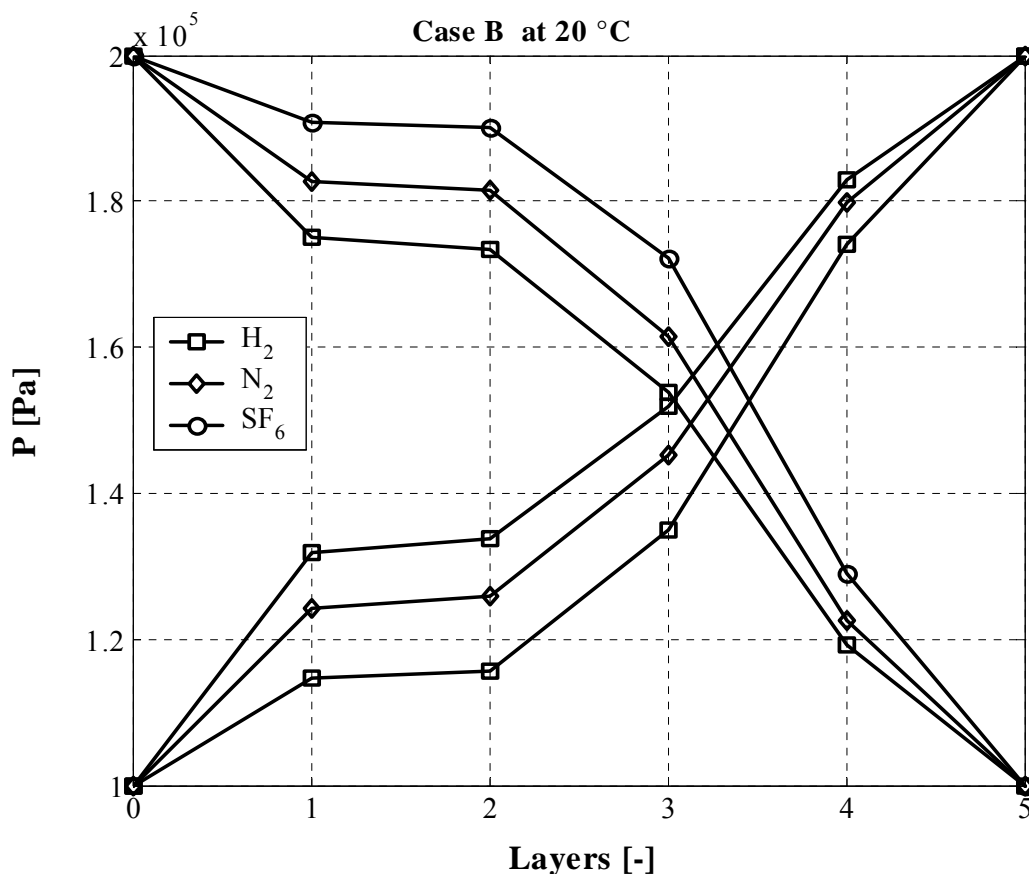


Fig. 4.21: As Fig. 4.20, though for case B membrane.

In a catalytic membrane reactor, pressure effects can contribute to a better accessibility of reactants to catalyst, which can improve the conversion rate in some reactions [125]. The analysis of pressure profiles shown in Figs 4.20 to 4.23 reveals that the pressure drop in case B (TiO₂ layer as a permselective layer), for all gases and temperatures, is comparatively higher than in case A (γ -Al₂O₃ as a permselective layer). The permselective layer influences the local distribution of pressure drop in every individual layer of the composite membrane. In spite of this, the pressure drop is higher in the 3rd layer of the membrane for all gases and temperatures in both cases. Moreover, it has been found in the analysis that the pressure drop in the permselective layer rises as the molar mass of the gas increases.

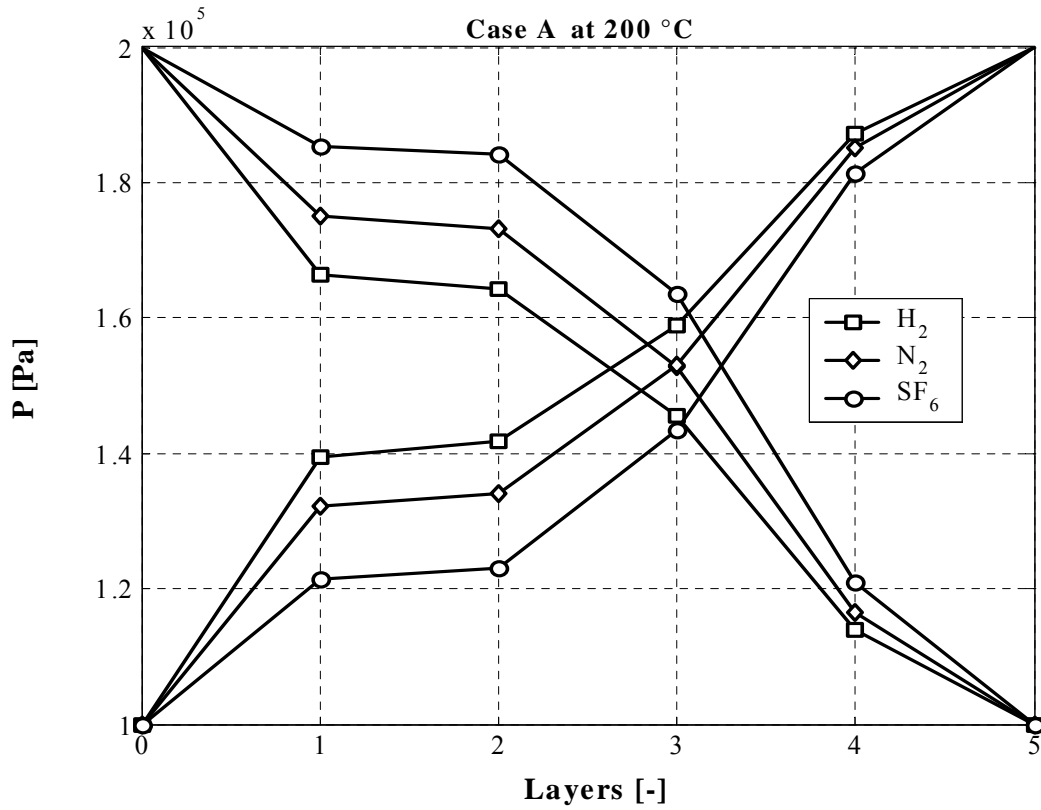


Fig. 4.22: Pressure profiles in the composite membrane at 200°C for three different gases at the pressure level of 1 & 2 bar.

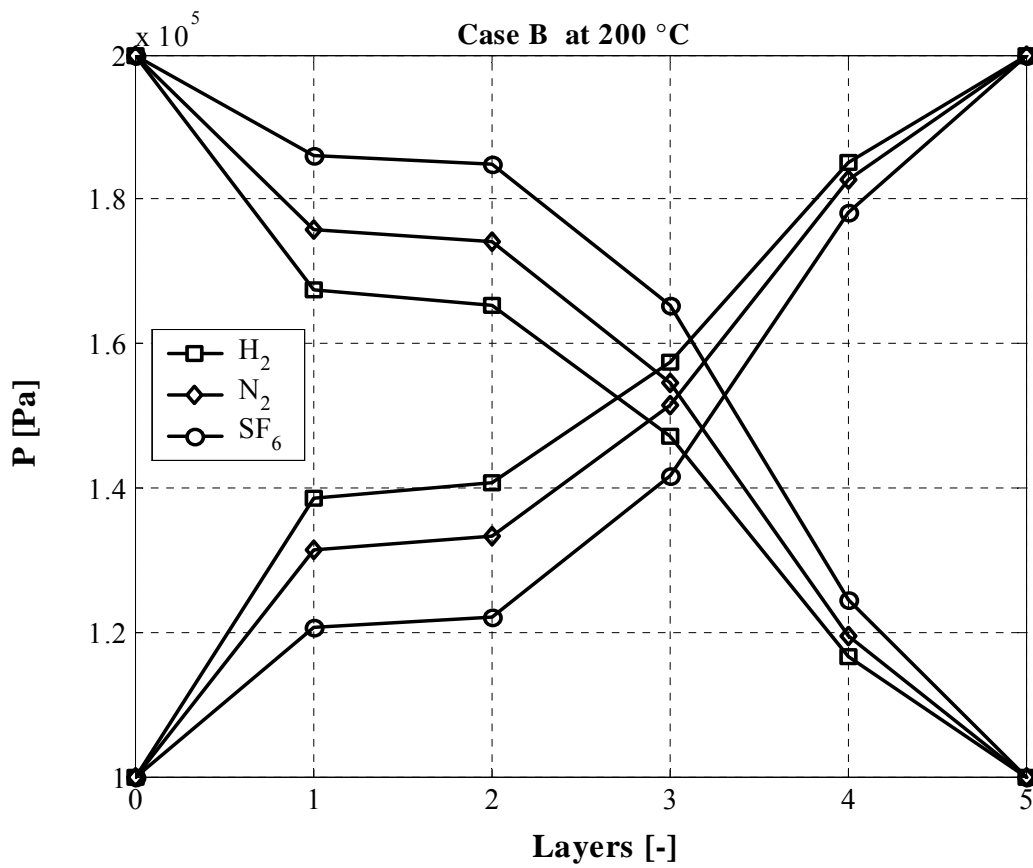


Fig. 4.23: As Fig. 4.22, though for case B membrane at 200 °C.

4.2 Validation experiment: Isobaric diffusion

Though the current investigations are not focused on a particular reaction system, this type of experiment gives an insight into the transport processes taking place in the membrane reactor. Also an additional validation of the parameters of the dusty gas model derived from single gas permeation experiments is provided by the isobaric diffusion experiment. In this experiment, constant but different flow rates of different gases are sent through the annulus and the tube of the measuring cell at constant temperature and pressure. Gas flow rates and molar fractions are measured at the outlet of the cell (Fig. 2.5d).

With similar assumptions as in section 4.1, the general equation of the dusty gas model (eq. (2.62)) reduces for the present experiment to

$$\sum_{k=1, k \neq j}^N \frac{\tilde{x}_k \dot{n}_j - \tilde{x}_j \dot{n}_k}{\varepsilon/\tau} \frac{D_{k,j}}{D_{jk}} + \dot{n}_j = - \frac{P}{\bar{R}T} D_{k,j} \frac{\Delta \tilde{x}_j}{\bar{r} \ln(r_{m,o}/r_{m,i})} \quad (4.3)$$

with $\bar{r} = (r_{m,o} + r_{m,i})/2$, and is applicable to every individual membrane layer.

The component mass balances in the two gas compartments are calculated by eqs (2.63) and (2.64), though neglecting axial dispersion in the present case [94, 95]. Gas-side mass transfer coefficients have been calculated after [126] for fully developed laminar flow (Appendix C).

Solution of model equations allows the determination of molar fractions and gas velocities at the outlet of the measuring cell. It has been implemented in the simulation environment ProMoT / Diva [127-129]. Experiments have been carried out with the composite membrane (M1), a constant flow velocity ($u_{g,o,in} = 0.06$ m/s) of pure nitrogen at the inlet of the annulus and various flow velocities of pure helium at the inlet of the tube ($u_{g,i,in} = 0.024$ to 0.096 m/s). Outlet gas compositions have been calculated by considering the transport parameters (K_0 , B_0 , F_0) of each membrane layer according to Table 4.1, in contrary to the previous works where either the transport parameters of the support layer [130] or the parameters of the selective membrane layer were taken [131].

Experimental results are plotted in Figs 4.24 to 4.26 as the helium molar fraction at the outlet of the tube, $\tilde{x}_{He,i,out}$, the helium molar fraction at the outlet of the annulus, $\tilde{x}_{He,o,out}$, the flow velocity at the outlet of the tube, $u_{g,i,out}$, and the flow velocity at the outlet of the annulus, $u_{g,o,out}$, versus the flow velocity of pure helium at the inlet of the tube, $u_{g,i,in}$. With increasing value of the latter, the change of the molar fraction of helium during the flow through the cell

decreases, so that $\tilde{x}_{\text{He},i,\text{out}}$ is closer to the inlet value of $\tilde{x}_{\text{He},i,\text{in}} = 1$ (Fig. 4.24). With decreasing $u_{g,i,\text{in}}$ the difference between helium molar fraction in the tube and helium molar fraction in the annulus decreases, that means equilibrium is, as expected, approached. Equilibrium means equality of molar fractions between tube and annulus, and in case of pure binary molecular diffusion it would have been approached without changes of the tube or annulus gas flow rates. This is not true according to the experiments. Actually, gas flow rate decreases in respect to the inlet value in the tube (Fig. 4.25) and increases in the annulus (Fig. 4.26), due to preferential Knudsen diffusion of the smaller molecule (helium) through the membrane. In other words, equimolarity is abrogated because of the presence of Knudsen diffusion, and Stefan fluxes occur even in case of a binary mixture. The calculations reveal a good agreement with measured data in Figs 4.30 to 4.32 and, since nothing has been fitted, validate additionally the previously identified mass transport parameters K_0 and F_0 , or d_p and ε/τ .

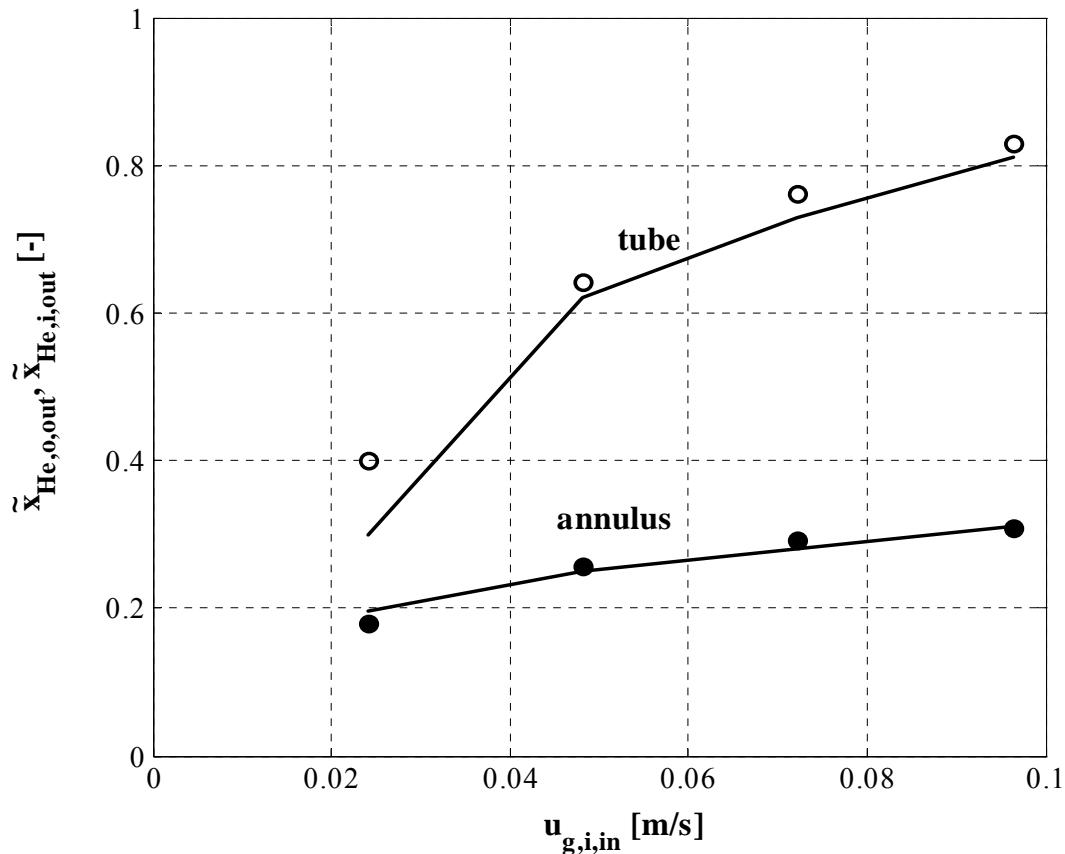


Fig. 4.24: Molar fraction of helium at the outlet of annulus and tube versus the flow velocity of gas (pure helium) at the inlet of tube; (composite membrane (M1), $T = 25^\circ\text{C}$, ambient pressure; Solid lines: Model prediction).

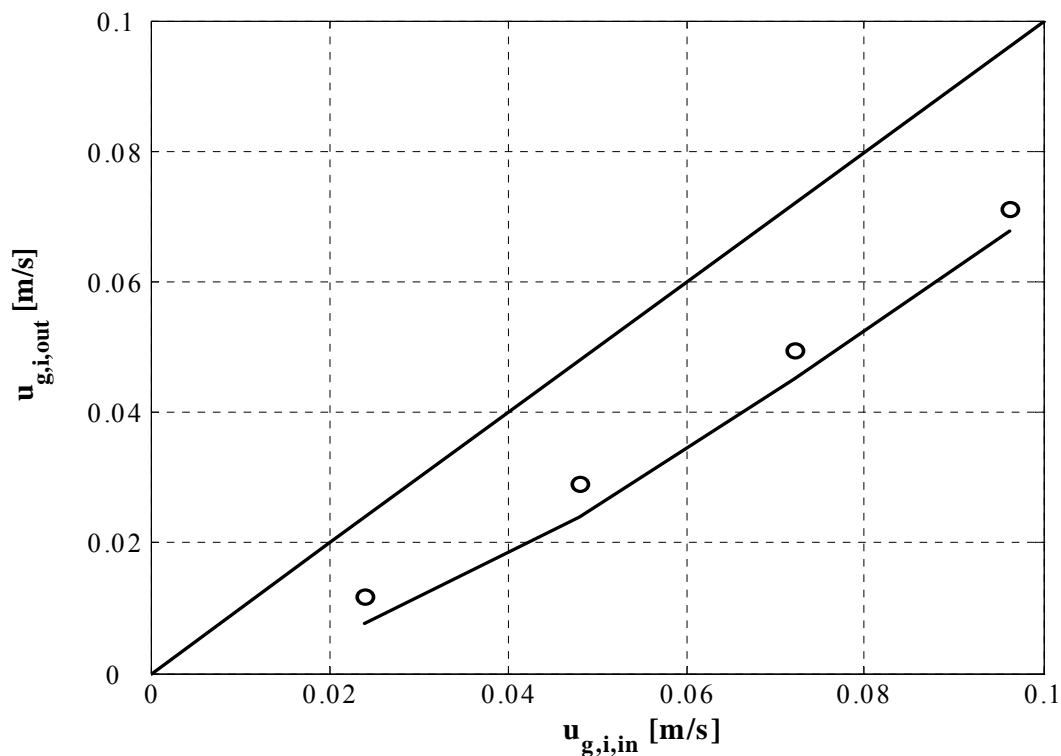


Fig. 4.25: Flow velocity of the gas at the outlet of the tube versus the flow velocity of gas (pure helium) at the inlet of tube.

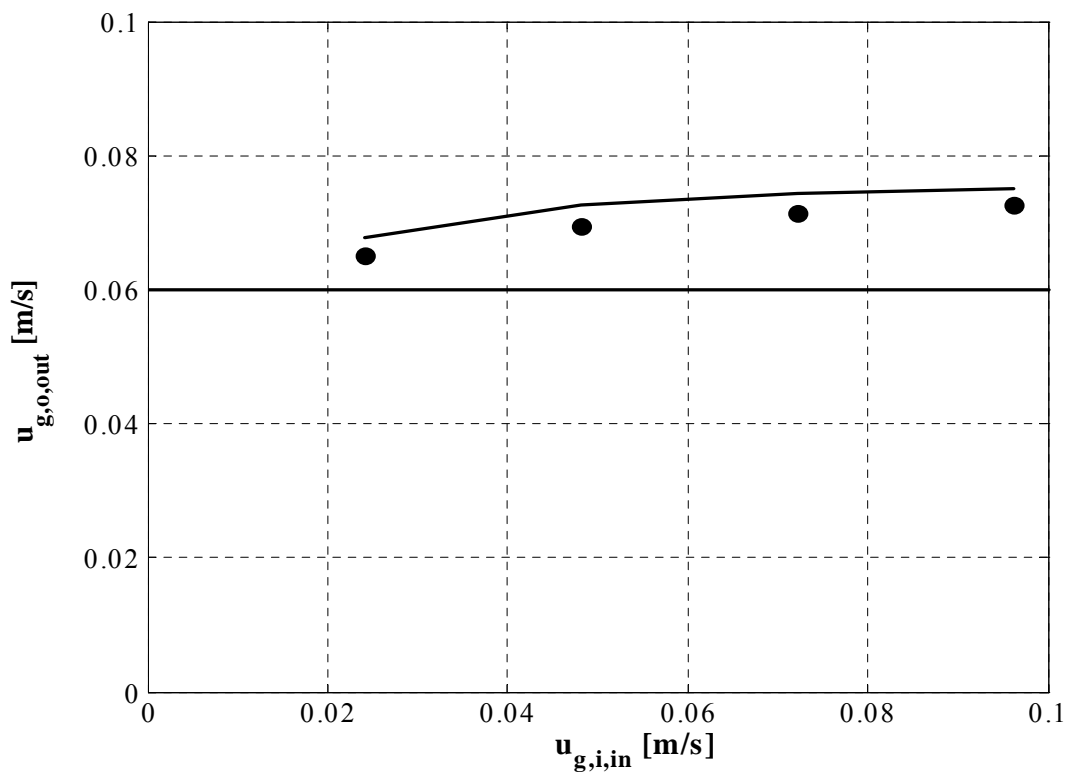


Fig. 4.26: Flow velocity of the gas at the outlet of the annulus versus the flow velocity of gas (pure helium) at the inlet of tube; $u_{g,o,in} = 0.06$ m/s .

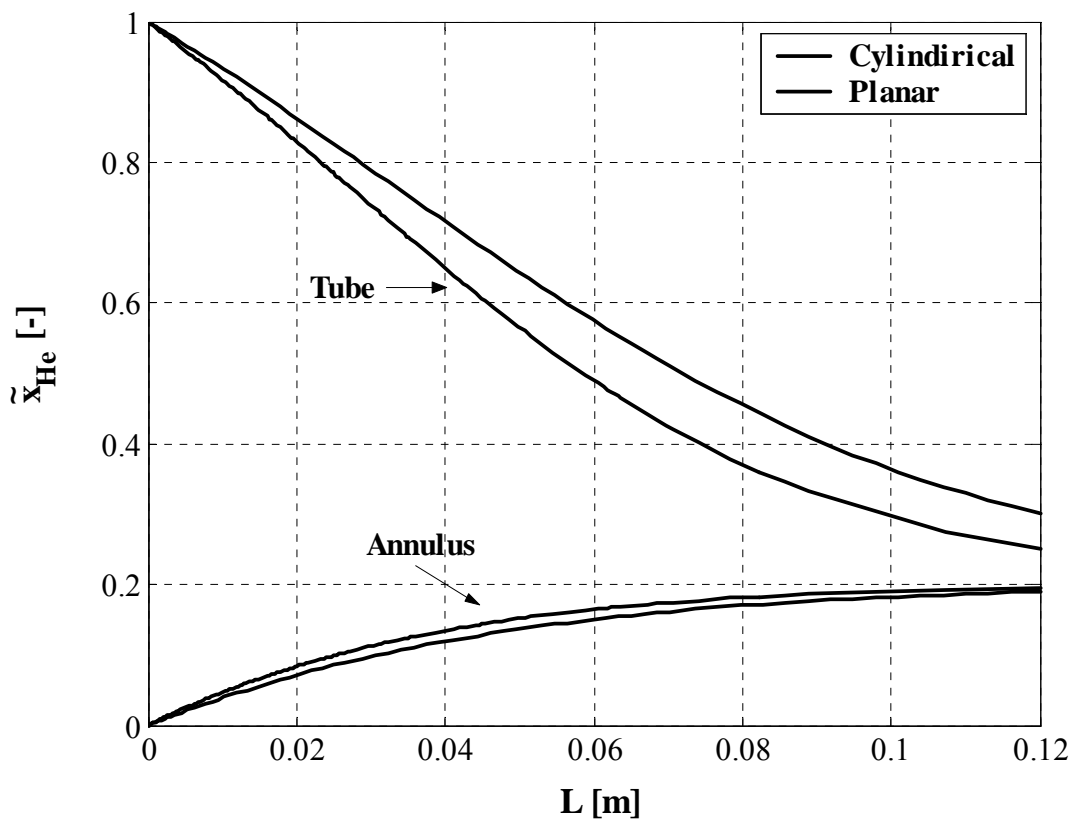


Fig. 4.27: Comparison between cylindrical and planar models at $u_{g,o,in} = 0.06$ m/s and $u_{g,i,in} = 0.024$ m/s; (composite membrane, $T = 25^\circ\text{C}$, ambient pressure).

In Fig. 4.27 axial mole fraction profiles of helium in the tube and the annulus, calculated for the cylindrical membrane, are compared with respective mole fraction profiles calculated for an assumed planar membrane. This comparison reveals that such an assumption can be misleading as the axial mole fraction profiles of helium, especially in the tube, are significantly influenced by the curvature of the membrane. It can be concluded that proper consideration of membrane geometry (thickness/diameter) leads to a reliable quantification of mass transport in tubular membranes.

Figure 4.28 shows the mole fraction of helium (calculated for different pore diameters) plotted against the dimensionless length of the membrane. It can be seen in the diagram that the mole fraction of helium decreases in the tube and increases in the annulus by increasing the pore diameter of the membrane, which results from an enhancement of the diffusion process. For wide pores of the membrane, molecular diffusion is dominant. Whereas by decreasing the pore diameter of the membrane, mass transport slows down because of the Knudsen effect. If the pore diameter further decreases, then, as expected, almost nothing will diffuse through the membrane.

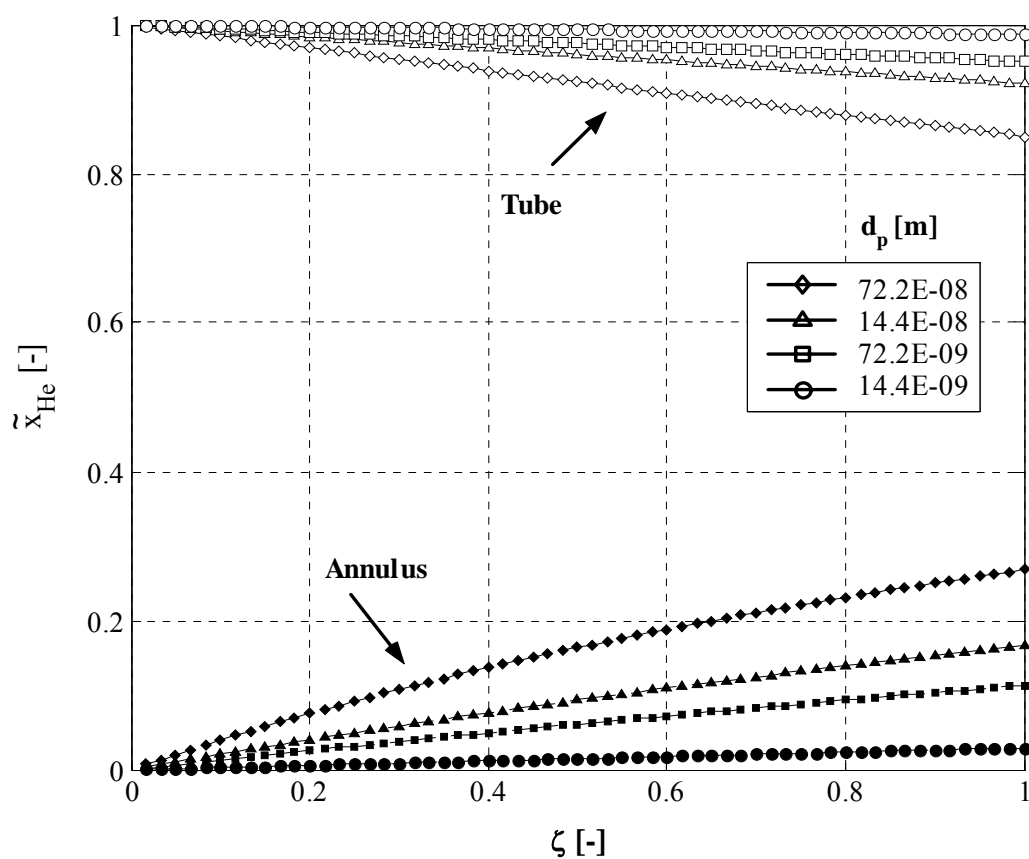


Fig. 4.28: Calculated axial profiles of helium mole fraction in tube and annulus for different membrane pore diameters at $T = 25^\circ\text{C}$, $P = 1.01$ bar by using the parameters of composite membrane M1.

4.3 Validation experiment: Transient diffusion

Due to the absence of bulk flow, the steady state isobaric diffusion experiments can validate only two structural parameters of the membrane, namely K_0 and F_0 . The transient diffusion experiments validate, in contrary, all structural parameters (K_0 , B_0 , F_0) by implementing the whole DGM equation (eq. (2.62)) [94, 95]. The transient diffusion measurements can also be regarded as determination of the accessible porosity. At the beginning of the experiment the void space inside the porous medium is entirely saturated with one gas and by the time it is swept off by the other gas. The general principle of these experiment is shown in Fig. 2.5e.

Transient diffusion experiments have been conducted by using two gases, N_2 and He, which have considerable difference in their molar masses. During the experiment, the inlet and outlet of the annulus are kept closed, so that gas flows only through the tube of the measuring cell. Before starting the measurement, only N_2 flows in the tube and the flow is maintained so long that the pressure on both sides of the membrane becomes equal and constant ($P_o = P_i$). The measurement starts at $t = 0$ by switching the gas flow into the tube from N_2 to He. Nonequimolar gas diffusion between both volumes of the measuring cell, annulus and tube, is the result. As the molecular weight of helium is less than that of N_2 , helium will diffuse preferentially through the membrane to the annulus, increasing there the pressure to $P_o(t) > P_i$. In general, the magnitude and direction of pressure rise depend on the ratio of molecular weights of the two gases, membrane structural parameters and the gas flow rate maintained in the tube. After reaching its maximum, the pressure in the annulus decreases again by decreasing diffusive flow and increasing viscous flow until the exchange process is completed ($P_o(t) \rightarrow P_i$).

To predict such pressure transients the complete DGM equation (2.62) is used. In absence of flow-through, spatially constant conditions can be assumed in the annulus. Consequently, and by application of the ideal gas law (eq. (2.15))

$$\frac{dP_o}{dt} = \frac{\tilde{R}TA_{m,o}}{V_o} (\dot{n}_{j,m,o} + \dot{n}_{k,m,o}) \quad (4.4)$$

is obtained. The mass balance of the tube is taken after eq. (2.64), neglecting the dispersion term.

Experiments have been carried out with the composite membrane (M1) and its support at ambient temperature with $u_{g,i,in} = 0.03$ m/s. The comparison between experimental and simulation results is shown in Figs 4.29 and 4.30. As expected, the composite membrane, which has layers with small pore diameters and offers more resistance to bulk flow, shows the higher pressure rise of about 30 mbar (Fig. 4.30). For the support membrane the pressure rise is with about 12 mbar (Fig. 4.29) lower, since higher permeability facilitates equilibration by bulk flow. Prediction of the measurements by the model is good. Experiments have also been conducted (Appendix D) at higher temperatures (373 K), without significant further insight.

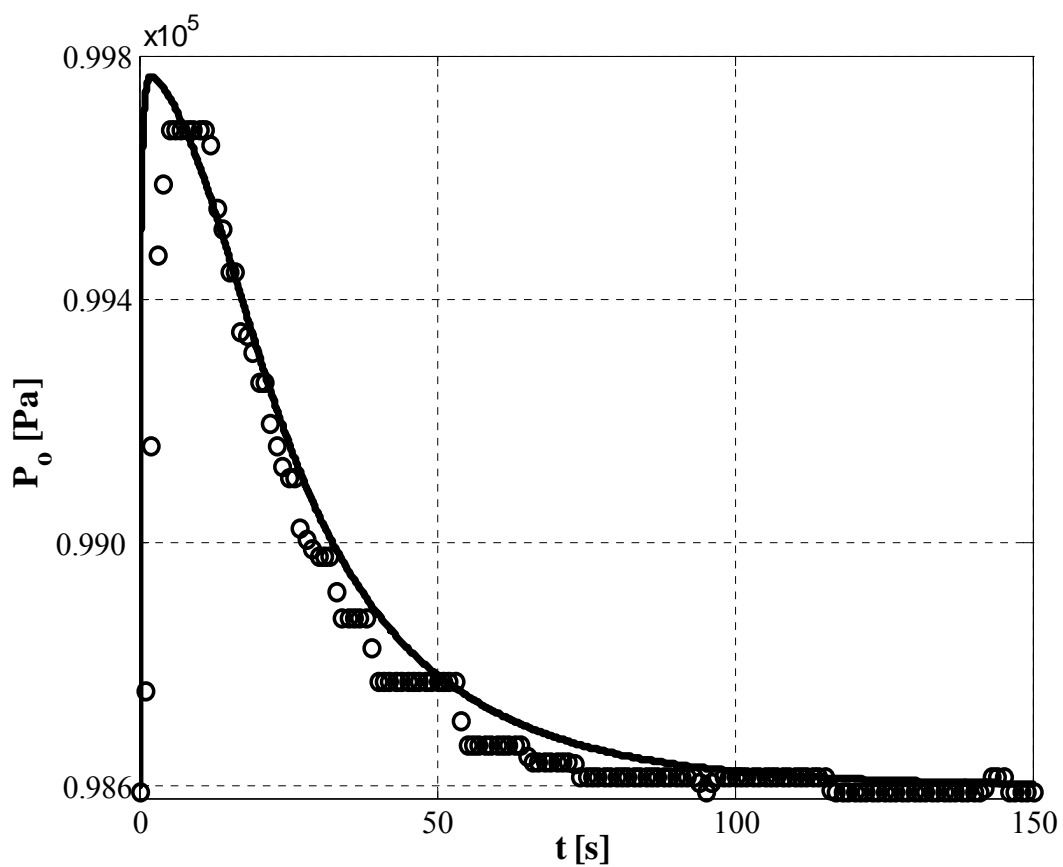


Fig. 4.29: Pressure rise in annulus versus time for the support membrane.

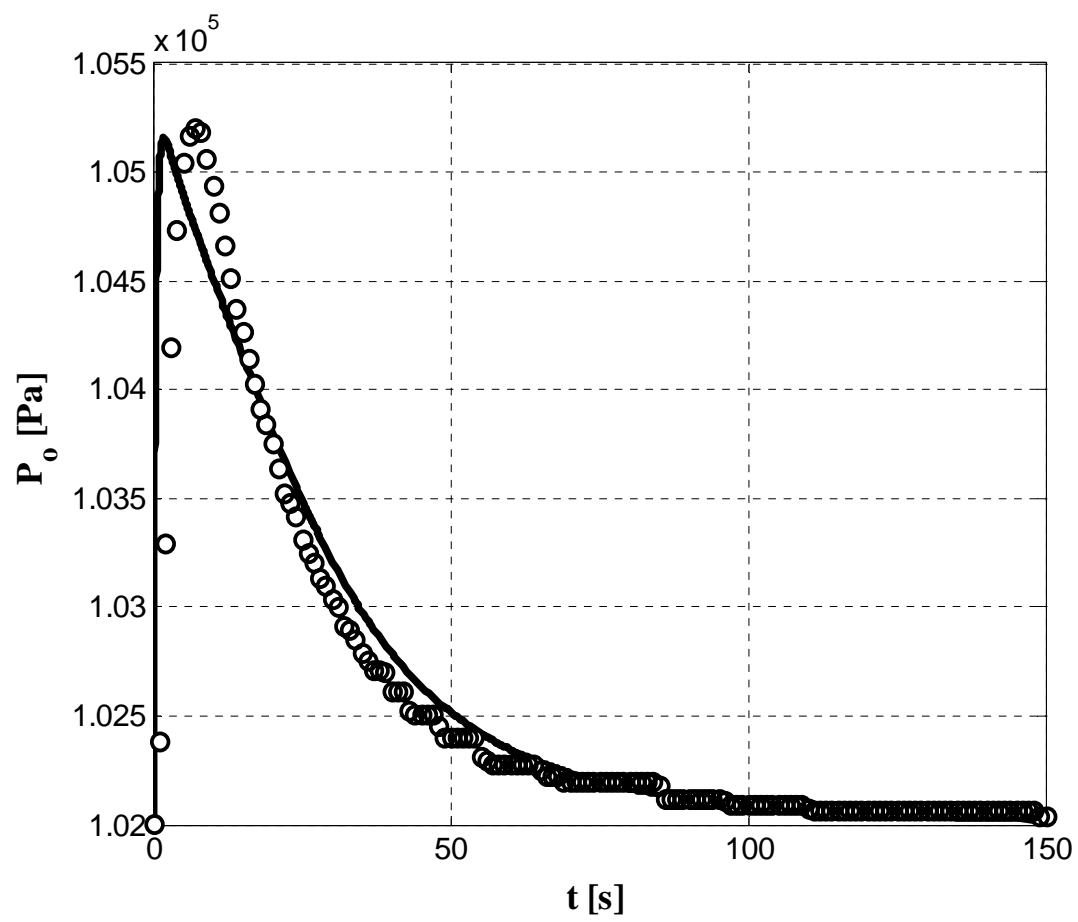


Fig. 4.30: Pressure rise in annulus versus time for the composite membrane.

5 Combined heat and mass transfer

The majority of studies have assumed isothermal conditions, as these are often used in laboratory experimentation. The temperature gradients are very often ignored in practical applications because these are considered as complicating the already difficult analysis [30, 100]. This assumption may lead to a limiting factor which, for many reactions employed in the chemical process industry, is heat and mass transfer to or from the regions where the chemical conversion occurs. To overcome this limitation, a better understanding of temperature and concentration gradients in these regions (membrane and flow channels) is essential. In catalytic gas phase reactions, mass transfer is often inhibited by internal transport processes within the porous catalyst medium, whereas mass transfer within the gas phase is comparatively fast. The opposite is found for the heat transfer problem, where the transport resistance is mainly due to the gas phase. It is therefore, important to investigate all undergoing transport processes in the membrane reactor, as sketched in Fig. 5.1.

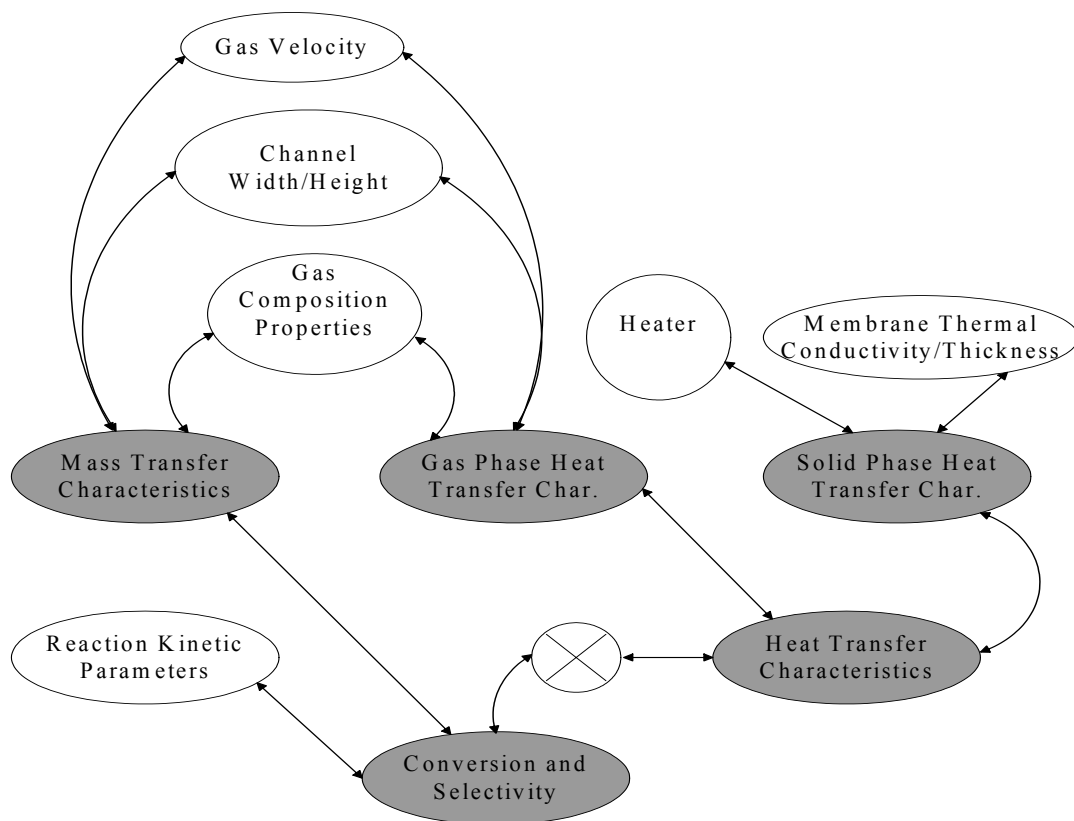


Fig. 5.1: Interaction between membrane reactor design parameters and its operating characteristics.

Comparative studies on membrane reactors reveal that the temperature plays a critical role in catalytic (dehydrogenation, partial oxidation) reactions. For example, on the one hand increased wall temperature contributes to the enhancement of conversion, but on the other hand this rise in temperature significantly increases the hot spot temperature (though lower in the membrane reactor compared to fixed bed reactor), which may be disadvantageous for selectivity to the desired products. Additionally, it is desirable to reduce the hot spot temperature to avoid subsequent problems like catalyst deactivation and run away reactions. The use of porous membrane to control the gas (oxygen) distribution to the reaction side can significantly reduce the hot spot temperature. So it is important to investigate the temperature distribution in and around the membrane prior to implementation in membrane reactor design.

Correspondingly, this chapter is focused on investigations on combined heat and mass transfer in the membrane (without reaction) and on the final validation of all transport parameters of the membrane conducted by combined heat and mass transfer experiments according to Fig. 2.5f. The combined heat and mass transfer experiment is similar to that of isobaric diffusion (Fig. 2.5d), with the important difference that now the inlet gases are at different temperatures and flow velocities for the tube and annulus, while in the isobaric diffusion experiments in sec. 4.2, the gas flow velocity in the annulus was kept constant and the flow velocity of helium (tube) was varied. Not only the outlet flow rates and composition, but also the outlet temperatures of the gases are measured and calculated. The temperature of the membrane is measured on both sides (annulus and tube) by in total four miniature thermocouples, pairwise fixed at two different axial positions of approximately $z = 125, 175$ mm. Again, pure nitrogen enters the annulus, and pure helium the tube. Only the composite membrane (M1) is investigated.

In the evaluation, the mass transfer equations of section 2.4.5 have been used without axial dispersion, and with the same reduced form of the dusty gas model as for isobaric diffusion (eq. (4.3)). Mass transfer coefficients, $\beta_{g,i}$ and $\beta_{g,o}$ (Appendix C), in the tube and annulus have been determined after [126], as previously indicated. Heat transfer in the membrane is treated as one dimensional by simplifying the steady-state eq. (2.1) in the radial direction. Heat transfer in the empty parts (annulus/tube) is considered as one dimensional in the axial direction. Heat transfer coefficients, $\alpha_{g,i}$ and $\alpha_{g,o}$, are calculated from the respective mass transfer coefficients by application of the Lewis-analogy ($Nu/Sh = [Pr/Sc]^{1/3}$). Axial dispersion is, again, neglected by setting the first left-hand side terms of eqs (2.8), (2.9) equal to zero. At the same time, the energy balance for the annulus (eq. (2.8)) is expanded to

$$-\frac{d(u_{g,o} n_{g,o} \tilde{c}_{p,g,o}^{av} T_{g,o})}{dz} + \left\{ \dot{q}_{m,o} + \dot{q}_{shell,o} + \sum_j (\dot{n}_{j,m,o} \tilde{c}_{p,g,j} T_{m,o}) \right\} \frac{2\pi r_{m,o}}{F_o} = 0, \quad (5.1)$$

with

$$\dot{q}_{shell,o} = \alpha_{g,o} (T_{shell} - T_{g,o}) \quad (5.2)$$

The heat flux $\dot{q}_{shell,o}$ describes heat transferred from the insulated shell of the reactor to the gas flowing in the annulus. In the experiments a heater was placed close to the inlet of the tube to heat the gas entering in the tube at desired temperatures. Thermal bridges to the shell lead to somewhat increased shell temperatures, T_{shell} , which were measured by additional thermocouples and found to be almost constant along the shell at steady-state. Since measured shell temperatures (Appendix D) are inserted in eq. (5.2), the correction does not involve any fitting. Its influence on the results is noticeable for the coupled heat and mass transfer experiment, though not too large. A further result of space, sealing and constructive restrictions at the ends of the membrane reactor is that the inlet gas temperature to the annulus is influenced by the operating conditions of the tube-side, so that $T_{g,o,in}$ can be measured accurately, but can not be accurately set to prescribed values.

The model equations have, again, been solved by ProMoT/Diva [127-129]. Figures 5.2 to 5.4 show the axial profiles of mole fraction, gas temperatures and membrane temperatures for two different gas inlet temperatures ($T = 373.15$ K, $T = 473.15$ K) in the tube, at constant inlet velocities ($u_{g,i,in} = 0.24$ m/s, $u_{g,o,in} = 0.145$ m/s). In all diagrams solid lines show the model predictions and points show the experimental data.

5.1 Influence of gas inlet temperature

Figure 5.2 shows the axial profiles of mole fraction of helium in the annulus. It can be seen that at higher gas inlet temperature more helium diffuses through the membrane (Fig. 5.2b). Temperature has a direct effect on membrane's transport parameters, effective Knudsen diffusion coefficient ($D_{K,j}$) is proportional to $T^{0.5}$ and the effective molecular diffusion coefficient (D_{jk}^e) is proportional to $T^{1.5}$. Due to the additional influence of density, Knudsen flux decreases with temperature ($\sim T^{-0.5}$) while molecular diffusion flux increases ($\sim T^{0.5}$).

Hence, the observed and predicted dependence on temperature indicates a higher importance of molecular diffusion in the composite.

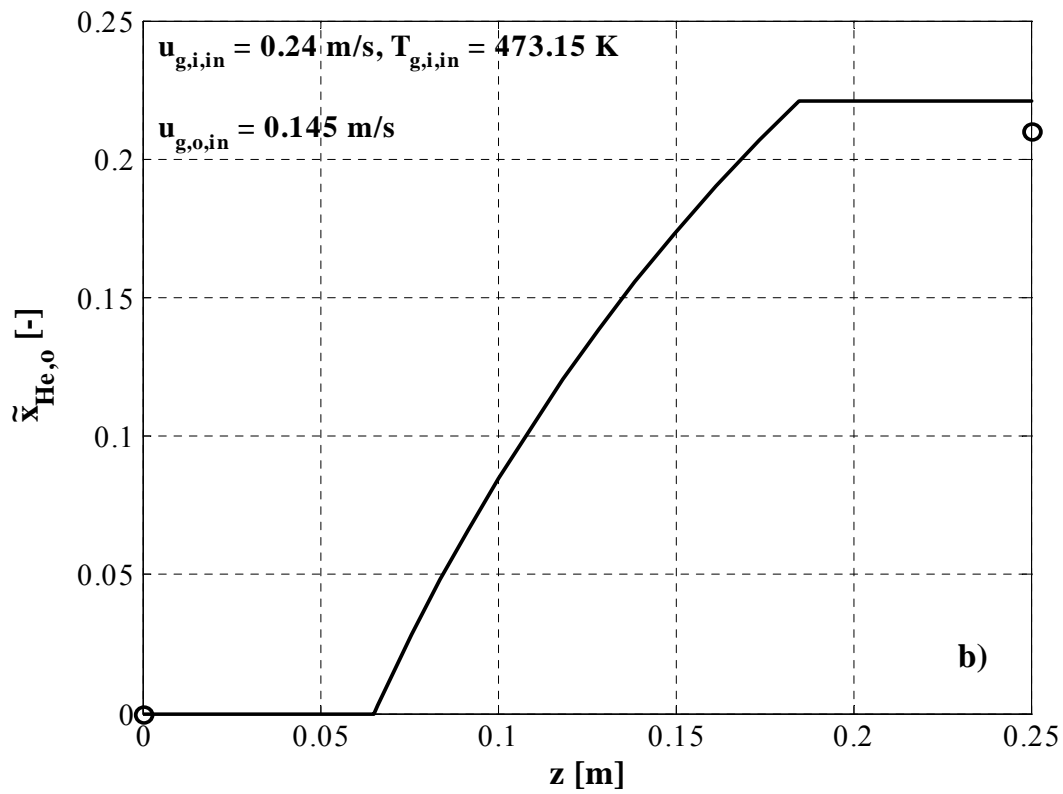
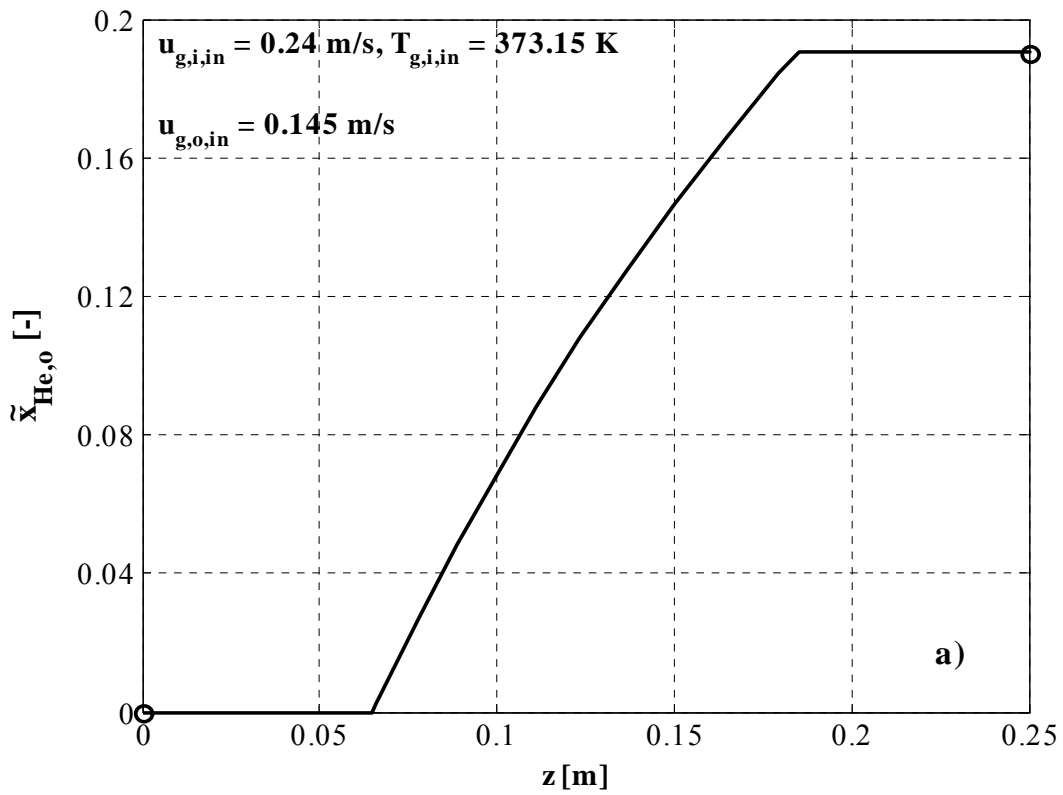


Fig. 5.2: Axial profile of the mole fraction of He in annulus for constant inlet velocities and for two different gas inlet temperatures.

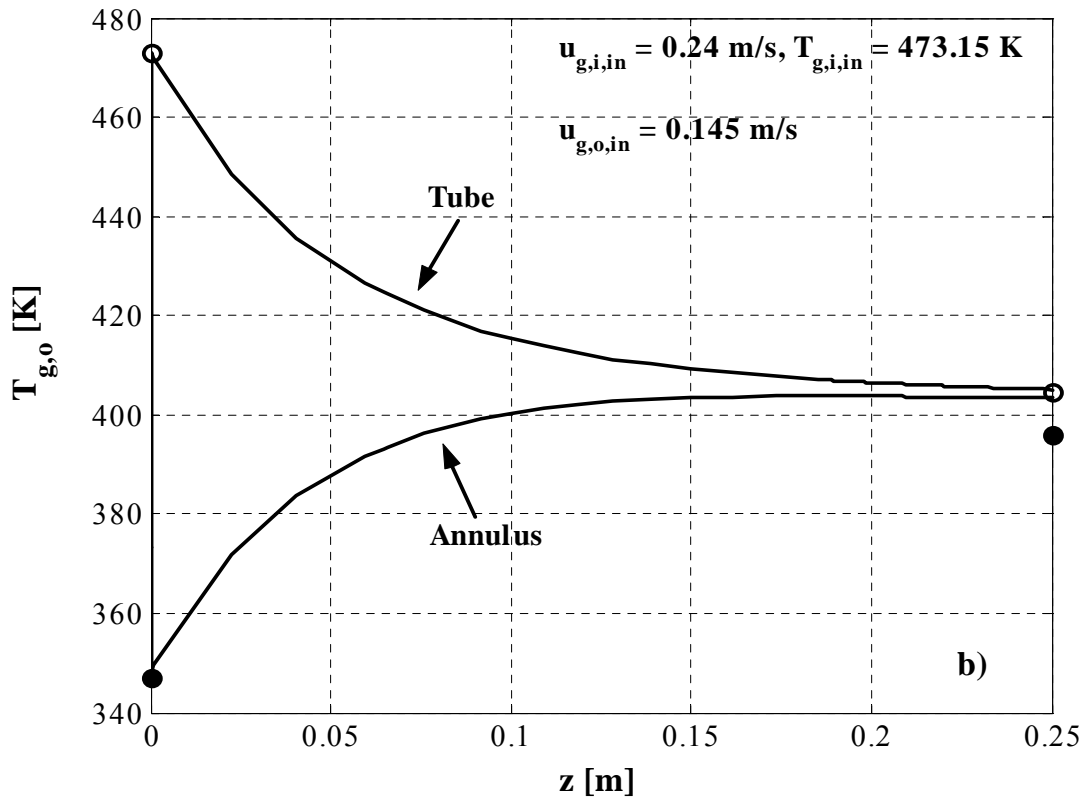
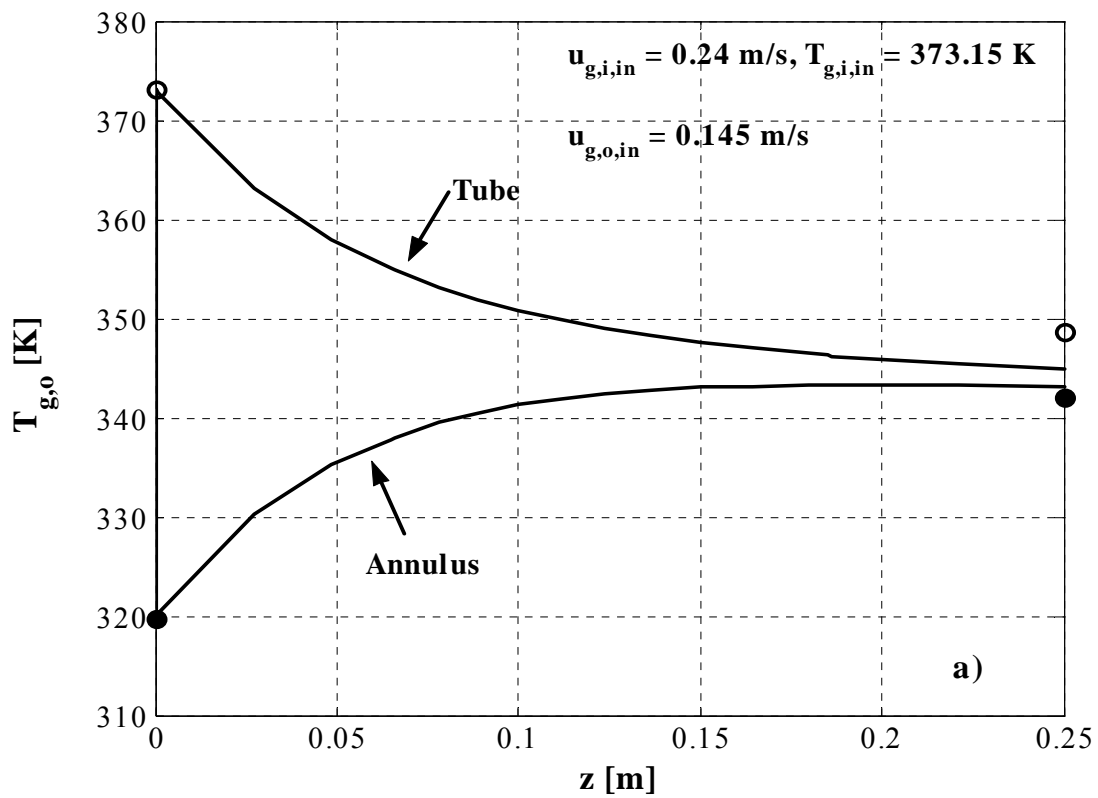


Fig. 5.3: Axial profile of the gas temperatures in the annulus and tube for constant inlet velocities and two different gas inlet temperatures.

It is important to mention here that both ends of the membrane (~ 6.5 cm) are glass coated (sealed), hence no diffusion is taking place in this region. Mass transfer is only taking place in the middle part of the membrane (12 cm).

Figure 5.3 shows the axial profiles of gas temperature in annulus and tube. These temperature profiles look similar to those of double pipe heat exchanger with co-current flow. The energy is given off by hot gas, in our case helium at the tube side, so its temperature decreases along the length of the membrane. Whereas, the cold gas, in our case nitrogen at the annulus side, is getting this energy and its temperature is rising as it moves along the membrane. The heat transfer is mainly taking place due to conduction and transmembrane enthalpy flux through the membrane. As previously mentioned, both membrane ends are glass coated, hence heat transfer in this region is due only to conduction. However, in the middle part of the membrane, which is permeable, heat is additionally transferred to the cold gas by transmembrane enthalpy flux. The diagram reveals that by increasing the gas inlet temperature in the tube thermal equilibrium can be attained earlier requiring a shorter membrane. Figure 5.4 shows the axial profiles of membrane temperature, both at the annulus and tube side, measured at two different axial positions (125 mm and 175 mm). Both plots show that the membrane temperature decreases with z due to the fact that cold gas (N_2) in the annulus takes heat from the membrane as it flows along the measuring cell. It also can be seen that there are moderate temperature gradients between the inner and outer membrane surfaces. Membrane temperatures approach thermal equilibrium along the cell.

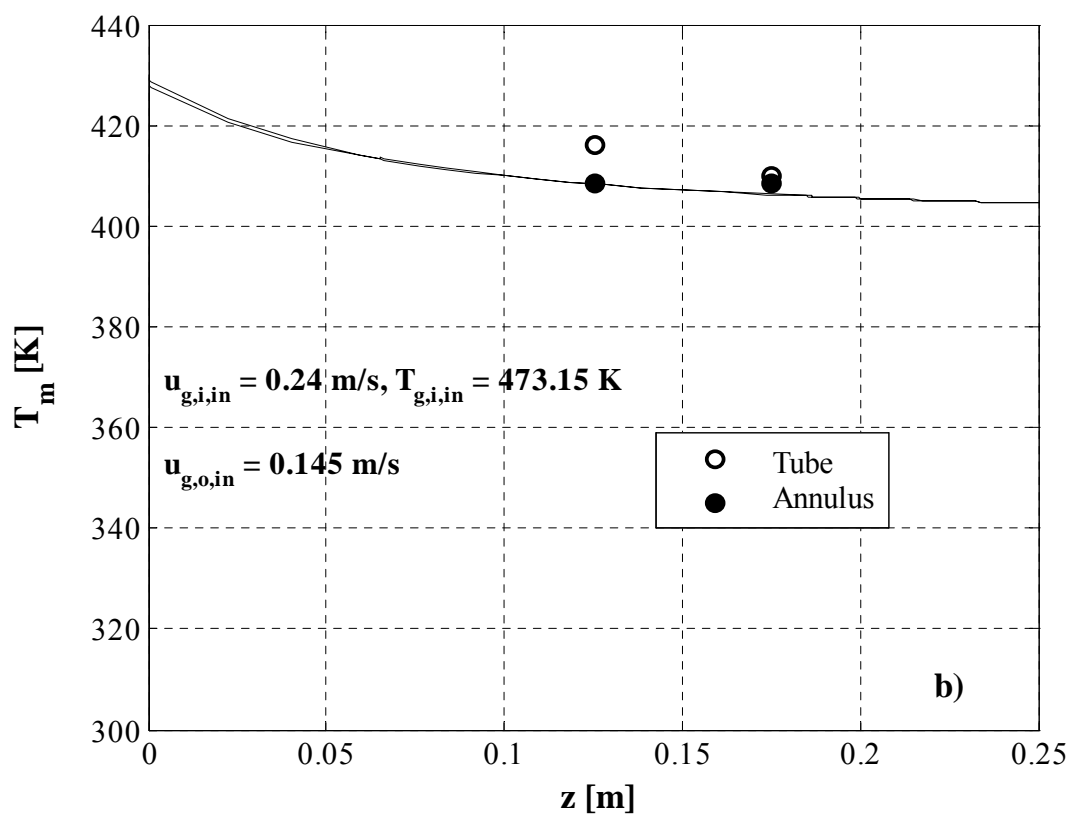
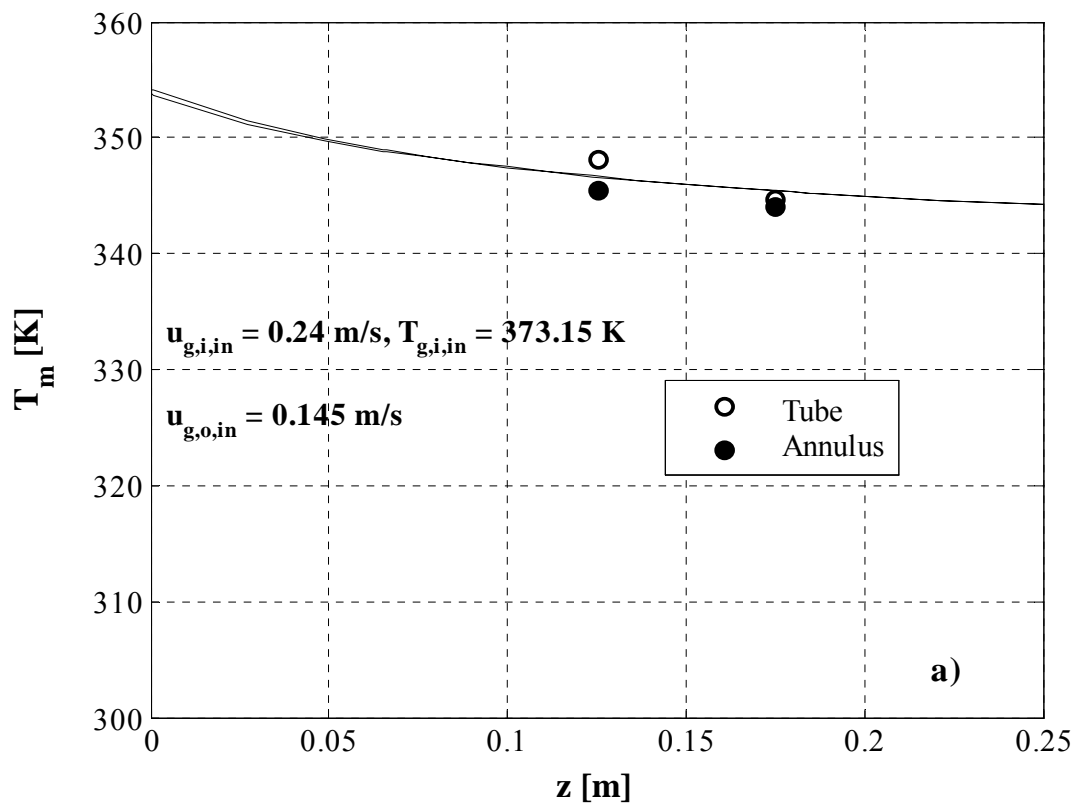


Fig. 5.4: Axial profile of the membrane temperature at the annulus and tube side for constant inlet velocities and two different gas inlet temperatures.

Further comparisons between selected experimental data and calculations are presented in Figs 5.5 to 5.11. Figure 5.5 shows the comparison between the measured and calculated values of molar fraction at the outlet of the annulus for different inlet gas temperatures and flow velocities. It can be seen that the mole fraction of He at the outlet of the annulus rises with temperature as both diffusion coefficients (Knudsen and molecular) increase with increasing temperature. Whereas the outlet molar fraction of helium decreases with increasing volumetric flow rate, which can be justified by decreasing residence time of gas in the tube.

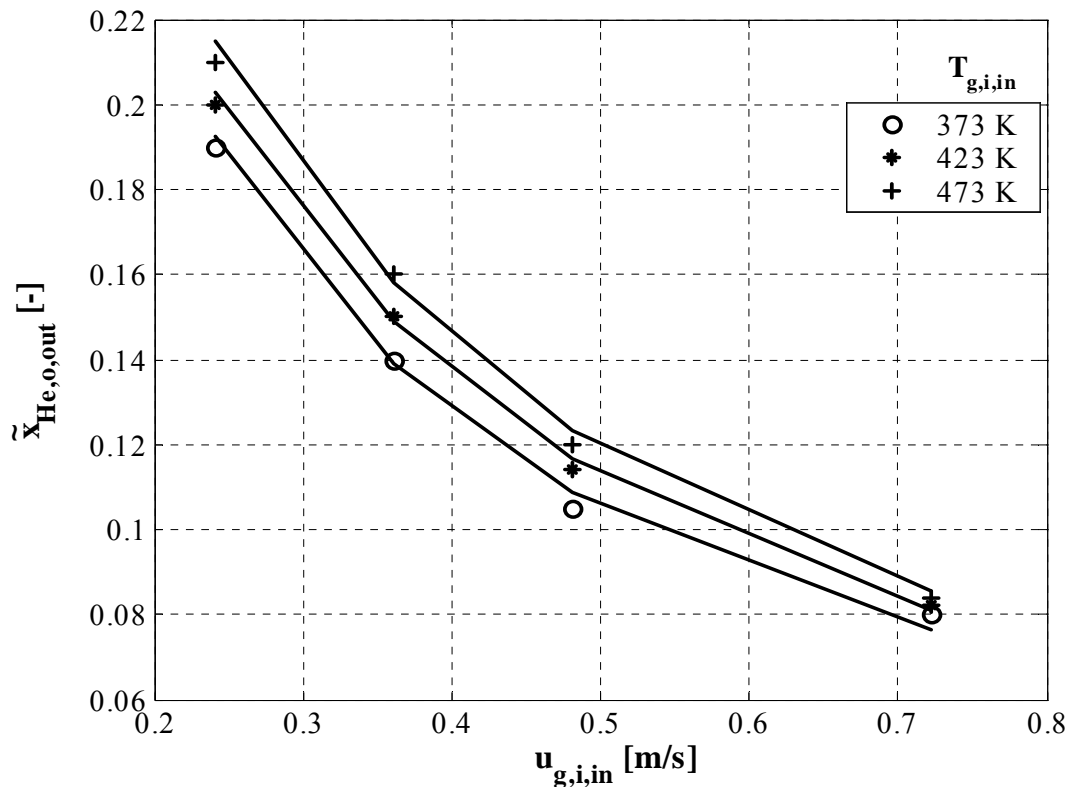


Fig. 5.5: Mole fraction of He at the outlet of annulus at different temperatures versus inlet gas flow velocity; for $u_{g,o,\text{in}}$ see Appendix D.

Figures 5.6 and 5.7 show the comparison between measured and calculated gas temperatures at the outlet of annulus and tube. The temperature of the gas at the outlet of the annulus decreases by increasing flow velocity due, again, to less residence time of hot helium flowing through the tube (Fig. 5.6). For the same reason, the temperature of gas at the outlet of the tube increases with increasing gas flow velocity (Fig. 5.7). Without shell correction, the trends in Figs 5.6, 5.7 would be stronger. As mentioned before, heat transfer takes place due to conduction along the entire length of the membrane, but in the middle part of the membrane, which is not sealed, heat is also transferred to the other side of the membrane due

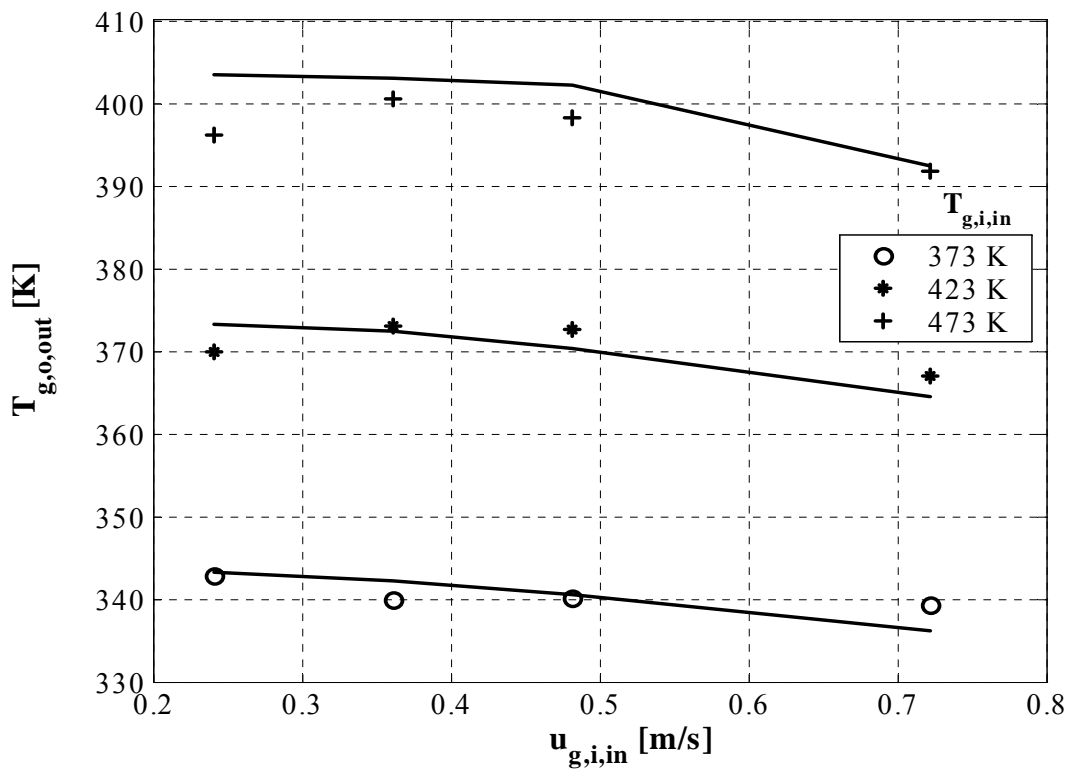


Fig. 5.6: Temperature of gas at the outlet of annulus at different gas inlet temperatures versus inlet gas flow velocity.

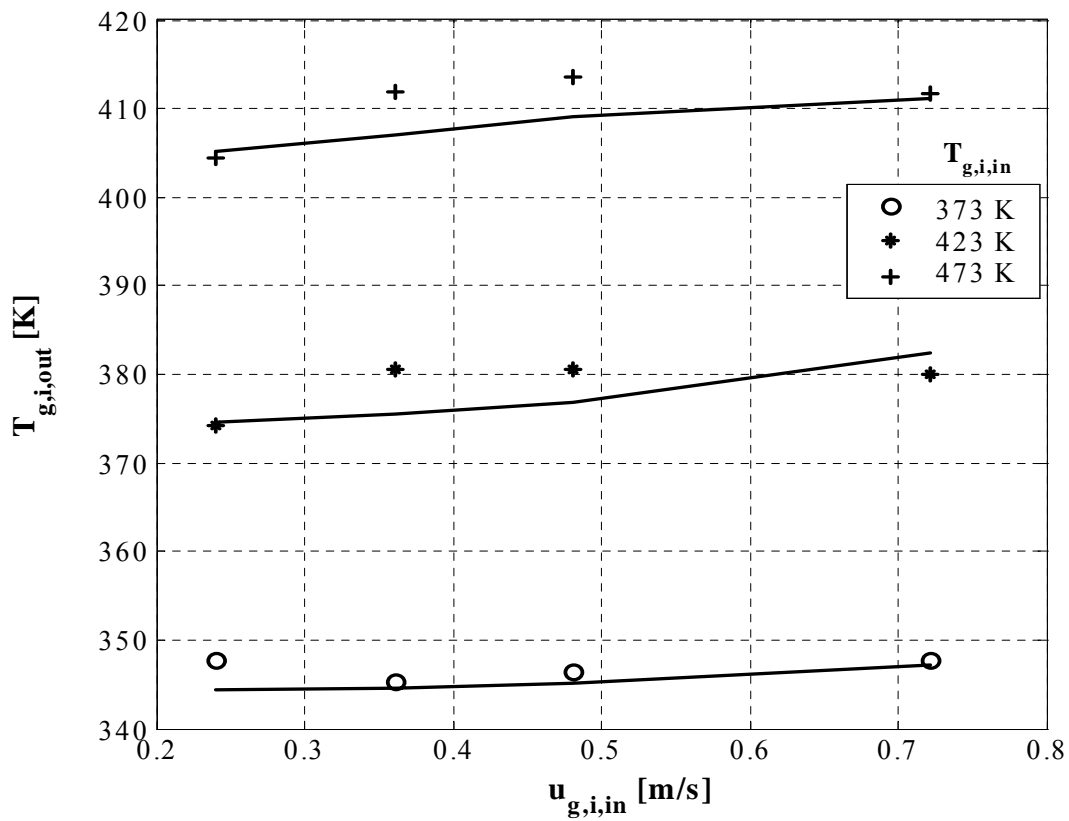


Fig. 5.7: Temperature of gas at the outlet of tube at different gas inlet temperatures versus inlet gas flow velocity.

to transmembrane enthalpy flux. The membrane and the gas temperatures are closely related to each other due to the combined heat transfer mode. Some calculated and measured membrane outer side temperatures are plotted against gas flow velocities in Figs. 5.8 and 5.9. In all comparisons, a reasonable agreement between measured and predicted values could be observed.

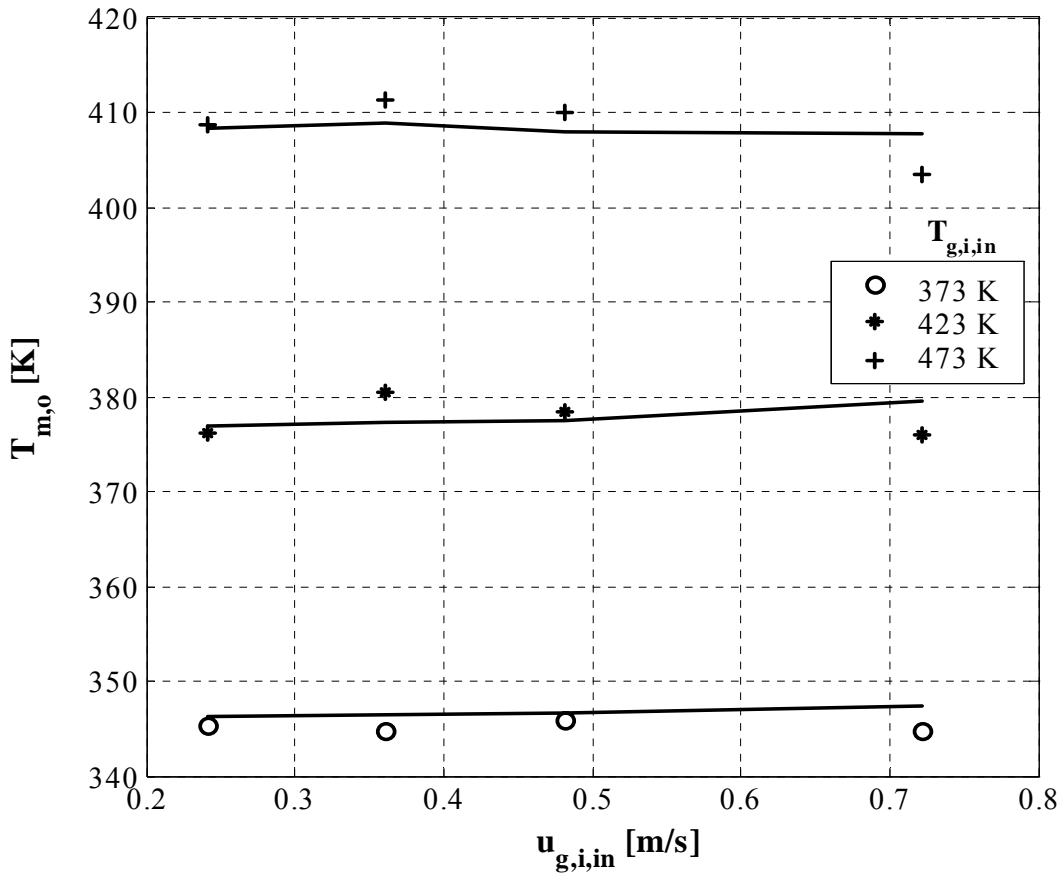


Fig. 5.8: Temperature of membrane (at 125 mm, annulus side) at different gas inlet temperatures versus inlet gas flow velocity.

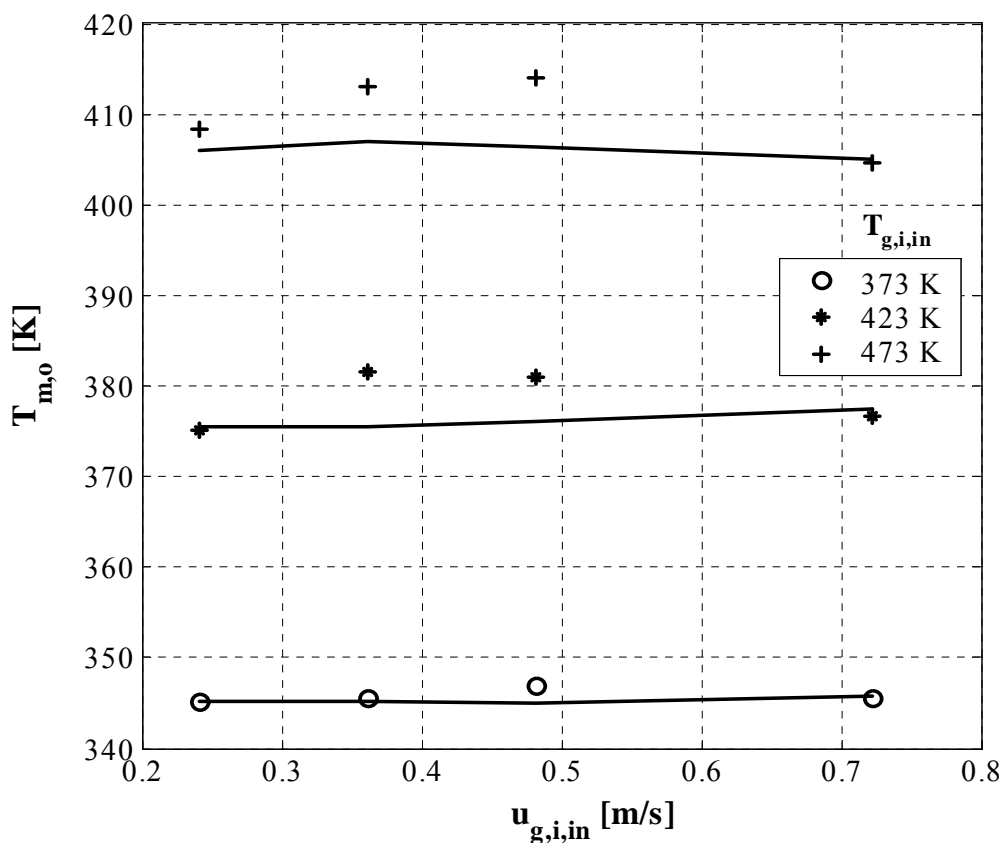


Fig. 5.9: Temperature of membrane (at 175 mm, annulus side) at different gas inlet temperatures versus inlet gas flow velocity.

5.2 Comparison between isothermal and non-isothermal case

In most of the available literature [4, 17, 24], experiments have been conducted at room temperature to quantify the gas diffusion in porous media using dusty gas model, ignoring the effect of temperature on diffusion which may lead to serious error while designing a membrane reactor. To study the effect of temperature on the diffusion process, at first isothermal, isobaric diffusion experiments were performed for various gas flow velocities. In contrary to the isobaric diffusion experiments with $u_{g,o,in} = \text{constant}$ of sec. 4.2, gas flow velocities both in annulus and tube were varied. It can be seen in Fig. 5.10 that by increasing the flow velocity of helium in tube, less helium diffuses through the membrane due to decreased residence time. The results of non-isothermal, isobaric diffusion experiments (Fig. 5.5) are compared to the isothermal case ($T = 293$ K) in Fig. 5.11. It can be seen that mole fraction of helium increases at the outlet of annulus by increasing the helium inlet temperature (tube side). This is due to the fact that molecular diffusion is more important than Knudsen diffusion for investigated composite.

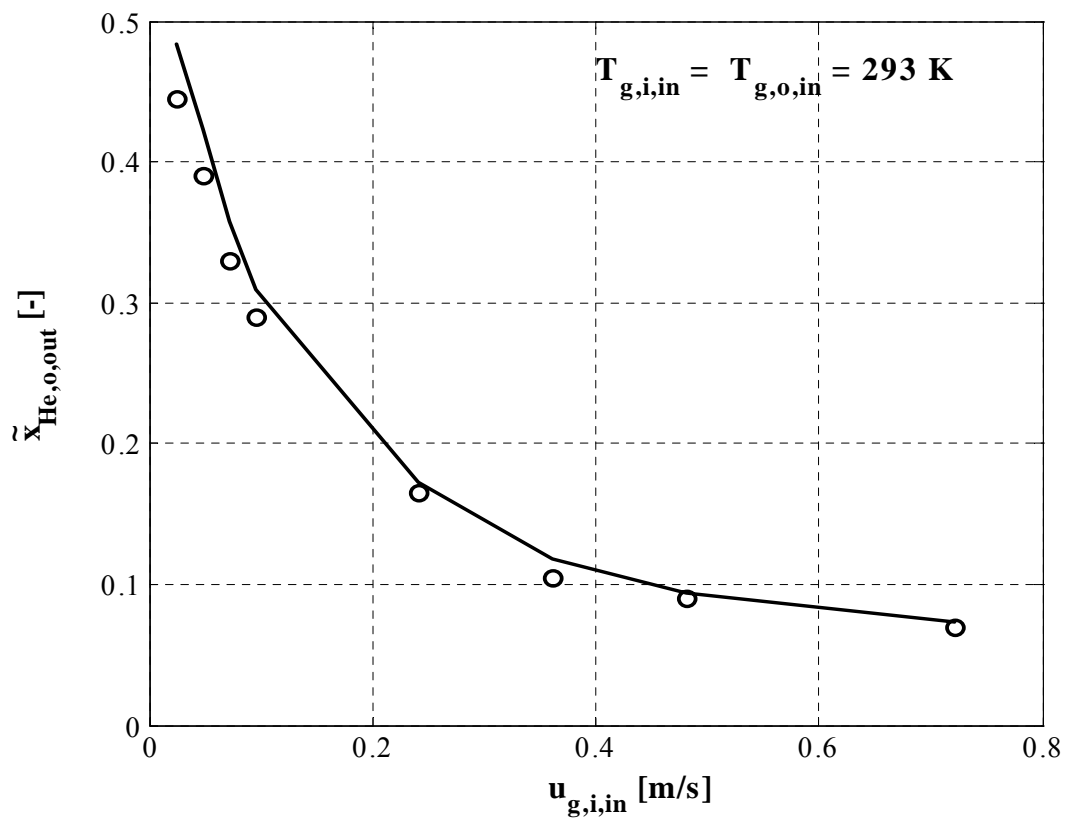


Fig. 5.10: Mole fraction of He at the outlet of annulus (isothermal, isobaric case) versus inlet gas flow velocity; values of $u_{g,o,\text{in}}$ in Appendix D.

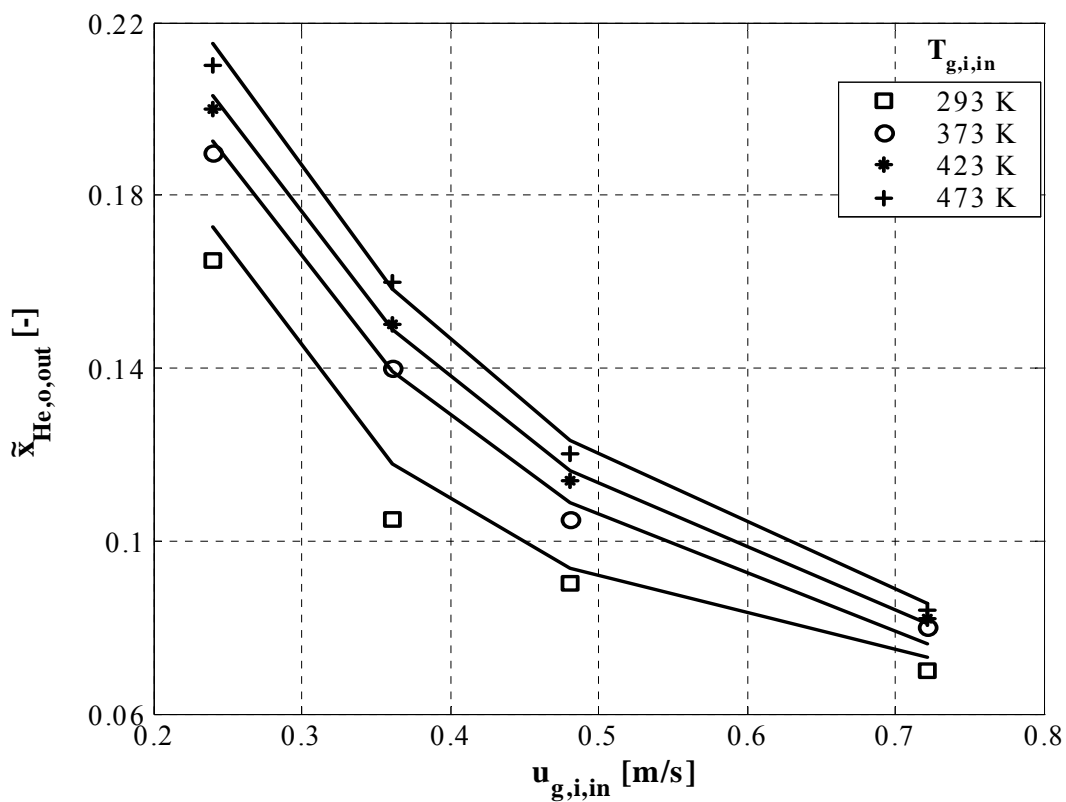


Fig. 5.11: Mole fraction of He at the outlet of annulus (non-isothermal, isobaric case) versus inlet gas flow velocity.

5.3 Influence of shell temperature

As mentioned earlier, the presence of thermal bridges to the shell led to the relatively higher shell temperatures, which not only became an additional heat source for gas flowing in the annulus but also influenced the temperature of gas entering the annulus. It was possible to measure the annulus gas inlet temperature accurately, but not possible to set it accurately. This hindered to exhibit clear trends in temperature profiles of gases flowing in annulus and tube. To see these trends, simulation was done by keeping constant gas inlet temperature to annulus and ignoring the shell side heat transfer term in eq. (5.1). Analysis of these simulation results (Figs 5.12 and 5.13) reveals that there is almost no change in the mole fraction of helium at the outlet of the annulus in comparison to Fig. 5.5, but the trends in the temperature profiles of the gases flowing in the annulus and the tube are quite stronger.

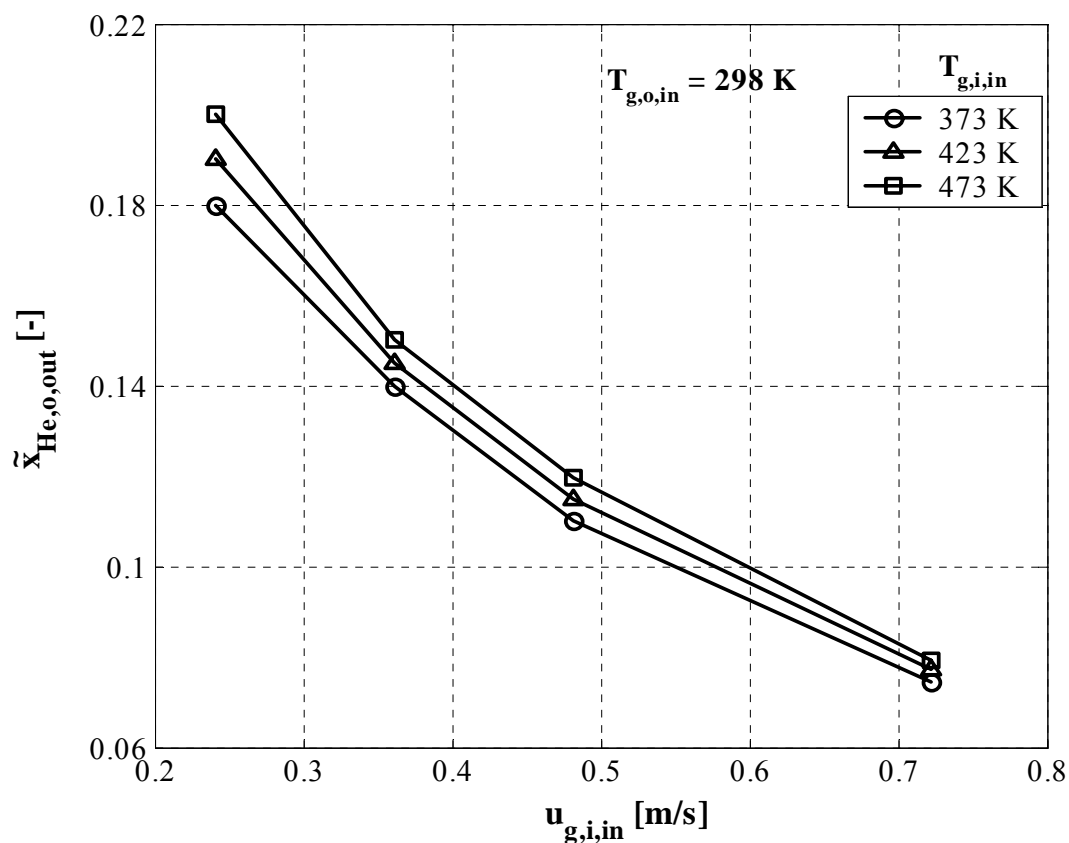


Fig. 5.12: Mole fraction of He at the outlet of annulus (simulation results with constant inlet gas temperature to annulus and without shell effect) versus inlet gas flow velocity; $u_{g,o,in}$ the same as for the experiments of Fig. 5.5.

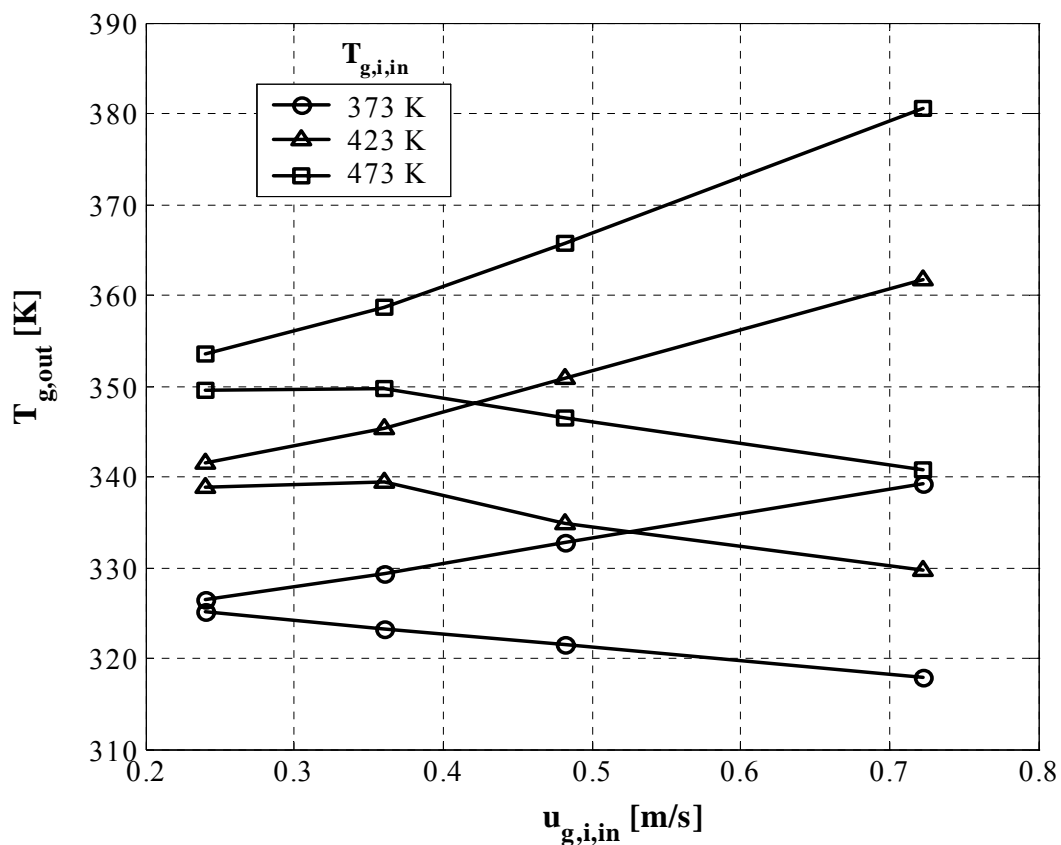


Fig. 5.13: Temperature of gas at the outlet of annulus (broken lines) and tube (solid lines) for the simulations of Fig. 5.12.

5.4 Simulation results for the case of ethane-oxygen

As the ultimate goal of this research is to use the membranes for the partial oxidation of hydrocarbons in a membrane reactor, it is interesting to see how the fluxes and gas temperatures change if the pair of gases, nitrogen-helium, is replaced by ethane-oxygen. The simulation results are presented in Figs 5.14 and 5.15. The energy and mass balance equations used for these calculations are same as for the case of nitrogen and helium. The boundary conditions, i.e., gas inlet temperatures, shell temperature, were taken the same as measured in the experiments with nitrogen and helium (experimental values of Fig. 5.5).

Figure 5.14 shows that more ethane diffuses through the membrane as its inlet temperature to the tube increases – a similar trend as in the case of nitrogen and helium, qualitatively verifying the influence of temperature on mass transfer. However, a quantitative equality can not be expected (compare Fig 5.14 with Fig. 5.5) as helium is much lighter than ethane so it diffuses faster through the membrane as compared to ethane. In Fig. 5.15, outlet gas temperatures at annulus and tube are plotted against ethane flow velocity in the tube for

three different ethane inlet temperatures to the tube. If Fig. 5.15 is compared to Fig. 5.13, it can be seen that the temperature difference between the tube and annulus gas for every gas inlet temperature to tube is smaller in the case of ethane-oxygen than nitrogen-helium. This is due to the fact that shell heat transfer is considered in this case (additional heat source). Moreover, the difference between the heat capacities of ethane (1621 J/kg K) and helium (5193 J/kg K) is significant, whereas the heat capacities of oxygen and nitrogen do not differ too much.

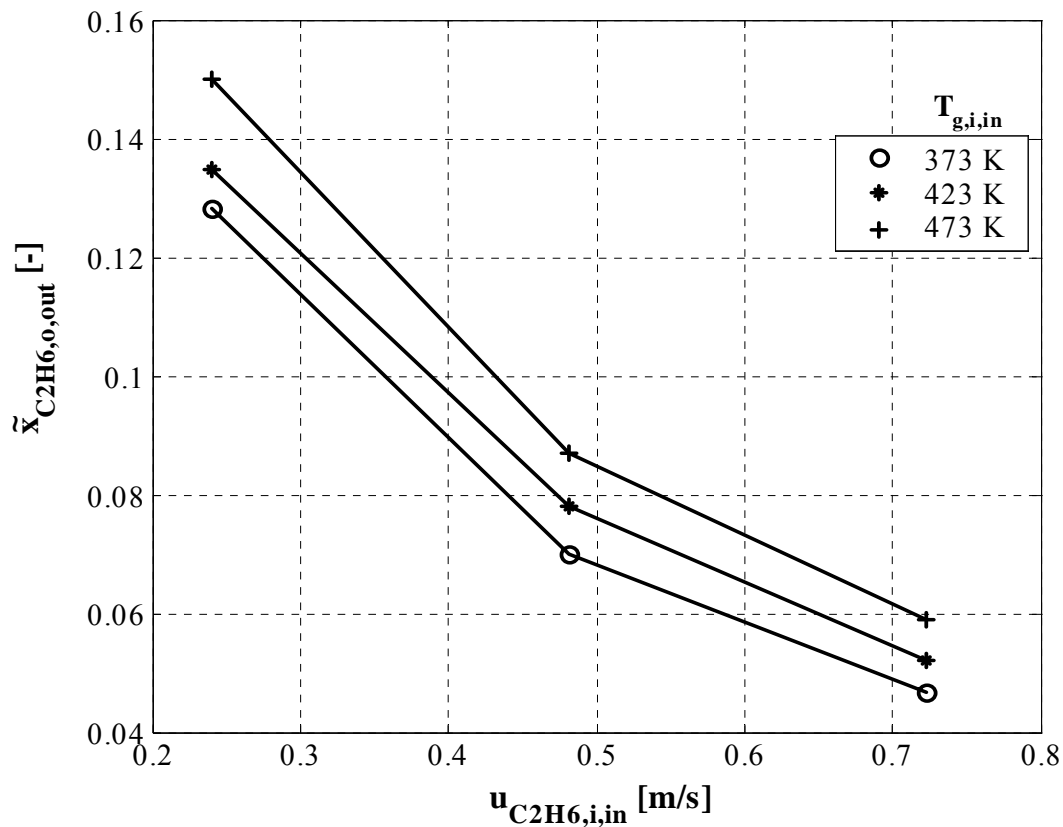


Fig. 5.14: Mole fraction of ethane at the outlet of annulus (simulation results) versus inlet ethane flow velocity to the tube; $u_{\text{g, o, in}}$, $T_{\text{g, o, in}}$ and T_{Shell} have been taken as for the experiments of Fig. 5.5.

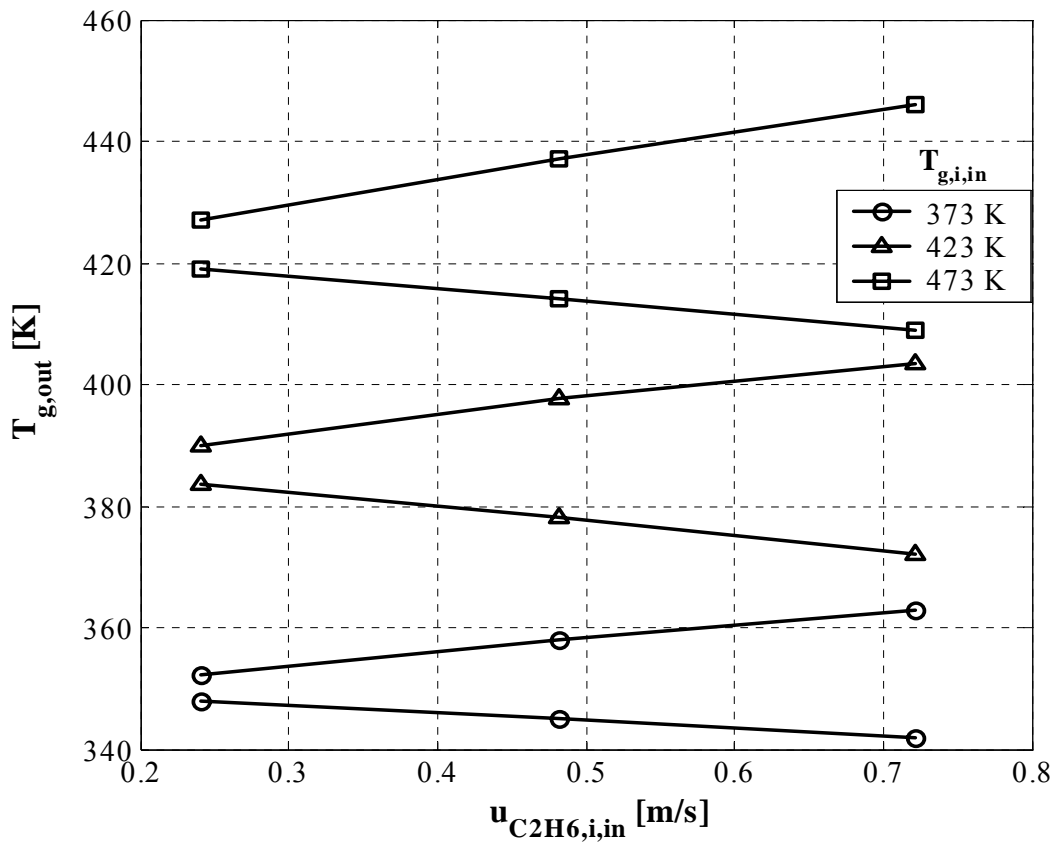


Fig. 5.15: Temperature of gas at the outlet of annulus (broken lines) and tube (solid lines) for the simulations of Fig. 5.14.

5.5 Influence of heat transfer coefficient

Furthermore, the influence of heat transfer coefficient on temperature profiles of membrane (M1 composite) and gas is shown in Figs 5.16 and 5.17. These simulations have been done for a constant heat transfer coefficient at the tube side ($\alpha_{g,i} = 30 \text{ W/m}^2 \text{ K}$) by changing the heat transfer coefficient on the annulus side for the operating conditions of

$$P_i = P_o = 1.052 \text{ bar,}$$

$$T_{g,o,in} = 319.95 \text{ K, } T_{g,i,in} = 373.15 \text{ K,}$$

$$u_{g,i,in} = 0.24 \text{ m/s, } u_{g,o,in} = 0.145 \text{ m/s.}$$

The results are plotted in form of dimensionless temperature and length, defined as

$$T_m^* = \frac{T_m - T_g^{\text{avg}}}{T_g^{\text{avg}}}, \quad (5.3)$$

$$T_g^* = \frac{T_g - T_g^{\text{avg}}}{T_g^{\text{avg}}}, \quad (5.4)$$

$$\zeta = \frac{z}{L}, \quad (5.5)$$

where T_g^{avg} is the average mixing cup temperature of the inlet streams:

$$T_g^{\text{avg}} = \frac{u_{g,o} F_o n_{g,o} \tilde{c}_{p,g,o}^{\text{avg}} T_{g,o} + u_{g,i} F_i n_{g,i} \tilde{c}_{p,g,i}^{\text{avg}} T_{g,i}}{u_{g,o} F_o n_{g,o} \tilde{c}_{p,g,o}^{\text{avg}} + u_{g,i} F_i n_{g,i} \tilde{c}_{p,g,i}^{\text{avg}}}. \quad (5.6)$$

Both figures show that by increasing the heat transfer coefficient, the rate of heat transfer increases in the annulus and the heat exchange between the gases requires a shorter membrane length to attain the thermal equilibrium.

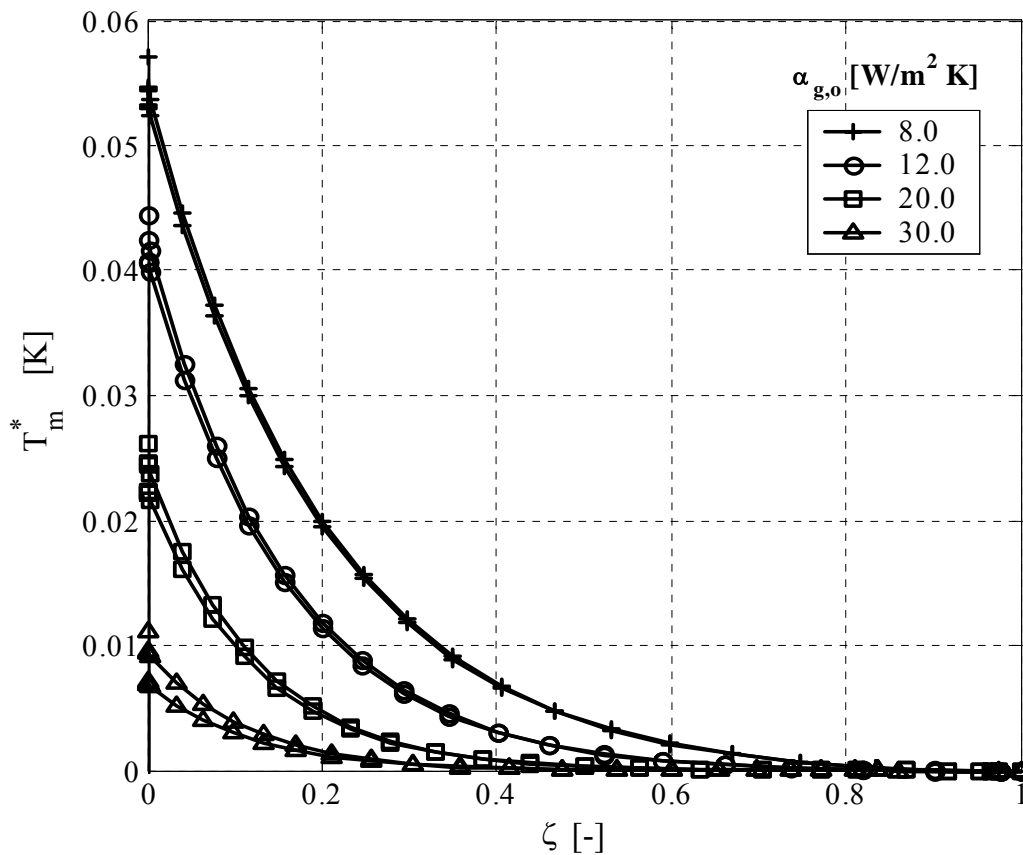


Fig. 5.16: Axial profiles of membrane temperature (simulation results) influenced by the heat transfer coefficient; solid lines: tube-side membrane temperature, broken lines : annulus-side membrane temperature.

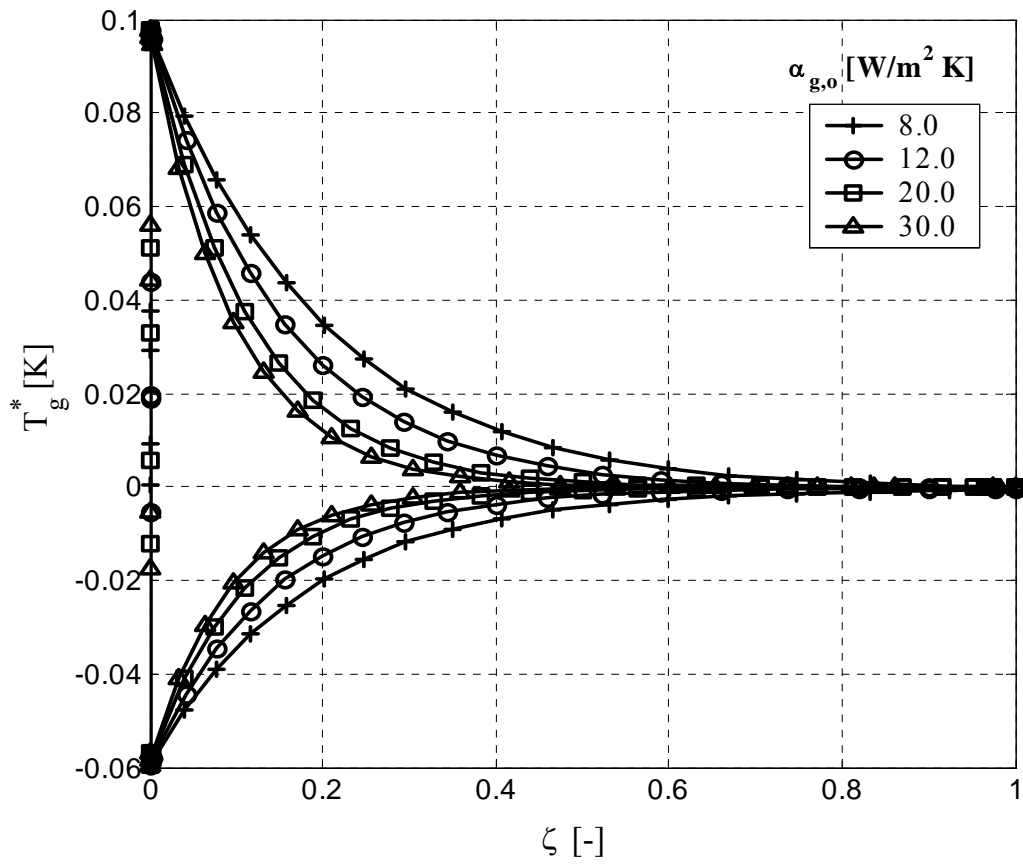


Fig. 5.17: Axial profiles of gas temperature (simulation results) influenced by the heat transfer coefficient; solid lines: tube-side gas temperature, broken lines: annulus-side gas temperature.

6 General analysis of diffusion process

A fluid flowing in a conduit, especially packed with particles, may portray an axial spread of its molecular constituents about the mean flow by diffusion and velocity profiling due to stagnancy of fluid in contact with particles and/or wall of the conduit. In case of shorter contact time this axial spreading is velocity dominated and in case of longer contact time, the role of diffusion is significant. The axial spreading is characterized by a dispersion coefficient depending on the diffusivity and the fluid velocity.

A generalized analysis of isobaric diffusion process has been conducted by considering axial dispersion on both membrane sides, which has been neglected while evaluating the isobaric diffusion experiments in section 4.2. This analysis is based on eq. (4.3), the reduced form of dusty gas model appropriate for isobaric diffusion experiments. The component mass balances in the two gas compartments are calculated by eqs (2.63) and (2.64), including axial dispersion in the present case. Results are presented in form of dimensionless quantities solved by subsequent transformations.

6.1 Non-dimensional form of the model equations

Axial dispersion represents the transport in axial direction superimposed on that due to the convection [132-133]. At low gas velocities, i.e. in the laminar flow regime, the dispersion is mainly caused by diffusion. The component mass balance equations (eqs (2.63) and (2.64)) considering simultaneous convection and diffusion in the flow system have been transformed to dimensionless form for annulus and tube respectively, yielding

$$\frac{1}{Bo_{o,in}} \frac{d^2 \tilde{x}_{j,o}^*}{d\zeta^2} - \frac{d(u_{g,o}^* n_{g,o}^* \tilde{x}_{j,o}^*)}{d\zeta} + \frac{\dot{N}_{j,o}^*}{\tilde{x}_{j,in}^{av}} = 0, \quad (6.1)$$

$$\frac{1}{Bo_{i,in}} \frac{d^2 \tilde{x}_{j,i}^*}{d\zeta^2} - \frac{d(u_{g,i}^* n_{g,i}^* \tilde{x}_{j,i}^*)}{d\zeta} + \frac{\dot{N}_{j,i}^*}{\tilde{x}_{j,in}^{av}} = 0, \quad (6.2)$$

where

$$\zeta = \frac{z}{L}, \quad (6.3)$$

$$\text{Bo}_{o,\text{in}} = \frac{u_{g,o,\text{in}} L}{D_{\text{ax},o}}, \quad \text{Bo}_{i,\text{in}} = \frac{u_{g,i,\text{in}} L}{D_{\text{ax},i}}, \quad (6.4\text{a,b})$$

$$\dot{N}_{j,o}^* = \frac{\dot{N}_j}{F_o n_{g,o,\text{in}} u_{g,o,\text{in}}}, \quad \dot{N}_{j,i}^* = \frac{\dot{N}_j}{F_i n_{g,i,\text{in}} u_{g,i,\text{in}}}, \quad (6.5\text{a,b})$$

$$u_{g,o}^* = \frac{u_{g,o}}{u_{g,o,\text{in}}}, \quad u_{g,i}^* = \frac{u_{g,i}}{u_{g,i,\text{in}}}, \quad (6.6\text{a,b})$$

$$n_{g,o}^* = \frac{n_{g,o}}{n_{g,o,\text{in}}}, \quad n_{g,i}^* = \frac{n_{g,i}}{n_{g,i,\text{in}}}, \quad (6.7\text{a,b})$$

$$\tilde{X}_{j,o}^* = \frac{\tilde{X}_{j,o}}{X_{j,\text{in}}^{\text{av}}}, \quad \tilde{X}_{j,i}^* = \frac{\tilde{X}_{j,i}}{X_{j,\text{in}}^{\text{av}}}. \quad (6.8\text{a,b})$$

The average inlet molar fraction of regarded component

$$\tilde{X}_{j,\text{in}}^{\text{av}} = \frac{u_{g,\text{in}}^* n_{g,\text{in}}^* F^* \tilde{X}_{j,o,\text{in}} + \tilde{X}_{j,i,\text{in}}}{u_{g,\text{in}}^* n_{g,\text{in}}^* F^* + 1}, \quad (6.9)$$

is calculated by considering

$$u_{g,\text{in}}^* = \frac{u_{g,o,\text{in}}}{u_{g,i,\text{in}}}, \quad n_{g,\text{in}}^* = \frac{n_{g,o,\text{in}}}{n_{g,i,\text{in}}}, \quad F^* = \frac{F_o}{F_i}. \quad (6.10\text{a,b,c})$$

The required boundary conditions for mass transfer are also transformed to

$$\zeta = 0: \quad u_{g,o}^* = 1, \quad u_{g,i}^* = 1, \quad (6.11\text{a,b})$$

$$\zeta = 1: \quad d\tilde{X}_{j,o}^*/d\zeta = 0, \quad d\tilde{X}_{j,i}^*/d\zeta = 0, \quad (6.12\text{a,b})$$

$$\zeta = 0: \quad \tilde{x}_{j,o,in}^* - \tilde{x}_{j,o}^* + \frac{1}{Bo_{o,in}} \frac{d\tilde{x}_{j,o}^*}{d\zeta} = 0, \quad (6.13)$$

$$\tilde{x}_{j,i,in}^* - \tilde{x}_{j,i}^* + \frac{1}{Bo_{i,in}} \frac{d\tilde{x}_{j,i}^*}{d\zeta} = 0, \quad (6.14)$$

$$\tilde{x}_{j,o,in}^* = \frac{\tilde{x}_{j,o,in}}{\tilde{x}_{j,in}^{av}}, \quad \tilde{x}_{j,i,in}^* = \frac{\tilde{x}_{j,i,in}}{\tilde{x}_{j,in}^{av}}.$$

(6.15a,b)

The convective boundary conditions at the membrane have been transformed as

$$\frac{\dot{N}_{j,o}^*}{\tilde{x}_{j,in}^{av}} = \frac{n_{g,m,o}}{n_{g,o,in}} NTU_{o,in} (\tilde{x}_{j,m,o}^* - x_{j,o}^*), \quad (6.16)$$

$$\frac{\dot{N}_{j,i}^*}{\tilde{x}_{j,in}^{av}} = \frac{n_{g,m,i}}{n_{g,i,in}} NTU_{i,in} (x_{j,i}^* - \tilde{x}_{j,m,i}^*), \quad (6.17)$$

by considering

$$\tilde{x}_{j,m,o}^* = \frac{\tilde{x}_{j,m,o}}{\tilde{x}_{j,in}^{av}}, \quad \tilde{x}_{j,m,i}^* = \frac{\tilde{x}_{j,m,i}}{\tilde{x}_{j,in}^{av}}, \quad (6.15a,b)$$

$$NTU_{o,in} = \frac{\beta_{g,o} A_{m,o}}{\dot{V}_{g,o,in}}, \quad NTU_{i,in} = \frac{\beta_{g,i} A_{m,i}}{\dot{V}_{g,i,in}}.$$

(6.16a,b)

Dimensionless gas volumetric flow rates are defined as

$$\dot{V}_{g,o}^* = \frac{\dot{V}_{g,o}}{\dot{V}_{g,o,in}}, \quad \dot{V}_{g,i}^* = \frac{\dot{V}_{g,i}}{\dot{V}_{g,i,in}}. \quad (6.17a,b)$$

and are equal to $u_{g,o}^*$ and $u_{g,i}^*$ (eqs (6.6)) for the isothermic case. All simulations have been conducted with ProMoT/Diva. As before, the dusty gas model will be applied for quantifying

mass transfer in every membrane layer (M1). A binary system of nitrogen (annulus) and helium (tube) has been considered for the simulations.

6.2 Non-dimensional analysis

6.2.1 Influence of axial dispersion coefficient

In contrary to the previous evaluation (sec. 4.2), where plug flow was assumed ($D_{ax} = 0$), this analysis represents the influence of axial dispersion coefficient on composition and flow velocity in terms of dimensionless quantities and numbers. By keeping all other parameters constant, the axial dispersion coefficient is varied from $D_{ax,i} = D_{ax,o} = D_{ax} = 0$ to $0.12 \text{ m}^2/\text{s}$. The boundary/operating conditions used for the simulations are given as,

$$\tilde{x}_{\text{He},i,\text{in}} = \tilde{x}_{\text{N}_2,o,\text{in}} = 1, \quad T_m = T_{g,i,\text{in}} = T_{g,o,\text{in}} = 295.15 \text{ K}, \quad P_i = P_o = 1 \text{ bar},$$

$$u_{\text{He},i,\text{in}} = 0.096 \text{ m/s}, \quad u_{\text{N}_2,o,\text{in}} = 0.058 \text{ m/s}.$$

Figures 6.1 and 6.2 show the influence of axial dispersion coefficient on the composition of helium in annulus and tube. In Fig. 6.1a profiles of helium's mole fraction are plotted against

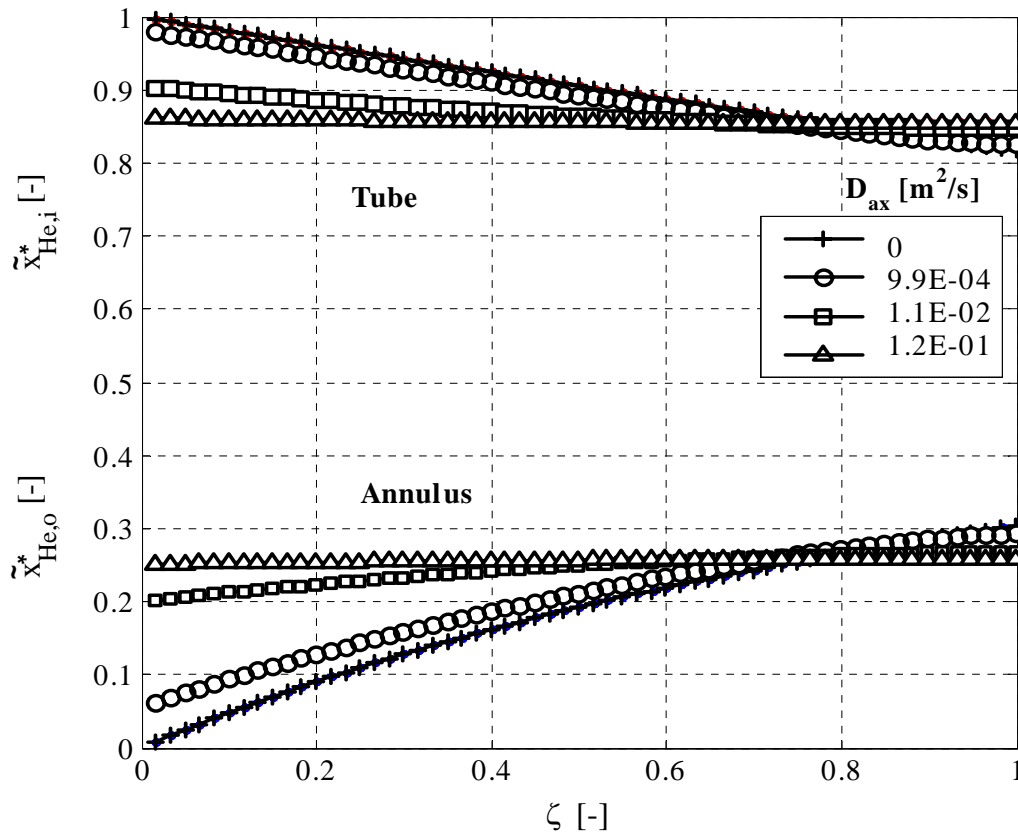


Fig. 6.1a: Mole fraction of helium (in annulus and tube) vs. dimensionless length; influence of axial dispersion coefficient on composition profiles of helium.

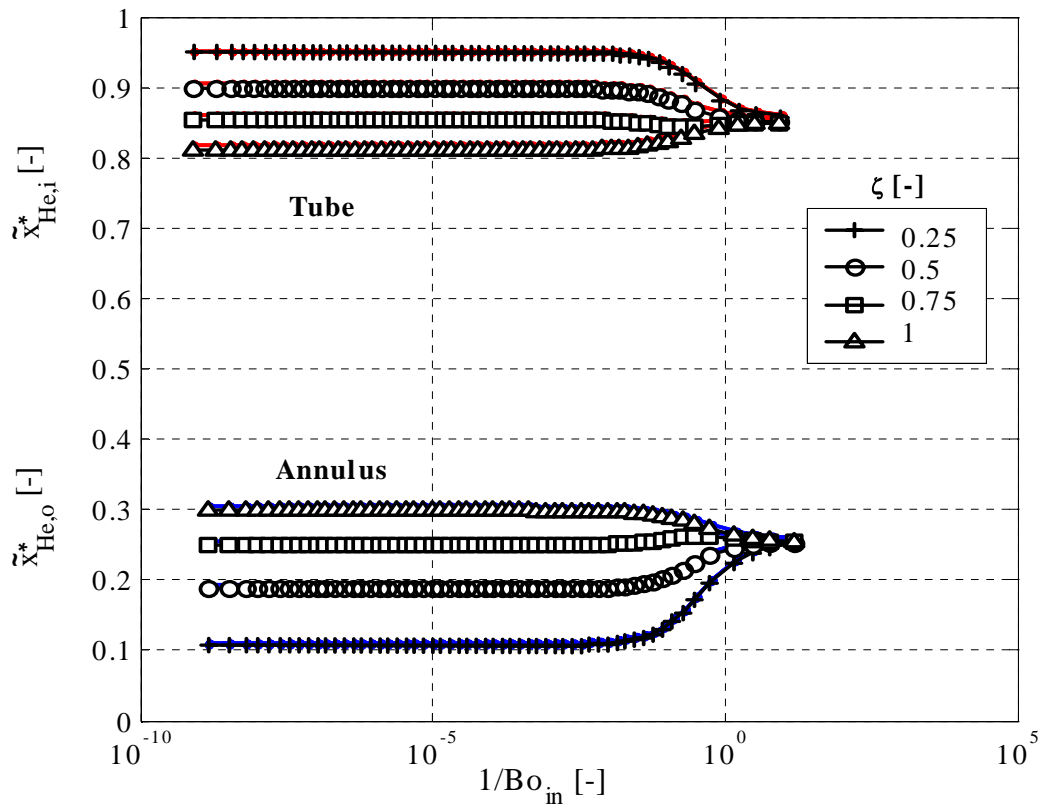


Fig. 6.1b: Mole fraction of helium vs. $1/\text{Bo}_{in}$ for annulus and tube; influence of axial dispersion coefficient on composition profiles of helium.

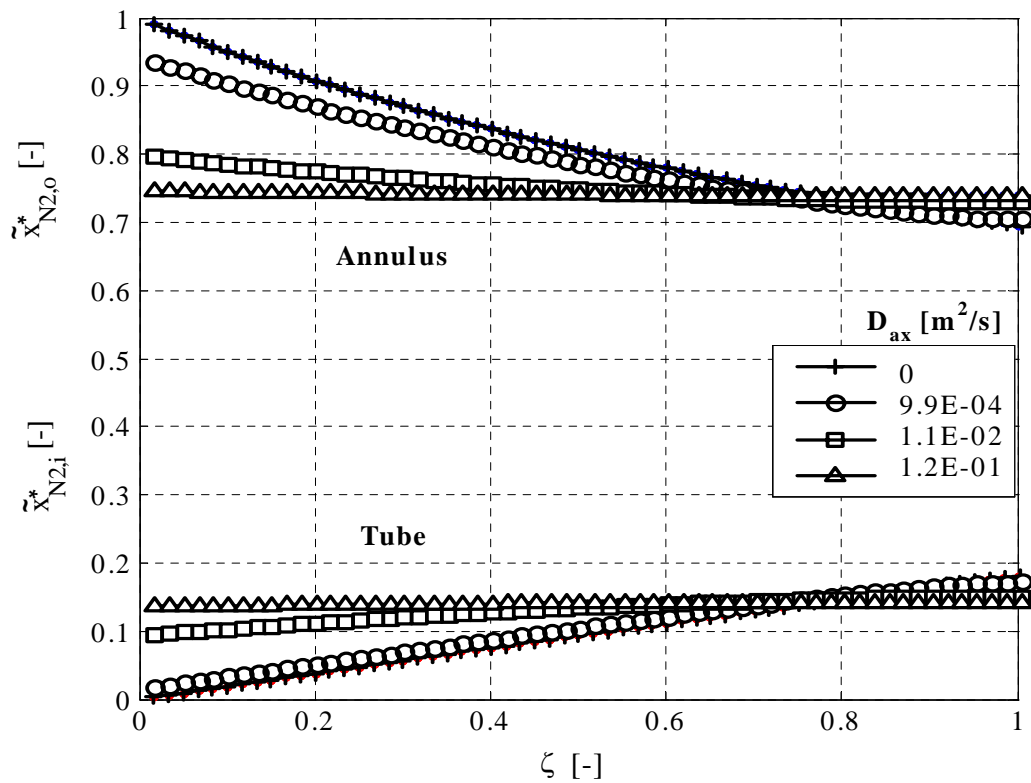


Fig. 6.2a: Same as Fig. 6.1a, for nitrogen.

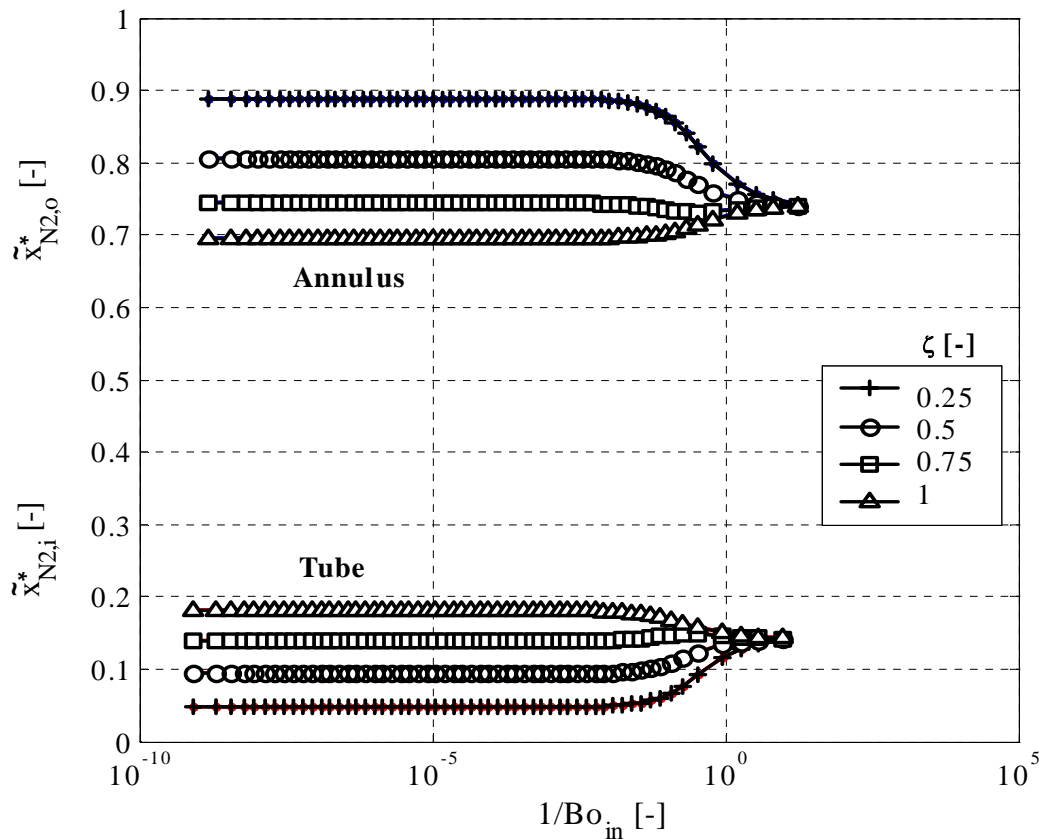


Fig. 6.2b: Same as Fig. 6.1b for nitrogen.

dimensionless length, whereas Fig. 6.1b shows the change in axial profiles of helium's mole fraction in the tube and the annulus with $1/Bo_{in}$. As a counterpart of Fig. 6.1, Fig. 6.2 shows the axial profiles of nitrogen plotted against the dimensionless length and $1/Bo_{in}$ respectively. From the simulation results two limiting cases for the axial dispersion coefficients can be inferred: 1) $D_{ax} \rightarrow 0$, large composition gradients means perfect plug flow, 2) $D_{ax} \rightarrow \infty$, no composition gradients, well mixed flow.

Figure 6.3 shows the profiles of dimensionless volumetric flow rate plotted against dimensionless length and $1/Bo_{in}$. From the diagrams it can be seen that there are considerable differences in gas flow rates, especially at the entrance of annulus and tube, for different axial dispersion coefficients. These differences gradually decrease along the membrane. This may be influenced by the assumption of Danckwert open-closed boundary conditions, which means composition differences at the inlet of the system ($\zeta = 0$) and no composition gradients in gas flow at the outlet ($\zeta = 1$). As we see, the effect of axial dispersion on compositions and volumetric flow rates is small at the exit as compared to the inlet. This justifies our neglect of axial dispersion in the isothermal isobaric diffusion case, compare

also between Figs 4.24 and 6.1a. However, inclusion of axial dispersion coefficient in the model shows that there are composition gradients at the entrance of the measuring cell, which may play a substantial role in catalytic reactions, where the selective and controlled dosing of educts is desired.

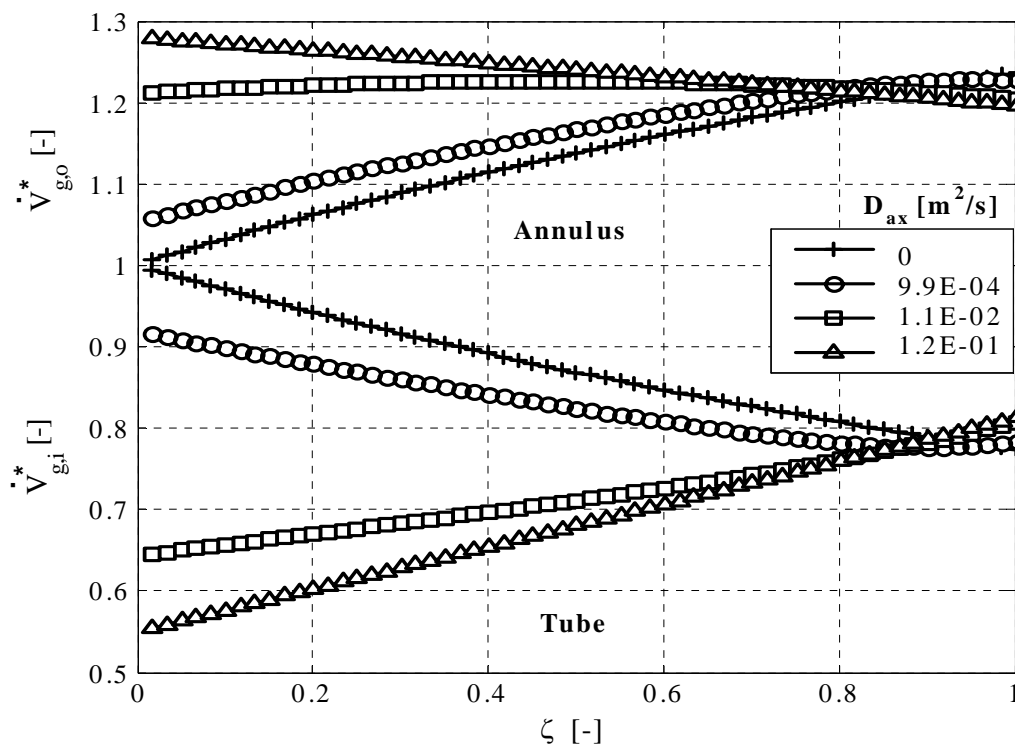


Fig. 6.3a: Dimensionless volumetric flow rate (in annulus and tube) vs. dimensionless length, influence of axial dispersion coefficient on profiles of dimensionless volumetric flow rate.

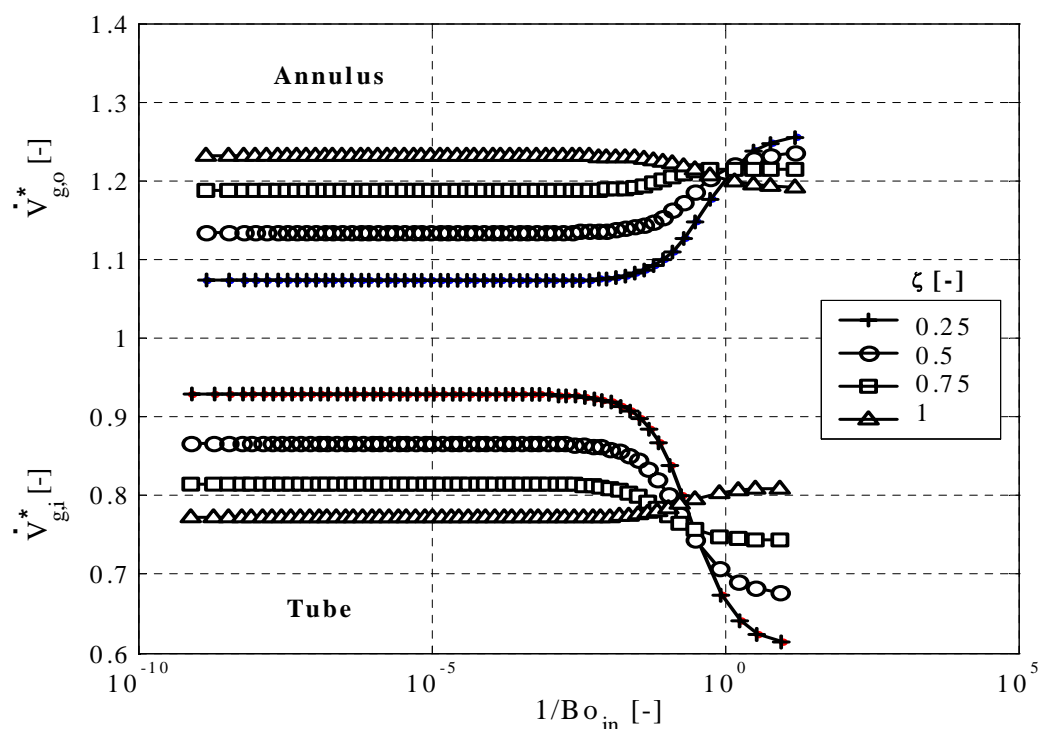


Fig. 6.3b: Dimensionless volumetric flow rate (in annulus and tube) vs. $1/Bo_{in}$, influence of axial dispersion coefficient on composition profiles of nitrogen.

6.2.2 Influence of volumetric flow rate

In this case plug flow is assumed outside the boundary layer ($D_{ax} = 0$) and the influence of volumetric flow rate ($\dot{V}_{g,i,in} = \dot{V}_{g,o,in}$) on composition in terms of dimensionless quantities and numbers is investigated. By keeping all other parameters constant at $D_{ax} = 0$, the inlet volumetric flow rate of tube (i) and annulus (o) is varied at the same rate from 1.02×10^{-6} to $3.87 \times 10^{-3} \text{ m}^3/\text{s}$. The boundary or operating conditions used for the simulations of Figs 6.4 and 6.5 are:

$$\tilde{x}_{\text{He},i,in} = \tilde{x}_{\text{N}_2,o,in} = 1, \quad T_m = T_{g,i,in} = T_{g,o,in} = 295.15 \text{ K} \quad P_i = P_o = 1 \text{ bar}.$$

Figure 6.4 shows the dimensionless molar composition of helium and nitrogen plotted against the dimensionless length for varying gas volumetric flow rate in annulus and tube. It can be seen in Fig. 6.4a that by increasing the inlet flow rates helium composition tends to unity ($\tilde{x}_{\text{He},i}^* \rightarrow 1$) in tube and tends to zero ($\tilde{x}_{\text{He},o}^* \rightarrow 0$) in annulus and vice versa in Fig. 6.4b for the case of nitrogen. Similar effects are shown in Figs 6.5a and b, however in these figures, mole fraction of nitrogen and helium at the outlet is plotted against NTU. For instance Fig. 6.5a reveals that by increasing NTU (lower gas flow rate) gas composition reaches the equilibrium values. At low NTU (higher gas flow rate) helium composition tends to unity ($\tilde{x}_{\text{He},i}^* \rightarrow 1$) in tube and tends to zero ($\tilde{x}_{\text{He},o}^* \rightarrow 0$) in annulus and vice versa in Fig. 6.5b for the case of nitrogen. This can be attributed to the lower residence time of gases in the tube and annulus retarding the mass transfer of gases.

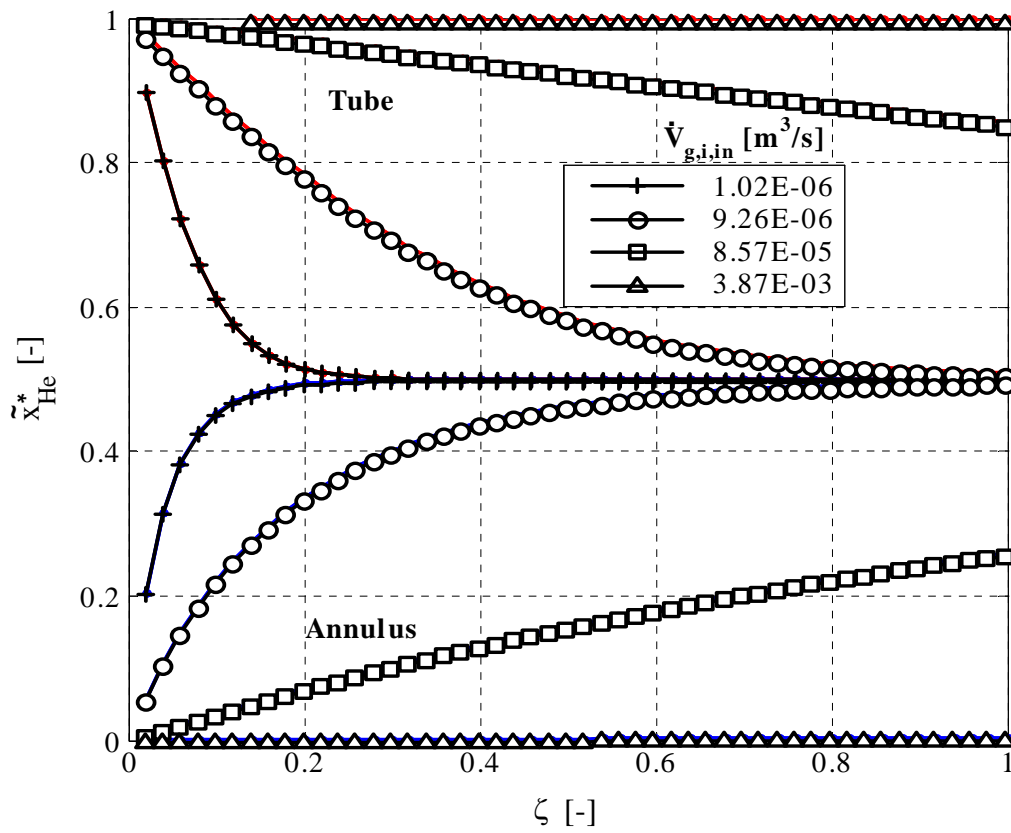


Fig. 6.4a: Mole fraction of helium (in annulus and tube) vs. dimensionless length; influence of volumetric flow rate on composition profiles of helium.

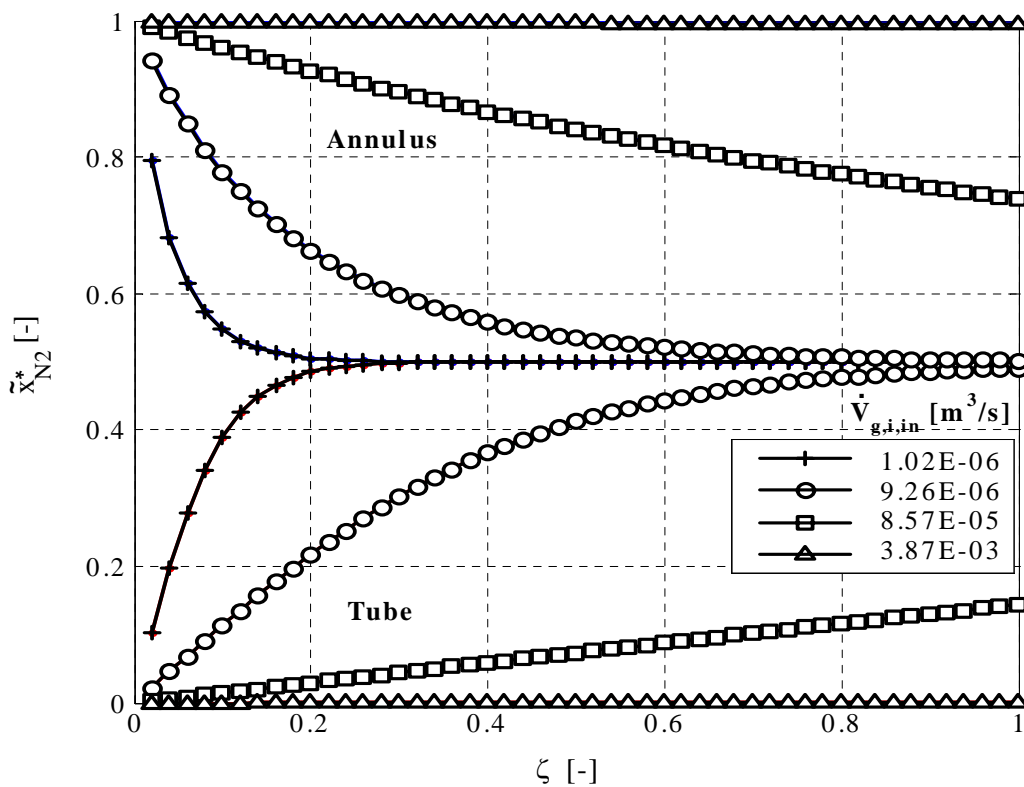


Fig. 6.4b: Mole fraction of nitrogen (in annulus and tube) vs. dimensionless length; influence of volumetric flow rate on composition profiles of nitrogen.

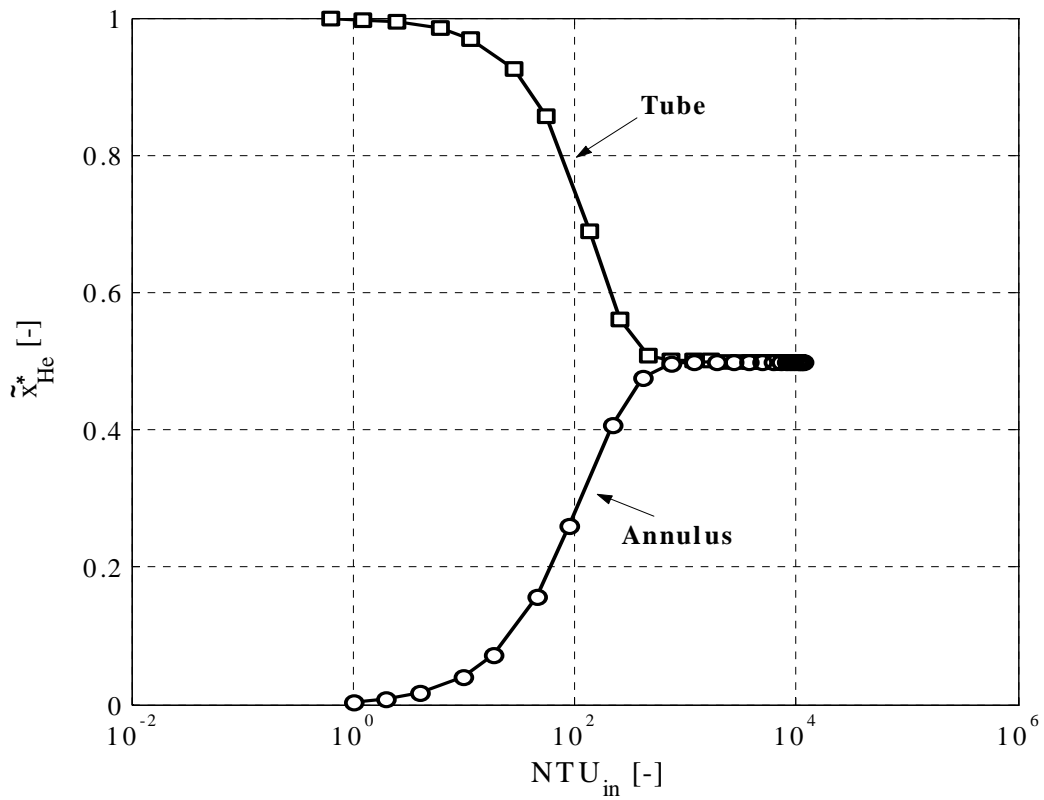


Fig. 6.5a: Mole fraction of helium (in annulus and tube) vs. the respective number of transfer units.

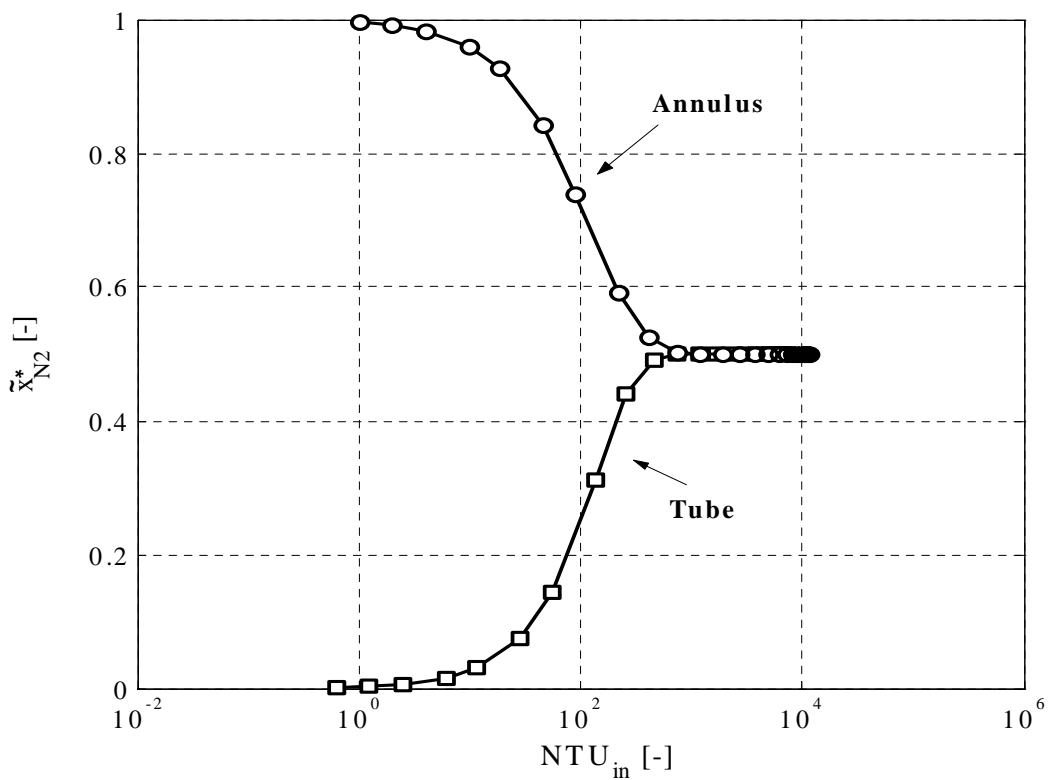


Fig. 6.5b: Mole fraction of nitrogen (in annulus and tube) vs. the respective number of transfer units.

6.2.3 Influence of temperature

The influence of temperature on mass transfer at isothermal conditions is presented in this section. Simulations are conducted by varying temperature from 295.15 to 1000 K and the results for the steady state isothermal case are depicted in Figs 6.6 and 6.7 for the following operating conditions:

$$\tilde{x}_{\text{He},i,\text{in}} = \tilde{x}_{\text{N}_2,o,\text{in}} = 1, \quad u_{g,i,\text{in}} = 0.096 \text{ m/s}, \quad u_{g,o,\text{in}} = 0.058 \text{ m/s}, \quad P_i = P_o = 1 \text{ bar}.$$

The temperature has a positive effect on membrane's transport parameters and a negative effect on density, which in the combination lead to increasing fluxes for higher temperatures and the here considered membrane. Consequently, an increase of temperature will enhance the diffusion process resulting in steeper composition profiles (Fig. 6.6) and higher differences in volumetric flow rate in tube and annulus (Fig. 6.7).

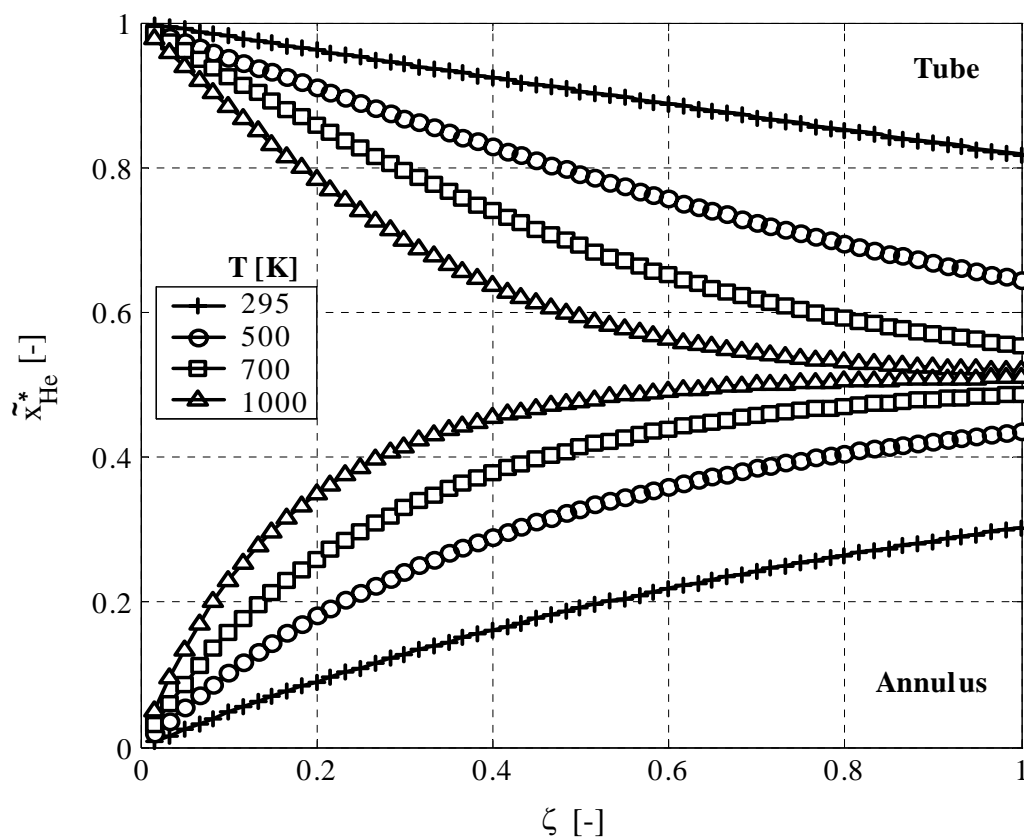


Fig. 6.6a: Mole fraction of helium (in annulus and tube) vs. dimensionless length; influence of temperature on composition profiles of helium.

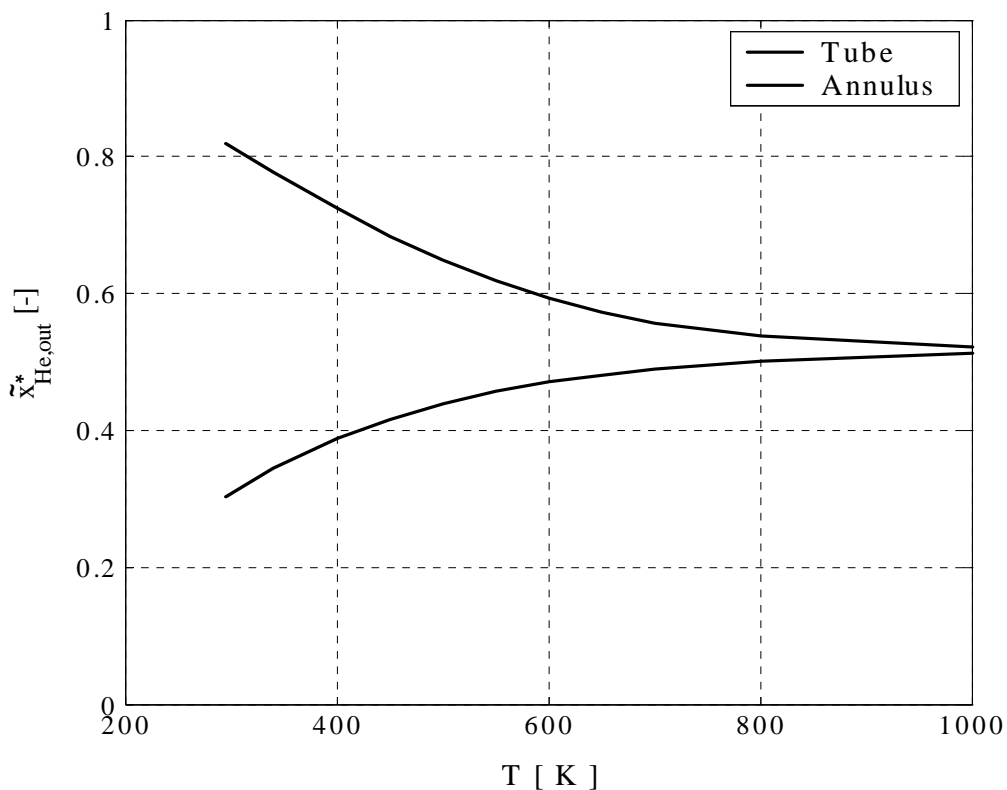


Fig. 6.6b: Mole fraction of helium at the outlet of annulus and tube vs. temperature.

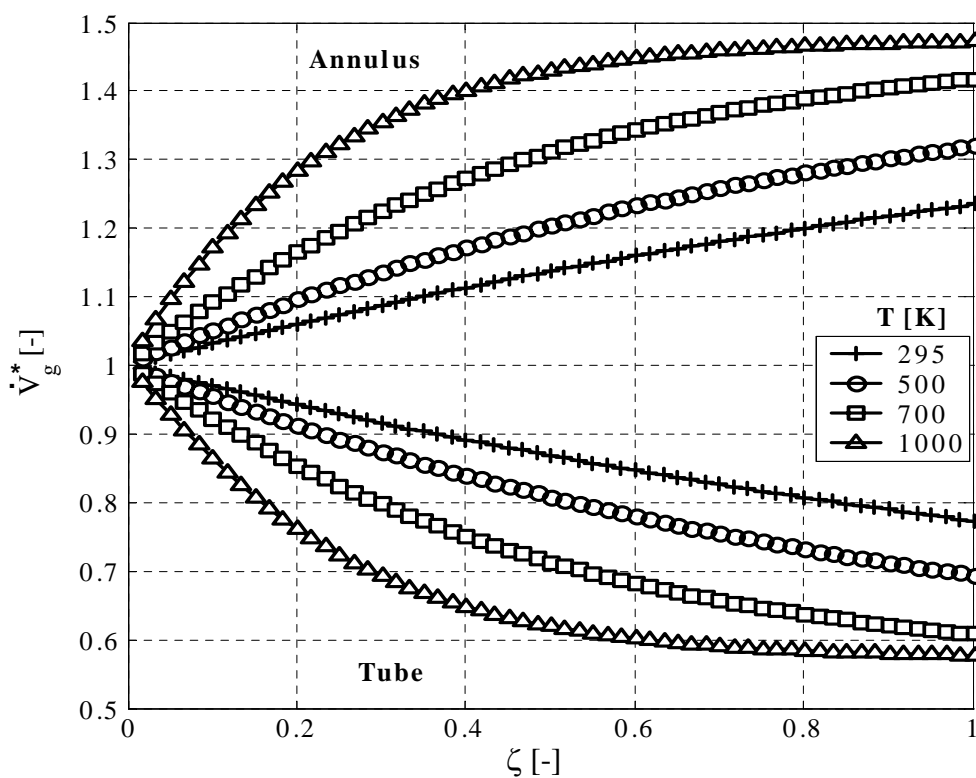


Fig. 6.7a: Dimensionless volumetric flow rate (in annulus and tube) vs. dimensionless length; influence of temperature on volumetric flow rates.

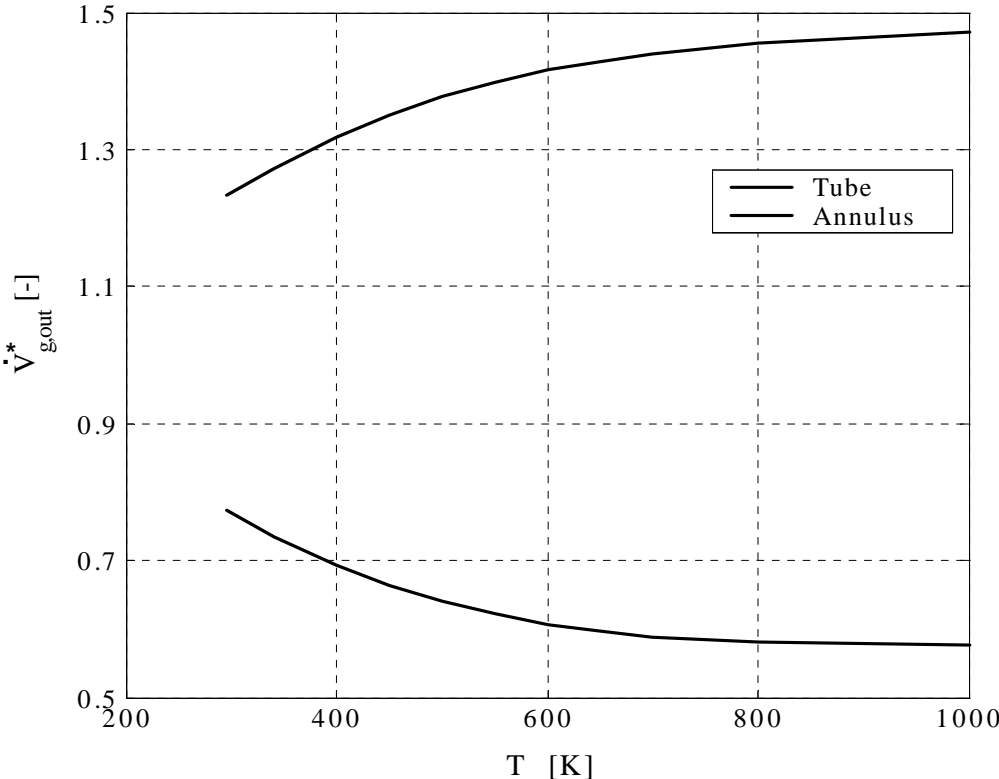


Fig. 6.7b: Dimensionless volumetric flow rate at the outlet of annulus and tube vs. temperature.

7 Conclusion

In the present work heat and mass transfer in tubular asymmetric ceramic membranes suitable for applications in membrane reactors have been investigated. To quantify the heat and mass transfer in the membrane, an experimental matrix has been employed. According to this experimental matrix steady state and dynamic heat/mass transfer measurements have been conducted separately. It successfully enables the identification and validation of heat and mass transfer parameters of the membrane in a comprehensive and consistent manner. These identified heat and mass transfer parameters are further validated in combined heat and mass transfer experiments. Two types of membranes have been investigated for the characterisation of their transport parameters. The main part of experiments have been carried out with the larger membranes (inner diameter of 21 mm) to investigate not only mass transfer but also the heat transfer parameters. With an inner diameter of 21 mm the membranes were larger than in previous work, getting closer to realistic dimensions for application on industrial scale. Thermal conductivity of the membrane has been identified by steady state heat transfer experiments and validated in dynamic heat transfer experiments. Structural parameters of the composite membrane (mass transfer parameters) are identified by single gas permeation experiments and validated by isobaric, steady state and transient diffusion experiments. The mentioned single gas permeation experiments have been carried out not only for the composite membrane, but also for every precursor and intermediate, starting from the support. In this way, the identification of mass transfer parameters could be conducted separately for every individual layer of the composite. Doing so, the influences of temperature, pressure and molar mass of the gas can be precisely understood and accurately predicted by means of the dusty gas model, which successfully combines the mechanisms of Knudsen diffusion, viscous flow and molecular diffusion. It has been further shown that it is important to characterize every single layer of the composite membrane. Assuming the composite membrane as a single layer can be misleading, as the structural parameters of the membrane identified by this assumption will not describe the mass transport of any gas in the entire range of temperatures, but only the data used for fitting.

A simulation analysis has been carried out to see the influence of flow direction and top layer on the mass transfer through the membrane. The analysis reveals that the choice of flow direction may be significant, especially when employing the membrane for the selective dosing of educts in a catalytic reactor. It has also been shown that the fluxes may depend on

the flow direction in a composite membrane. Also the choice of the material of permselective layer is substantial in terms of pressure drop and fluxes. It is evident from the simulation analysis that different permselective layers can considerably shift the pressure profile in the composite membrane.

Single gas permeation experiments have also been carried out for the characterization of smaller asymmetric membranes, with an inner diameter of 7 mm, by means of dusty gas model demonstrating that model is capable to describe the mass transport in porous media.

A non-dimensional analysis of isobaric diffusion, based on simulations, has been done to see the influences of axial dispersion, volumetric flow rate and temperature on the isobaric diffusion process in terms of mole fraction and gas flow rates. The consideration of axial dispersion in diffusion process is notable, especially in the entrance of the reactor, and it may be substantial for reactions, where controlled dosing of educts is aimed at.

While identification and validation of membrane transport parameters are one important aspect, the work also shows that membrane reactor configurations can be reliably modelled in the limiting case without chemical reaction. Even in this case, thermal effects and the interrelation between heat and mass transfer should be accounted for. Treatment of catalytically active membranes and packed bed membrane reactors will be the next steps of research.

8 Nomenclature

a	m	Inter-atomic distance
B_0	m^2	Permeability constant in dusty gas model
Bo	-	Bodenstein number
C	-	Component in ProMoT
C	$m^3 s kg^{-1}$	Permeability constant in Darcy equation
c_v	$J m^{-3} K$	Volumetric heat capacity
c	$J kg^{-1} K$	Heat capacity
\tilde{c}	$J mol^{-1} K$	Molar heat capacity
d	m	Diameter
D_{ax}	$m^2 s^{-1}$	Axial dispersion coefficient
D	$m^2 s^{-1}$	Diffusion coefficient
F_0	-	Ratio of effective to molecular diffusion coefficient
F	m^2	Cross-sectional area
g	-	Jacobian
J	-	Flux vector in ProMoT
K_0	m	Knudsen coefficient in dusty gas model
L	m	Length
\dot{M}	kg/s	Mass flow rate
\tilde{M}	$kg mol^{-1}$	Molar mass
n	$mol m^{-3}$	Molar density
n	-	Number of moles
\dot{n}	$mol m^{-2} s^{-1}$	Molar flux
\dot{N}	$mol s^{-1}$	Molar flow rate
Nu	-	Nusselt number
NTU	-	Number of transfer units
P	Pa	Pressure
Pr	-	Prandtl number
\dot{q}	$W m^{-2}$	Heat flux
\dot{Q}	W	Heat flow rate
r	-	Radial coordinate
\bar{r}	m	Mean membrane radius
\tilde{R}	$J mol^{-1} K^{-1}$	Universal gas constant
Re	-	Reynolds number
Sc	-	Schmidt number

Sh	-	Sherwood number
t	s	Time
T	°C, K	Temperature
U	m	Perimeter
u	m s ⁻¹	Flow velocity
\dot{V}	m ³ s ⁻¹	Volumetric flow rate
V	m ³	Volume
X	-	Potential vector in ProMoT
\tilde{x}	-	Mole fraction
z	-	Axial coordinate

Greek symbols

α	K ⁻¹	Thermal expansion coefficient
α	W m ⁻² K ⁻¹	Heat transfer coefficient
β	m s ⁻¹	Mass transfer coefficient
γ	-	Gruneisen parameter
ε	-	Porosity
ζ	-	Dimensionless length
η	Pa s ⁻¹	Viscosity
κ	m ² s ⁻¹	Thermal diffusivity
λ	W m ⁻¹ K ⁻¹	Thermal conductivity
Λ_{ax}	W m ⁻¹ K ⁻¹	Axial thermal dispersion coefficient
Λ	m	Mean free path
ν	m ² s ⁻¹	Kinematic viscosity
ρ	kg m ⁻³	Density
σ	m	Collision diameter
ϕ	-	Viscosity parameter
Ω	-	Collision integral
ω	-	Probability factor

Indices

av	Average
D	Diffusivity
e	Effective
g	Gas
h	hydraulic
in	Inlet
i	Inner, tube side
j,k,l	Species in the mixture
K	Knudsen
m	Membrane
mol	Molecular
o	Outer, annulus side
out	Outlet
p	Pore
P	At constant pressure
Shell	Shell (reactor cage)
tot	total
vis	viscous
*	Dimensionless quantity

9 References

- [1] D.W. Agar, Multifunctional reactors: Old preconceptions and new dimensions, *Chem. Eng. Sci.* 54 (10) (1999) 1299-1305.
- [2] G. Saracco, V. Specchia, Present experience and future opportunities, *Cat. Rev. Sc.& Eng.* 36 (2) (1994) 305-384.
- [3] A.S. Michaels, Separation technique for the Chemical Processes Industry, *Chem. Eng. Progress* 64 (1968) 31-43.
- [4] G. Kolios, J. Frauhammer, G. Eigenberger, Efficient reactor concepts for coupling of endothermic and exothermic reaction, *Chem. Eng. Sci.* 57 (2002) 1505-1510.
- [5] J.W. Veldsink, R.M.J. van Damme, G.F. Versteeg, W.P.M. van Swaaij, A catalytically active membrane reactor for fast, heterogeneous catalysed reactions, *Chem. Eng. Sci.* 47(9-11) (1992) 2939-3944.
- [6] G. Saracco, J.W. Veldsink, G.F. Versteeg, W.P.M. van Swaaij, Catalytic combustion of propane in a membrane reactor with separate feed of reactants II. Operation in presence of a transmembrane pressure gradients, *Chem. Eng. Sci.* 50 (1995) 2833-2841.
- [7] J. P. Collins, R.W. Schwartz, R. Sehgal, T.L. Ward, C.J. Brinker, G.P Hagen, C.A. Udovich, Catalytic dehydrogenation of propane in hydrogen permselective membrane reactors, *Ind. & Eng. Chem. Research* 35 (1996) 4398-4405.
- [8] H. Weyten, K. Keizer, A. Kinoo, J. Luyten, R. Leysen, Dehydrogenation of propane using a packed-bed catalytic membrane reactor, *AIChE Journal* 43 (7) (1997) 1819-1827.
- [9] P. Quicker, V. Höllein, R. Dittmeyer, Catalytic dehydrogenation of hydrocarbons in palladium composite membrane reactors, *Catal. Today* 56 (1-3) (2000) 21-34.
- [10] H. Weyten, J. Luyten, K. Keizer, L. Willems, R. Leysen, Membrane performance: the key issues for dehydrogenation reactions in a catalytic membrane reactor, *Catal. Today* 56 (1-3) (2000) 3-11.
- [11] H.P. Hsieh, *Inorganic membranes for separation and reaction*, Vol. 3, Elsevier, Amsterdam, 1996.

- [12] A. G. Dixon, Innovations in catalytic membrane reactors, Specialist periodical Reports: Catalysis 14 (1999) 40-92.
- [13] Y. Zeng, Y.S. Lin, S.L. Swartz, Perovskite-type ceramic membrane: synthesis, oxygen permeation and membrane reactor performance for oxidative coupling of methane, J. of Mem. Sci. 150 (1) (1998) 87-98.
- [14] Y. Lu, A.G. Dixon, W.R. Moser, Y.H. Ma, U. Balachandaran, Oxidative coupling of methane using oxygen-permeable dense membrane reactors, Catal. Today 56 (1-3) (2000) 297-305.
- [15] C.Y. Tasi, Y.H. Ma, W.R. Moser, A.G. Dixon, Modeling and simulation of a non-isothermal catalytic membrane reactor, Chem. Eng. Comm. 134 (1995) 107.
- [16] J. Sanchez, T.T. Tsotsis, Catalytic membranes and membrane reactors, Wiley VCH, New York, Weinheim, 2002.
- [17] A.G. Dixon, Recent research in catalytic inorganic membrane reactors, Intern. J. of Chem. Reactor Eng. 1 (2003) R6.
- [18] A. M. Champagnie, T. T. Tsotsis, R. G. Minet, A. I. Webster, A high temperature catalytic membrane reactor for ethane dehydrogenation, Chem. Eng. Sci. 45 (8) (1990) 2423-2429.
- [19] M.P. Harold, C. Lee, A.J. Burggraaf, K. Keizer, V.T. Zaspalis, R.S.A. De Lange, Catalysis with inorganic membranes, MRS bulletin 9 (4) (1994) 44
- [20] J. Coronas, J. Santamaria, Catalytic reactors based on porous membranes, Catal. Today 51 (1999) 377-389.
- [21] R. Mallada, M. Menendez, J. Santamaria, Synthesis of maleic anhydride in a membrane reactor using a butane-rich feed, in: S. Nakao (Ed.), Proceedings of the ICIM5 (Inorganic Membranes), Nagoya, Japan, 1998, pp. 612–615.
- [22] J. Yung, H. Halm, M. Alibrando, E.E. Wolf, Methane partial oxidation in a fast flow non-selective membrane reactor, in: P.E. Hojlund, H. Nielsen, A.S. Topsoe (Eds.), Proceedings of the 3rd International Conference on Catalysis in Membrane Reactors, Copenhagen, Denmark, September 1998, p. 4.
- [23] J. Coronas, M. Menendez, J. Santamaria, Development of ceramic membrane reactors with a non-uniform permeation pattern: application to methane oxidative coupling, Chem. Eng. Sci. 49 (24A) (1994) 4749–4757.

- [24] Y.K. Kao, L. Luo, Y.S. Lin, A comparative study on oxidative coupling of methane in fixed-bed and membrane reactors, *Ind. Eng. Chem. Res.* 36 (1997) 3583–3593.
- [25] A.M. Ramachadran, Y. Lu, Y.H. Ma, W.R. Moser, A.G. Dixon, Oxidative coupling of methane in porous Vycor membrane reactors, *J. of Mem. Sci.* 116 (1996) 253-264.
- [26] V. Papavassiliou, C. Lee, J. Nestlerode, M.P. Harold, Pneumatically controlled transport in inorganic membranes, *Ind. Eng. Chem. Res.* 36 (1997) 4954-4964.
- [27] A. Pantazidis, Oxidative dehydrogenation of propane on catalytic membrane reactors, *Catal. Today* 25 (1995) 403–408.
- [28] J. Coronas, J. Santamaria, Catalytic reactors based on porous membranes, Methane oxidative coupling using porous ceramic membrane reactors, Part II Reactor studies, *Chem. Eng. Sci.* 49 (1994a) 2015-2025.
- [29] Z. Shao, H. Dong, G. Xiong, Y. Cong, W. Yang, Performance of a mixed-conducting ceramic membrane reactor with high oxygen permeability for methane conversion, *J. of Mem. Sci.* 183 (2) (2001) 181-192.
- [30] M.P. Harold, V.T. Zaspalis, K. Keizer, A.J. Burggraaf, Intermediate product yield enhancement with catalytic inorganic membrane-I. Analytical model for the case of isothermal and differential operation, *Chem. Eng. Sci.* 48 (1993) 2705-2725.
- [31] M. Nakajima, N. Jimbo, K. Nishizawa, H. Nabetani, A. Watanabe, Conversion of sucrose by immobilized invertase in an asymmetric membrane reactor, *Process Biochemistry* 23 (32) 1(988) 4-5.
- [32] J. Sanchez, T.T. Tsotsis, Current developments and future research in catalytic membrane reactors, in: A.J. Burggraaf, L. Cot (Eds.), *Fundamentals of Inorganic Membrane Science and Technology*, Mem. Sci. and Tech. Series, Vol. 4, Elsevier, Amsterdam, 1996 (Chapter 11).
- [33] H.J. Sloot, G.F. Versteeg, W.P.M. van Swaaij, A nonpermselective membrane reactor for chemical processes normally requiring stoichiometric feed rate of reactants, *Chem. Eng. Sci.* 45 (1990) 2415-2421.
- [34] J.W. Veldsink, G.F. Versteeg, W.P.M. van Swaaij, A catalytically active membrane reactor for fast, highly exothermic, heterogenous gas reactions: a pilot plant study, *Ind. Eng. Chem. Res.* 34 (1995) 763-772.
- [35] A. Julbe, D. Farrusseng, C. Guizard, Porous ceramic membranes for catalytic reactors-overview and new ideas, *J. of Mem. Sci.* 181 (2001) 3-20
- [36] J. Zaman, A. Chakma, Inorganic membrane reactors, *J. of Mem. Sci.* 92 (1994) 1-28.

- [37] J.A. Dalmon, Catalytic membrane reactors, in: G. Ertl, H. Knözinger, J. Weitkamp (Eds.), *Handbook of Heterogeneous Catalysis*, VCH Publishers, Weinheim, 1997 (Chapter 9.3).
- [38] S. Uemiya, N. Sato, H. Ando, E. Kukuchi, The water gas shift reaction assisted by a palladium membrane reactor, *Ind. Eng. Chem. Res.* 30 (1991) 585-589.
- [39] N. Itoh, A membrane reactor using Palladium, *AIChE Journal* 33 (1987) 1576.
- [40] S. Agarwalla, C.R.F. Lund, Use of a membrane reactor to improve selectivity to intermediate products in consecutive catalytic reactions, *J. of Mem. Sci.* 70 (2) (1992) 129-141.
- [41] L.A. Bernstein, C.R.F. Lund, Membrane reactors for catalytic series and series-parallel reactions, *J. of Mem. Sci.* 77 (2) (1993) 155-164.
- [42] C.M. Reo, L.A. Bernstein, C.R.F. Lund, Defining conditions where the use of porous membrane reactors can be justified solely on the basis of improved yield, *Chem. Eng. Sci.* 52 (18) (1997) 3075-3083.
- [43] A.G. Dixon, Analysis of intermediate product yield in distributed-feed nonisothermal tubular membrane reactors, *Catal. Today* 67 (1-3) (2001) 189-203.
- [44] V.T. Zaspalis, W. Van Praag, K. Keizer, J.G. Van Ommen, J.R.H. Ross, A.J. Burggraaf, Reaction of methanol over catalytically active alumina membranes, *Appl. Catal.* 74 (1991) 205.
- [45] K.K. Chan, A.M. Brownstein, Ceramic membranes growth prospects and opportunities, *Ceram. Bull.* 70 (1991) 703-707.
- [46] R. Soria, Overview on industrial membranes, *Catal. Today* 25 (1995) 285-290.
- [47] N.J. Armor, Application of catalytic inorganic membrane reactors to refinery products, *J. Mem. Sci.* 147 (1998) 217-233.
- [48] V.M. Gryaznov, Membrane catalysis, *Catal. Today* 51 (1999) 391-395.
- [49] J. Coronas, J. Santamaria, Catalytic reactors based on porous ceramic membranes, *Catal. Today* 51 (1999) 377-389.
- [50] G. Saracco, H.W.J.P. Neomagus, G.F. Versteeg, W.P.M. Van Swaaij, High temperature membrane reactors: potential and problems, *Chem. Eng. Sci.* 54 (1999) 1997-2017.
- [51] H.P. Hsieh, *Inorganic membrane separation technology*, Blackie, London, 1996.

- [52] J. Romero, C. Gijiu, J. Sanchez, G.M. Rios, A unified approach of gas, liquid and supercritical solvent transport through microporous membranes, *Chem. Eng. Sci.* 59 (7) (2004) 1569-1576.
- [53] P.M. Biesheuvel, H. Verweij, Design of ceramic membrane supports: permeability, tensile strength and stress, *J. of Mem. Sci.* 156 (1) (1999) 141-152.
- [54] J.C.S. Wu, H. Sabol, G.W. Smith, D.L. Flowers, P.K.T. Liu, Characterisation of hydrogen-permselective microporous ceramic membranes, *J. of Mem. Sci.* 96 (1994) 275-287.
- [55] R. Ramos, M.J. Alfonso, M. Menendez, J. Santamaria, Oxidative dehydrogenation of propane using membrane reactors, in: S. Nakao (Ed.), *Proceedings of the ICIM5 (Inorganic Membranes)*, Nagoya, Japan, 1998, pp. 358–361.
- [56] S. Irusta, M.P. Pina, M. Menendez, J. Santamaria, Development and application of perovskite-based catalytic membrane reactor, *Catal. Lett.* 54 (1998) 69-78.
- [57] C. Guizard, Sol-gel chemistry and its application to porous membrane processing, in: A.J. Burggraaf, L. Cot (Eds.), *Fundamentals of Inorganic Membrane Science and Technology*, Membrane Science and Technology Series, Vol. 4, Elsevier, Amsterdam, 1996 (Chapter 6).
- [58] A.J. Burggraaf, Fundamentals of membrane top-layer synthesis and processing, in: A.J. Burggraaf, L. Cot (Eds.), *Fundamentals of Inorganic Membrane Science and Technology*, Membrane Science and Technology Series, Vol. 4, Elsevier, Amsterdam, 1996 (Chapter 8).
- [59] A. Julbe, C. Guizard, A. Larbot, L. Cot, A. Giroir-Fendler, The sol-gel approach to prepare candidate microporous inorganic membranes for membrane reactors, *J. of Mem. Sci.* 77 (2/3) (1993) 137-153.
- [60] J. Szegner, A. King Lun Yeung, A. Varma, Effect of catalyst distribution in a membrane reactor: experiments and model, *AIChE Journal* 43 (8) (1997) 2059–2072.
- [61] K.L. Yeung, J.M. Sebastian, A. Varma, Mesoporous alumina membranes: synthesis, characterisation, thermal stability and non-uniform distribution of catalyst, *J. Mem. Sci.* 131 (1997) 9–28.
- [62] T.V. Gestel, C. Vandecasteele, A. Buekenhoudt, C. Dotremont, J. Luyten, R. Leysen, Alumina and titania multilayer membranes for nanofiltration: preparation, characterization and chemical stability, *J. of Mem. Sci.* 207 (2002) 73–89.

- [63] R. Ramos, M. Menendez, J. Santamaria, Oxidative dehydrogenation of propane in an inert membrane reactor, *Catal. Today* 56 (1-3) (2000) 239–245.
- [64] D. Lafarga, J. Santamaria, M. Menendez, Methane oxidative coupling using porous ceramic membrane reactors-I. reactor development, *Chem. Eng. Sci.* 49 (12) (1994) 2005-2013.
- [65] S. Irusta, M.P. Pina, M. Menendez, J. Santamaria, Development and application of perovskite-based catalytic membrane reactors, *Catal. Lett.* 54 (1998) 69-78.
- [66] A.J. Burggraaf, K. Keizer, *Inorganic Membranes: Synthesis, Characteristics and Applications*. Chapman & Hall, New York, 1991 (pp. 11–63).
- [67] S. Vercauteren, K. Keyzer, E.F Vansant, J. Luyten, R. Leysen, Porous ceramic membranes: preparation, transport properties and applications, *J. of Por. Mat.* 5, (1998), 241–258.
- [68] Y. Hao, J. Li, X. Yang, L. Lu, Preparation of ZrO₂-Al₂O₃ composite membranes by sol-gel process and their characterization, *Mat. Sci. Eng. A* 367 (2004) 243-247.
- [69] T. Tsuru, Inorganic porous membranes for liquid phase separation, *Separation Purification Methods* (30) (2001), 191–220.
- [70] L. Cot, A. Ayrat, J. Durand, C. Guizard, N. Hovnanian, A. Julbe, Inorganic membranes and solid state sciences, *Solid State Science* 2 (2000), 313–334.
- [71] C. Guizard, *Fundamentals of Inorganic Membrane Science and Technology*, ed. A. J. Burggraaf and L. Cot., Elsevier B.V., The Netherlands, 1996, 227–258.
- [72] T.V.Gestel, C. Vandecasteele, A. Buekenhoudt, C. Dotremont, J. Luyten, R. Leysen, Alumina and titania multilayer membranes for nanofiltration: preparation, characterization and chemical stability, *J. of Mem. Sci.* 207 (2002), 73–89.
- [73] N. Corbitt, *Inorganic Membranes: Markets, Technologies, Players, Business Communications Company, INC*, 1997.
- [74] J.M. Benito, A. Conesa, F. Rubio, M.A. Rodríguez, Preparation and characterization of tubular ceramic membranes for treatment of oil emulsions, *J. Eur. Ceram. Soc.* (2004) 1-9.
- [75] B. E. Yoldas, Alumina sol preparation from alcoxides, *Ceram. Bull.* 54 (1975) 289–290.
- [76] X.R. Huang, G.L. Meng, Z.T. Huang, J.M. Geng, Preparation of unsupported alumina membrane by sol-gel techniques, *J. of Mem. Sci.* 133 (1997) 145–150.
- [77] A.F.M. Leenaars, A. J. Burggraaf, The preparation and characterization of alumina membranes with ultrafine pores, *J. Coll. Interf. Sci.* 105 (1985) 27–40.

- [78] E. S. Kikkinides, K. A. Stoitsas, V. T. Zaspalis, Correlation of structural and permeation properties in sol–gel-made nanoporous membranes, *J. Coll. Interf. Sci.* 259 (2) (2003) 322–330.
- [79] C. Agrafiotis, A. Tsetsekou, Deposition of meso-porous α -alumina coatings on ceramic honeycomb by sol–gel methods, *J. Eur. Ceram. Soc.* 22 (2002) 423–434.
- [80] A.F.M. Leenaars, K. Keizer, A.J. Burggraaf, The preparation and characterization of alumina membranes with ultra-fine pores, *J. Mater. Sci.* 19 (2003) 1077–1088.
- [81] A.G. Dixon, W.R. Moser, Y.H. Ma, Waste reduction and recovery using O₂-permeable membrane reactors, *Ind. & Eng. Chem. Res.* 33 (12) (1994) 3015-3024.
- [82] C.-Y. Tsai, Y.H. Ma, W.R. Moser, A.G. Dixon, Modeling and simulation of a nonisothermal catalytic membrane reactor, *Chem. Eng. Commun.* 134 (1995) 107-132.
- [83] W. Jin, X. Gu, S. Li, P. Huang, N. Xu, J. Shi, Experimental and simulation study on a catalyst packed tubular dense membrane reactor for partial oxidation of methane to syngas, *Chem. Eng. Sci.* 55 (14) (2000) 2617-2625.
- [84] X. Tan, K. Li, Investigation of novel membrane reactors for removal of dissolved oxygen from water, *Chem. Eng. Sci.* 55 (7) (2000) 1213-1224.
- [85] M. Pedernera, R. Mallada, M. Menendez, J. Santamaria, Simulation of an inert membrane reactor for the synthesis of maleic anhydride, *AIChE Journal* 46 (12) (2000) 2489-2498.
- [86] M.A. Al-Juaied, D. Lafarga, A. Varma, Ethylene epoxidation in a catalytic packed-bed membrane reactor: experiments and model, *Chem. Eng. Sci.* 56 (2) (2001) 395-402.
- [87] C. Fukuhara, A. Igarashi, Two-dimensional simulation of a membrane reactor for dehydrogenation of ethylbenzene, considering heat and mass transfer, *J. of Chem. Eng. of Japan* 36 (5) (2003) 530-539.
- [88] G. Bramhall, Mathematical model for lumber drying, *Wood Science* 12 (1) (2002) 14-21.
- [89] H.P. Hsieh, Inorganic membrane reactors, *Catal. Rev.- Sci. and Eng.* 33 (1991) 1-70.
- [90] J. Sanchez, T.T. Tsotsis, *Fundamental of inorganic membrane science and technology*, Elsevier, Amsterdam, 1996, pp. 529-568.
- [91] D.L. Meixner, P.N. Dyer, Characterization of the transport properties of microporous inorganic membranes, *J. of Mem. Sci.* 140 (1) (1998) 81-95.

- [92] U. Beuscher, C.H. Gooding, The permeation of binary gas mixtures through support structures of composite membranes, *J. of Mem. Sci.* 150 (1) (1998) 57-73.
- [93] U. Beuscher, C.H. Gooding, The influence of the porous support layer of composite membranes on the separation of binary gas mixtures, *J. of Mem. Sci.* 152 (1) (1999) 99-116.
- [94] A. Tuchlenski, O. Schramm, A. Seidel-Morgenstern, Steady state and dynamic mass transfer of gases in porous materials, *Collection of Czechoslovak Chem. Commun.* 62 (7) (1997) 1043-1056.
- [95] A. Tuchlenski, P. Uchytil, A. Seidel-Morgenstern, An experimental study of combined gas phase and surface diffusion in porous glass, *J. of Mem. Sci.* 140 (2) (1998) 165-184.
- [96] P. Capek, A. Seidel-Morgenstern, Multicomponent mass transport in porous solids and estimation of transport parameters, *Applied Catalysis A: General* 211 (2) (2001) 227-237.
- [97] P. Uchytil, O. Schramm, A. Seidel-Morgenstern, Influence of the transport direction on gas permeation in two-layer ceramic membranes, *J. of Mem. Sci.* 170 (2) (2000) 215-224.
- [98] S. Thomas, R. Schäfer, J. Caro, A. Seidel-Morgenstern, Investigation of mass transfer through inorganic membranes with several layers, *Catal. Today* 67 (1-3) (2001) 205-216.
- [99] S. Thomas, *Kontrollierte Eduktzufuhr in Membranreaktoren zur Optimierung der Ausbeute gewünschter Produkte in Parallel- und Folgereaktionen*, PhD thesis, Otto-von-Guericke-Universität Magdeburg, Germany, 2003.
- [100] E.A. Mason & A.P. Malinauskas, *Gas Transport in Porous Media: The Dusty Gas Model*, Elsevier, Amsterdam, 1983.
- [101] P. Schneider, D. Gelbin, Direct transport parameters measurement versus their estimation from mercury penetration in porous solids, *Chem. Eng. Sci.* 40 (1985) 1093-1099.
- [102] O. Solcova, P. Schneider, Multicomponent counter-current gas diffusion: Determination of transport parameters, *Appl. Catal. A: General* 244 (1) (2003) 1-9.
- [103] R. Jackson, *Transport in Porous Catalysts*. Elsevier, Amsterdam, 1977.

- [104] F. Keil, Diffusion und chemische Reaktionen in der Gas/Feststoffkatalyse, Springer Berlin Heidelberg, 1999.
- [105] O. Solcova, H Snajdaufova, V. Hejtmanek, P. Schneider, Textural properties of porous Solids in relation to gas transport, Chem. Papers 53 (6) (1999) 396-402.
- [106] C.V. Heer, Statistical Mechanics, Kinetic Theory, and Stochastic Processes, Academic Press, New York, 1972.
- [107] G. Standart, The second law of thermodynamics for heterogeneous flow systems-I basic relations and the Curie theorem, Chem. Eng. Sci. 22 (11) (1967) 1417-1438.
- [108] J.W. Veldsink, R.M.J. van Damme, G.F. Versteeg, W.P.M. van Swaaij, The use of the dusty-gas model for the description of mass transport with chemical reaction in porous media, Chem. Eng. J. 57 (1995) 115.
- [109] P.V. Danckwerts, Continuous flow systems; distribution of residence times, Chem. Eng. Sci. 2 (1953) 2-3.
- [110] N. Siyakatshana, V. Kudrna, V. Machoň, Incorporating Danckwerts' boundary conditions into the solution of the stochastic differential equation, Chem. Eng. Sci. 60 (2005) 1987-1994.
- [111] R.C. Reid, J.M. Prausnitz, B.E. Poling, The properties of gases and liquids, McGraw Hill, New York, 1987.
- [112] M. Bengisu, Engineering Ceramics, Springer, Berlin, 2001.
- [113] J. S. Dugdale, D.K.C. McDonald, Lattice thermal conductivity, Physical Review 98 (1955) 1751-1752.
- [114] A. W. Lawson, On the high temperature heat conductivity of insulators, J. of Physics and Chemistry of Solids (1-2) (1957) 155-156.
- [115] B. M. Zawilski, R. T. Littleton IV, T.M. Tritt, Investigation of the thermal conductivity of the mixed pentatellurides $Hf_{1-x}Zr_xTe_5$, Appl. Phys. Lett. 77 (15) (2000) 2319-2321.
- [116] H. Martin, Section Gd in VDI-Waermeatlas, 6th ed., VDI Verlag, Düsseldorf, 1991
- [117] C. Fernández-Pineda, M.A. Izquierdo-Gil, M.C. García Payo, Gas permeation and direct contact membrane distillation experiments and their analysis using different models, J. of Mem. Sci. 198 (1) (2002) 33-49.
- [118] E.U. Schlünder, E. Tsotsas, Wärmeübertragung in Festbetten, durchmischten Schüttungen und Wirbelschichten, Thieme Verlag, Stuttgart, 1988.

- [119] E. Tsotsas, Section Deb in VDI-Waermeatlas, 9th ed., Springer Verlag, Berlin, 2002.
- [120] J.M.S. Henis, M.K. Tripodi, Composite membranes for gas separation: The resistance model approach, *J. of Mem. Sci.* 8 (1981) 233-246.
- [121] A. Fouada, Y. Chen, J. Bai, T. Matsuura, Wheatstone bridge model for the laminated polydimethylsiloxane/polyethersulfone membrane for gas separation, *J. of Mem. Sci.* 64 (1991) 263-271.
- [122] M. Mulder, *Basic Principles of Membrane Technology*, Kluwer Academic Press, Boston, 1991.
- [123] P. Drechsel, J.L. Hoard, F.A. Long, Diffusion of acetone into cellulose nitrate films and study of the accompanying orientation, *J. Polym. Sci.* 10 (1953) 241-252.
- [124] A.E. Polotsky, G.A. Polotskaya, Study on the top layer structure of the composite membranes, *J. of Mem. Sci.* 140 (1998) 97-102.
- [125] E. E. Iojoiu, J. C. Walmsley, H. Raeder, S. Miachon, J.-A. Dalmon, Catalytic membrane structure influence on the pressure effects in an interfacial contactor catalytic membrane reactor applied to wet air oxidation, *Catal. Today* 104 (2-4) (2005) 329-335.
- [126] F. Lipnizki, R.W. Field, Mass transfer performance for hollow fibre modules with shell side axial feed flow: using an engineering approach to develop a framework, *J. of Mem. Sci.* 193 (2) (2001) 195-208.
- [127] M. Mangold, S. Motz, E.D. Gilles, A network theory for the structured modelling of chemical processes, *Chem. Eng. Sci.* 57 (19) (2002) 4099-4116.
- [128] E.D. Gilles, Network Theory for Chemical Processes, *Chem. Eng. Tech.* 21 (2) (1998) 121-132.
- [129] M. Mangold, G. Ginkel, E.D. Gilles, A model library for membrane reactors implemented in the process modelling tool ProMoT, *Comp. and Chem. Eng.* 28 (2004) 319-332.
- [130] O. Schramm, Zur Durchführung reversibler Reaktionen in Membranreaktoren, PhD thesis, Otto-von-Guericke-Universität Magdeburg, Germany, 2000.
- [131] A. Tuchlenski, Charakterisierung poröser Membranen und ihre Anwendung in Membranreaktoren, PhD thesis, Otto-von-Guericke-Universität Magdeburg, Germany, 1998.
- [132] D.J. Gunn, An analysis of convective dispersion and reaction in the fixed-bed reactor, *Int. J. of Heat and Mass Transfer* 47 (2004) 2861-2875.

- [133] E. Tsotsas, E.U. Schlünder, On axial dispersion in fixed beds with fluid flow, *Chem. Eng. Process.* 24 (1988) 15-31.
- [134] J. W. Ponton, P.J. Gawthrop, Systematic construction of dynamic models for phase equilibrium processes, *Comp. and Chem. Eng.* 15 (1991) 803-808.
- [135] J.D. Perkins, R.W.H. Sargent, R. Vaquez-Roman, J.H. Cho, Computer generation of process models, *Com. and Chem. Eng.* 20 (1996) 635-639.
- [136] H. A. Preisig, Computer-aided modelling : Two paradigms on control, *Comp. and Chem. Eng. (suppl)* (1996) 981-986.
- [137] S.E. Mattson, G. Söderlind, Index reduction in differential-algebraic equations using dummy derivatives, *SIAM J. of Sci. and Comp.* 14 (1993) 677-692.
- [138] F.P. Incropera, D. P. De Witt, *Introduction to heat transfer*, 2nd ed., John Willey and Sons, New York, 1995.
- [139] B. Gebhart, *Heat conduction and mass diffusion*, McGraw-Hill Inc., New York, 1994.
- [140] L. S. Verdelli, H. C. Miller, J. F. Gall, Some Physical Properties of Sulfur Hexafluoride; *Ind. Eng. Chem.* 43 (1951) 1126-1135.

Appendix A

A.1 Structured process modelling in ProMoT

Multifunctional reactor concepts allow for integration of process elements and interconnect these through material, energy and momentum flow. This requires an efficient modelling of the process unit. Mathematical models are considered as a useful tool for the development of processes and control systems. Though many modelling tools for the process analysis of complex chemical systems are available, the formulation of an efficient model is still a challenging work. Usually, flow sheets are created to develop models of chemical processes, where the model of each process unit or apparatus is the smallest modelling unit. Consequently, the modelling units may be rather complicated and tailored to one specific application. Any modification of the model of an existing apparatus or even modelling a new process unit leads to re-implementation of the complete model. Therefore, an efficient model development needs stronger modularisation of process models and a structuring of the models on a level below the process unit. In the past, several authors proposed general concepts for the structuring of process models [134-136]. Based on general structuring concepts, modelling tools have been developed which provided a powerful framework for the development of model libraries based on simple, flexible, and reusable modelling units. This enables the actual formulation and implementation of a model library for chemical process models. The combination of a modelling tool and a comprehensive model library simplifies and accelerates the process of model development considerably. The model library, which needs a good theoretical concept, should comprise all elements essential to build up a process model and at the same time ensure compatibility between the modelling entities in the library. The Network Theory of Chemical Processes proposed by [128], offers such a modelling concept.

A.2 Network Theory

Process unit models are considered as the smallest entity ordered in a plant model. The model formulations, based on a limited number of physical assumptions and phenomenological descriptions, consist of balance equations derived from the laws of energy, mass, and momentum conservation. The same formulations for diffusion, convection, heat or mass transfer are repeatedly used in many apparatus models. The vast range of different process unit models mainly originates from the many possibilities to combine the existing modelling approaches. Therefore, the aim to collect modelling knowledge in a library

becomes much more attainable if pursued below the level of process units that can be considered as an aggregation of interacting thermodynamic phases. The modularity principle of structured modelling is based on two main ideas:

- 1) Two types of elementary units suffice to give a structural description of all kind of chemical processes. These two types are called *components* and *coupling elements*. Components possess a hold-up for physical quantities like energy, mass and momentum.
- 2) Components and coupling elements can be defined at different hierarchical modelling levels. For example, a component may be a single thermodynamic phase or it may be a process unit consisting of several interacting phases. These two ideas are discussed subsequently [127].

Components are able to store energy, mass, or momentum (accumulation terms). They can be interpreted as representatives of multidimensional potentials. In the following, they will be symbolised by a circle framed by a square (see Fig. A.1). Coupling elements describe the interactions, i.e. the fluxes, between components. They can be considered as representatives of multidimensional fluxes and will be symbolised by a rectangle without a circle.

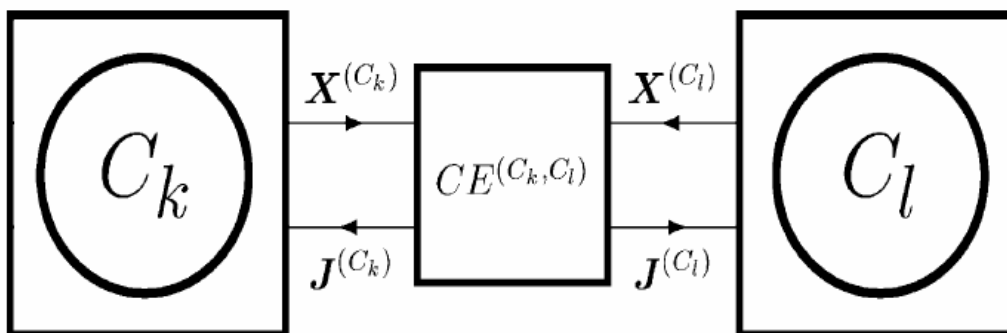


Fig. A.1: Interconnection of two components

When two components C_k and C_l interact via a coupling element $CE^{(C_k, C_l)}$, the direction of flow of information is defined according to Fig. A.1. The potential vector $X^{(C_k)}$ characterises the inner state of component C_k and is an output of this component. The flux vector $J^{(C_k)}$ represents an input quantity of component C_k . Component C_k establishes a relation between its input quantities $J^{(C_k)}$ and its output quantities $X^{(C_k)}$. From the viewpoint of the coupling element $CE^{(C_k, C_l)}$, $X^{(C_k)}$ and $X^{(C_l)}$ are input quantities. The fluxes $J^{(C_k)}$ and $J^{(C_l)}$ are outputs of the coupling element $CE^{(C_k, C_l)}$. By choosing this direction of signal transfer it is assumed that the coupling element supplies relationships for $J^{(C_k)}$ and $J^{(C_l)}$, when $X^{(C_k)}$ and $X^{(C_l)}$ are given. This assumption complies with the physical concept according to which fluxes are driven by

potential differences. If a process model strictly obeys the proposed direction of signal transfer, a differential index of 1 is guaranteed for the resulting system of model equations, as the following consideration will show. For a lumped system, the potential vector X of all components is given by differential equations

$$\dot{X} = \sum_{i=1}^{NJ} J_i \quad (\text{A.1})$$

where NJ is the number of flux vectors in the system. Each flux vector J_i is defined by algebraic equations in the coupling element

$$0 = g_i(J_i, X). \quad (\text{A.2})$$

Because the Jacobean $\partial g_i / \partial J$ is non-singular by definition, a single derivation in time of (A.2) suffices to turn the model equations into a system of ordinary differential equations. Simplifying modeling assumptions tend to violate the proposed direction of signal transfer. Typical examples are equilibrium assumptions or assumptions of vanishing mass or heat transfer resistances. If such an assumption is made, the coupled components will be no longer independent, but will lose a degree of freedom. This type of coupling is therefore termed rigid coupling and it may lead to a system of differential algebraic equations with a differential index larger than 1. The index problem can be overcome by methods for systematic index reduction [137] or by choosing alternative formulation for the components at equilibrium, e.g. by the formulation of pseudo-homogeneous balance equations [128, 134].

A.2.1 Process structuring levels

The model of a chemical plant can be structured on different levels. The top level is regarded as the level of process units. On this level, different process units like distillation columns, reactors, or heat exchangers are considered as the elementary components. They are connected by coupling elements such as pipes, valves, pumps etc. The elementary process units on this level are described by very complex models in many cases. In order to improve the structuring of the process models, it is helpful to decompose the models of process units into smaller units. A process unit is formed by a system of interacting components and coupling elements on a lower level (level of phases). A process unit usually contains several

phases, e.g. a liquid and a gaseous phase. Each phase is considered as an elementary component and the interaction between different phases takes place by heat transfer, mass transfer, or transfer of momentum on the level of phases. Phase boundaries like membranes, diffusive layers, e.g. are the corresponding coupling elements to describe this interaction. The macroscopic thermodynamic quantities like energy, mass, and momentum describe the state of a thermodynamic phase. This phase can be decomposed into smaller units by considering it as a system of interacting storages of mass, energy, and momentum, which are the components on the next lower level (the level of storages). The components on the level of storages interact by transport processes like reaction, diffusion, and convection. The coupling elements on the level of storages describe the fluxes of energy, mass, and momentum inside a thermodynamic phase. The state of a thermodynamic phase is determined by the interactions of all the molecules in this phase. The macroscopic view is sufficiently precise for nearly all technical applications. However, the inclusion of molecular level in a concept of structured modeling can be useful.

A.3 Process modeling tool (ProMoT) and simulating tool (DIVA)

ProMoT is a knowledge-based tool for equation based object oriented modelling of chemical and biochemical process. [102]. ProMoT facilitates structured and equation based rigorous modelling. Modules are structural modelling entities that represent control volumes or signal transformers and are called subsystems in the model. ProMoT provides basic modelling entities which enable the development of a new model by inheritance and aggregation. So a model of a system is an aggregated form of structural and behavioural entities as illustrated in Fig. A.2.

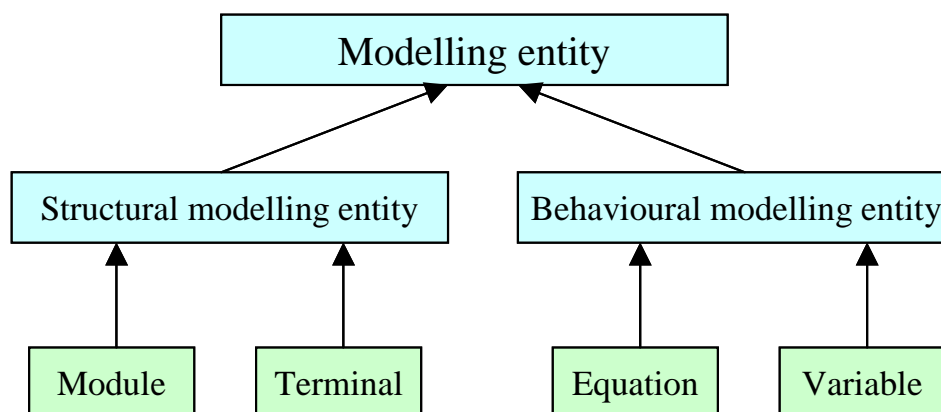


Fig. A.2: Hierarchy of the basic modelling entities in ProMoT; arrows show the inheritance relationship.

Structural modeling entities describe the part of the system under consideration. These are categorized as *modules* and *terminals*. *Modules* can be component or coupling elements. They are separable part of the system under consideration, e.g. storages (substances in phases), control volumes or surfaces (membrane, phase boundaries). The boundary of a system is described by its *terminals*. Modules can exchange mass, energy and momentum by the help of terminals. The behavioral modeling entity is the super class of all *variables* and *equations*. Behavioural modelling entities are scalar or indexed ordinary differential equations, state variables, inputs, outputs, parameters, intermediate variables and indices. Modules and terminals along with behavioural modelling entities form a mathematical model.

Models generated in ProMoT can be implemented using either modelling language (MDL) or a graphical user interface (GUI). A screen shot of the structured model editor is shown in Fig. A.3. Modelling in the visual editor works as drawing a flow sheet. Models are selected from the model library and can be linked with terminal in the work space. ProMoT allows to perform the modelling process interactively; useful libraries can be loaded from MDL source files into an internal knowledge-based modelling system. Users can explore libraries as well models in a graphical way using class browser and different graphical viewers. ProMoT generates a system of linear algebraic equations from the model information. This system of equations is transformed into simulation environment DIVA.

The modelling philosophy of DIVA considers that a chemical engineering plant usually consists of a number of unit operations (reactions, separations) performed in modular units (reactors, distillation columns), interconnected, e.g. by pipes, and controlled by process control instruments. So the idea behind DIVA is to develop models for different parts of the plant and then aggregate these to get a complete plant model.

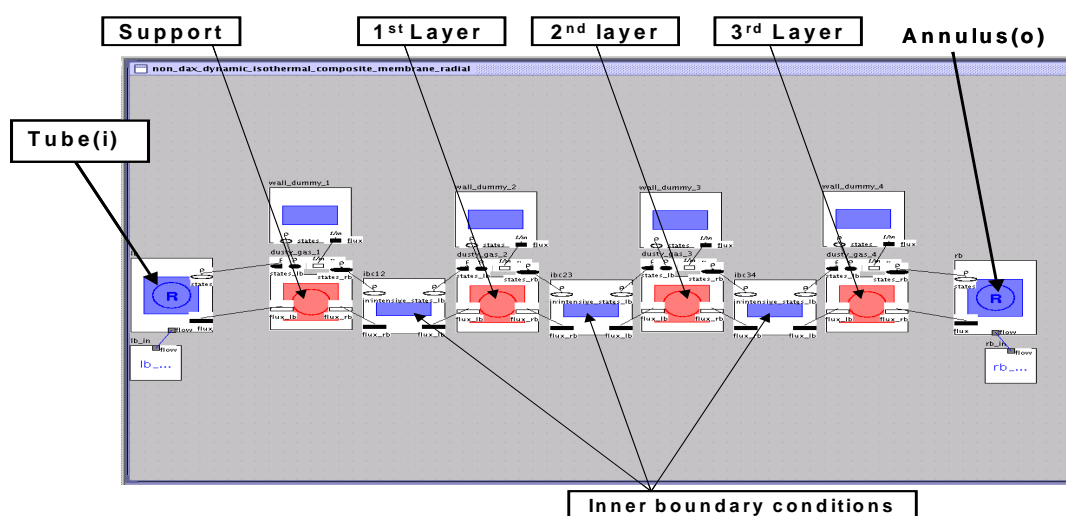


Fig. A.3: Screen shot of graphical user interface of ProMoT showing the asymmetric composite membrane.

Appendix B

Analytical solution of 1D heat transfer equation

For steady state condition and cylindrical coordinates, one dimensional heat conduction equation can be written as

$$\frac{1}{r} \frac{d}{dr} \left(\lambda_m r \frac{dT_m}{dr} \right) = 0 \quad r_i < r < r_o. \quad (1B)$$

The required boundary conditions on both sides of the membrane are given as:

$$\left. \frac{dT_m}{dr} \right|_{r=r_i} = -\frac{\dot{q}_i}{\lambda_m}, \quad (2B)$$

$$\left. \frac{dT_m}{dr} \right|_{r=r_o} = -\frac{\alpha_{g,o}}{\lambda_m} (T_{m,o} - T_{g,o}), \quad (3B)$$

Integrating eq. (1B) gives successively

$$\frac{d}{dr} \left(\lambda_m r \frac{dT_m}{dr} \right) = 0, \quad (4B)$$

$$\frac{dT_m}{dr} = \frac{1}{\lambda_m} \frac{C_1}{r}, \quad (5B)$$

and the membrane temperature as

$$T_m = \frac{1}{\lambda_m} C_1 \ln r + C_2. \quad (6B)$$

By combining the inner boundary condition (eq. (2B)) and eq. (5B)

$$-\frac{\dot{q}_i}{\lambda_m} = \frac{1}{\lambda_m} \frac{C_1}{r_i} \quad (7B)$$

and the constant

$$C_1 = -\dot{q}_i r_i \quad (8B)$$

is obtained. Equation (6B) then becomes

$$T_m = -\frac{\dot{q}_i r_i}{\lambda_m} \ln r + C_2, \quad (9B)$$

which can also be written for $r = r_o$ as

$$T_{m,o} = -\frac{\dot{q}_i r_i}{\lambda_m} \ln r_o + C_2. \quad (10B)$$

Subtracting eq. (10B) from eq. (9B) yields

$$T_m = T_{m,o} + \frac{\dot{q}_i r_i}{\lambda_m} \ln\left(\frac{r_o}{r}\right). \quad (11B)$$

Applying eq. (5B) at $r = r_o$ and combining with (eq. (3B)) and eq. (8B)

$$-\frac{\alpha_{g,o}}{\lambda_m} (T_{m,o} - T_{g,o}) = -\frac{\dot{q}_i r_i}{\lambda_m r_o} \quad (12B)$$

and

$$T_{m,o} = T_{g,o} + \frac{\dot{q}_i r_i}{\alpha_{g,o} r_o} \quad (13B)$$

is obtained. Equations (13B) and (11B) lead to

$$T_m = T_{g,o} + \frac{\dot{q}_i r_i}{\alpha_{g,o} r_o} + \frac{\dot{q}_i r_i}{\lambda_m} \ln\left(\frac{r_o}{r}\right), \quad (14B)$$

which can be re-written for the inner side of the membrane ($r = r_i$) as

$$T_{m,i} = T_{g,o} + \frac{\dot{q}_i r_i}{\alpha_{g,o} r_o} + \frac{\dot{q}_i r_i}{\lambda_m} \ln\left(\frac{r_o}{r_i}\right), \quad (15B)$$

The gas temperature can be calculated by the energy balance of the gas flowing in the annulus

$$\dot{M}_g c_g \frac{dT_g}{dz} = \alpha_{g,o} U_o (T_{m,o} - T_{g,o}). \quad (16B)$$

Insertion of the value of $T_{m,o}$ (eq. (13B)) in eq. (16B) and integration yields the temperature of gas in the annulus

$$T_{g,o} = T_{g,o,in} + \frac{U_o \dot{q}_i r_i z}{\dot{m}_g c_g r_o}. \quad (17B)$$

To calculate the thermal conductivity of the membrane eq. (9B) is written for the inner and outer side of the membrane respectively

$$T_{m,i} = -\frac{\dot{q}_i r_i}{\lambda_m} \ln r_i + C_2, \quad (18B)$$

$$T_{m,o} = -\frac{\dot{q}_i r_i}{\lambda_m} \ln r_o + C_2. \quad (19B)$$

Subtraction of eq. (19B) from eq. (18B) yields

$$T_{m,i} - T_{m,o} = \frac{\dot{q}_i r_i}{\lambda_m} \ln\left(\frac{r_o}{r_i}\right), \quad (20B)$$

which can be re-written for the heat flow rate instead of heat flux at the inner side of the membrane

$$T_{m,i} - T_{m,o} = \frac{\dot{Q} r_i}{2\pi r_i L \lambda_m} \ln\left(\frac{r_o}{r_i}\right).$$

(21B)

Equation (21B) can be transformed to

$$\lambda_m = \frac{\dot{Q}}{2\pi L (T_{m,i} - T_{m,o})} \ln\left(\frac{r_o}{r_i}\right), \quad (22B)$$

yielding the thermal conductivity of the membrane.

Appendix C

C.1 Single gas properties

C.1.1 Air

Molar mass

$$\frac{\tilde{M}}{\text{kg/mol}} = 29.01 \times 10^{-3}$$

Thermal conductivity [138]

$$\frac{\lambda}{\text{W/(mK)}} = 3.0 \times 10^{-4} + 9.50 \times 10^{-5} T - 3.0 \times 10^{-8} T^2$$

$$273.15 \leq T(\text{K}) \leq 1000$$

Viscosity [138]

$$\frac{\eta}{\text{kg/(ms)}} \times 10^7 = 19.134 + 0.6T - 2.0 \times 10^{-4} T^2$$

$$273.15 \leq T(\text{K}) \leq 1000$$

Specific heat capacity [138]

$$\frac{c_{p,g}}{\text{J/(kgK)}} = 1.0196 - 8.0 \times 10^{-5} T - 2.0 \times 10^{-7} T^2$$

$$273.15 \leq T(\text{K}) \leq 1000$$

Density [138]

$$\frac{\rho}{\text{kg/m}^3} = 360.77 T^{-1.0055}$$

$$273.15 \leq T(\text{K}) \leq 1000$$

C.1.2 Nitrogen

Molar mass

$$\frac{\tilde{M}}{\text{kg/mol}} = 28.0 \times 10^{-3}$$

Thermal conductivity [111]

$$\frac{\lambda}{\text{W}/(\text{mK})} = 3.919 \times 10^{-4} + 9.816 \times 10^{-5} T - 5.067 \times 10^{-8} T^2 + 1.504 \times 10^{-11} T^3$$

$$273.15 \leq T(\text{K}) \leq 1270$$

Viscosity [138]

$$\frac{\eta}{\text{kg}/(\text{ms})} \times 10^7 = 19.719 + 0.577T - 2.0 \times 10^{-4} T^2$$

$$273.15 \leq T(\text{K}) \leq 1000$$

Specific heat capacity [111]

$$\frac{c_{p,g}}{\text{J}/(\text{kgK})} = 3.115 \times 10^1 + 1.357 \times 10^{-2} T + 2.680 \times 10^{-5} T^2 - 1.168 \times 10^{-8} T^3$$

$$273.15 \leq T(\text{K}) \leq 1270$$

Density [138]

$$\frac{\rho}{\text{kg}/\text{m}^3} = 349.66 T^{-1.0059}$$

$$273.15 \leq T(\text{K}) \leq 1000$$

C.1.3 Oxygen**Molar mass**

$$\frac{\tilde{M}}{\text{kg}/\text{mol}} = 32.0 \times 10^{-3}$$

Thermal conductivity [111]

$$\frac{\lambda}{\text{W}/(\text{mK})} = -3.273 \times 10^{-4} + 9.966 \times 10^{-5} T - 3.743 \times 10^{-8} T^2 + 9.732 \times 10^{-12} T^3$$

$$273.15 \leq T(\text{K}) \leq 1470$$

Viscosity [138]

$$\frac{\eta}{\text{kg}/(\text{ms})} \times 10^7 = 17.031 + 0.6911T - 2.0 \times 10^{-4} T^2$$

$$273.15 \leq T(\text{K}) \leq 1000$$

Specific heat capacity [111]

$$\frac{c_{p,g}}{\text{J}/(\text{kgK})} = 2.811 \times 10^1 - 3.68 \times 10^{-6} T + 1.746 \times 10^{-5} T^2 - 1.065 \times 10^{-8} T^3$$

$$273.15 \leq T(\text{K}) \leq 1470$$

Density [138]

$$\frac{\rho}{\text{kg}/\text{m}^3} = 402.87 T^{-1.0072}$$

$$273.15 \leq T(\text{K}) \leq 1000$$

C.1.4 Hydrogen

Molar mass

$$\frac{\tilde{M}}{\text{kg}/\text{mol}} = 2.0 \times 10^{-3}$$

Thermal conductivity [111]

$$\frac{\lambda}{\text{W}/(\text{mK})} = 8.099 \times 10^{-3} + 6.689 \times 10^{-4} T - 4.158 \times 10^{-7} T^2 + 1.562 \times 10^{-10} T^3$$

$$273.15 \leq T(\text{K}) \leq 1470$$

Viscosity [138]

$$\frac{\eta}{\text{kg}/(\text{ms})} \times 10^7 = 21.416 + 0.2411 T - 6.0 \times 10^{-5} T^2$$

$$273.15 \leq T(\text{K}) \leq 1000$$

Specific heat capacity [111]

$$\frac{c_{p,g}}{\text{J}/(\text{kgK})} = 2.714 \times 10^1 + 9.274 \times 10^{-6} T - 1.381 \times 10^{-5} T^2 + 7.64504 \times 10^{-9} T^3$$

$$273.15 \leq T(\text{K}) \leq 1470$$

Density [138]

$$\frac{\rho}{\text{kg/m}^3} = 24.236T^{-1}$$

$$273.15 \leq T(\text{K}) \leq 1000$$

C.1.5 Helium**Molar mass**

$$\frac{\tilde{M}}{\text{kg/mol}} = 4.0 \times 10^{-3}$$

Thermal conductivity [111]

$$\frac{\lambda}{\text{W/(mK)}} = 3.722 \times 10^{-2} + 3.896 \times 10^{-4}T - 7.45 \times 10^{-8}T^2 + 1.290 \times 10^{-11}T^3$$

$$273.15 \leq T(\text{K}) \leq 1470$$

Viscosity [138]

$$\frac{\eta}{\text{kg/(ms)}} \times 10^7 = 46.717 + 0.5003T - 1.0 \times 10^{-4}T^2$$

$$273.15 \leq T(\text{K}) \leq 1000$$

Specific heat capacity [111]

$$\frac{c_{p,g}}{\text{J/(kgK)}} = 2.08 \times 10^1$$

Density [138]

$$\frac{\rho}{\text{kg/m}^3} = 48.5T^{-0.9993}$$

$$273.15 \leq T(\text{K}) \leq 1000$$

C.1.6 Ethane**Molar mass**

$$\frac{\tilde{M}}{\text{kg/mol}} = 30.0 \times 10^{-3}$$

Thermal conductivity [111]

$$\frac{\lambda}{\text{W}/(\text{mK})} = -3.174 \times 10^{-2} + 2.201 \times 10^{-4} T - 1.923 \times 10^{-7} T^2 + 1.664 \times 10^{-10} T^3$$

$$273.15 \leq T(\text{K}) \leq 1470$$

Viscosity [139]

$$\frac{\eta}{\text{kg}/(\text{ms})} \times 10^7 = -51.396 + 0.5208T - 2.0 \times 10^{-4} T^2$$

$$273.15 \leq T(\text{K}) \leq 873.15$$

Specific heat capacity [111]

$$\frac{c_{p,g}}{\text{J}/(\text{kgK})} = 5.409 + 1.7811 \times 10^{-1} T - 6.938 \times 10^{-5} T^2 + 8.713 \times 10^{-9} T^3$$

$$273.15 \leq T(\text{K}) \leq 1470$$

Density [139]

$$\frac{\rho}{\text{kg}/\text{m}^3} = 366.97T^{-1.0001}$$

$$273.15 \leq T(\text{K}) \leq 873.15$$

C.1.7 Sulfur Hexafluoride**Molar mass**

$$\frac{\tilde{M}}{\text{kg}/\text{mol}} = 146.0 \times 10^{-3}$$

Viscosity [140]

$$\frac{\eta}{\text{kg}/(\text{ms})} \times 10^5 = 0.0436 + 0.0054T - 1.0 \times 10^{-6} T^2$$

C.2 Mixture properties

C.2.1 Binary diffusion coefficient (Chapman-Enskog equation) [111]

$$D_{jk} = 0.00186 \frac{T^{1.5}}{P \sigma_{j,k}^2 \Omega_D} \sqrt{\frac{1}{\tilde{M}_j} + \frac{1}{\tilde{M}_k}}$$

where $\sigma_{j,k}^2$ is the collision cross-section and Ω_D the collision integral, which is a function of temperature.

C.2.2 Mixture viscosity (Wilke) [111]

Viscosity of a binary gas mixture can be calculated as

$$\eta = \frac{\tilde{x}_i \eta_i}{\tilde{x}_i + \tilde{x}_j \phi_{i,j}} + \frac{\tilde{x}_j \eta_j}{\tilde{x}_j + \tilde{x}_i \phi_{j,i}},$$

where $\phi_{i,j}$ and $\phi_{j,i}$ can be found as

$$\phi_{i,j} = \frac{\left[1 + (\eta_i/\eta_j)^{0.5} (\tilde{M}_j/\tilde{M}_i)^{0.25} \right]^2}{\left[8(1 + \tilde{M}_i/\tilde{M}_j) \right]^{0.5}},$$

$$\phi_{j,i} = \frac{\eta_j}{\eta_i} \frac{\tilde{M}_i}{\tilde{M}_j} \phi_{i,j}.$$

C.3 Heat and mass transfer coefficients

C.3.1 Heat transfer coefficient [116]

Steady state and transient heat transfer experiments

$$Nu_o = \frac{\alpha_{g,o} d_h}{\lambda_{g,o}}$$

$$d_h = d_o - d_i$$

$$Nu_o = 4.364 + \left[4 - \frac{0.102}{(d_i/d_o) + 0.02} \right] \left(\frac{d_i}{d_o} \right)^{0.04}$$

C.3.2 Mass transfer coefficient [126]**Isobaric diffusion experiments****Annulus side:**

$$Sh_o = \frac{\beta_o d_h}{D_{jk}}$$

$$Sh_o = 1.25 \left(Re \frac{d_h}{L} \right)^{0.93} Sc^{0.33}$$

$$Re = 244$$

Tube side:

$$Sh_i = \frac{\beta_i d_i}{D_{jk}}$$

$$Sh_i = 1.25 \left(Re \frac{d_i}{L} \right)^{0.93} Sc^{0.33}$$

$$Re = 857$$

C.3.3 Heat and mass transfer coefficients [126]**Combined heat and mass transfer experiments**

Mass transfer coefficients for tube and annulus have been calculated as for the isobaric diffusion case (Appendix C.3.2). However, heat transfer coefficient for tube and annulus have been calculated by the analogy between heat and mass transfer, Lewis-analogy,

$$\frac{Nu}{Sh} = \left[\frac{Pr}{Sc} \right]^{1/3}.$$

Dimensionless numbers used in the above correlations are defined as

$$Re = \frac{ud}{\nu}, \quad Sc = \frac{\nu}{D_{jk}}, \quad \nu = \frac{\eta}{\rho}, \quad Pr = \frac{\nu}{\kappa},$$

however for the calculations a constant value of $Pr = 0.707$ has been taken.

Appendix D

Experimental data

D.1 Steady state heat transfer experiments

Figs. 3.2 & 3.3

$$u_{g,o,in} = 0.15 \text{ m/s}$$

$T_{g,o,in}$ [K]	\dot{Q}_i [W]	$z = 0.13 \text{ m}$				$z = 0.07 \text{ m}$			
		$T_{m,i}$ [K]	$T_{m,o}$ [K]	ΔT_m [K]	λ_m [W/mK]	$T_{m,i}$ [K]	$T_{m,o}$ [K]	ΔT_m [K]	λ_m [W/mK]
304.2	13.4	359.20	358.14	1.06	3.41	356.25	355.74	0.50	7.14
305.8	17.9	380.30	378.70	1.60	3.00	376.21	375.45	0.76	6.38
312.8	26.8	421.86	419.40	2.46	2.92	416.17	414.81	1.37	5.28
317.4	35.6	456.19	452.75	3.44	2.77	449.03	447.03	2.00	4.77
324.1	54.2	527.11	520.64	6.48	2.25	516.07	511.96	4.11	3.54
326.4	70.9	582.07	572.18	9.89	1.92	568.44	561.66	6.78	2.81
335.6	81.9	614.77	602.97	11.80	1.86	600.39	591.70	8.68	2.53

Fig. 3.4 & 3.5

\dot{Q}_i [W]	$u_{g,o,in} = 0.15 \text{ m/s}$			$u_{g,o,in} = 0.29 \text{ m/s}$			$u_{g,o,in} = 0.44 \text{ m/s}$		
	$T_{g,o,in}$ [K]	dT_m/dr [K/cm]	dT_m/dz [K/cm]	$T_{g,o,in}$ [K]	dT_m/dr [K/cm]	dT_m/dz [K/cm]	$T_{g,o,in}$ [K]	dT_m/dr [K/cm]	dT_m/dz [K/cm]
25	312.8	2.545	2.655	302.8	2.545	2.064	301.3	2.909	1.873
30	314.2	4.727	3.954	305.6	4.012	2.681	303.4	6.010	2.601
50	320.7	7.273	5.591	306.7	9.636	5.491	306.1	9.818	3.927
65	326.2	13.270	7.545	308.4	14.180	7.064	307.5	15.640	6.309
75	329.2	18.021	8.423	311.2	19.455	8.427	309.1	21.455	7.602
100	339.4	23.820	9.450	315.4	26.550	9.336	311.2	26.910	8.682

Figs 3.7 & 3.8

$\dot{Q}_i = 100\text{W}$, $T_{g,o,in} = 311.2\text{K}$, $u_{g,o,in} = 0.44\text{m/s}$, over time at steady state

z = 0.12 m		z = 0.07 m	
$T_{m,i}$ [K]	$T_{m,o}$ [K]	$T_{m,i}$ [K]	$T_{m,o}$ [K]
559.90	543.90	499.40	492.42
559.94	543.95	499.41	492.44
559.97	543.97	499.43	492.48
559.97	544.04	499.41	492.51
559.97	544.09	499.40	492.52
559.98	544.12	499.40	492.55
559.97	544.12	499.41	492.54
559.98	544.16	499.42	492.56
559.99	544.18	499.44	492.56

D.2 Transient heat transfer experiments

Fig. 3.9

$\dot{Q}_i = 50\text{W}$, $T_{g,o,in} = 306.07\text{K}$, $u_{g,o,in} = 0.44\text{m/s}$.

t [min]	z = 0.12 m $T_{m,o}$ [K]	z = 0.07 m $T_{m,o}$ [K]
0	299.69	299.69
10	326.03	324.58
20	366.68	356.12
30	389.36	372.25
40	401.87	380.97
50	409.50	386.32
60	414.42	389.70
70	417.82	392.04
80	420.25	393.69
90	421.97	394.84
100	423.26	395.71
110	424.20	396.36
120	424.93	396.82
130	425.47	397.17
140	426.00	397.50
150	426.38	397.73
160	426.66	397.96
170	426.99	398.14
180	427.17	398.33
190	427.41	398.47
200	427.60	398.62
210	427.80	398.73
220	427.93	398.91
230	428.10	399.00
240	428.30	399.09
250	428.40	399.30
260	428.58	399.40
270	428.65	399.50

Fig. 3.10

$\dot{Q}_i = 100\text{W}$, $T_{g,o,in} = 311.2\text{K}$, $u_{g,o,in} = 0.44\text{m/s}$.

t [min]	$T_{m,o}$ [K]	$T_{m,o}$ [K]
0	300.01	300.09
10	373.09	363.12
20	461.50	429.96
30	500.32	457.54
40	520.24	471.66
50	532.04	480.14
60	539.72	485.60
70	544.93	489.25
80	548.66	491.85
90	551.24	493.63
100	553.23	494.96
110	554.61	495.87
120	555.73	496.65
130	556.60	497.18
140	557.26	497.59
150	557.80	497.90
160	558.23	498.22
170	558.56	498.48
180	558.77	498.61
190	559.06	498.78
200	559.17	498.90
210	559.36	499.07
220	559.52	499.13
230	559.63	499.21
240	559.70	499.22
250	559.82	499.32
260	559.90	499.40
270	559.98	499.40

Fig. 3.11

$\dot{Q}_i = 100\text{W}$, $T_{g,o,in} = 307.7\text{K}$, $u_{g,o,in} = 0.59\text{m/s}$.

t [min]	z = 0.12 m	z = 0.07 m
	$T_{m,o}$ [K]	$T_{m,o}$ [K]
0	299.61	299.63
10	375.97	369.20
20	440.20	416.38
30	467.81	435.61
40	481.67	445.15
50	489.62	450.53
60	494.59	453.81
70	497.80	455.92
80	499.90	457.32
90	501.50	458.41
100	502.62	459.21
110	503.46	459.80
120	504.14	460.21
130	504.60	460.54
140	505.00	460.81
150	505.39	461.10
160	505.81	461.45
170	506.06	461.62
180	506.48	461.79
190	506.71	462.05
200	506.94	462.11
210	507.05	462.25
220	507.28	462.44
230	507.48	462.53
240	507.68	462.64
250	507.70	462.81
260	507.82	462.96
270	508.05	463.08

Fig. 3.12

$\dot{Q}_i = 75 \text{ W}$, $T_{g,o,in} = 332.5 \text{ K}$, $u_{g,o,in} = 0.22 \text{ m/s}$.

t [min]	z = 0.12 m	z = 0.07 m
	$T_{m,i}$ [K]	$T_{m,i}$ [K]
0	299.78	299.58
10	299.76	299.63
20	370.89	347.08
30	464.96	414.12
40	507.83	449.59
50	533.51	470.38
60	550.26	484.87
70	563.69	496.09
80	575.03	504.94
90	583.90	512.02
100	590.82	517.79
110	596.34	522.47
120	601.37	526.35
130	605.79	529.64
150	612.86	535.04
160	615.66	537.17
170	618.00	538.94
180	619.98	540.45
190	622.17	541.83
200	623.78	542.98
210	625.16	544.05
220	626.04	544.78
230	626.99	545.53
240	628.08	546.37
250	628.97	547.00
260	629.68	547.57
270	630.54	548.06

Fig. 3.13

$\dot{Q}_i = 100\text{W}$, $T_{g,o,in} = 315.4\text{K}$, $u_{g,o,in} = 0.29\text{m/s}$.

t [min]	z = 0.12 m	z = 0.07 m
	$T_{m,o}$ [K]	$T_{m,o}$ [K]
0	299.90	299.94
10	399.39	389.60
20	475.70	449.09
30	513.39	477.44
40	537.33	495.82
50	555.10	509.21
60	567.76	518.53
70	576.92	525.24
80	584.05	530.42
90	589.79	534.45
100	594.27	537.76
110	598.02	540.37
120	600.97	542.52
130	603.56	544.34
140	605.59	545.86
150	607.46	547.22
160	608.92	548.26
170	610.39	549.34
180	611.70	550.21
190	612.72	551.06
200	613.64	551.78
210	614.64	552.38
220	615.52	553.06
230	616.12	553.56
240	616.90	554.03
250	617.41	554.52
260	618.01	554.95
270	618.67	555.44

D.3 Gas permeation experiments

Fig. 4.2

T = 25°C, Membrane M1 (Support layer).

Air		N ₂		He	
\bar{P} [Pa]	$\dot{N}/\Delta P$ [mol/s.Pa]	\bar{P} [Pa]	$\dot{N}/\Delta P$ [mol/s.Pa]	\bar{P} [Pa]	$\dot{N}/\Delta P$ [mol/s.Pa]
115489	1.94E-07	115489	2.01E-07	115489	2.22E-07
201869	2.81E-07	201869	2.92E-07	201869	3.14E-07
301716	3.99E-07	301716	4.15E-07	301716	4.19E-07

Fig. 4.3

Nitrogen; Membrane M1 (Support layer).

T = 25°C		T = 100°C		T = 200°C	
\bar{P} [Pa]	$\dot{N}/\Delta P$ [mol/s.Pa]	\bar{P} [Pa]	$\dot{N}/\Delta P$ [mol/s.Pa]	\bar{P} [Pa]	$\dot{N}/\Delta P$ [mol/s.Pa]
132036.163	2.0081E-07	134670.974	1.487E-07	138083.45	1.083E-07
205703.877	2.9172E-07	206151.843	2.0957E-07	206448.856	1.4698E-07
305751.525	4.1518E-07	306071.638	2.9466E-07	306590.385	2.0363E-07
T = 300°C		T = 400°C		T = 500°C	
\bar{P} [Pa]	$\dot{N}/\Delta P$ [mol/s.Pa]	\bar{P} [Pa]	$\dot{N}/\Delta P$ [mol/s.Pa]	\bar{P} [Pa]	$\dot{N}/\Delta P$ [mol/s.Pa]
142713.862	8.5727E-08	141157.042	6.8892E-08	148445.658	5.9932E-08
206854.169	1.1193E-07	205573.85	8.8823E-08	206156.838	7.41E-08
306750.824	1.5275E-07	305879.874	1.1986E-07	307377.155	9.895E-08

Fig. 4.4

P = 1.06 bar, Membrane M1 (Support layer).

T [°C]	26	98	196	294	396	499
	$\dot{N}/\Delta P$					
Gases	[mol/s.Pa]					
Air	1.94E-07	1.45E-07	1.05E-07	8.39E-08	6.73E-08	5.84E-08
N ₂	2.01E-07	1.49E-07	1.08E-07	8.57E-08	6.89E-08	5.99E-08
He	2.22E-07	1.81E-07	1.48E-07	1.26E-07	1.09E-07	9.39E-08

Fig. 4.5

Nitrogen, T = 25 °C bar, Membrane M1 (Composite).

Support		1st layer		2nd layer		3rd layer	
\bar{P} [Pa]	$\dot{N}/\Delta P$ [mol/s.Pa]	\bar{P} [Pa]	$\dot{N}/\Delta P$ [mol/s.Pa]	\bar{P} [Pa]	$\dot{N}/\Delta P$ [mol/s.Pa]	\bar{P} [Pa]	$\dot{N}/\Delta P$ [mol/s.Pa]
115283	1.8263E-07	109530	1.60110E-07	116449	1.3999E-07	122718	1.1074E-07
202389	2.9816E-07	197836	2.64460E-07	199865	1.4567E-07	197260	1.190E-07
301371	4.239E-07	298438	3.77120E-07	300082	1.8223E-07	298162	1.398E-07

Fig. 4.6

T = 25 °C bar, Membrane M1 (Composite).

Air		N ₂		He	
\bar{P} [Pa]	$\dot{N}/\Delta P$ [mol/s.Pa]	\bar{P} [Pa]	$\dot{N}/\Delta P$ [mol/s.Pa]	\bar{P} [Pa]	$\dot{N}/\Delta P$ [mol/s.Pa]
121945.864	7.8609E-08	121342.285	8.1705E-08	114047.703	1.5116E-07
200099.184	9.2374E-08	200003.314	9.6324E-08	200257.602	1.7984E-07
300386.803	1.017E-07	300194.382	1.0841E-07	300031.348	2.055E-07

Fig. 4.7

P = 1.21 bar, Membrane M1 (Composite).

T [°C]	26	98	196	294	396	499
Gases	$\dot{N}/\Delta P$ [mol/s.Pa]					
	Air	7.8609E-08	6.5476E-08	5.3807E-08	4.6781E-08	4.2938E-08
N2	8.1694E-08	6.804E-08	5.5317E-08	4.8378E-08	4.4437E-08	4.1046E-08
He	1.5116E-07	1.2981E-07	1.1098E-07	9.8117E-08	8.9779E-08	8.3132E-08

Fig. 4.8

T = 25°C, Membrane M2 (Support layer).

N ₂		Air		O ₂	
\bar{P} [Pa]	$\dot{N}/\Delta P$ [mol/s.Pa]	\bar{P} [Pa]	$\dot{N}/\Delta P$ [mol/s.Pa]	\bar{P} [Pa]	$\dot{N}/\Delta P$ [mol/s.Pa]
106198.9003	3.48687E-07	106266.6366	3.39588E-07	105604.4943	3.04835E-07
199546.3609	5.9285E-07	199363.4097	5.73398E-07	199593.9004	5.14995E-07
299305.8267	8.49581E-07	298957.6197	8.21926E-07	299071.0974	7.37348E-07

Fig. 4.9

Nitrogen, Membrane M2 (Support layer).

T = 20°C		T = 100°C		T = 200°C	
\bar{P} [Pa]	$\dot{N}/\Delta P$ [mol/s.Pa]	\bar{P} [Pa]	$\dot{N}/\Delta P$ [mol/s] [mol/s.Pa]	\bar{P} [Pa]	$\dot{N}/\Delta P$ [mol/s] [mol/s.Pa]
106198.9	3.4869E-07	106204.439	2.7455E-07	106034.846	2.1209E-07
199546.361	5.9285E-07	199192.264	4.5473E-07	199539.299	3.4102E-07
299305.827	8.4958E-07	298935.17	6.4796E-07	299410.786	4.7846E-07
T = 300°C		T = 400°C		T = 500°C	
\bar{P} [Pa]	$\dot{N}/\Delta P$ [mol/s] [mol/s.Pa]	\bar{P} [Pa]	$\dot{N}/\Delta P$ [mol/s] [mol/s.Pa]	\bar{P} [Pa]	$\dot{N}/\Delta P$ [mol/s] [mol/s.Pa]
106278.261	1.7296E-07	106351.324	1.4584E-07	106560.761	1.261E-07
199440.921	2.706E-07	199782.952	2.2297E-07	199945.168	1.8902E-07
299458.974	3.748E-07	299504.363	3.0539E-07	299500.733	2.5516E-07

Fig 4.10

P = 1.06 bar, Membrane M2 (Support layer).

T [°C]	26	98	196	294	396	499
	$\dot{N}/\Delta P$					
Gases	[mol/s.Pa]					
N2	3.49E-07	2.75E-07	2.12E-07	1.73E-07	1.46E-07	1.26E-07
Air	3.40E-07	2.67E-07	2.05E-07	1.68E-07	1.41E-07	1.23E-07
O2	3.05E-07	2.41E-07	1.85E-07	1.51E-07	1.28E-07	1.10E-07

Fig 4.11

Oxygen, Membrane M2 (Third layer).

T = 20°C		T = 100°C		T = 200°C	
\bar{P} [Pa]	$\dot{N}/\Delta P$ [mol/s.Pa]	\bar{P} [Pa]	$\dot{N}/\Delta P$ [mol/s.Pa]	\bar{P} [Pa]	$\dot{N}/\Delta P$ [mol/s.Pa]
102855.461	2.6877E-07	102422.001	2.4111E-07	102552.301	2.1426E-07
200050.506	2.9497E-07	200253.648	2.607E-07	200274.927	2.2821E-07
300071.852	3.2194E-07	300036.129	2.8068E-07	300289.299	2.4249E-07
T = 300°C		T = 400°C		T = 500°C	
\bar{P} [Pa]	$\dot{N}/\Delta P$ [mol/s.Pa]	\bar{P} [Pa]	$\dot{N}/\Delta P$ [mol/s.Pa]	\bar{P} [Pa]	$\dot{N}/\Delta P$ [mol/s.Pa]
102663.062	1.9472E-07	102521.328	1.7901E-07	102618.688	1.6633E-07
200416.726	2.0523E-07	199960.265	1.8713E-07	200217.509	1.7282E-07
300525.446	2.1599E-07	300132.004	1.9548E-07	300123.626	1.7947E-07

Fig. 4.12

Oxygen, Membrane M2 (Third layer).

	$\dot{N}/\Delta P$ [mol/s.Pa]		
T [°C]	1 bar	2 bar	3 bar
26	2.688E-07	2.9497E-07	3.2194E-07
83	2.4111E-07	2.607E-07	2.8068E-07
165	2.1426E-07	2.2821E-07	2.4249E-07
240	1.9472E-07	2.0523E-07	2.1599E-07
320	1.7901E-07	1.8713E-07	1.9548E-07
400	1.6633E-07	1.7282E-07	1.7947E-07

D.4 Isobaric diffusion experiments

Fig. 4.24

Gases: Nitrogen-Helium,

$$\tilde{x}_{\text{He},i,\text{in}} = 1, \tilde{x}_{\text{He},o,\text{in}} = 0,$$

$$\tilde{x}_{\text{N}_2,i,\text{in}} = 0, \tilde{x}_{\text{N}_2,o,\text{in}} = 1.$$

$u_{g,o,\text{in}} = 0.058 \text{ m/s}$, $P = 1.01 \text{ bar}$, $T = 296 \text{ K}$, Membrane M1 (Composite).

$u_{g,i,\text{in}} \text{ [m/s]}$	$\tilde{x}_{\text{He},i,\text{out}} \text{ [-]}$	$\tilde{x}_{\text{He},o,\text{out}} \text{ [-]}$
0.024	0.399	0.179
0.048	0.641	0.257
0.072	0.761	0.292
0.096	0.830	0.308

Figs. 4.25 & 4.26

Gases: Nitrogen-Helium,

$$\tilde{x}_{\text{He},i,\text{in}} = 1, \tilde{x}_{\text{He},o,\text{in}} = 0,$$

$$\tilde{x}_{\text{N}_2,i,\text{in}} = 0, \tilde{x}_{\text{N}_2,o,\text{in}} = 1.$$

$u_{g,o,\text{in}} = 0.058 \text{ m/s}$, $P = 1.01 \text{ bar}$, $T = 296 \text{ K}$, Membrane M1 (Composite).

$u_{g,i,\text{in}} \text{ [m/s]}$	$u_{g,i,\text{out}} \text{ [-]}$	$u_{g,o,\text{out}} \text{ [-]}$
0.0241	0.0118	0.0651
0.048	0.0290	0.0694
0.072	0.0495	0.0714
0.096	0.0712	0.0723

D.5 Transient diffusion experiments

Fig. 4.29

$T = 293 \text{ K}$, $u_{g,i,\text{in}} = 0.096 \text{ m/s}$, $t = 0$: $P_i = P_o = 0.986 \text{ bar}$, Membrane M1 (Support layer).

t [s]	P _o [bar]	t [s]	P _o [bar]	t [s]	P _o [bar]
1	0.98590	51	0.98771	101	0.98616
2	0.98758	52	0.98771	102	0.98616
3	0.99158	53	0.98771	103	0.98616
4	0.99472	54	0.98706	104	0.98616
5	0.99590	55	0.98667	105	0.98616
6	0.99679	56	0.98667	106	0.98616
7	0.99679	57	0.98667	107	0.98616
8	0.99679	58	0.98667	108	0.98616
9	0.99679	59	0.98667	109	0.98616
10	0.99679	60	0.98667	110	0.98616
11	0.99679	61	0.98667	111	0.98616
12	0.99679	62	0.98667	112	0.98616
13	0.99655	63	0.98667	113	0.98616
14	0.99550	64	0.98667	114	0.98616
15	0.99517	65	0.98648	115	0.98616
16	0.99446	66	0.98641	116	0.98594
17	0.99446	67	0.98641	117	0.98594
18	0.99345	68	0.98641	118	0.98594
19	0.99342	69	0.98641	119	0.98594
20	0.99313	70	0.98641	120	0.98594
21	0.99264	71	0.98641	121	0.98594
22	0.99264	72	0.98641	122	0.98590
23	0.99196	73	0.98637	123	0.98590
24	0.99160	74	0.98616	124	0.98590
25	0.99125	75	0.98616	125	0.98590
26	0.99109	76	0.98616	126	0.98590
27	0.99109	77	0.98616	127	0.98590
28	0.99024	78	0.98616	128	0.98590
29	0.99005	79	0.98616	129	0.98590
30	0.98991	80	0.98616	130	0.98590
31	0.98979	81	0.98616	131	0.98590
32	0.98979	82	0.98616	132	0.98590
33	0.98979	83	0.98616	133	0.98590
34	0.98920	84	0.98616	134	0.98590
35	0.98875	85	0.98616	135	0.98590
36	0.98875	86	0.98616	136	0.98590
37	0.98875	87	0.98616	137	0.98590
38	0.98875	88	0.98616	138	0.98590
39	0.98875	89	0.98616	139	0.98590
40	0.98826	90	0.98616	140	0.98590
41	0.98771	91	0.98616	141	0.98590
42	0.98771	92	0.98616	142	0.98590
43	0.98771	93	0.98616	143	0.98590
44	0.98771	94	0.98606	144	0.98590
45	0.98771	95	0.98590	145	0.98590
46	0.98771	96	0.98607	146	0.98590
47	0.98771	97	0.98616	147	0.98590
48	0.98771	98	0.98616	148	0.98590
49	0.98771	99	0.98616	149	0.98590
50	0.98771	100	0.98616	150	0.98590

Fig. 4.30: $T = 293 \text{ K}$, $u_{g,i,in} = 0.096 \text{ m/s}$, $t = 0$: $P_1 = P_o = 1.02 \text{ bar}$, Membrane M1 (Composite).

t [s]	P _o [bar]	t [s]	P _o [bar]	t [s]	P _o [bar]
1	1.02382	51	1.02404	101	1.02093
2	1.03291	52	1.02404	102	1.02093
3	1.04192	53	1.02404	103	1.02093
4	1.04736	54	1.02404	104	1.02093
5	1.05043	55	1.02318	105	1.02093
6	1.05172	56	1.02300	106	1.02093
7	1.05207	57	1.02274	107	1.02093
8	1.05182	58	1.02274	108	1.02093
9	1.05064	59	1.02274	109	1.02093
10	1.04936	60	1.02274	110	1.02078
11	1.04814	61	1.02274	111	1.02067
12	1.04664	62	1.02274	112	1.02067
13	1.04513	63	1.02274	113	1.02067
14	1.04375	64	1.02274	114	1.02067
15	1.04271	65	1.02252	115	1.02067
16	1.04145	66	1.02222	116	1.02067
17	1.04024	67	1.02222	117	1.02067
18	1.03914	68	1.02222	118	1.02067
19	1.03845	69	1.02201	119	1.02067
20	1.03753	70	1.02196	120	1.02067
21	1.03638	71	1.02196	121	1.02067
22	1.03525	72	1.02196	122	1.02067
23	1.03479	73	1.02196	123	1.02067
24	1.03416	74	1.02196	124	1.02067
25	1.03314	75	1.02196	125	1.02067
26	1.03252	76	1.02196	126	1.02067
27	1.03208	77	1.02196	127	1.02067
28	1.03135	78	1.02196	128	1.02067
29	1.03105	79	1.02196	129	1.02067
30	1.03035	80	1.02196	130	1.02067
31	1.03001	81	1.02196	131	1.02067
32	1.02918	82	1.02196	132	1.02067
33	1.02897	83	1.02196	133	1.02067
34	1.02850	84	1.02196	134	1.02067
35	1.02793	85	1.02177	135	1.02067
36	1.02756	86	1.02119	136	1.02067
37	1.02715	87	1.02119	137	1.02067
38	1.02715	88	1.02119	138	1.02067
39	1.02701	89	1.02119	139	1.02067
40	1.02612	90	1.02119	140	1.02067
41	1.02612	91	1.02119	141	1.02067
42	1.02612	92	1.02119	142	1.02067
43	1.02522	93	1.02119	143	1.02067
44	1.02508	94	1.02119	144	1.02067
45	1.02508	95	1.02119	145	1.02067
46	1.02508	96	1.02114	146	1.02067
47	1.02508	97	1.02093	147	1.02067
48	1.02451	98	1.02093	148	1.02067
49	1.02404	99	1.02093	149	1.02041
50	1.02404	100	1.02093	150	1.02041

T = 373 K, $u_{g,i,in} = 0.096$ m/s, t = 0: $P_i = P_o = 1.02$ bar, Membrane M1 (Composite).[not plotted]

t [s]	P _o [bar]	t [s]	P _o [bar]	t [s]	P _o [bar]
1	1.02041	51	1.03001	101	1.02690
2	1.02020	52	1.03001	102	1.02690
3	1.02228	53	1.03001	103	1.02690
4	1.03022	54	1.03001	104	1.02690
5	1.04341	55	1.02980	105	1.02690
6	1.05284	56	1.02897	106	1.02690
7	1.05886	57	1.02897	107	1.02690
8	1.06107	58	1.02897	108	1.02690
9	1.06193	59	1.02897	109	1.02690
10	1.06162	60	1.02897	110	1.02690
11	1.06033	61	1.02897	111	1.02690
12	1.05878	62	1.02895	112	1.02690
13	1.05752	63	1.02845	113	1.02690
14	1.05597	64	1.02845	114	1.02690
15	1.05447	65	1.02845	115	1.02690
16	1.05295	66	1.02845	116	1.02690
17	1.05157	67	1.02845	117	1.02690
18	1.05020	68	1.02845	118	1.02690
19	1.04900	69	1.02845	119	1.02690
20	1.04806	70	1.02845	120	1.02690
21	1.04678	71	1.02845	121	1.02690
22	1.04559	72	1.02793	122	1.02690
23	1.04489	73	1.02793	123	1.02690
24	1.04362	74	1.02793	124	1.02688
25	1.04298	75	1.02793	125	1.02586
26	1.04171	76	1.02793	126	1.02586
27	1.04125	77	1.02793	127	1.02586
28	1.04063	78	1.02793	128	1.02586
29	1.03935	79	1.02793	129	1.02586
30	1.03920	80	1.02793	130	1.02586
31	1.03831	81	1.02793	131	1.02586
32	1.03755	82	1.02793	132	1.02586
33	1.03727	83	1.02793	133	1.02586
34	1.03638	84	1.02793	134	1.02586
35	1.03624	85	1.02793	135	1.02586
36	1.03538	86	1.02793	136	1.02560
37	1.03520	87	1.02793	137	1.02560
38	1.03421	88	1.02793	138	1.02560
39	1.03416	89	1.02793	139	1.02560
40	1.03401	90	1.02793	140	1.02560
41	1.03312	91	1.02793	141	1.02560
42	1.03312	92	1.02793	142	1.02560
43	1.03294	93	1.02717	143	1.02560
44	1.03208	94	1.02690	144	1.02560
45	1.03208	95	1.02690	145	1.02560
46	1.03208	96	1.02690	146	1.02560
47	1.03116	97	1.02690	147	1.02558
48	1.03105	98	1.02690	148	1.02418
49	1.03105	99	1.02690	149	1.02193
50	1.03105	100	1.02690	150	1.02036

$T = 373 \text{ K}$, $u_{g,i,in} = 0.096 \text{ m/s}$, $t = 0$: $P_i = P_o = 0.986 \text{ bar}$, Membrane M1 (Support layer) [not plotted].

t [s]	P_o [bar]	t [s]	P_o [bar]	t [s]	P_o [bar]
1	0.98758	51	0.98771	101	0.98616
2	0.99158	52	0.98771	102	0.98616
3	0.99472	53	0.98771	103	0.98616
4	0.99590	54	0.98706	104	0.98616
5	0.99679	55	0.98667	105	0.98616
6	0.99679	56	0.98667	106	0.98616
7	0.99679	57	0.98667	107	0.98616
8	0.99679	58	0.98667	108	0.98616
9	0.99679	59	0.98667	109	0.98616
10	0.99679	60	0.98667	110	0.98616
11	0.99679	61	0.98667	111	0.98616
12	0.99655	62	0.98667	112	0.98616
13	0.99550	63	0.98667	113	0.98616
14	0.99517	64	0.98667	114	0.98616
15	0.99446	65	0.98648	115	0.98616
16	0.99446	66	0.98641	116	0.98594
17	0.99345	67	0.98641	117	0.98590
18	0.99342	68	0.98641	118	0.98590
19	0.99313	69	0.98641	119	0.98590
20	0.99264	70	0.98641	120	0.98590
21	0.99264	71	0.98641	121	0.98590
22	0.99196	72	0.98641	122	0.98590
23	0.99160	73	0.98637	123	0.98590
24	0.99125	74	0.98616	124	0.98590
25	0.99109	75	0.98616	125	0.98590
26	0.99109	76	0.98616	126	0.98590
27	0.99024	77	0.98616	127	0.98590
28	0.99005	78	0.98616	128	0.98590
29	0.98991	79	0.98616	129	0.98590
30	0.98979	80	0.98616	130	0.98590
31	0.98979	81	0.98616	131	0.98590
32	0.98979	82	0.98616	132	0.98590
33	0.98920	83	0.98616	133	0.98590
34	0.98875	84	0.98616	134	0.98590
35	0.98875	85	0.98616	135	0.98590
36	0.98875	86	0.98616	136	0.98590
37	0.98875	87	0.98616	137	0.98590
38	0.98875	88	0.98616	138	0.98590
39	0.98826	89	0.98616	139	0.98590
40	0.98771	90	0.98616	140	0.98590
41	0.98771	91	0.98616	141	0.98590
42	0.98771	92	0.98616	142	0.98596
43	0.98771	93	0.98616	143	0.98616
44	0.98771	94	0.98606	144	0.98616
45	0.98771	95	0.98590	145	0.98616
46	0.98771	96	0.98607	146	0.98590
47	0.98771	97	0.98616	147	0.98590
48	0.98771	98	0.98616	148	0.98590
49	0.98771	99	0.98616	149	0.98590
50	0.98771	100	0.98616	150	0.98590

D.6 Combined heat and mass transfer experiments

These experiments have been conducted with the composite membrane M1. Shell temperatures, inlet gas temperatures and flow velocities for annulus and tube (for all combined heat and mass transfer experiments) are summarised for three different gas inlet temperatures ($T_{g,i,in}$) in the following tables.

$$T_{g,i,in} = 373.15 \text{ K}$$

$u_{g,i,in}$ [m/s]	$u_{g,o,in}$ [m/s]	$T_{g,o,in}$ [K]	T_{Shell} [K]
0.24	0.15	319.75	342.01
0.36	0.22	313.65	343.15
0.48	0.29	311.05	343.98
0.72	0.44	308.15	344.99

$$T_{g,i,in} = 423.15 \text{ K}$$

$u_{g,i,in}$ [m/s]	$u_{g,o,in}$ [m/s]	$T_{g,o,in}$ [K]	T_{Shell} [K]
0.24	0.15	331.45	372.11
0.36	0.22	325.45	373.02
0.48	0.29	320.35	374.10
0.72	0.44	315.25	375.00

$$T_{g,i,in} = 473.15 \text{ K}$$

$u_{g,i,in}$ [m/s]	$u_{g,o,in}$ [m/s]	$T_{g,o,in}$ [K]	T_{Shell} [K]
0.24	0.15	347.15	402.12
0.36	0.22	338.15	404.02
0.48	0.29	329.55	410.10
0.72	0.44	320.85	412.04

Fig. 5.2 a & b

$$\tilde{x}_{\text{He},i,\text{in}} = 1, \tilde{x}_{\text{He},o,\text{in}} = 0,$$

$$\tilde{x}_{\text{N}_2,i,\text{in}} = 0, \tilde{x}_{\text{N}_2,o,\text{in}} = 1.$$

$$u_{g,i,\text{in}} = 0.24 \text{ m/s}, u_{g,o,\text{in}} = 0.145 \text{ m/s}.$$

$T_{g,i,\text{in}}$ [K]	$T_{g,o,\text{in}}$ [K]	T_{Shell} [K]	$\tilde{x}_{\text{He},o,\text{out}}$ [-]
373.15	319.75	342.01	0.19
473.15	347.15	402.12	0.21

Fig. 5.3 a & b

$$u_{g,i,\text{in}} = 0.24 \text{ m/s}, u_{g,o,\text{in}} = 0.145 \text{ m/s}.$$

$T_{g,i,\text{in}}$ [K]	$T_{g,o,\text{in}}$ [K]	$T_{g,i,\text{out}}$ [K]	$T_{g,o,\text{out}}$ [K]	T_{Shell} [K]
373.15	319.75	348.65	342.05	342.01
473.15	347.15	404.45	396.05	402.12

Fig. 5.4 a & b

$$u_{g,i,\text{in}} = 0.24 \text{ m/s}, u_{g,o,\text{in}} = 0.145 \text{ m/s}.$$

z [m]	$T_{g,i,\text{in}} = 373 \text{ K}$		$T_{g,i,\text{in}} = 473 \text{ K}$	
	$T_{m,i}$ [K]	$T_{m,o}$ [K]	$T_{m,i}$ [K]	$T_{m,o}$ [K]
0.125	348.15	345.45	416.35	408.75
0.175	344.75	344.15	409.95	408.45

Fig. 5.5

$$\tilde{x}_{\text{He},i,\text{in}} = 1, \tilde{x}_{\text{He},o,\text{in}} = 0,$$

$$\tilde{x}_{\text{N}_2,i,\text{in}} = 0, \tilde{x}_{\text{N}_2,o,\text{in}} = 1.$$

$u_{g,i,\text{in}}$ [m/s]	$T_{g,i,\text{in}}$ [K]	373	423	473
	$u_{g,o,\text{in}}$ [m/s]	$\tilde{x}_{\text{He},o,\text{out}}$ [-]	$\tilde{x}_{\text{He},o,\text{out}}$ [-]	$\tilde{x}_{\text{He},o,\text{out}}$ [-]
0.241	0.145	0.19	0.2	0.21
0.361	0.218	0.14	0.15	0.16
0.481	0.29	0.105	0.114	0.12
0.722	0.435	0.08	0.082	0.084

Fig. 5.6

	$T_{g,i,in}$ [K]	373	423	473
$u_{g,i,in}$ [m/s]	$u_{g,o,in}$ [m/s]	$T_{g,o,out}$ [K]	$T_{g,o,out}$ [K]	$T_{g,o,out}$ [K]
0.241	0.145	342.75	369.85	396.05
0.361	0.218	339.95	372.95	400.45
0.481	0.29	340.15	372.57	398.25
0.722	0.435	339.25	367.05	391.75

Fig. 5.7

	$T_{g,i,in}$ [K]	373	423	473
$u_{g,i,in}$ [m/s]	$u_{g,o,in}$ [m/s]	$T_{g,i,out}$ [K]	$T_{g,i,out}$ [K]	$T_{g,i,out}$ [K]
0.241	0.145	347.65	374.15	404.45
0.361	0.218	345.35	380.65	411.95
0.481	0.29	346.45	380.65	413.65
0.722	0.435	347.75	380	411.75

Fig. 5.8

		$z = 0.125$ m		
	$T_{g,i,in}$ [K]	373	423	473
$u_{g,i,in}$ [m/s]	$u_{g,o,in}$ [m/s]	$T_{m,o}$ [K]	$T_{m,o}$ [K]	$T_{m,o}$ [K]
0.241	0.145	345.35	376.15	408.75
0.361	0.218	344.85	380.55	411.35
0.481	0.29	345.95	378.35	410.05
0.722	0.435	344.75	376.05	403.55

Fig. 5.9

		$z = 0.175$ m		
	$T_{g,i,in}$ [K]	373	423	473
$u_{g,i,in}$ [m/s]	$u_{g,o,in}$ [m/s]	$T_{m,o}$ [K]	$T_{m,o}$ [K]	$T_{m,o}$ [K]
0.241	0.145	345.15	375.2	408.45
0.361	0.218	345.65	381.65	413.15
0.481	0.29	346.95	380.95	414.05
0.722	0.435	345.55	376.75	404.55

Fig. 5.10

$$\tilde{x}_{\text{He},i,\text{in}} = 1, \tilde{x}_{\text{He},o,\text{in}} = 0,$$

$$\tilde{x}_{\text{N}_2,i,\text{in}} = 0, \tilde{x}_{\text{N}_2,o,\text{in}} = 1.$$

	$T_{g,i,\text{in}}$ [K]	293
$u_{g,i,\text{in}}$ [m/s]	$u_{g,o,\text{in}}$ [m/s]	$\tilde{x}_{\text{He},o,\text{out}}$ [-]
0.024	0.0145	0.445
0.048	0.0290	0.390
0.072	0.0435	0.330
0.096	0.0580	0.290
0.241	0.1451	0.165
0.361	0.2177	0.105
0.481	0.2902	0.090
0.722	0.4353	0.070

Fig. 5.11

$$\tilde{x}_{\text{He},i,\text{in}} = 1, \tilde{x}_{\text{He},o,\text{in}} = 0,$$

$$\tilde{x}_{\text{N}_2,i,\text{in}} = 0, \tilde{x}_{\text{N}_2,o,\text{in}} = 1.$$

	$T_{g,i,\text{in}}$ [K]	293	373	423	473
$u_{g,i,\text{in}}$ [m/s]	$u_{g,o,\text{in}}$ [m/s]	$\tilde{x}_{\text{He},o,\text{out}}$ [-]	$\tilde{x}_{\text{He},o,\text{out}}$ [-]	$\tilde{x}_{\text{He},o,\text{out}}$ [-]	$\tilde{x}_{\text{He},o,\text{out}}$ [-]
0.241	0.145	0.165	0.19	0.2	0.21
0.361	0.218	0.105	0.14	0.15	0.16
0.481	0.290	0.09	0.105	0.114	0.12
0.722	0.435	0.07	0.08	0.082	0.084

D.7 Value pair of K_0 (m) and B_0 (m²) for every temperature and gas for M1 (support layer)

T = 25°C			T = 100°C		
Air	K_0	B_0	Air	K_0	B_0
	8.40E-08	2.98E-14		8.87E-08	2.76E-14
He	K_0	B_0	He	K_0	B_0
	9.54E-08	3.01E-14		8.41E-08	3.00E-14
Nitrogen	K_0	B_0	Nitrogen	K_0	B_0
	7.45E-08	3.15E-14		7.47E-08	2.96E-14
T = 200°C			T = 300°C		
Air	K_0	B_0	Air	K_0	B_0
	8.06E-08	2.84E-14		6.59E-08	2.88E-14
He	K_{0eff}	B_0	He	K_0	B_0
	8.95E-08	3.10E-14		8.29E-08	2.98E-14
Nitrogen	K_0	B_0	Nitrogen	K_0	B_0
	7.28E-08	2.89E-14		8.55E-08	2.69E-14
T = 400°C			T = 500°C		
Air	K_0	B_0	Air	K_0	B_0
	8.94E-08	2.86E-14		8.06E-08	2.92E-14
He	K_0	B_0	He	K_0	B_0
	9.09E-08	3.05E-14		7.91E-08	3.33E-14
Nitrogen	K_0	B_0	Nitrogen	K_0	B_0
	7.35E-08	3.05E-14		7.57E-08	2.87E-14

Appendix E

Equipment

1. Rohrofen FRHT-3-100/1000/1100

- Linn High Therm GmbH, 06567 Bad Frankenhausen
3-Zonen-Rohrofen bis 1100°C

2. Gasdosierung mit MFC

- Bronkhorst HI-TEC, Niederlande
Über: Mättig Mess- und Regeltechnik Vertriebs GmbH, 59423 Unna

Genauigkeit: +/- 0,5% v. MW +/- 0,1% v. EW

3. Messdatenerfassungssystem

- Gantner Electronic GmbH, 64297 Darmstadt

Mehrkanalige ADU 16 bit: ISM 111

8-kanaliger Multiplexer IMX 102 für 8 Thermoelemente

Datenerfassungssoftware: TRENDOWS_Xp

- Kirsten Controlsystems GmbH, 71732 Tamm

4. Thermoelemente

- CONATEX Mess- und Regeltechnik GmbH, 66606 St. Wendel

Mantelthermoelement Form 7M, Typ K, Durchmesser 0,5mm, Messstelle 5mm aus dem Mantelrohr herausragend

Genauigkeit nach DIN EN 60584-1 Klasse 1:

Temperaturbereich -40°C - 375°C +/- 1,5°C

Temperaturbereich 375°C - 1000°C +/- 0,004*T(°C)

5. Drucksensoren

- Sensortech GmbH, 82178 Puchheim

BTE 5000 für Differenzdruck 25mbar, 100 mbar, -1bar - +1bar.

Genauigkeit: +/- 1% der Messspanne

BTE 6000 für Absolutdruck 2bar, 5bar

Genauigkeit: +/- 0,2% der Messspanne

6. Drehkolbengaszähler

- Common Mess- und Strömungstechnik, 14480 Potsdam

Drehkolbengaszähler CGR Typ G16 Q(max)=25m³/h, Q(min)=0,2m³/h

Messfehler < 1%

Kalibrierprotokoll: Durchfluss (m ³ /h):	3,3	1,7	0,8	0,4	0,2
Relative Abweichung:	0,2%	0,0%	-0,2%	-0,5%	-0,6%

7. Trommelgaszähler

- Dr.-Ing. Ritter Apparatebau GmbH, 44892 Bochum

Trommelgaszähler TG 50, Q(max)=18 m³/h, Q(min)=0,2 m³/h,

Genauigkeit +/- 0,1% bei 10m³/h

Trommelgaszähler TG 5, Q(max)=10 l/min, Q(min)=0,17 l/min,

Genauigkeit +/- 0,1% bei 8,3 l/min

8. Film-Flow-Meter

- STEC – INC. Japan, Horiba Europe GmbH, 65843 Sulzbach

Film-Flow-Meter SF 2, Messbereich: 20 - 1000 ml/min

Genauigkeit: 20 - 200 ml/min +/- 0,5%

200 - 1000 ml/min +/- 1,0%

9. Druckkalibrator

- Druck Limited, Leicester LE6 OFH England (Hersteller)
- Newport Electronics GmbH, 75392 Deckenpfronn (Vertrieb)

Druckkalibrator DPI 610,

Messbereich -1 bar - 2 bar gegen Atmosphäre: Genauigkeit +/- 1 mbar

Messbereich +/- 200 mbar Differenzdruck: Genauigkeit +/- 0,1 mbar

Kurzreferat

Membranreaktoren können als multifunktionale Reaktoren eingestuft werden, da unterschiedliche Prozessschritte (selektive Dosierung von Edukten oder Abführung von Produkten, Reaktion) in einer Baueinheit verbunden werden. Sie sind durch die Kopplung der chemischen Reaktion mit Stoff- oder Wärmetransportprozessen, die ein genaues Verständnis der Transportprozesse in der Membran erfordert, gekennzeichnet. Typische industrielle Reaktionen wie die partielle Oxidation von Kohlenwasserstoffen finden bei relativ hohen Temperaturen statt. Hierfür müssen anorganische Membranen verwendet werden. Die Stoff- und Wärmeübertragung in solchen Membranen müssen unabhängig und separat untersucht werden.

In der vorliegenden Arbeit sind solche Untersuchungen für mikroporöse, röhrenförmige Membranen aus Al_2O_3 durchgeführt worden. Die Untersuchungsmethode basiert auf einer experimentellen Matrix. Sie ermöglicht es, die Wärme- und Stofftransportparameter separat oder in kombiniertem Modus, ohne chemische Reaktion, zu ermitteln und zu validieren. Sowohl bei den Experimenten zum Wärmetransport als auch zum Stofftransport werden röhrenförmige, anorganische Membranen (Innendurchmesser 21 mm) in einem Reaktor platziert. Stationäre sowie instationäre Wärme- und Stofftransportexperimente wurden durchgeführt. Diese werden ausgewertet, um die effektiven Stoff- und Wärmetransportparameter der Membran zu identifizieren. Um den Stofftransport durch eine mehrschichtige poröse Membran quantitativ bestimmen zu können, ist es notwendig, die strukturellen Parameter jeder Schicht festzustellen. Zu diesem Zweck werden Gaspermeationsexperimente bei Variation des Drucks und der Temperatur durchgeführt. Das Dusty-Gas-Model wurde angewendet, um den Stofftransport durch die mehrschichtige poröse Membran auszuwerten und die strukturellen Parameter (d_p , ε/τ) der Membran abzuleiten. Diese experimentell ermittelten strukturellen Parameter wurden durch stationäre und dynamische Diffusionsversuche validiert.

Durch eine Simulationsanalyse wurde gezeigt, daß jede einzelne Schicht separat charakterisiert werden muß. Bei Betrachtung der Kompositmembran als eine homogene Schicht kann der Stofftransport nicht für alle Temperaturen und Gasen richtig beschrieben werden. Es wurde gezeigt, daß die Stromungrichtung und die Materialeigenschaften der Trennschicht eine wichtige Rolle spielen, insbesondere in katalytischen Membranreaktoren, wo kontrollierte Dosierungen von Edukten erwünscht sind. Die unterschiedlichen Trennschichten in der Kompositmembran ergeben unterschiedliche Druckprofile.

Permeationsexperimente mit reinen Gasen wurden auch für kleine Membranen (Innendurchmesser 7 mm) durchgeführt.

Zur Validierung der bereit identifizierten Transportparameter der Membran wurden Untersuchungen des gekoppelten Stoff- und Wärmetransports ohne chemischer Reaktion durchgeführt. Diese Untersuchungen tragen nicht nur zur besseren Erkenntnis des Wärme- und Stofftransports in der Membran sondern auch zur Validierung der vorher ermittelten Transportparameter bei.

Mit Hilfe einer Simulationsanalyse wurde der Einfluss der axialen Dispersion und der Temperatur auf die Zusammensetzung und die Strömungsgeschwindigkeit untersucht. Dabei kam zum Ausdruck, daß die axiale Dispersion eine Bedeutung, insbesondere im Eintrittsbereich des Reaktors haben kann.

Die Identifizierung und Validierung der Transportparameter der Membran ist von großer Bedeutung. Diese Arbeit zeigt, daß die Konfiguration des Membranreaktors zuverlässig, für verschiedene Grenzfälle ohne chemische Reaktion, modelliert werden kann. Es wird deutlich, daß auch in diesem Fall (ohne chemische Reaktion) die thermischen Effekte und der Zusammenhang zwischen Wärme- und Stofftransport betrachtet werden müssen.

Arshad Hussain

Curriculum Vitae

- 03.08.1970 geboren in Kot-Adu, Pakistan
- 1988 Intermediate (Pre-Eng.)
- 1993 B.E. Chemieingenieurwesen, N.E.D. Universität Karachi, Pakistan
- 1994-1996 Prozess-Ingenieur, Zuckerfabrik Layyah, Pakistan
- 1996-1997 Postgraduation in Lebensmitteltechnologie, TU Berlin,
Kampagne-Assistent, Zuckerverbund Nord AG, Braunschweig
- 1997-1999 Prozess-Ingenieur, Zuckerfabrik Layyah, Pakistan
- 1999-2001 M.Sc. Chemieingenieurwesen, Friedrich-Alexander Universität,
Erlangen
- 2002-2005 Wissenschaftlicher Mitarbeiter am Lehrstuhl für Thermische
Verfahrenstechnik der Otto-von-Guericke-Universität Magdeburg